

Diss. ETH ex. B

Diss. ETH No. 11873

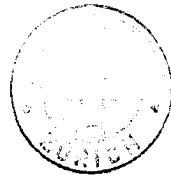
**New Concepts in Solid-State Pulse
Electron Spin Resonance**

DISSERTATION
submitted to the
SWISS FEDERAL INSTITUTE OF TECHNOLOGY ZÜRICH

for the degree of
Doctor of Natural Sciences

presented by
Gunnar Jeschke
Dipl. Chem. Technical University Dresden
born May 19, 1966
citizen of Germany

accepted on the recommendation of
Prof. Arthur Schweiger, examiner
Prof. Richard R. Ernst, co-examiner



C 118

Leer - Vide - Empty

*To see a world in a grain of sand
And a heaven in a wild flower,
Hold infinity in the palm of your hand,
And eternity in an hour.*

William Blake

Meinen Eltern

To my parents

Leer - Vide - Empty

Table of contents

Symbols and Abbreviations	9
Abstract	13
Zusammenfassung	15
1. Introduction	17
2. Tools for the description of spin dynamics	23
2.1 Spin Hamiltonians	23
2.2 Density operators and the equation of motion	30
2.3 Product operator formalism	33
2.4 Boltzmann equilibrium	34
2.5 Detection	35
3. Theory of electron-nuclear spin systems	39
3.1 Nuclear frequencies and electron spin transition moments	39
3.1.1 Reduction of dimensionality	39
3.1.2 Nuclear spins $I=1/2$	45
3.1.3 Nuclear spins $I>1/2$	55
3.2 Description of excitation	56
3.2.1 Rotating frame	56
3.2.2 Ideal non-selective microwave pulses	58
3.2.3 Ideal selective microwave pulses	60
3.2.4 Ideal semi-selective microwave pulses	63
3.2.5 <i>Non-ideal selective microwave pulses</i>	65
3.2.6 Non-ideal semi-selective microwave pulses	68
3.2.7 Non-ideal pulses of arbitrary strength and duration	70
3.2.8 Selective radio frequency pulses	80
3.2.9 Radio frequency chirp pulses	83
3.2.10 Combined microwave and radio frequency excitation	88

4. Manipulation of nuclear coherence	93
4.1 Nuclear coherence generators	93
4.1.1 SENSE generator	93
4.1.2 Mims generator	97
4.1.3 Single microwave pulse	98
4.1.4 Monochromatic radio frequency pulse	100
4.1.5 Chirp generators	101
4.1.6 Three-pulse generator	103
4.1.7 ELDOR generator	104
4.2 Nuclear coherence detectors	108
4.2.1 FID detection	108
4.2.2 Echo detection	109
4.2.3 Remote echo detection	109
4.2.4 Coherent Raman beat detection	110
4.2.5 Pulse train detection	113
4.2.6 Radio frequency detection	114
4.3 Manipulation of nuclear coherence	116
4.3.1 Sublevel transfer by a microwave p pulse	116
4.3.2 Refocusing by a radio frequency p pulse	122
4.3.3 Refocusing by microwave excitation	123
4.3.4 Correlation within the same electron spin manifold	124
4.4 Chirp time-domain ENDOR spectroscopy	126
4.4.1 One-dimensional time-domain ENDOR	126
4.4.2 HYSORE-type correlation experiment	128
4.4.3 TRIPLE-type correlation experiment	129
5. Matched two-pulse ESEEM	131
5.1 Features of two-pulse ESEEM	131
5.1.1 Practical considerations	131
5.1.2 Coherence transfer echo description	132
5.2 Sensitivity improvement and peak discrimination	135
5.2.1 Theoretical considerations	135
5.2.2 Simulations	137
5.3 Experimental examples	139
5.3.1 Nuclear-frequency enhanced ESEEM	139
5.3.2 Hyperfine-frequency enhanced ESEEM	142
6. Hyperfine decoupling	145
6.1 Basics	145
6.1.1 Decoupling in solid-state ESR	145
6.1.2 Theory	146
6.2 Pulse sequences	148
6.2.1 Spin-locked ESEEM	148
6.2.2 DECENT	150
6.2.3 Hyperfine-decoupled ENDOR	151
6.3 Experimental examples	154
6.3.1 Nuclear spin $I=1$ in an ordered system	154

6.3.2 Nuclear spin $I=1$ in a disordered system	156
6.3.3 Electron spin $S>1/2$	158
7. Hyperfine spectroscopy	165
7.1 Basics	165
7.1.1 General approach	165
7.1.2 Second order effects	167
7.2 Pulse sequences	171
7.2.1 ESEEM hyperfine spectroscopy	171
7.2.2 Chirp hyperfine spectroscopy	174
7.2.3 HYEND	175
7.3 Experimental examples	179
7.3.1 Ordered systems	179
7.3.2 Disordered systems	183
7.4 Proposed experiments	190
7.4.1 Probe-pulse detected HYEND	190
7.4.2 Refocussed HYEND	192
8. Zero-field ESEEM and ENDOR	193
8.1 Theory	193
8.1.1 Basics of zero-field ESR	193
8.1.2 Description of pulse experiments at zero magnetic field	196
8.1.3 Conditions for the observation of echo modulations	199
8.2 Experimental	202
8.2.1 Two-pulse ESEEM	202
8.2.2 Three-pulse ESEEM	204
8.2.3 ENDOR	208
8.2.4 Correlation experiments	210
9. Transient electron spin nutation	213
9.1 Resolution and assignment in ESR spectra	213
9.2 Nutation frequency	214
9.3 PEANUT sequence	220
10. Future trends	225
10.1 High-field high-frequency ESR	225
10.2 Quadrupole nuclei	229
10.3 ESR resolution	230
10.4 Technical problems	232
10.5 Technical opportunities	234
11. Conclusion	237
Appendix A	
Exact eigenvalues of the $S'=1/2, I=1/2$ spin Hamiltonian	241

Appendix B	
Instrumentation for chirped radio frequency pulses	243
Appendix C	
Residual splittings and second order shift for $I > 1/2$ nuclei during decoupling	249
Appendix D	
Spin Hamiltonian for $S' = 1/2$, $I = 1/2$ with orthorhombic hyperfine matrix	251
References	253
Subject Index	261
Acknowledgements	265
Curriculum vitae	267

Symbols and Abbreviations

Symbols

A	hyperfine interaction matrix
A	secular part of the hyperfine coupling
B	pseudo-secular part of the hyperfine coupling
B_0	external static magnetic field
B_1	effective part of the external microwave field
B_2	effective part of the external radio frequency field
D	zero-field splitting tensor
D	secular part of the zero-field splitting tensor
d_{HS}	dimension of the Hilbert space
E	pseudo-secular part of the zero-field splitting tensor
h	quantum of action, 6.626176×10^{-34} Js
\mathcal{H}	Hamilton operator
I	spin quantum number of the nuclear spin
k	Boltzmann's constant 1.380662×10^{-23} JK ⁻¹ , or
k	modulation depth parameter
m_I	magnetic quantum number of the nuclear spin
m_S	magnetic quantum number of the electron spin
$m_S^{(\alpha, \beta)}$	effective magnetic quantum number of the electron spin corresponding to the α (β) state of a fictitious spin 1/2

M_S	transition moment of an electron spin transition
$M_{x,y}$	magnetization in x-direction (y-direction)
P	nuclear quadrupole tensor
S	spin quantum number of the electron spin
T_1	longitudinal relaxation time
T_2	transverse relaxation time
T_m	phase memory time of the electron spin
t_p	pulse length
U	unitary propagator
β	pulse flip angle
β_e	electron Bohr magneton
β_n	nuclear Bohr magneton
Γ	linewidth (full width at half height) of an inhomogenously broadened line
$\hat{\Gamma}$	relaxation superoperator
η	one half of the angle between the nuclear spin quantization axes in the two electron spin manifolds
η_D	asymmetry of the zero-field splitting tensor
$\eta_{\alpha,\beta}$	angle between the nuclear spin quantization axis in the electron spin α (β) manifold and the direction of the external magnetic field
θ	polar angle between z -axis and radius vector
θ_k	tilt angle of an effective field
ν_{mw}	microwave frequency
σ	density operator of a spin system
σ_{eq}	density operator in Boltzmann equilibrium
τ	interpulse delay
ϕ	polar angle in the xy -plane
ϕ	phase
ω_1	on-resonant angular nutation frequency of the electron spin in an mw field
ω_2	on-resonant angular nutation frequency in an rf field
ω_I	nuclear Zeeman frequency in angular frequency units
ω_{Ix}'	pseudo-secular part of the hyperfine coupling for $S > 1/2$ system that behaves like a pseudo-secular part of the nuclear Zeeman interaction

ω_{mw}	angular microwave frequency
ω_{HF}	hyperfine <i>splitting</i> in angular frequency units
ω_{NZ}	nuclear Zeeman <i>splitting</i> in angular frequency units, may contain a first-order hyperfine contribution for $S > 1/2$
ω_{rf}	angular radio frequency
ω_S	resonance frequency of the electron spins in the laboratory frame
Ω_S	resonance <i>offset</i> of the electron spins
$\omega_{\alpha\beta}$	frequency of transition $ \alpha\rangle \leftrightarrow \beta\rangle$
$\mathbb{1}$	unity operator

Abbreviations

1D	one-dimensional
2D	two-dimensional
AFG	arbitrary function generator
CRB	coherent Raman beat
C-band	4-8 GHz
DECENT	decoupled ESEEM correlated to nuclear transition frequencies
DEFENCE	deadtime free ESEEM by nuclear coherence-transfer echoes
EC	electron coherence
ELDOR	electron-electron double resonance
ENDOR	electron nuclear double resonance
ESEEM	electron spin echo envelope modulation
ESR	electron spin resonance
EZI	electron Zeeman interaction
F-band	90-140 GHz
HFI	hyperfine interaction
HYEND	hyperfine-correlated ENDOR
HYSORE	hyperfine sublevel correlated ESEEM spectroscopy
mw	microwave
NC	nuclear coherence

NMR	nuclear magnetic resonance
NQR	nuclear quadrupole resonance
NZI	nuclear Zeeman interaction
PEANUT	phase-inverted echo-amplitude detected nutation
rf	radio frequency
S-band	2-4 GHz
SENSE	selective non-selective pulse pair
SOC	spin-orbit coupling
TEMPOL	4-hydroxy-2,2,6,6-tetramethyl-piperidin-1-oxyl
TEMPO	4-oxo-2,2,6,6-tetramethyl-piperidin-1-oxyl
W-band	75-110 GHz
X-band	8-12 GHz
ZFS	zero-field splitting

Abstract

Solid-state pulse electron spin resonance (ESR) is examined as a tool for the investigation of the dynamics of electron spins and of the nuclear spins coupled to them. A theoretical framework is established for the discussion of pulse ESR and electron nuclear double resonance (ENDOR) experiments on spin systems with arbitrary effective electron spin S and arbitrary nuclear spins. The excitation of electron and nuclear transitions by both microwave (mw) and radio frequency (rf) irradiation is treated comprehensively by taking into account existing approaches for several situations, defining the conditions for their validity, and extending the theory to non-ideal mw pulses of arbitrary strength and duration, to rf chirp pulses, and to combined mw/ rf probe pulses.

The generation, manipulation, and detection of nuclear coherence is discussed in some detail as a basis for time-domain experiments including two-dimensional correlation methods. Different approaches of nuclear coherence generation are compared to each other and their compatibility with nuclear coherence detectors is examined. Broad-band time-domain ENDOR experiments are introduced that use rf chirp pulses in a new type of nuclear coherence generators and detectors.

The newly derived theory of non-ideal mw pulses is applied to sensitivity enhancement and peak discrimination in the two-pulse electron spin echo envelope modulation (ESEEM) experiment. The resulting nuclear-frequency enhanced and hyperfine-enhanced matched ESEEM experiments make use of prolonged pulses with the mw field

matched to the nuclear Zeeman field. Signal gains compared to standard two-pulse ESEEM are obtained that may exceed one order of magnitude in favourable cases.

ESEEM and ENDOR experiments with hyperfine decoupling are introduced, among them the two-dimensional DECENT experiment that correlates decoupled nuclear frequencies to the spectrum observed with three-pulse ESEEM. The meaning of the term hyperfine decoupling for $S > 1/2$ systems is discussed and an experimental example is provided.

Hyperfine spectroscopy, i.e., the direct measurement of hyperfine splittings is investigated as a tool for resolution enhancement and spectrum simplification for both ordered and disordered systems. Several pulse sequences are introduced that are based on ESEEM, chirp ENDOR, and selective time-domain ENDOR methodology. The correlation of the hyperfine spectrum to the ENDOR spectrum in the HYEND experiment is shown to provide information that cannot be obtained with either of the one-dimensional experiments.

The first zero-field ESEEM and pulse ENDOR spectra are presented and a theory of pulse ESR at zero-field for Kramers systems is provided. Well resolved ESEEM and ENDOR spectra are obtained at zero field for a disordered system and their analysis is described.

Transient electron spin nutation is investigated as a means to obtain additional information on ESR transitions and to improve ESR resolution by introducing a second dimension. Influences of several parameters on nutation frequencies are discussed thoroughly and it is found that an experiment is needed that can detect transient nutation indirectly and can recover broad distributions of nutation frequencies. The PEANUT sequence is introduced that fulfils these requirements by echo detection of a rotary echo.

Future trends in the field of solid-state pulse ESR are discussed, in particular it is examined which impact the advent of high-field high-frequency pulse ESR will have on method development and applications.

Zusammenfassung

Gegenstand dieser Arbeit ist die Puls-Festkörper-ESR als ein Werkzeug zur Untersuchung der Dynamik von Elektronenspins und den mit ihnen gekoppelten Kernspins. Ein theoretischer Formalismus wird hergeleitet, mit dem Puls-ESR-Experimente und Elektron-Kern-Doppelresonanz- (ENDOR-) Experimente an Spinsystemen mit beliebigem effektivem Elektronenspin S und beliebigen Kernspins beschrieben werden können. Die Anregung von Elektronenspins und Kernspins durch Einstrahlung von Mikrowellen (MW) oder Radiowellen (RF) wird eingehend behandelt. Dabei werden verschiedene vorhandene Ansätze und die Bedingungen für deren Gültigkeit diskutiert, und die Theorie wird durch neue Ansätze für nichtideale MW-Pulse beliebiger Stärke und Dauer, für RF-Chirp-Pulse und kombinierte MW/RF-Abtastpulse erweitert.

Die Erzeugung, Manipulation und Detektion von Kernkohärenz wird im Detail erörtert um die Grundlagen für die Beschreibung von Zeitbereichsexperimenten einschließlich zweidimensionaler Korrelationsexperimente zu schaffen. Verschiedene Methoden zur Kernkohärenzzeugung werden miteinander verglichen und ihre Kompatibilität mit Detektionsmethoden wird untersucht. Als Beispiele für die Anwendung einer Klasse neuer Kernkohärenzgeneratoren werden Zeitbereichs-ENDOR-Experimente mit Breitbandanregung durch RF-Chirp-Pulse vorgestellt.

Die in dieser Arbeit neu eingeführte Theorie nichtidealer MW-Pulse wird auf die Empfindlichkeitsverbesserung und Unterscheidung verschiedener Spektralliniertypen im Zweipuls-Echomodulationsexperiment (ESEEM) angewendet. Durch den Einsatz verlängerter Pulse, bei denen das MW-Feld dem Kern-Zeeman-Feld angepaßt wird, wer-

den kernfrequenzverstärkte und hyperfeinfrequenzverstärkte Spektren erhalten, in denen der Signalgewinn im Vergleich zu Zweipuls-ESEEM in günstigen Fällen mehr als eine Größenordnung betragen kann.

ESEEM- und ENDOR-Experimente mit Hyperfeinentkopplung werden eingeführt, unter ihnen das zweidimensionale DECENT-Experiment, das die entkoppelten Kernfrequenzen mit dem Dreipuls-ESEEM-Spektrum korreliert. Die Bedeutung des Begriffes Hyperfeinentkopplung für $S > 1/2$ wird theoretisch und anhand eines experimentellen Beispiels diskutiert.

Hyperfeinspektroskopie als die direkte Messung von Hyperfeinaufspaltungen wird in Hinblick auf die Verwendung zur Auflösungsverbesserung und Spektrenvereinfachung sowohl für geordnete als auch ungeordnete Systeme untersucht. Pulssequenzen auf der Basis von ESEEM-, Chirp-ENDOR- und selektiver Zeitbereichs-ENDOR-Methodik werden vorgestellt. Information, die weder mit ENDOR-Spektroskopie noch mit eindimensionaler Hyperfeinspektroskopie erhalten werden kann, wird durch das HYEND-Experiment zugänglich, das die Spektren beider Methoden miteinander korreliert.

Die ersten Nullfeld-ESEEM- und Nullfeld-Puls-ENDOR-Spektren werden vorgestellt und eine theoretische Beschreibung für Puls-ESR-Experimente im Nullfeld wird gegeben. Gut aufgelöste ENDOR-Spektren werden im Nullfeld für ein ungeordnetes System erhalten und ihre Analyse wird beschrieben.

Zusätzliche Information über ESR-Übergänge und eine verbesserte ESR-Auflösung durch Einführung einer zweiten Dimension können mit transientser Elektronenspinrotation erreicht werden. Der Einfluß verschiedener Parameter auf die Nutationsfrequenzen wird eingehend untersucht, und es wird der Schluß gezogen, daß ein geeignetes Experiment die indirekte Beobachtung der transienten Nutation und die getreue Wiedergabe breiter Nutationsfrequenzverteilungen ermöglichen sollte. Diese Anforderungen werden von der PEANUT-Sequenz erfüllt, die ein Rotationsecho über eine weitere Echobildung detektiert.

Zukunftstendenzen auf dem Gebiet der Festkörper-Puls-ESR werden erörtert, insbesondere wird untersucht, welchen Einfluß das Aufkommen der Hochfeld/Hochfrequenz-ESR auf die Methodenentwicklung und Anwendung haben wird.

Species with unpaired electrons play an important role in chemistry. Among them are free radicals that are the reactive intermediates in photoreactions and in a number of thermal reactions, and transition metal ions that are the most important redox catalysts and the active centres of a number of other catalysts used in organic syntheses. There is also an considerable interest in such species in bioscience, since radicals figure as intermediates in photosynthesis, and transition metal ions are constituents of metalloproteins with enzymatic activity. The role of free radicals and transition metal catalysts in industrial polymerization processes as well as the fact that defect centres and impurities in semiconductors, glasses and ceramics are often connected with unpaired electrons, imply a considerable importance in materials science. Furthermore, radiation damage in materials and foodstuffs can be assessed by studying the resulting defect centres and free radicals. The occurrence of free radicals in biological tissues is discussed as a possible cause of cancer. It is therefore of utmost interest to obtain precise information on the structure and dynamics of these species.

With few exceptions, unpaired electrons lead to a non-vanishing spin of a particle that can be used as a spectroscopic probe. It turns out that transitions between electron spin states can be induced by on-resonant electromagnetic radiation which is chemically non-destructive, and that the energies of the electron spin states depend on a number of structure-related parameters. The measurement of electron spin transition frequencies and the evaluation of structural information from them is the main purpose of electron spin reso-

nance (ESR) spectroscopy. In many cases, it is however possible to obtain much more detailed information by interpreting ESR spectroscopy in a broader sense as the investigation of the dynamics of electron spins and of the nuclear spins coupled to them.

ESR spectroscopy in the narrower sense of the term has largely remained a domain of continuous-wave (cw) methods. The main reason for this lies in the fact that, except for organic radicals in solution and for a few defect centres in single crystals, it is hitherto technically impossible to excite the whole spectrum by a pulse of electromagnetic radiation. Therefore, Fourier-transform (FT) ESR cannot make use of the multiplex advantage to the same extent as FT nuclear magnetic resonance (NMR) spectroscopy. Furthermore, cw ESR records derivatives of absorption spectra by using magnetic field modulation between about 10 to 100 kHz; a method that enjoys the advantages of narrow-band detection at the modulation frequency and of better resolution of the derivative as compared to the absorption lineshape. Calculating the derivative from the absorption lineshape obtained with pulse methods results in a decrease in signal-to-noise ratio. For these reasons, cw ESR is usually more sensitive than pulse ESR at a given resolution. Furthermore, pulse methods rely on relaxation times of the transverse magnetization that are longer than the spectrometer deadtime, a condition that is much more restrictive than the conditions on relaxation times for the observation of cw ESR. Therefore, for a number of transition metal ions, cw ESR can be measured at ambient temperature while pulse ESR measurements require liquid helium cooling. Nevertheless, there is at least one case where the measurement of electron spin transition frequencies by pulse ESR is advantageous even if not the whole spectrum can be excited at once. To measure broad spectral features, cw ESR is a poor method, since field modulation amplitudes larger than about 4 mT cannot be easily obtained and the derivative is then very small. Such features are either invisible in cw ESR or perturbed even by small baseline drifts, while they can be well distinguished in the absorption spectra obtained with pulse ESR methods [1].

On the other hand, ESR in the broader sense of the term, i.e., the detailed investigation of spin dynamics and the investigation of nuclear spins coupled to the electron spin is the playground of pulse methods. Though the interaction with nuclear spins can also be investigated with cw electron nuclear double resonance (ENDOR) and electron electron double resonance (ELDOR), these methods depend on a critical balance of several relax-

ation times. Therefore, it may be cumbersome to find suitable experimental parameters, in particular a suitable temperature, and the effects are usually as small as a few percent of the cw ESR signal even at optimum conditions. The absence of a cw ENDOR or ELDOR effect does not indicate the absence of coupled nuclei, it may result just from unfortunate ratios of the relaxation times. In contrast, pulse ENDOR effects are typically comparable in magnitude with pulse ESR signals, the experiment can be performed whenever such a signal is observed, and it registers all nuclei with significant couplings.

However, the main advantage of pulse ESR with respect to cw ESR lies in the possibilities to manipulate the spin system nearly at will and to obtain just the needed information. Examples for such manipulations include spectral editing [2], establishing correlations via two-dimensional (2D) spectroscopy [3], separation of different contributions to relaxation [4,5], direct measurement of transition probabilities [6] and the enhancement of forbidden transitions [7]. The design of pulse ESR experiments for such purposes requires a thorough understanding of the dynamics of electron-nuclear spin systems both in the absence and presence of external perturbations. After discussing the basic tools for the description of spin dynamics in Chapter 2, this thesis attempts to provide the needed theoretical framework for the description and design of state-of-the-art pulse ESR experiments in Chapter 3 and 4. In doing that, we will restrict ourselves to spectroscopy on solid-state samples. It is obvious from the list given at the beginning of this chapter that the majority of the interesting problems is covered in spite of this restriction. Moreover, the differences between the description of NMR and ESR experiments are much larger in solid-state work than for experiments in solution, and this thesis generally does not attempt to relate the concepts that are commonplace in NMR and are described in a number of good textbooks [8-11].

The necessity to supplement the theory of spin dynamics developed for NMR spectroscopy with ESR-specific modifications arises from a number of major differences in the relative size of interactions. First, both scalar and dipolar *nuclear-nuclear* couplings are much smaller than nuclear Zeeman interactions at the usual high static fields. This allows one to make use of the so-called high-field approximation in which the quantization of the nuclear spins is assumed to be solely due to the Zeeman interaction and other interactions only introduce comparatively small splittings. However, in ESR spectroscopy

copy the high-field approximation breaks down fairly often for the electron spin and almost generally for the nuclear spins (see Chapter 3). This breakdown is the source of many of the more interesting effects in pulse EPR, namely the possibility to excite *nuclear* spins solely by irradiation on-resonant with *electron* spin transitions, and of the rich information content of transient nutation frequencies (see Chapter 9). Second, the vast majority of NMR literature is dedicated to ideal pulses that are assumed to excite the whole spectrum uniformly and are short compared with the times needed for significant evolution of the spin system under the unperturbed Hamiltonian. In §3.2 it is shown that this is a poor assumption in pulse EPR and that a number of interesting effects can be explained only by considering non-ideal pulses. Third, experiments on an electron spin coupled to nuclear spins differ from heteronuclear NMR experiments due to the fact that the Zeeman interaction of the electron spin is by nearly three orders of magnitude larger than the one of all nuclear spins, while in heteronuclear NMR this ratio is almost never larger than one order of magnitude. While the first two differences complicate ESR theory with respect to NMR theory, the third one simplifies it, as will be detailed in §3.1. This simplification often allows one to partition large spin systems into subsystems consisting of only one electron spin transition and one nuclear spin, an approach that can be valuable also for the simulation of cw ESR spectra of transition metal complexes with explicit consideration of ligand hyperfine interactions. Chapter 4 provides an overview of methods to observe and manipulate the behaviour of nuclear spins coupled to electron spins. Time-domain ENDOR with broadband excitation by chirp pulses is introduced as an example of a new approach to this task.

The theoretical approach to non-ideal pulses is applied in Chapter 5 to the design of matched two-pulse electron spin echo envelope modulation (ESEEM) experiments that allow for the selective enhancement of peaks in two-pulse ESEEM spectra. These experiments are the first example for the sensitivity gains that are possible by using a special kind of Hartmann-Hahn match [12] between electron spins in a rotating frame (or dressed electron spin states [13,14]) and nuclear spins in the laboratory frame. Chapter 6 introduces hyperfine decoupling that differs from typical NMR decoupling schemes by the fact that the observation of the nuclear spins is performed via the electron spins which are decoupled during the evolution time of the experiment.

A new type of spectroscopy, namely the direct measurement of hyperfine splittings, termed hyperfine spectroscopy, is described in Chapter 7. Hyperfine spectroscopy reduces the number of lines to one per inequivalent nucleus irrespective of the electron and nuclear spin quantum number, so that it is very useful to simplify spectra and overcome assignment ambiguities. The correlation of nuclear and hyperfine frequencies in a 2D experiment allows one to separate spectral features that overlap in both dimensions and reintroduces the information lost in the spectrum simplification.

One of the major problems of magnetic resonance spectroscopy in the solid state is the low intrinsic resolution, since the external magnetic field removes the isotropy of space, so that the interactions become orientation dependent and line broadening arises. In a number of relevant systems, the zero-field splitting of electron spin energy levels is so large that measurements with sufficient sensitivity can be performed in the absence of an external static magnetic field. Chapter 8 develops the theory of pulse ESR spectroscopy under such conditions and describes the first ESEEM and pulse ENDOR experiments at zero field.

While all preceding chapters are concerned with the observation of nuclear spin dynamics via the electron spin, Chapter 9 discusses the unravelling of complicated ESR spectra. In some cases, knowledge of the electron spin transition frequencies may not be sufficient to obtain the full information on the interactions of the electron spin or it may be too complicated to evaluate the parameters from the spectrum. It is then of great value to know also the transition probabilities that depend in another way on the same parameters. These transition probabilities cannot be obtained with high precision from the intensities in cw or pulse ESR spectra, since intensities are influenced by additional factors, the main problem being different relaxation times for different transitions. A much more direct approach to the measurement of transition probabilities or to the separation of spectral features corresponding to different transition probabilities are transient nutation experiments. Chapter 9 discusses the echo-detected rotary echo as a way to measure transient nutation frequencies and discusses the parameters on which these frequencies depend.

Finally, Chapter 10 is concerned with future trends in solid-state pulse ESR spectroscopy. It is examined how the advent of high-field-high-frequency ESR is expected to

influence the methodology for studying nuclear spins coupled to the electron spin, which spectroscopic tasks cannot be solved satisfactorily with existing experiments, which technical problems restrict the performance of these experiments and which new technical opportunities are not yet applied.

Tools for the description of spin dynamics

2.1 Spin Hamiltonians

At this point it should be mentioned that the term “electron spin resonance” is actually a simplification, since the electron spin is almost always coupled to some extent to the orbital momentum of the electron. This phenomenon is termed spin-orbit coupling (SOC). Orbital momenta are almost completely quenched by chemical bonding in organic radicals (with the exception of cases where the energies of two orbitals are nearly degenerate), but SOC is significant for first row transition metal ions and nearly complete for rare earth ions. Especially in the last case, where the total angular momentum is the sum of the spin and orbital momenta, the term electron *spin* resonance seems to be hardly appropriate, so that one often uses “electron paramagnetic resonance” (EPR) instead. Nevertheless, we stick here with the term pulse ESR without excluding cases of strong SOC, since electron *spin* echo and electron *spin* echo envelope modulation (ESEEM) are commonly used terms without a “paramagnetic” equivalent. In addition, the coupling of angular momenta always results in another angular momentum, so that even complete SOC does not lead to qualitative changes. It is then always possible to describe a set of $2S+1$ states that differ in just their angular momenta by an *effective* spin S , where S is a half-integer or an integer. Whenever we speak of an electron spin S in the following, the reader should be aware that this term can be substituted by “effective spin” without any changes in the theory. Accordingly, effective spins $S > 1/2$ in high-spin transition metal complexes will be designated as electron spins $S > 1/2$ hereafter.

To obtain the transition frequencies and transition probabilities between the $2S+1$ states, we obviously need to consider all interactions that lead to energy differences between states with different angular momenta. The contributions of all these interactions make up the spin Hamiltonian that will be given in angular frequency units throughout this work.

The first contribution we consider here is the electron Zeeman interaction (EZI), i.e. the coupling of the magnetic dipole moment of the electron spin to the external static magnetic field. Obviously, the EZI is isotropic for a *free* electron spin for symmetry reasons. On the other hand, the interaction of orbital momenta with an external magnetic field is anisotropic also for symmetry reasons. An admixture of orbital moments by the SOC therefore leads to an anisotropic EZI, which is usually formulated as

$$\mathcal{H}_{EZ} = \frac{2\pi\beta_e}{h} \mathbf{B} \mathbf{g} \mathbf{S} , \quad (2.1)$$

where \mathbf{B} and \mathbf{S} are the vector representations of the external magnetic field and of the electron spin, respectively, and \mathbf{g} is an interaction matrix of dimension 3×3 (*g*-matrix)¹. The relation of spin Hamiltonian parameters like the *g*-matrix to the structure of a paramagnetic centre is not the subject of this thesis, but note that a good introduction into the problem is given in [10].

For $S > 1/2$ in symmetries less than cubic one observes also a field-independent level splitting (zero-field splitting, ZFS), for which the Hamiltonian is given by

$$\mathcal{H}_{ZFS} = \mathbf{S} \mathbf{D} \mathbf{S} , \quad (2.2)$$

where \mathbf{D} is the zero-field interaction tensor or fine structure tensor. For triplet states of organic molecules ($S=1$) this interaction arises from spin-spin coupling. Its notation is formally identical with the one of the nuclear quadrupole interaction (see below), so that

1. In most of the literature, \mathbf{g} is referred to as *g* tensor, but this is not exact and may lead to errors since \mathbf{g} does not have the same transformation properties as a tensor. The key difference is that the *g* matrix links *two* coordinate frames, namely the ones of the magnetic field and of the spin, that do not necessarily coincide, while the matrix representation of a tensor is defined with respect to *one* frame. A more detailed discussion of this point can be found in [15].

Abraham and Bleaney call it electronic 'quadrupole' fine structure for transition metal ions [16]. In fact, these authors show that it can be considered as arising from a quadrupolar distortion of the magnetization density. This distortion in turn, is caused by a second order effect of the SOC. It can be shown that the trace of \mathbf{D} is of no spectroscopic significance, since it shifts all levels by the same energy. As a traceless tensor, \mathbf{D} can be written in its principal axes frame with only two parameters

$$\mathcal{H}_{\text{ZFS}}^{(0)} = D \left[S_z^2 - \frac{1}{3} S(S+1) \right] + \frac{E}{2} (S_+^2 + S_-^2) \quad (2.3)$$

where S_+ and S_- are raising and lowering operators, respectively. One may define an asymmetry η of the \mathbf{D} tensor by

$$\eta_{\mathbf{D}} = \frac{E}{D} . \quad (2.4)$$

The case of $\eta_{\mathbf{D}}=0$ ($E=0$) corresponds to an axial ZFS tensor. For spins $S>2$, there may be a higher order ZFS contribution to the Hamiltonian that corresponds to a hexadecapolar distortion of the magnetization density. This term is given by

$$\mathcal{H}'_{\text{ZFS}} = \frac{a}{6} \left[S_x^4 + S_y^4 + S_z^4 - \frac{1}{5} S(S+1)(3S^2 + 3S - 1) \right] . \quad (2.5)$$

As is apparent from the form of $\mathcal{H}'_{\text{ZFS}}$, this contribution does not vanish in cubic symmetry. \mathcal{H}_{ZFS} and $\mathcal{H}'_{\text{ZFS}}$ can be expressed elegantly in terms of irreducible tensor operators for the electron spin of second and fourth degree, respectively [16]. In symmetries less than cubic, there may also be other higher-order ZFS terms.

In the following, we assume that n nuclear spins I_1, I_2, \dots, I_n are coupled to the electron spin. In this case, the coupling of the electron spin's magnetic dipole moment with the magnetic dipole moments of the nuclear spins provides another contribution to the state energies. This so-called hyperfine interaction (HFI) can be written as

$$\mathcal{H}_{\text{HF}} = \sum_{k=1}^n \mathbf{S} \mathbf{A}_k \mathbf{I}_k , \quad (2.6)$$

where the \mathbf{A}_k are the HFI matrices (see footnote on page 24) and the \mathbf{I}_k are vector representations of the nuclear spin. The HFI consists of two parts. First there is a dipolar coupling (through space) between the electron spin and the nuclear spins. In the so-called point-dipole approximation, where both spins are assumed to be located, this part is given by [17]

$$\mathcal{H}_{\text{HFDD}} = \frac{\hbar^2 \mu_0}{4\pi r_{\text{en},k}^3} \beta_e g_e \beta_n g_{n,k} \left[\mathbf{S} \mathbf{I}_k - \frac{3}{r_{\text{en},k}^2} (\mathbf{S} \cdot \mathbf{r}_{\text{en},k})(\mathbf{I}_k \cdot \mathbf{r}_{\text{en},k}) \right], \quad (2.7)$$

where $\mathbf{r}_{\text{en},k}$ is the vector connecting the electron spin with the k -th nuclear spin, $r_{\text{en},k}$ the length of this vector, g_e and $g_{n,k}$ are the g -value of the free electron¹ of the k -th nucleus, respectively and β_e and β_n are the corresponding Bohr magnetons. Second, there is a finite spin density of the electron spin at a nucleus if the s -orbital of this atom contributes to the molecular orbital occupied by the electron spin. Such s -orbital spin density leads to isotropic hfi, the contribution is called the Fermi contact interaction. In contrast, spin density of the unpaired electron in p -, d -, or f -orbitals leads to a purely anisotropic coupling, since these orbitals feature vanishing electron density at the nucleus and are of non-spheric symmetry. A more detailed discussion of the second mechanism of HFI can be found in [17]. If different isotopes of the same element exhibit hyperfine couplings, their ratio is determined by the ratio of the nuclear g values. Small deviations from this ratio may occur for the Fermi contact interaction, since the electron probes the inner structure of the nucleus if it is in an s -orbital. However, this so-called hyperfine anomaly is usually smaller than 1% [16]. For transition metal ion complexes, the HFI with the transition metal nucleus (central atom) is often by one or even two orders of magnitude larger than the one with the ligand nuclei; the latter is sometimes called superhyperfine interaction. In this case, it is convenient to treat central atom and ligand hfi separately, as will be shown in §3.1.1. It should be noted here that for very strong couplings between electron and nuclear spin, there may also be higher-order terms of the form $\mathbf{S}^l \mathbf{A}^{(lm)} \mathbf{I}^m$ with even $l+m$, for instance quadrupole hyperfine terms with $l+m=2$ [18].

1. g_e has to be replaced by the actual g -value for an isotropic g -matrix. For anisotropic g -matrices, Eq. (2.7) is not valid. Nevertheless it is often used as an approximation in cases where the anisotropy is small.

While all contributions to the spin Hamiltonian considered so far involve the electron spin and cause first order energy shifts or splittings in the ESR spectrum, there are also terms that involve only nuclear spins. Aside from their importance for the calculation of ENDOR and ESEEM spectra, these terms may influence the ESR spectrum significantly in situations where the high-field approximation for the *nuclear* spin breaks down and second order effects become important. The first of these interactions is the coupling of the nuclear spin to the external static magnetic field, termed nuclear Zeeman interaction (NZI). For our purposes, it can be considered isotropic and written as

$$\mathcal{H}_{\text{NZ}} = -\frac{2\pi\beta_n}{h} B_0 \sum_{k=1}^n g_{n,k} I_{z,k}, \quad (2.8)$$

where the z -axis of the nuclear spin is chosen along the axis of the external static magnetic field with magnitude B_0 . In the following, we use the abbreviation

$$\omega_{Ik} = -\frac{2\pi\beta_n g_{n,k} B_0}{h}. \quad (2.9)$$

The negative sign implies that, unlike for electron spins, states with larger magnetic quantum number m_{Ik} have smaller energy for positive g_n values. In principle, there is a small anisotropic contribution to the NZI, the chemical shift anisotropy. It is usually smaller than 0.1% and not resolved in ENDOR or ESEEM spectra (see Fig. 2-1 on page 29).

Since atomic nuclei are not exactly spherical, their spin leads to an electric quadrupole moment if $I_k > 1/2$. This moment interacts with the electric field gradient at the point of the nucleus which in turn arises from an uneven charge distribution over the radical, complex or other paramagnetic centre. The nuclear quadrupole interaction (NQI) can be written as

$$\mathcal{H}_{\text{NQ}} = \sum_{I_k > \frac{1}{2}} \mathbf{I}_k \mathbf{P}_k \mathbf{I}_k. \quad (2.10)$$

Comparison with Eq. (2.2) shows that the NQI can be formally treated in an analogous way as the ZFS. Note however, that a representation as in Eq. (2.3) refers to another

frame than the representation of the NZI in Eq. (2.8). Furthermore, higher order terms as in Eq. (2.5) are not significant in the case of NQI.

Finally, we have to consider the coupling of nuclear spin magnetic dipole moments with each other. The form of this interaction is given by Eq. (2.7) where the electron spin S is substituted by a second nuclear spin I_j . Nuclear dipole-dipole coupling is usually unresolved in ESEEM and ENDOR spectra, it is however often the main contribution to the linewidth. In most treatments, this interaction is not considered explicitly in the spin Hamiltonian but accounted for in an “effective” transverse relaxation time T_{2n} of the nuclear spins. It should be noted that the assumption of exponential decay and a common T_{2n} for transverse nuclear magnetization in the solid state is not well founded in theory [8] and does not necessarily account for the exact lineshapes even in the absence of dipolar line broadening. Nevertheless, this assumption is often sufficient for the interpretation of ENDOR and ESEEM spectra when there is no particular interest in the lineshapes.

The complete spin Hamiltonian for the description of pulse ESR experiments except for higher order hyperfine and ZFS terms that are significant only in a few cases, is then given by

$$\mathcal{H}_0 = \mathcal{H}_{EZ} + \mathcal{H}_{ZFS} + \mathcal{H}_{HF} + \mathcal{H}_{NZ} + \mathcal{H}_{NQ} . \quad (2.11)$$

This Hamiltonian is often referred to as the Abragam-Pryce spin Hamiltonian, since it was first derived by these two authors [19]. For the calculation of the eigenvalues and eigenstates of a Hamiltonian it is of considerable importance to know the approximate magnitude of the terms in Eq. (2.11), since interactions can be treated separately if they differ in at least two orders of magnitude. An overview of typical interaction strengths is given in Fig. 2-1 on page 29.

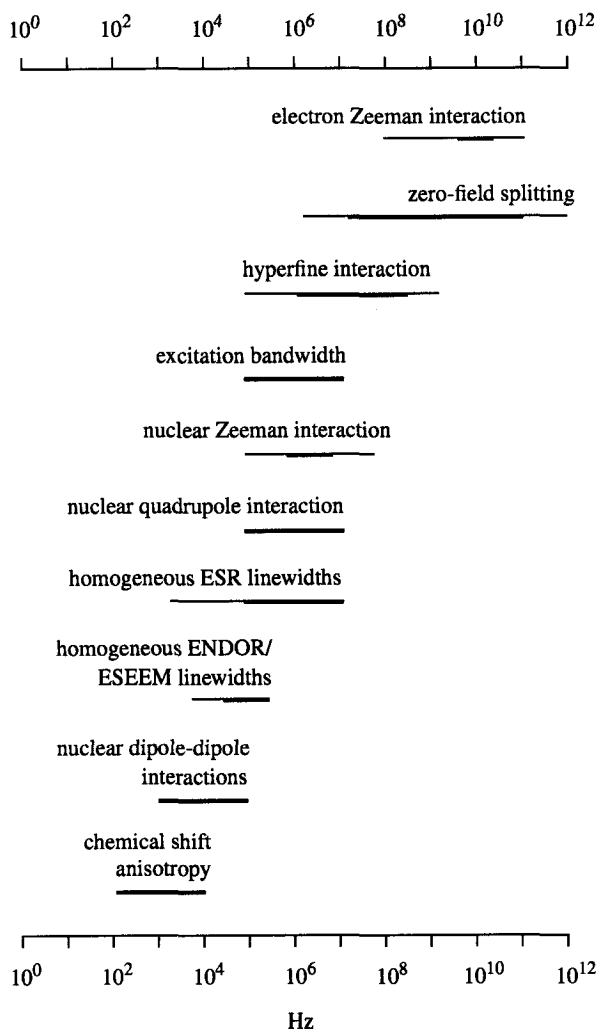


Fig. 2-1 Typical magnitude of interactions of electron and nuclear spins in the solid state (logarithmic scale). Bold lines correspond to X-band measurements on free radicals or transition metal complexes, narrow lines include defect centres and measurements at frequencies between L-band and W-band.

2.2 Density operators and the equation of motion

Any state of an ensemble¹ of isolated spins S can be described by a superposition of $2S+1$ mutually orthogonal wavefunctions, the so-called basis functions or basis states. The basis states thus span a Hilbert space of dimension $2S+1$. For reasons that become apparent later, it is convenient to characterize the state not by the set of $2S+1$ complex coefficients in the linear combination of the basis functions but by a matrix of dimension $2S+1$. Actually, this matrix is the representation of an operator, called the density operator that is defined by

$$\sigma(t) = \sum_{i=1}^{2S+1} \sum_{j=1}^{2S+1} \overline{c_i(t) c_j^*(t)} |i\rangle \langle j|, \quad (2.12)$$

where $|i\rangle$ and $\langle j|$ are a ket and a bra corresponding to the i th and j th basis state and the bar denotes the ensemble average. From Eq. (2.12) it is obvious that $\sigma_{ji} = \sigma_{ij}^*$, so that $\sigma(t)$ is a hermitian operator. For the system of an electron spin S coupled to n nuclear spins I_1, I_2, \dots, I_n , the Hilbert space is given by the tensor product of the Hilbert spaces of the single spins and has the dimension

$$d_{\text{HS}} = (2S+1) \prod_{k=1}^n (2I_k + 1). \quad (2.13)$$

Therefore, the density operator of this system can be represented by a $d_{\text{HS}} \times d_{\text{HS}}$ matrix. We will see however in Chapter 3 that for the description of pulse ESR experiments the Hilbert space can be partitioned into subspaces and that experiments can often be described in terms of n density operators of dimension $2I_k$.

1. Although the density operator formalism has been developed with an ensemble interpretation in mind, a probabilistic interpretation for a single spin is also feasible. This is obvious for ergodic systems, i.e., systems in which energy is the only constant of motion. A key feature of ergodic systems is the equality of ensemble and time averages. The fact is of importance for the description of *repeated* experiments on a single spin [20-22] by density operator approaches.

The convenience of the density operator approach arises mainly from the fact that one can apply to σ the well developed algebra of hermitian operators. In addition, one obtains a simple equation for the description of the time evolution of σ , namely

$$\frac{d}{dt}\sigma(t) = -i[\mathcal{H}, \sigma(t)] - \hat{\Gamma}[\sigma(t) - \sigma_{\text{eq}}] \quad (2.14)$$

where $\hat{\Gamma}$ is the relaxation superoperator with Liouville space dimension d_{HS}^2 and σ_{eq} the density operator at Boltzmann equilibrium (see §2.4). This equation is the quantum mechanical master equation and applies *generally* to the evolution of density operators as long as we allow for time-dependent Hamiltonians $\mathcal{H}(t)$ and relaxation superoperators $\hat{\Gamma}(t)$. This equation can be regarded as a separation of the motion of the density operator into an oscillating term (first term on the right hand side of Eq. (2.14)) corresponding to the internal interactions of the spin system and a decay term (second term) corresponding to the interaction of the spin system with its environment. The first term is invariant under time reversal, i.e., it describes a reversible motion, while the second term describes an irreversible process. The critical point in the application of Eq. (2.14) is clearly the partitioning of the whole system into a spin system and its environment, which may be complicated for solid-state samples since there is no clear borderline between large and small spin-spin interactions. The partitioning may also depend on the particular experiment, for instance, even very small interactions may have a significant influence on the oscillatory motion, if they are on-resonant with a degenerate or nearly degenerate transition (see §3.2.7).

The solution of Eq. (2.14) is particularly simple if both \mathcal{H} and $\hat{\Gamma}$ do not depend on time. Usually, the assumption of a time-independent $\hat{\Gamma}$ is well justified for experiments that rely on only microwave (mw) and radio frequency (rf) irradiation since these do not perturb strongly the environment of the spin system. It should be checked however in cases where transient species are created by irradiation with visible or ultraviolet light, x-rays, or γ -quants and observed immediately by ESR spectroscopy. \mathcal{H} is time-independent in the absence of dynamic external perturbations and chemical exchange. If dynamic external perturbations are present, it is often possible to transform the master equation

into a rotating frame where the significant part of the Hamiltonian either becomes time-independent or can be approximated with sufficient precision by a time-independent average Hamiltonian, see for instance §3.2.8.

If one is only interested in the oscillatory part of the motion, i.e., in transition frequencies and relative line intensities, one can neglect the relaxation term in Eq. (2.14) and obtains the Liouville-von-Neumann equation

$$\frac{d\sigma}{dt} = -i[\mathcal{H}, \sigma(t)] . \quad (2.15)$$

For a time-independent \mathcal{H} , the solution of the Liouville-von-Neumann equation is given by

$$\sigma(t) = \exp(-i\mathcal{H}t) \sigma(0) \exp(i\mathcal{H}t) . \quad (2.16)$$

This equation can be applied with different Hamiltonians \mathcal{H} and times t for subsequent steps of an experiment, a method that is called density operator formalism. Eq. (2.16) can be further simplified by transforming it to a frame where \mathcal{H} is diagonal. In this case, one obtains

$$\sigma_{jj}(t) = \sigma_{jj}(0) , \quad (2.17a)$$

and

$$\sigma_{jk}(t) = \sigma_{jk}(0) \exp\{i(\mathcal{H}_{jj} - \mathcal{H}_{kk})t\} . \quad (2.17b)$$

Eqs. (2.17a,b) lead to a simple interpretation of the matrix elements of the density operator in the frame where \mathcal{H} is diagonal. The σ_{jj} are probabilities to find the system in the pure j -th eigenstate of \mathcal{H} (population of the state $|j\rangle$), while the σ_{jk} quantify the occurrence of coherent superpositions (hereafter coherences) of two eigenstates. Because of the large differences in the behaviour of electron and nuclear spins, it is useful to characterize coherences according to the difference in the electron and nuclear spin states. Suppose that we can solve the eigenproblem of \mathcal{H} for the electron spin and the nuclear spins separately¹. Any eigenstate of the whole system is then a product of an electron spin eigenstate and a nuclear spin eigenstate. Coherences between two states that differ in only their nuclear (electron) spin part are then called nuclear coherences (allowed elec-

1. This assumption will be justified in §3.1.1.

tron coherences), and coherences between states that differ in their electron *and* nuclear spin parts are forbidden electron spin coherences. This terminology is discussed in some more detail in Chapter 3.

A density operator that does not contain off-diagonal elements (coherences) in the frame where \mathcal{H} is diagonal is obviously invariant under a time evolution governed by \mathcal{H} (cf. Eq. (2.17a,b)). In addition, the dimension of the relaxation superoperator $\hat{\Gamma}$ can be reduced from d_{HS}^2 to d_{HS} , since only populations must be considered. With the new reduced relaxation matrix \mathbf{W} and the vector of populations \mathbf{p} we obtain from Eq. (2.14)

$$\frac{d}{dt}\mathbf{p} = -\mathbf{W} [\mathbf{p}(t) - \mathbf{p}_{\text{eq}}], \quad (2.18)$$

which is a master equation for populations [9]. In contrast to Eq. (2.14), this equation does not pose particular theoretical problems in the solid state, since an exponential relaxation of a group of similar spins (spin bath) towards an equilibrium state can well be justified by the concept of spin temperature [8], so that one can usually assume longitudinal relaxation times T_{1e} , $T_{1f,k}$ and $T_{1n,k}$ for allowed electron spin transitions, forbidden electron spin transitions, and nuclear spin transitions, respectively. Problems in defining spin baths correctly may however arise if \mathcal{H} contains an external perturbation [23]. Eq. (2.18) can be solved analogously to Eq. (2.15), i.e., in a frame where \mathbf{W} is diagonal, we obtain for the elements of the vector \mathbf{p}' (that are linear combinations of the elements of \mathbf{p})

$$p'_j(t) = p'_{\text{eq},j} + \exp(-W_j t) [p'_j(0) - p'_{\text{eq},j}], \quad (2.19)$$

where $p'_{\text{eq},j}$ is the equilibrium value of p'_j .

2.3 Product operator formalism

In a frame where the unperturbed Hamiltonian \mathcal{H}_0 is diagonal, many pulse ESR experiments can be conveniently described as sequences of pulses that cause transfers between the different elements of σ and of periods of free evolution of σ . It turns out that such a description can be highly formalized by calculating the transfer of components of σ to each other during ideal microwave pulses of a given flip angle and during free evolution

of duration t [9,24]. To that end, a decomposition of the density operator has to be found that leads to simple expressions for the transfers and evolutions. The most popular partition in NMR spectroscopy uses cartesian basis operators I_x , I_y , and I_z and the unit operator $\mathbb{1}$ for each spin $I=1/2$ and combines them to all possible products. It can be shown that the resulting set of product operators forms a complete basis and that normalization can be achieved by multiplying products of n cartesian spin operators with 2^{n-1} . For two cartesian product operators A and B in any system consisting of only spins $1/2$, the relation

$$\exp(-i\beta A)B\exp(i\beta A) = \cos\beta B - i\sin\beta [A, B] \quad (2.20)$$

holds [25] and can be used to simplify Eq. (2.16) if \mathcal{H} is also expressed in terms of product operators. By means of Eq.(2.20) one can calculate a table of transfers and evolutions of all product operators under the relevant pulses and Hamiltonians. With this table it is then possible to discuss experiments and calculate analytically the expected signal by means of the product operator decomposition of σ . This method is called product operator formalism. A convenient basis set for pulse ESR experiments concerned with the dynamics of nuclear spins will be introduced in §3.1.2.

2.4 Boltzmann equilibrium

To apply the density operator formalism to the description of pulse ESR experiments, we have to know σ_{eq} that provides the starting condition and is also needed for the calculation of relaxation effects. For a system in thermal equilibrium (which will be designated as Boltzmann equilibrium hereafter) the j -th eigenstate of \mathcal{H} is populated according to

$$p(\epsilon_j) = \frac{\exp(-\epsilon_j/kT)}{\sum_i \exp(-\epsilon_i/kT)}, \quad (2.21)$$

where ϵ_i is the energy of the i -th eigenstate, k is the Boltzmann constant and the sum is over the whole multitude of eigenstates of \mathcal{H} . If we refer the energies to the centre of gravity of all levels ($\sum_i \epsilon_i = 0$), we can assume $\epsilon_i \ll kT$ for all states at temperatures significantly above 1 K at X-band frequencies (8..10 GHz). This assumption is called the

high-temperature approximation. Note that it is no longer fulfilled at W-band frequencies of about 95 GHz at liquid helium temperature (4.2 K), where $h\nu \approx 6.3 \times 10^{-23}$ J and $kT = 5.8 \times 10^{-23}$ J. As long as the high-temperature approximation is valid, we may expand the exponentials in Eq. (2.21) in a series and neglect terms higher than first order and obtain

$$p(\epsilon_j) = 1 - \frac{\epsilon_j}{kT} . \tag{2.22}$$

In addition, it can be shown that in thermal equilibrium all coherences are zero since equilibrium is a state of maximum entropy. The ϵ_j are the eigenvalues of \mathcal{H} expressed in energy units, so that we have

$$\sigma_{\text{eq}} = \mathbb{1} - C \mathcal{H} , \tag{2.23}$$

in the frame where \mathcal{H} is diagonal. C is a constant factor that can be calculated easily from Eq. (2.22) considering the units in which \mathcal{H} is given. Since the unity operator is invariant under any external perturbation, we can neglect its contribution to σ . Furthermore, it is often sufficient to consider only the dominating terms in \mathcal{H} , for instance the electron Zeeman term for an $S=1/2$ system at high field or the zero-field splitting for an $S>1/2$ system at zero field. In the former case, we find

$$\sigma_{\text{eq}} = -C' S_z , \tag{2.24}$$

where we can drop the new constant C' if we are only interested in relative line intensities. In the latter case, assuming $E \ll D$ we have

$$\sigma_{\text{eq}} = -C'' S_z^2 . \tag{2.25}$$

2.5 Detection

In pulse ESR experiments, macroscopic transverse magnetization is detected *via* its interaction with a resonator. By substituting an equivalent circuit for the resonator, the process can be described as induction of a voltage in a coil by a magnetic field varying

with time. Without loosing generality we may assume that the coil is oriented along the x -axis of the laboratory frame. The signal voltage V_S is then given by

$$V_S = C_D \frac{dM_x}{dt}, \quad (2.26)$$

where M_x is the magnetization in x -direction and C_D is a constant factor that depends on the resonator. Eq. (2.26) has to be applied with some caution. First, the resonator acts as a bandpass filter, i.e., it detects only transverse magnetization that oscillates with a frequency close to its own resonance frequency. Second, it is necessary to sample the signal according to Eq. (2.26) in time intervalls that are smaller than $1/2\nu_{\max}$, where ν_{\max} is the maximum frequency contained in the signal. This is wasteful, since one is usually interested only in variations of the signal that are by about two orders of magnitude slower. The latter problem is solved in the experimental setup by down-converting the signal to video frequencies with the help of a reference frequency. Almost all spectrometers use the excitation frequency ν_{mw} for this purpose. Detection and down-conversion can be combined in the theoretical treatment and correspond to the observation of M_x (and not its time derivative) in a frame rotating with frequency ν_{mw} . In fact, resonators usually do not discriminate between the M_x and M_y components of transverse magnetization, the axes are defined by the phase of the reference frequency. This allows one to detect a quadrature signal by splitting the output of the resonator to two channels and using two reference signals for the channels that are phase shifted by 90° with respect to each other.

The theoretical description of detection boils down now to the calculation of $M_x(t)$ and $M_y(t)$ in a frame rotating with frequency ν_{mw} . In Chapter 3 it will be shown that it is convenient to describe the whole experiment in such a frame. $M_x(t)$ is then given by¹

$$M_{x,y}(t) = C_{\text{det}} \langle S_{x,y} \rangle (t) = C_{\text{det}} \text{trace} \{ \sigma(t) S_{x,y} \}, \quad (2.27)$$

1. The magnetization of the nuclear spins can be neglected, first, since it is much smaller, and second, since it is suppressed by the bandpass properties of the resonator.

where $\langle S_x \rangle$ is the expectation value of S_x and C_{det} is a constant factor that depends on the number of spins and on an effective g value in the xy -plane. Completely analogous expressions can be used for any operator that corresponds to an observable.

In the product operator formalism, the expectation value of S_x can be calculated by transforming the expression for $\sigma(t)$ into the rotating frame, i.e., by undoing all transformations that were necessary to diagonalize the effective rotating frame Hamiltonian. Since S_x is a product operator itself, the expectation value is then given by its coefficient in the product operator decomposition of $\sigma(t)$.

It is usually assumed in magnetic resonance that the spin system is only weakly coupled to the detector, so that the perturbation of the system by the detection process (radiation damping) can be neglected. Note that the influence of significant radiation damping on relaxation measurements can be eliminated by using the Carr-Purcell [4] or Carr-Purcell-Meiboom-Gill sequence [5] as has been shown in [8].

Theory of electron- nuclear spin systems

3.1 Nuclear frequencies and electron spin transition moments

3.1.1 Reduction of dimensionality

In §2.2 we have seen that the Hilbert space of a spin system consisting of an electron spin S coupled to n nuclear spins I_1, I_2, \dots, I_n has the dimension d_{HS} given by Eq. (2.13). It has also become apparent in Chapter 2 that simple descriptions which provide insight into the time evolution of the spin system require the diagonalization of the spin Hamiltonian. However, analytical matrix diagonalization is possible only for $d_{\text{HS}} \leq 4$ for arbitrary matrices. Furthermore, the expressions for the eigenvalues and in particular for the eigenvectors become unwieldy already for $d_{\text{HS}} > 2$. It is therefore of utmost importance to find approximations that allow one to reduce d_{HS} . Such a reduction can be achieved for instance by partitioning contributions to the spin Hamiltonian into groups and requiring that elements of the same group are of similar magnitude while two elements of different groups differ by at least two orders of magnitude. It is then possible to write Hamiltonians of lower dimensionality than d_{HS} for each group and treat them separately. This partition is particularly convenient if it can be applied not only during free evolution periods but also during excitation, i.e., if pulses do not mix contributions of different groups.

The scheme in Fig. 2-1 on page 29 can be used as a guide for the partition. We assume here that the electron Zeeman interaction and for transition metal ions the central atom hyperfine interaction are much larger than the excitation bandwidth, while the ligand hyperfine interactions, nuclear Zeeman interactions, and nuclear quadrupole interactions are smaller. For $S > 1/2$ we also assume that the zero-field splitting is much larger than the excitation bandwidth. While the former assumption is true almost without any exceptions, the latter one may break down in cubic symmetry. The Hamiltonian for a subsystem consisting of only the electron spin and the central atom (ca) can then be written as

$$\mathcal{H}_{eca} = \mathcal{H}_{EZ} + \mathcal{H}_{ZFS} + S \mathbf{A}_{ca} \mathbf{I}_{ca} + \mathbf{I}_{ca} \mathbf{P}_{ca} \mathbf{I}_{ca}, \quad (3.1)$$

where the nuclear Zeeman interaction of the central atom can be neglected since it is much smaller than the other terms and does not result in a first order contribution to the frequencies or eigenstates. According to our assumptions, the spectrum of \mathcal{H}_{eca} consists of transitions that differ in frequency by more than the excitation bandwidth of the mw pulses, i.e., pulse experiments are transition-selective with respect to \mathcal{H}_{eca} . We can then assign fictitious spins $1/2$ [8] with the two states $|\alpha\rangle$ and $|\beta\rangle$ to each of the transitions. Note that this fictitious spin approach is even possible if the pulse excites two (or more) transitions of \mathcal{H}_{eca} at the same time, as long as these transitions do not share a common level. The transition frequencies, transition moments and states $|\alpha\rangle$ and $|\beta\rangle$ of all the fictitious spins can be calculated either by diagonalizing \mathcal{H}_{eca} numerically or by perturbation theory. In some cases, the high-field approximation can be used for the electron spin and \mathcal{H}_{eca} can be further subdivided into electron Zeeman and zero-field splitting terms on the one hand and hyperfine and nuclear quadrupole terms on the other hand (for an example of this approach see [26]). For a number of relevant systems, results can be found or are referenced in standard textbooks [15,16,27]. The general form of the two states of the fictitious spin $1/2$ is given by

$$|\alpha\rangle, |\beta\rangle = \sum_{m_S = -S}^S \sum_{m_I = -I}^I c_{m_S, m_I}^{(\alpha, \beta)} |m_S, m_I\rangle, \quad (3.2)$$

where the $|m_S, m_I\rangle$ are pure states characterized by the magnetic quantum numbers of the electron and nuclear spin (m_S and m_I), and where we have written I instead of I_{ca} for

briefly. For the following considerations it is convenient to characterize the states by their effective m_S values which we define as

$$m_S^{(\alpha, \beta)} = \sum_{m_S = -S}^S \sum_{m_I = -I}^I c_{m_S, m_I}^{(\alpha, \beta)} m_S. \quad (3.3)$$

In the most simple case of no mixing between different electron spin states, we have

$m_S^\alpha = m_S$ and $m_S^\beta = m_S - 1$, ($-S + 1 < m_S < S$), i.e., each fictitious spin is completely

characterized by the m_S value of its upper state. In the following, we omit the prime in

$m_S^{\alpha, \beta}$.

Another simplification arises, since the interactions between the ligand nuclear spins are much smaller than the hyperfine interactions and are usually not resolved, see Fig. 2-1 on page 29. This leads to a much simplified topology of the spin system as compared to heteronuclear NMR experiments as can be seen in Fig. 3-1.

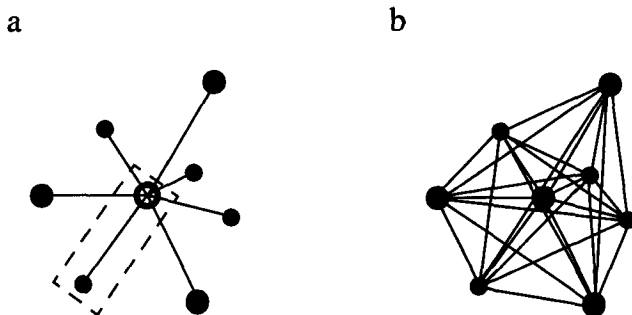


Fig. 3-1 Topology of spin systems. Lines symbolize significant interactions between spins, full circles nuclear spins and the hollow circle an electron spin. a) Electron-nuclear spin system. The system can be partitioned in two-spin subsystems as indicated by the dashed rectangle. b) Heteronuclear spin system. No partition is possible.

We can then factorize the tensor space into subspaces consisting of the fictitious electron spin $S^z = 1/2$ and *one* nuclear spin, treat the subspaces separately, and combine the results in a simple fashion to characterize the behaviour of the whole system. This idea was introduced by Mims and led to the product rules for the calculation of two-pulse and

three-pulse ESEEM patterns [28]. Since the nuclear spins are connected with each other via the electron spin (see Fig. 3-1), the factorization is only correct as long as *none of the neglected nuclear spins influences the quantization direction of the electron spin*. This is certainly the case in the absence of external perturbations and with the central atom already considered, since the S' spin transition energy is much larger than the HFI. It is also possible to use this approach for the description of selective excitation. Non-selective mw excitation can be integrated into the approach if the pulses can be treated as ideal, i.e., if the static Hamiltonian \mathcal{H}_0 can be neglected during the pulses. Although the assumption of ideal mw pulses is not well justified in most cases in pulse ESR (see §3.2.2), it still leads to a *qualitative* understanding of the behaviour of the spin system and allows one to get much of the physical insight that is needed to design experiments. Moreover, the quantitative deviations resulting from a breakdown of the assumption concern only relative intensities but not frequencies as long as only evolution under \mathcal{H}_0 is observed. It is therefore appropriate to discuss the general features of experiments in the framework of ideal pulses whenever possible and to account for the non-ideality by numerical calculations.

At this point, we have to treat $n-1$ single ligand nucleus problems of dimension $2(2I_k+1)$ for each electron spin transition. Any experiment applying only mw pulses can be described for such a system if we know the nuclear frequencies¹ as well as the transition moments of all allowed and forbidden electron spin transitions. The two nuclear spin Hamiltonians for the k -th ligand nucleus in the α and β manifold of S' must consider all interactions that have not been accounted for in \mathcal{H}_{cca} . To obtain them, we have to calculate the hyperfine fields imposed by S' in its α and β manifold on the nuclear spin from

1. The transition frequency of the isolated fictitious spin S' can be characterized by an offset Ω_S from the excitation frequency ω_{mw} . Usually we deal with samples where there is a distribution of Ω_S that is later accounted for by an integration. A group of spin systems with the same Ω_S is called a spin packet.

the HFI between the real electron spin S and I_k (in the following the index k is omitted for brevity). We have

$$\begin{aligned} \mathcal{H}_{\text{HF}} = \mathbf{S A I} = & A_{zZ} S_z I_Z + A_{zX} S_z I_X + A_{zY} S_z I_Y \\ & + A_{xZ} S_x I_Z + A_{xX} S_x I_X + A_{xY} S_x I_Y \\ & + A_{yZ} S_y I_Z + A_{yX} S_y I_X + A_{yY} S_y I_Y . \end{aligned} \quad (3.4)$$

In a frame where the S spin z -axis is its quantization axis, we can neglect the terms in the second and third line on the right hand side of Eq. (3.4), since they are small off-diagonal elements that connect diagonal elements with a large energy difference (i.e., they are non-secular terms). By using

$$\langle m_S | S_z | m_S \rangle = m_S , \quad (3.5)$$

and Eqs. (3.2 and 3.3), we can then write for the HFI part of the nuclear Hamiltonians in the α and β manifold of S'

$$\mathcal{H}_{\text{HF}}^{(\alpha, \beta)} = m_S^{(\alpha, \beta)} (A_{zZ} I_Z + A_{zX} I_X + A_{zY} I_Y) . \quad (3.6)$$

In the I -spin frame, only the Z -axis has been fixed so far by the form of Eq. (2.8)¹, so that we can define a new x -axis along the effective field caused by the terms $A_{zX} I_X$ and $A_{zY} I_Y$. We obtain

$$\mathcal{H}_{\text{HF}}^{(\alpha, \beta)} = m_S^{(\alpha, \beta)} (A I_z + B I_x) , \quad (3.7)$$

with $A=A_{zZ}$ and $B = (A_{zX}^2 + A_{zY}^2)^{1/2}$. The two complete nuclear Hamiltonians are then given by

$$\mathcal{H}^{(\alpha, \beta)} = \mathbf{I P I} + m_S^{(\alpha, \beta)} (A I_z + B I_x) + \omega_I I_z . \quad (3.8)$$

These Hamiltonians have the dimension $2I+1$, so that exact diagonalization is possible for $I \leq 3/2$.

1. The I_z axis is parallel to the external static magnetic field.

Assume that we know the eigenvalues and eigenvectors of $\mathcal{H}^{(\alpha)}$ and $\mathcal{H}^{(\beta)}$ either from exact or from numerical diagonalization and that the transition moment for S' disregarding all ligand interactions is f_S . Consider now the transition between the states $|\alpha, i\rangle$ and $|\beta, j\rangle$, where $|i\rangle$ and $|j\rangle$ are eigenstates of $\mathcal{H}^{(\alpha)}$ and $\mathcal{H}^{(\beta)}$, respectively¹. The transition moment is obviously given by

$$f(|\alpha, i\rangle, |\beta, j\rangle) = f_S \langle i|j\rangle, \quad (3.9)$$

i.e., for a given f_S all electron spin transition moments can be calculated with the scalar products of the known nuclear eigenvectors. Note that it is not necessary to know f_S if one is only interested in *relative* intensities in ESEEM spectra.

The behaviour of the whole system consisting of the fictitious spin S' and $n-1$ ligand nuclei can now be calculated from the results for the subsystems. Any state in this system is of the form $|\alpha, i_1, i_2, \dots, i_{n-1}\rangle$ or $|\beta, j_1, j_2, \dots, j_{n-1}\rangle$ and has the energy

$$\omega(|\alpha, i_1, i_2, \dots, i_{n-1}\rangle) = \frac{\omega_S}{2} + \sum_{k=1}^{n-1} \omega(|i_k\rangle), \quad (3.10a)$$

or

$$\omega(|\beta, j_1, j_2, \dots, j_{n-1}\rangle) = -\frac{\omega_S}{2} + \sum_{k=1}^{n-1} \omega(|j_k\rangle), \quad (3.10b)$$

where the $\omega(|i_k\rangle)$ and $\omega(|j_k\rangle)$ are eigenvalues of $\mathcal{H}_k^{(\alpha)}$ and $\mathcal{H}_k^{(\beta)}$, respectively. The transition moment for the transition between these two arbitrary states is given by

$$f(|\alpha, i_1, i_2, \dots, i_{n-1}\rangle, |\beta, j_1, j_2, \dots, j_{n-1}\rangle) = f_S \prod_{k=1}^{n-1} \langle i_k|j_k\rangle. \quad (3.11)$$

With these equations it is straightforward to derive product rules for any given pulse ESR experiment that utilizes only mw pulses.

1. Any electron spin transition in the considered subsystem is of this form where $|\alpha, i\rangle$ is an abbreviation for $|\alpha\rangle|i\rangle$.

3.1.2 Nuclear spins $I=1/2$

Some of the isotopes that are relevant in samples mentioned in the introduction have nuclear spin $I=1/2$, e.g. ^1H , ^{13}C , ^{19}F , ^{29}Si , and ^{31}P . ^{15}N , which is used to label specific nitrogens in biological samples also belongs to this group. Additional insight can be gained in this case since the Hilbert space dimension is four and the analytical diagonalization of $\mathcal{H}^{(\alpha)}$ and $\mathcal{H}^{(\beta)}$ is simple. In Eq. (3.8), the term $\mathbf{I P I}$ vanishes and the Hamiltonians can be diagonalized by the unitary transformation $U_{\alpha, \beta} \mathcal{H}^{(\alpha, \beta)} U_{\alpha, \beta}^{-1}$ with

$$U_{\alpha, \beta} = \exp\{-i\eta_{\alpha, \beta} I_y\}, \quad (3.12)$$

and

$$\eta_{\alpha, \beta} = \text{atan}\left(\frac{m_S^{(\alpha, \beta)} B}{m_S^{(\alpha, \beta)} A + \omega_I}\right). \quad (3.13)$$

The nuclear frequencies are given by

$$\omega_{\alpha, \beta} = \left[(m_S^{(\alpha, \beta)} A + \omega_I)^2 + (m_S^{(\alpha, \beta)} B)^2 \right]^{1/2}. \quad (3.14)$$

For an electron spin $S=1/2$, this equation simplifies to the well known formulas derived by Mims (Eq. (48) in Ref. [28]). In some cases, it is more convenient to use signed values for the nuclear frequencies, which are given by

$$\omega_{12} = \cos\eta_{\alpha} (m_S^{(\alpha)} A + \omega_I) + \sin\eta_{\alpha} (m_S^{(\alpha)} B), \quad (3.15a)$$

and

$$\omega_{34} = \cos\eta_{\beta} (m_S^{(\beta)} A + \omega_I) + \sin\eta_{\beta} (m_S^{(\beta)} B). \quad (3.15b)$$

1. A convention for the choice of quadrants for η_{α} and η_{β} will be introduced below.

The level enumeration used in these equations can be inferred from Fig. 3-2 on page 47. With these frequencies one can express the hyperfine splitting

$$\omega_{\text{HF}} = \omega_{12} - \omega_{34} , \quad (3.16)$$

as it would be observed in a sufficiently resolved ESR spectrum and the nuclear Zeeman splitting

$$\omega_{\text{NZ}} = \omega_{12} + \omega_{34} . \quad (3.17)$$

Note that due to second order effects the nuclear Zeeman *splitting* is slightly larger than $2\omega_I$ in systems with electron spin $S=1/2$.

For the transition moments f_a and f_f of the allowed and forbidden transitions, respectively, we find

$$f_a = f(|\alpha\alpha\rangle, |\beta\alpha\rangle) = f(|\alpha\beta\rangle, |\beta\beta\rangle) = \cos\eta , \quad (3.18a)$$

and

$$f_f = f(|\alpha\alpha\rangle, |\beta\beta\rangle) = f(|\alpha\beta\rangle, |\beta\alpha\rangle) = \sin\eta , \quad (3.18b)$$

with

$$\eta = \frac{\eta_\alpha - \eta_\beta}{2} . \quad (3.19)$$

For Eq. (3.18a,b, and 3.19) to be valid independently of the relative magnitude of ω_I and the $m_S^{(\alpha, \beta)} A$, the quadrants for η_α and η_β must be chosen, so that $-45^\circ < \eta \leq 45^\circ$. This convention also ensures, that the level enumeration in Fig. 3-2 is defined (via Eqs. (3.15a,b)) in cases where m_I is no longer a good quantum number and where no α and β states of the nuclear spin exist in a strict sense.

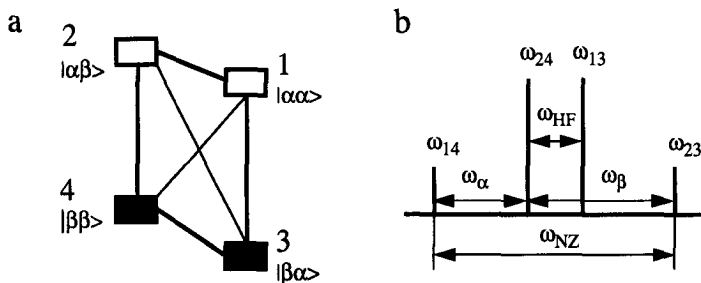


Fig. 3-2 Level scheme in Boltzmann equilibrium (a) and schematic ESR spectrum (b) of the $S'=1/2, I=1/2$ system. It is assumed that both g_n and A are positive and that $|\omega_I| > |m_S^{(\alpha/\beta)} A|$ (weak coupling case). The state symbol $|\alpha\beta\rangle$ means that the fictitious electron spin S' is in its α state and the nuclear spin in its β state. The filled rectangles designate populations $1+\epsilon$ and the hollow rectangles designate populations $1-\epsilon$.

We can now construct a Hamiltonian for the whole four-level system. In the frame, where it is diagonal, this Hamiltonian is given by

$$\mathcal{H}'_0 = \Omega_S S_z + \omega_{12} S^\alpha I_z + \omega_{34} S^\beta I_z, \tag{3.20}$$

where $\Omega_S = \omega_S - \omega_{mw}$ is the resonance offset, ω_S the resonance frequency of the isolated fictitious spin, ω_{mw} the microwave frequency and S^α and S^β are polarization operators defined by $S^{\alpha,\beta} = \frac{1}{2} \mathbb{1} \pm S_z$. \mathcal{H}'_0 has been written in a frame rotating with frequency ω_{mw} about the S_z axis (see §3.2.1), all terms of the nuclear Hamiltonians are invariant under this rotation. This Hamiltonian can be transformed to the frame defined in Eq. (3.7) by $U^{-1} \mathcal{H}'_0 U$ with

$$U = \exp\{-i(\eta_\alpha S^\alpha I_y + \eta_\beta S^\beta I_y)\} = \exp\{-i(\eta 2S_z I_y + \xi I_y)\}, \tag{3.21}$$

where

$$\xi = \frac{\eta_\alpha + \eta_\beta}{2}. \tag{3.22}$$

We obtain

$$\mathcal{H}_0 = \Omega_S S_z + A' S_z I_z + B' S_z I_x + \omega_I I_z + \omega_{I_x'} I_x, \tag{3.23}$$

with

$$A' = (m_S^{(\alpha)} - m_S^{(\beta)})A, \quad (3.24a)$$

$$B' = (m_S^{(\alpha)} - m_S^{(\beta)})B, \quad (3.24b)$$

$$\omega_I' = \omega_I + \frac{(m_S^{(\alpha)} + m_S^{(\beta)})}{2}A, \quad (3.24c)$$

and

$$\omega_{Ix}' = \frac{(m_S^{(\alpha)} + m_S^{(\beta)})}{2}B. \quad (3.24d)$$

Except for the additional term $\omega_{Ix}'I_x$, \mathcal{H}_0 in Eq. (3.23) has the same form as the Hamiltonian for a system consisting of an electron spin $S=1/2$ and a nuclear spin $I=1/2$. Moreover, the propagator U for the diagonalization of \mathcal{H}_0 (Eq. (3.21)) and the form of the diagonalized Hamiltonian \mathcal{H}_0' are exactly the same (cf. Ref. [29]). This means that the whole theory developed for the description of $S=1/2$, $I=1/2$ systems [28-35] can be applied straightforwardly to systems with any number of spins $I=1/2$ coupled to an arbitrary electron spin S as long as the conditions for the fictitious spin treatment are fulfilled. In the following, we write S instead of S' and refer to the fictitious spin only in cases where it behaves differently from an electron spin $1/2$.

With regard to the analogy of the fictitious spin with $S=1/2$ it is of some interest to discuss Eq. (3.24c). For $m_S^{(\alpha)} + m_S^{(\beta)} \neq 0$, there is a HFI contribution to the effective nuclear Zeeman field ω_I' . This is of importance in experiments that refocus the hyperfine coupling (e.g. [36]), since the HFI contribution to ω_I' is *not* refocused. In Chapter 5 it will be shown by experiments that this part of the HFI also does not vanish in hyperfine decoupling schemes, so that these are useful to determine the character of an ESR transition. By this method one can obtain useful results from ESEEM or ENDOR measurements even if one is not able to determine the state functions $|\alpha\rangle$ and $|\beta\rangle$ of the fictitious spin (and therefore the $m_S^{(\alpha)}$ and $m_S^{(\beta)}$) *a priori*.

It has become apparent above that the description of nuclear spin dynamics becomes particularly simple if one subdivides the system into the fictitious spin α and β manifolds. For experiments that deal with the generation, evolution, and detection of nuclear coherence (NC), it is therefore convenient to use a basis in the product operator formalism that is slightly different from the one usually applied in NMR. For that, we combine I_L and S_z to the polarization operators S^α and S^β , which results in another complete basis set for S . Concerning normalization, the polarization operators behave like cartesian operators, i.e., they must be counted in determining the normalization factor. Most of the ESEEM experiments developed so far may be described if one knows how the product operators evolve under the Hamiltonian \mathcal{H}_0 and under mw pulses of arbitrary flip angle β_p along the x - and y -axis. For the calculation of the table of transformations (Tab. 3-1), the cartesian product basis has been used, since Eq. (2.20) is valid only in this basis.

Table 3-1 Transformation of product operators K for the $S=1/2, I=1/2$ system under the unperturbed Hamiltonian and under pulses of nominal flip angle β_p along the x - and y -axis. All expressions refer to the eigenbasis of the unperturbed Hamiltonian.

K	$\exp(-i\mathcal{H}_0 t) K \exp(i\mathcal{H}_0 t)$	$U \exp(-i\beta_p S_x) U^{-1} K U \exp(i\beta_p S_x) U^{-1}$	$U \exp(-i\beta_p S_y) U^{-1} K U \exp(i\beta_p S_y) U^{-1}$
S^α	S^α	$\frac{1 + \cos\beta_p}{2} S^\alpha + \frac{1 - \cos\beta_p}{2} S^\beta$ $-\cos\eta \sin\beta_p S_y + \sin\eta \sin\beta_p 2S_x I_y$	$\frac{1 + \cos\beta_p}{2} S^\alpha + \frac{1 - \cos\beta_p}{2} S^\beta$ $+\cos\eta \sin\beta_p S_x + \sin\eta \sin\beta_p 2S_y I_y$
S^β	S^β	$\frac{1 - \cos\beta_p}{2} S^\alpha + \frac{1 + \cos\beta_p}{2} S^\beta$ $+\cos\eta \sin\beta_p S_y - \sin\eta \sin\beta_p 2S_x I_y$	$\frac{1 - \cos\beta_p}{2} S^\alpha + \frac{1 + \cos\beta_p}{2} S^\beta$ $-\cos\eta \sin\beta_p S_x - \sin\eta \sin\beta_p 2S_y I_y$
$2S^\alpha I_z$	$2S^\alpha I_z$	$\frac{1}{2}(1 + \cos\beta_p) 2S^\alpha I_z$ $+\left(\cos^2\eta - \frac{1}{2}\right)(1 - \cos\beta_p) 2S^\beta I_z$ $-\sin\eta \cos\eta(1 - \cos\beta_p) 2S^\beta I_x$ $-(\cos\eta \sin\beta_p 2S_y I_z + \sin\eta \sin\beta_p 2S_y I_x)$	$\frac{1}{2}(1 + \cos\beta_p) 2S^\alpha I_z$ $+\left(\cos^2\eta - \frac{1}{2}\right)(1 - \cos\beta_p) 2S^\beta I_z$ $-\sin\eta \cos\eta(1 - \cos\beta_p) 2S^\beta I_x$ $+(\cos\eta \sin\beta_p 2S_x I_z - \sin\eta \sin\beta_p 2S_x I_x)$

Table 3-1 continued.

K	$\exp(-i\mathcal{H}_0 t) K \exp(i\mathcal{H}_0 t)$	$U \exp(-i\beta_p S_x) U^{-1} K U \exp(i\beta_p S_x) U^{-1}$	$U \exp(-i\beta_p S_y) U^{-1} K U \exp(i\beta_p S_y) U^{-1}$
$2S_x^\beta I_z$	$S^\beta I_z$	$\frac{1}{2}(1 + \cos\beta_p) 2S^\beta I_z$ + $\left(\cos^2\eta - \frac{1}{2}\right)(1 - \cos\beta_p) 2S^\alpha I_z$ + $\sin\eta \cos\eta(1 - \cos\beta_p) 2S^\alpha I_x$ + $(\cos\eta \sin\beta_p 2S_y I_z + \sin\eta \sin\beta_p 2S_y I_x)$	$\frac{1}{2}(1 + \cos\beta_p) 2S^\beta I_z$ + $\left(\cos^2\eta - \frac{1}{2}\right)(1 - \cos\beta_p) 2S^\alpha I_z$ + $\sin\eta \cos\eta(1 - \cos\beta_p) 2S^\alpha I_x$ - $(\cos\eta \sin\beta_p 2S_x I_z + \sin\eta \sin\beta_p 2S_x I_x)$
S_x	$\cos(\Omega_S t) \cos(\omega_{\text{HF}} t/2) S_x$ + $\sin(\Omega_S t) \cos(\omega_{\text{HF}} t/2) S_y$ - $\sin(\Omega_S t) \sin(\omega_{\text{HF}} t/2) 2S_x I_z$ + $\cos(\Omega_S t) \sin(\omega_{\text{HF}} t/2) 2S_y I_z$	$[\cos^2\eta(1 - \cos\beta_p) + \cos\beta_p] S_x$ - $\sin\eta \sin\beta_p (S^\alpha I_y - S^\beta I_y)$ - $\sin\eta \cos\eta(1 - \cos\beta_p) 2S_y I_y$	$[1 - \cos^2\eta(1 - \cos\beta_p)] S_x$ - $\frac{1}{2} \cos\eta \sin\beta_p (S^\alpha - S^\beta)$ - $\sin\eta \cos\eta(1 - \cos\beta_p) 2S_y I_y$
S_y	$\cos(\Omega_S t) \cos(\omega_{\text{HF}} t/2) S_y$ - $\sin(\Omega_S t) \cos(\omega_{\text{HF}} t/2) S_x$ - $\sin(\Omega_S t) \sin(\omega_{\text{HF}} t/2) 2S_y I_z$ - $\cos(\Omega_S t) \sin(\omega_{\text{HF}} t/2) 2S_x I_z$	$[1 - \cos^2\eta(1 - \cos\beta_p)] S_y$ + $\frac{1}{2} \cos\eta \sin\beta_p (S^\alpha - S^\beta)$ + $\sin\eta \cos\eta(1 - \cos\beta_p) 2S_x I_y$	$[\cos^2\eta(1 - \cos\beta_p) + \cos\beta_p] S_y$ - $\sin\eta \sin\beta_p (S^\alpha I_y - S^\beta I_y)$ - $\sin\eta \cos\eta(1 - \cos\beta_p) 2S_x I_y$

Table 3-1 continued.

K	$\exp(-i\alpha t_0 t) K \exp(i\beta t_0 t)$	$U \exp(-i\beta_p S_y) U^{-1} K U \exp(i\beta_p S_x) U^{-1}$	$U \exp(-i\beta_p S_y) U^{-1} K U \exp(i\beta_p S_y) U^{-1}$
$2S_x I_z$	$\cos(\Omega_S t) \cos(\omega_{HF} t/2) 2S_x I_z$ $+ \sin(\Omega_S t) \cos(\omega_{HF} t/2) 2S_y I_z$ $- \sin(\Omega_S t) \sin(\omega_{HF} t/2) S_x$ $+ \cos(\Omega_S t) \sin(\omega_{HF} t/2) S_y$	$2S_x I_z$	$\cos \beta_p 2S_x I_z - \cos \eta \sin \beta_p (S^\alpha - S^\beta)$ $- \sin \eta \sin \beta_p (S^\alpha I_x - S^\beta I_x)$
$2S_y I_z$	$\cos(\Omega_S t) \cos(\omega_{HF} t/2) 2S_y I_z$ $- \sin(\Omega_S t) \cos(\omega_{HF} t/2) 2S_x I_z$ $- \sin(\Omega_S t) \sin(\omega_{HF} t/2) S_y$ $- \cos(\Omega_S t) \sin(\omega_{HF} t/2) S_x$	$\cos \beta_p 2S_y I_z + \cos \eta \sin \beta_p (S^\alpha - S^\beta)$ $+ \sin \eta \sin \beta_p (S^\alpha I_x + S^\beta I_x)$	$2S_y I_z$
$2S^\alpha I_x$	$\cos(\omega_{12} t) 2S^\alpha I_x + \sin(\omega_{12} t) 2S^\alpha I_y$	$\frac{1 + \cos \beta_p}{2} 2S^\alpha I_x + \cos(2\eta) \sin^2\left(\frac{\beta_p}{2}\right) 2S^\beta I_x$ $+ \frac{1}{2} \sin(2\eta) (1 - \cos \beta_p) 2S^\beta I_z$ $- (\cos \eta \sin \beta_p 2S_y I_x + \sin \eta \sin \beta_p 2S_y I_z)$	$\frac{1 + \cos \beta_p}{2} 2S^\alpha I_x + \cos(2\eta) \sin^2\left(\frac{\beta_p}{2}\right) 2S^\beta I_x$ $+ \frac{1}{2} \sin(2\eta) (1 - \cos \beta_p) 2S^\beta I_z$ $+ (\cos \eta \sin \beta_p 2S_x I_x + \sin \eta \sin \beta_p 2S_x I_z)$

Table 3-1 continued.

K	$\exp(-i\mathcal{H}_0 t) K \exp(i\mathcal{H}_0 t)$	$U \exp(-i\beta_p S_x) U^{-1} K U \exp(i\beta_p S_x) U^{-1}$	$U \exp(-i\beta_p S_y) U^{-1} K U \exp(i\beta_p S_y) U^{-1}$
$2S^\beta I_x$	$\cos(\omega_{34} t) 2S^\beta I_x + \sin(\omega_{34} t) 2S^\beta I_y$	$\frac{1 + \cos\beta_p}{2} 2S^\beta I_x + \cos(2\eta) \sin^2\left(\frac{\beta_p}{2}\right) 2S^\alpha I_x$ $-\frac{1}{2} \sin(2\eta)(1 - \cos\beta_p) 2S^\alpha I_z$ $+ \cos\eta \sin\beta_p 2S_y I_x - \sin\eta \sin\beta_p 2S_y I_z$	$\frac{1 + \cos\beta_p}{2} 2S^\beta I_x + \cos(2\eta) \sin^2\left(\frac{\beta_p}{2}\right) 2S^\alpha I_x$ $-\frac{1}{2} \sin(2\eta)(1 - \cos\beta_p) 2S^\alpha I_z$ $- \cos\eta \sin\beta_p 2S_x I_x - \sin\eta \sin\beta_p 2S_x I_z$
$2S^\alpha I_y$	$\cos(\omega_{12} t) 2S^\alpha I_y - \sin(\omega_{12} t) 2S^\alpha I_x$	$\frac{1}{2}(1 + \cos\beta_p) 2S^\alpha I_y + \frac{1}{2}(1 - \cos\beta_p) 2S^\beta I_y$ $- \cos\eta \sin\beta_p 2S_y I_y - \sin\eta \sin\beta_p S_x$	$\frac{1}{2}(1 + \cos\beta_p) 2S^\alpha I_y + \frac{1}{2}(1 - \cos\beta_p) 2S^\beta I_y$ $+ \cos\eta \sin\beta_p 2S_x I_y + \sin\eta \sin\beta_p S_y$
$2S^\beta I_y$	$\cos(\omega_{34} t) 2S^\beta I_y - \sin(\omega_{34} t) 2S^\beta I_x$	$\frac{1}{2}(1 + \cos\beta_p) 2S^\beta I_y + \frac{1}{2}(1 - \cos\beta_p) 2S^\alpha I_y$ $+ \cos\eta \sin\beta_p 2S_y I_y - \sin\eta \sin\beta_p S_x$	$\frac{1}{2}(1 + \cos\beta_p) 2S^\alpha I_y + \frac{1}{2}(1 - \cos\beta_p) 2S^\beta I_y$ $- \cos\eta \sin\beta_p 2S_x I_y + \sin\eta \sin\beta_p S_y$

Table 3-1 continued.

K	$\exp(-i\vartheta_0 t) K \exp(i\vartheta_0 t)$	$U \exp(-i\beta_p S_x) U^{-1} K U \exp(i\beta_p S_x) U^{-1}$	$U \exp(-i\beta_p S_y) U^{-1} K U \exp(i\beta_p S_y) U^{-1}$
$2S_x I_x$	$\cos(\Omega_S t) \cos(\omega_{NZ} t/2) 2S_x I_x$ + $\sin(\Omega_S t) \cos(\omega_{NZ} t/2) 2S_y I_x$ + $\sin(\Omega_S t) \sin(\omega_{NZ} t/2) 2S_y I_y$ + $\cos(\Omega_S t) \sin(\omega_{NZ} t/2) 2S_x I_y$	$2S_x I_x$	$\cos\beta_p 2S_x I_x - \cos\eta \sin\beta_p (S^\alpha I_x - S^\beta I_x)$ + $\sin\eta \sin\beta_p (S^\alpha I_z - S^\beta I_z)$
$2S_y I_y$	$\cos(\Omega_S t) \cos(\omega_{NZ} t/2) 2S_y I_y$ - $\sin(\Omega_S t) \cos(\omega_{NZ} t/2) 2S_x I_y$ + $\sin(\Omega_S t) \sin(\omega_{NZ} t/2) 2S_x I_x$ - $\cos(\Omega_S t) \sin(\omega_{NZ} t/2) 2S_y I_x$	$[1 - \cos^2\eta(1 - \cos\beta_p)] 2S_y I_y$ + $\cos\eta \sin\beta_p (S^\alpha I_y - S^\beta I_y)$ + $\sin(2\eta)(1 - \cos\beta_p) S_x$	$[\cos\beta_p - \cos^2\eta(1 - \cos\beta_p)] 2S_y I_y$ - $\sin\eta \sin\beta_p (S^\alpha - S^\beta)$ - $\sin 2\eta(1 - \cos\beta_p) S_x$
$2S_x I_y$	$\cos(\Omega_S t) \cos(\omega_{NZ} t/2) 2S_x I_y$ + $\sin(\Omega_S t) \cos(\omega_{NZ} t/2) 2S_y I_y$ - $\sin(\Omega_S t) \sin(\omega_{NZ} t/2) 2S_y I_x$ - $\cos(\Omega_S t) \sin(\omega_{NZ} t/2) 2S_x I_x$	$[\cos\beta_p - \cos^2\eta(1 - \cos\beta_p)] 2S_x I_y$ - $\sin\eta \sin\beta_p (S^\alpha - S^\beta)$ + $\sin 2\eta(1 - \cos\beta_p) S_y$	$[1 - \cos^2\eta(1 - \cos\beta_p)] 2S_x I_y$ - $\cos\eta \sin\beta_p (S^\alpha I_y - S^\beta I_y)$ - $\sin 2\eta(1 - \cos\beta_p) S_y$
$2S_y I_x$	$\cos(\Omega_S t) \cos(\omega_{NZ} t/2) 2S_y I_x$ - $\sin(\Omega_S t) \cos(\omega_{NZ} t/2) 2S_x I_x$ - $\sin(\Omega_S t) \sin(\omega_{NZ} t/2) 2S_x I_y$ + $\cos(\Omega_S t) \sin(\omega_{NZ} t/2) 2S_y I_y$	$\cos\beta_p 2S_y I_x + \cos\eta \sin\beta_p (S^\alpha I_x - S^\beta I_x)$ - $\sin\eta \sin\beta_p (S^\alpha I_z + S^\beta I_z)$	$2S_y I_x$

3.1.3 Nuclear spins $I > 1/2$

The most important isotopes with nuclear spin $I > 1/2$ are ^{14}N , ^2D ($I=1$), ^{11}B , ^{29}K , ^{23}Na , ^{35}Cl , ^{37}Cl ($I=3/2$), and ^{27}Al ($I=5/2$). Analytical expressions for the ESEEM modulations of nuclei with $I=1$ and $I=3/2$ would be useful for the development of new pulse sequences and of measurement strategies. Even if they are too complicated to provide immediate insight, they may still be used for computationally efficient simulations, to check the validity of the simpler expressions obtained with perturbation treatments, and as a basis for simplified expressions in special cases that cannot be treated easily with perturbation theory. The principles for such an analytical treatment for an electron spin $S=1/2$ have been given in [37]. Since the diagonalization procedures and results for isolated nuclear spins $I=1$ [38] and $I=3/2$ [39] are known, it is only necessary to bring the Hamiltonians in Eq. (3.8) into the form from which the corresponding treatments start. In both cases, the nuclear quadrupole Hamiltonian is written in the form

$$\mathcal{H}_{\text{NQ}} = P \left[3I_z^2 - I(I+1) + \frac{\eta}{2}(I_+^2 + I_-^2) \right], \quad (3.25)$$

where P is the nuclear quadrupole coupling constant and η the asymmetry parameter and where it is assumed that the only additional term in the Hamiltonian is the Zeeman interaction in a local field, characterised by the field amplitude and two polar angles θ and ϕ that define its orientation with respect to the principal axes frame of \mathcal{H}_{NQ} . With that it is also ensured that the eigenvectors in the two manifolds refer to the same frame. The Hamiltonian for a nuclear spin I coupled to a fictitious spin $S^=1/2$ can be written as

$$\mathcal{H}^{(\alpha, \beta)} = \mathcal{H}_{\text{NQ}} + F_x^{(\alpha, \beta)} I_x + F_y^{(\alpha, \beta)} I_y + F_z^{(\alpha, \beta)} I_z, \quad (3.26)$$

with

$$F_x^{(\alpha, \beta)} = m_S^{(\alpha, \beta)} B_x' - \sin\theta \cos\phi \omega_I, \quad (3.27a)$$

$$F_y^{(\alpha, \beta)} = m_S^{(\alpha, \beta)} B_y' - \sin\theta \sin\phi \omega_I, \quad (3.27b)$$

and

$$F_z^{(\alpha, \beta)} = m_S^{(\alpha, \beta)} A' - \cos\theta \omega_I . \quad (3.27c)$$

The terms F_x , F_y , and F_z can also be formulated as an effective field \mathbf{F} , given by

$$|\mathbf{F}| = (F_x^2 + F_y^2 + F_z^2)^{1/2} , \quad (3.28a)$$

with its orientation characterized by the polar angles

$$\theta' = \text{atan} \left[\frac{(F_x^2 + F_y^2)^{1/2}}{F_z} \right] , \quad \theta' \in [0; \pi] , \quad (3.28b)$$

and

$$\phi' = \text{atan} \left(\frac{F_y}{F_x} \right) . \quad (3.28c)$$

Obviously, the eigenvectors in the two manifolds will be different and hence forbidden transitions will occur whenever $|\mathbf{F}|$ is of the same order of magnitude as P and either the magnitude or the orientation of \mathbf{F} or both are different in the α and β manifold of S' .

3.2 Description of excitation

The description of excitation in this work adapts an earlier description by Hoffmann [40] to the theoretical framework presented above and extends it to rf excitation, non-ideal pulses of arbitrary strength, and combined mw and rf excitation. After a short introduction into the concept of the rotating frame, treatments of mw excitation are presented in the order of increasing complexity. It is therefore advantageous to use the first treatment that is a good approximation to the problem under consideration. Excitation by rf is treated on the basis of an average Hamiltonian approach first introduced into ESR by Cho et al. [42]. For simplicity, we assume a nuclear spin 1/2 in the following.

3.2.1 Rotating frame

Consider first an electron spin $S=1/2$ with isotropic g matrix. The Hamiltonian in the presence of a linearly polarized oscillating mw field is given by

$$\mathcal{H}_1(t) = \omega_S S_z + 2 \cos(\omega_{mw} t) \omega_I S_x . \quad (3.29)$$

where $\omega_1 = 2\pi g\beta_e B_1/\hbar$ is the microwave field strength expressed in angular frequency units and where the S_z axis is parallel to the external magnetic field axis. For a fictitious spin 1/2, an additional factor is involved in the expression for ω_1 that depends on the m_S values of the two levels (see §9.2).

The linearly polarized mw field can be written as the sum of a right-hand and a left-hand circularly polarized component,

$$\begin{aligned} \mathcal{H}_1(t) = & \omega_S S_z \\ & + \cos(\omega_{mw}t)\omega_1 S_x + \sin(\omega_{mw}t)\omega_1 S_y \\ & + \cos(\omega_{mw}t)\omega_1 S_x - \sin(\omega_{mw}t)\omega_1 S_y \end{aligned} \quad (3.30)$$

The left-hand rotating component of the mw field does not interact significantly with the electron spins and can be neglected. In a frame rotating with frequency ω_{mw} about the S_z axis, \mathcal{H}_1 can then be written as

$$\mathcal{H}_1' = \Omega_S S_z + \omega_1 S_x. \quad (3.31)$$

Note that the step from $\mathcal{H}_1(t)$ to \mathcal{H}_1' is not simply a unitary transformation¹, but a change from a Schrödinger representation of the Hamiltonian to an interaction representation.

In the general case of an anisotropic g matrix or in the presence of a significant zero-field splitting, the quantization axis of the fictitious spin is no longer parallel to the external magnetic field axis. We also assume an arbitrary angle θ between the quantization axis and the mw field. In a frame where the z -axis is parallel to the quantization axis and the x -axis is the projection of the direction of the linearly polarized mw field onto a plane perpendicular to the quantization axis, the Hamiltonian during irradiation is given by

$$\tilde{\mathcal{H}}_1(t) = \omega_S S_z + 2(\sin(\theta)g_x S_x + \cos(\theta)g_z S_z) \frac{2\pi\beta_e B_1}{\hbar} \cos(\omega_{mw}t), \quad (3.32)$$

where g_x and g_z are g -values along the axes of the new frame, and θ is the angle between the vectors \mathbf{B}_0 and \mathbf{B}_1 . The time-dependent $\cos(\theta)g_z S_z$ term in Eq. (3.33) modulates the

1. A unitary transformation with a time-dependent propagator would lead to a Hamiltonian that does not fulfill Eq. (2.15). See also [40].

level energies on a time scale that is fast with respect to the experiments; it does not induce transitions. This term can therefore be neglected. Furthermore, since Eq. (3.32) does not contain g_y , the solution must also be independent of g_y and, in particular, we can do our calculations with $g_y=g_x$ without losing generality. The rotating frame Hamiltonian can then be obtained in the same way as for the isotropic case and we recover Eq. (3.31) with

$$\omega_1' = \sin(\theta) \frac{2\pi\beta_e}{h} g_x B_1. \quad (3.33)$$

Obviously, the nutation frequency is maximum if the *effective* mw field direction is perpendicular to the quantization axis, $\theta=90^\circ$. Since the transformation of an external field to a local field by the g matrix is the same for the static and the mw field, this also means that the direction of the applied mw field should always be perpendicular to the static field.¹

All terms in the Hamiltonian of an electron-nuclear spin system that describe interactions of the ligand nuclear spins² remain unchanged in going from the Schrödinger representation to the interaction representation, since the corresponding energies are far off-resonant from ω_{mw} . The effective rotating-frame Hamiltonian of an electron-nucleus subsystem with $I=1/2$ during mw irradiation is therefore given by

$$\mathcal{H}_{ex}' = \Omega_S S_z + A' S_z I_z + B' S_z I_x - \omega_1' I_z + \omega_{Ix}' I_x + \omega_1' S_x. \quad (3.34)$$

3.2.2 Ideal non-selective microwave pulses

The most simple description of mw pulses is obtained if we can assume that

$$\omega_1' \gg \Omega_S, A', B', \omega_I', \omega_{Ix}'. \quad (3.35)$$

1. Note that the transformation to the rotating frame is a *formal mathematical operation* in this case, i.e., the two circularly polarized fields in Eq. (3.30) have no physical reality for an anisotropic g matrix. In fact, the electron spin sees two *elliptically* polarized mw field components instead of the circularly polarized ones because of the anisotropy of g , and photons from *both* field components can now be absorbed. Nevertheless, the *net effect of a linearly polarized field* is correctly described by Eqs. (3.31, 3.33).

2. This includes the hyperfine interaction.

In this case, and in particular for short pulses (pulse length $t_p \leq 1/\omega_1'$), we may neglect the static part of the Hamiltonian and consider the mw pulse with phase x as a rotation of the spin space about the x axis by an angle β_p in an infinitesimally short time. This can be described by the propagator

$$P_x = \exp\{-i\beta_p S_x\}, \quad (3.36)$$

with $\beta_p = \omega_1' t_p$; an analogous equation holds for pulses with phase y . Eq. (3.36) has been used in the calculation of Tab. 3-1. This Table can be applied to determine in the framework of the product operator formalism the transformation of a given density operator by ideal non-selective mw pulses.

In experiments without direct excitation of nuclear spins by rf irradiation, mw pulses can also be described as ideal pulses if

$$\omega_I' \gg \omega_1' \gg \Omega_S, A', B' \quad (3.37)$$

holds, since then no NC or forbidden EC exist. Actually, ESR lines in the solid state are usually inhomogeneously broadened (see §3.2.3) with a linewidth Γ that exceeds ω_1' , i.e., there are spin packets for which $\Omega_S > \omega_1'$. However, the effects of this violation of the conditions in Eq.(3.35 and 3.37) are not dramatic and can often be discussed in terms of a dependence of β_p on Ω_S .¹ It is therefore often sufficient to calculate an analytical formula for an experiment under the assumption of ideal non-selective pulses with arbitrary flip angles. Some effects of flip angle imperfections can be eliminated by phase cycling [24,43].

When ω_1' and A and ω_I' are of the same order of magnitude, new phenomena occur that cannot even be described qualitatively by treatments assuming ideal mw pulses (see §3.2.7). Such phenomena are different flip angles for the two allowed transitions, a resonance condition for ω_1' with respect to ω_I' for the maximum excitation of forbidden transitions, and the generation of NC from Boltzmann equilibrium by a single mw pulse.

1. In fact, the rotation is no longer about the x -axis but about an effective field axis that lies between the x - and z - axis. In addition to differences in the apparent flip angle, this also leads to differences in the phase of the EC for different Ω_S .

3.2.3 Ideal selective microwave pulses

Another simple description of mw pulses is possible for small ω_1 and sufficiently long pulses. In particular, if

$$\omega_1, \frac{2\pi}{t_p} \gg \min(\omega_\alpha, \omega_\beta), \quad (3.38a)$$

$$\omega_1, \frac{2\pi}{t_p} \gg \omega_{\text{HF}}, \quad (3.38b)$$

and

$$\omega_1, \frac{2\pi}{t_p} \gg \omega_{\text{NZ}}, \quad (3.38c)$$

the mw field interacts significantly with only one of the four electron spin transitions for any offset frequency Ω_S [40,44]. This situation can best be described in the frame where the product basis is the eigenbasis of the static Hamiltonian \mathcal{H}_0 . The mw excitation term in this frame is given by

$$\mathcal{H}_{\text{mw}} = U(\omega_1 \sin \theta_q S_x)U^{-1} = \omega_1' \cos \eta S_x + \omega_1' \sin \eta S_y I_y. \quad (3.39)$$

In Eq. (3.39), the term with factor $\cos \eta$ corresponds to the excitation of allowed electron spin transitions and the term with factor $\sin \eta$ to the excitation of forbidden transitions. \mathcal{H}_{mw} can also be written in terms of single transition operators

$$\mathcal{H}_{\text{mw}} = \omega_1' \cos \eta (S_x^{(13)} + S_x^{(24)}) + \omega_1' \sin \eta (S_x^{(14)} + S_x^{(23)}), \quad (3.40)$$

with

$$S_x^{(13, 24)} = S_x I^{\alpha, \beta}, \quad (3.41a)$$

and

$$S_x^{(14, 23)} = S_y I_y \mp S_x I_x. \quad (3.41b)$$

Levels are numbered according to Fig. 3-2 on page 47. Furthermore we define the offset of the single transitions from the mw frequency by

$$\Omega_S^{(kl)} = \omega_{kl} - \omega_{mw} . \quad (3.42)$$

If the conditions in Eq. (3.38a-c) hold, we can describe the excitation of each transition separately, since $\Omega_S^{(kl)} \gg \omega_1$ for at least three of the four transitions. In fact, this approach is a fictitious spin description like the one used in §3.1.1 for a different problem.

An ideal pulse treatment for selective excitation, i.e., neglecting the static Hamiltonian \mathcal{H}_0 during the pulse, is strictly allowed only if the density operator σ_0 before the pulse commutes with \mathcal{H}_0 . In this case, we can treat the excited transition as an isolated two-level subsystem and use Eq. (3.36) where we have to replace S_x by $S_x^{(kl)}$ for transition kl and β_p by $\beta_a = \beta_p \cos \eta$ and $\beta_f = \beta_p \sin \eta$ for allowed and forbidden transitions, respectively. This situation occurs for instance in ESR hole-burning experiments that begin with a selective pulse which acts on a state of Boltzmann equilibrium [45]. The hole-burning approach allows one to increase the resolution in ESR experiments on inhomogeneously broadened lines (see Fig. 3-3). Inhomogeneously broadened lines result from the superposition of the transitions of spins with slightly different parameters in \mathcal{H}_0 . If we describe a system of n nuclear spins coupled to an electron spin by using a partition into single-nucleus subsystems as shown in §3.1.1, we find that Ω_S for a subsystem depends on the states of all the other ligand nuclear spins. This would lead to a discrete distribution of 2^{n-2} Ω_S values ¹; however, because of homogeneous line broadening caused by transverse relaxation, a homogeneous distribution results that can often be approximated by a Gaussian function ². With sufficiently weak and long mw irradiation, it is possible to excite only spin packets with $\Omega_S^{(kl)} \approx 0$.

-
1. We have assumed here that one of the n spins belongs to the central atom.
 2. For the evolution of the spin system under the Hamiltonian it is irrelevant if Ω_S results from homogeneous or inhomogeneous broadening. The point is that an inhomogeneous line has to be described by a superposition of spin packets with different Hamiltonians.

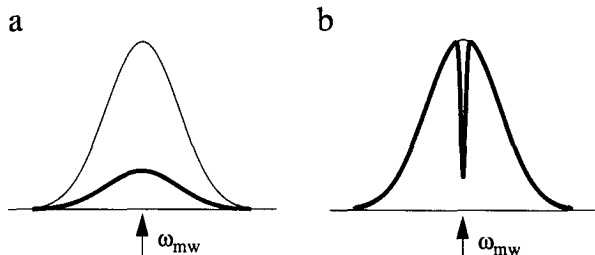


Fig. 3-3 Selective excitation of a broad ESR line. a) Homogeneously broadened line. The polarization decreases throughout the whole line. b) Inhomogeneously broadened line. Only spin packets close to resonance are excited, a polarization hole is burnt into the line.

The simple description of selective excitation given above is sufficient to describe hole-burning experiments qualitatively [45]. To calculate hole shapes, one has to consider the term $\Omega_S^{(kk)} S_z$ which leads to non-ideal selective pulses (see §3.2.5). In practice, one often uses pulse lengths t_p that are not short compared to electron spin-spin relaxation. In this case, the description of selective pulses can be provided by Bloch equations for a two-level system [8], while the above treatment yields the correct scaling factor for ω_1 . Furthermore, hole-burning experiments often use Gaussian-shaped mw pulses because of the smoother hole profile obtained with them. In this case it is necessary to apply numerical simulations to obtain good agreement with experimental results.

With the condition $[\mathcal{H}_0, \sigma_0] = 0$, treatments using ideal selective pulses can only be applied to states that feature no coherence. An exception is the presence of coherence on the transition that is on-resonant with the mw irradiation ($\Omega_S^{(kk)} = 0$), since we can find an interaction representation for which the frequency of this transition is zero. In fact, it is even possible to subdivide σ_0 in this representation into one part σ_c that commutes with \mathcal{H}_0 and one part σ_{nc} that does not. If

$$[\sigma_{nc}, S_x^{(kl)}] = 0, \quad (3.43)$$

we can write

$$\sigma''(t) = P_x \sigma_c P_x^{-1} + \exp(-i\mathcal{H}_0'' t) \sigma_{nc} \exp(i\mathcal{H}_0'' t), \quad (3.44)$$

where the two primes indicate the interaction representation where $\omega_{\mu k}=0$. The conversion to the usual rotating frame can be done by applying a unitary transformation with

$$U_{\text{rot}} = \exp\{-i(\Omega_S - \Omega_S^{(lk)})t\} \quad (3.45)$$

to $\sigma''(t)$. The condition given by Eq. (3.43) is fulfilled if and only if there are no coherences on transitions that share a common level with the transition lk . Therefore, the concept of ideal selective pulses cannot be applied in the presence of NC, and for excitation of allowed (forbidden) transitions in the presence of EC on forbidden (allowed) transitions.

3.2.4 Ideal semi-selective microwave pulses

Another type of ideal pulses can be defined with the condition

$$\omega_{\alpha, \beta} \gg \omega_I \gg \omega_{\beta, \alpha} \quad (3.46)$$

that can be fulfilled, if

$$|\omega_I'| = 2A' \quad (3.47)$$

i.e., close to exact cancellation [46] of the nuclear Zeeman field and the secular part of the hyperfine field in one of the electron spin manifolds. In this case, the allowed and the forbidden transition that are split by the smaller nuclear frequency can be excited at the same time while the other two transitions are far off-resonant (see Fig. 3-4 on page 68). The intensity of the allowed and forbidden transitions is nearly equal. The situation is designated as semi-selective excitation and has been treated by analytical calculation of the propagator for the ideal semi-selective pulse in the rotating frame [40,47]. For consistency with the other treatments in this work and as a basis for a description of non-ideal semi-selective pulses, we choose here the alternative approach of diagonalizing the Hamiltonian that acts during the pulse. This Hamiltonian is given by

$$\mathcal{H}_{\text{ss}} = \omega_I'(\cos \eta S_x^{(13)} + \sin \eta S_x^{(14)}) \quad (3.48)$$

where we have singled out a certain pair of an allowed and a forbidden transition. The other three cases are completely analogous and require only a simple reordering of the

matrices given below. The matrix representation of the Hamiltonian in Eq. (3.48) is given by

$$\mathcal{H}_{ss} = \begin{bmatrix} 0 & \frac{\cos \eta \omega_1}{2} & 0 & 0 \\ \frac{\cos \eta \omega_1}{2} & 0 & \frac{-\sin \eta \omega_1}{2} & 0 \\ 0 & \frac{-\sin \eta \omega_1}{2} & 0 & 0 \\ 0 & 0 & 0 & 0 \end{bmatrix}. \quad (3.49)$$

This equation shows that semi-selective excitation can be described in a three-level subsystem. \mathcal{H}_{ss} can be diagonalized by the unitary transformation $U_{ss} \mathcal{H}_{ss} U_{ss}^T$ where the superscript T denotes the matrix transpose and where

$$U_{ss} = \begin{bmatrix} \frac{-\sqrt{2}}{2} \cos \eta & \frac{-\sqrt{2}}{2} & \frac{\sqrt{2}}{2} \sin \eta & 0 \\ \frac{-\sqrt{2}}{2} \cos \eta & \frac{\sqrt{2}}{2} & \frac{\sqrt{2}}{2} \sin \eta & 0 \\ \sin \eta & 0 & \cos \eta & 0 \\ 0 & 0 & 0 & 1 \end{bmatrix}. \quad (3.50)$$

The diagonalized Hamiltonian has the form

$$\tilde{\mathcal{H}}_{ss} = \begin{bmatrix} \omega_1'/2 & 0 & 0 & 0 \\ 0 & -\omega_1'/2 & 0 & 0 \\ 0 & 0 & 0 & 0 \\ 0 & 0 & 0 & 0 \end{bmatrix}. \quad (3.51)$$

The evolution of the density operator during the semi-selective pulse can then be described by

$$\sigma(t_p) = U^T \exp(-i \tilde{\mathcal{H}}_{ss} t_p) U \sigma_0 U^T \exp(i \tilde{\mathcal{H}}_{ss} t_p) U. \quad (3.52)$$

Note that Eq. (3.52) is only valid if there are no coherences involving level 2, i.e., only if the problem can be reduced to the three-level system on which the semi-selective pulse acts. This assumption can be made if the semi-selective pulse is applied to a system in Boltzmann equilibrium or if no non-selective mw pulses or rf pulses at the larger nuclear frequency have been applied before. In other cases, one has to apply the description given in §3.2.6.

3.2.5 Non-ideal selective microwave pulses

Since the introduction of the coherent Raman beat experiment [48,49] there has been a considerable interest in a theoretical description of the detection of NC by a (selective) mw probe pulse [50,51]. We have seen in §3.2.3 that this requires the consideration of the static Hamiltonian during the mw irradiation. As long as the conditions in Eq. (3.38a-c) hold, we can however neglect the off-resonant single transition terms of the mw excitation in Eq (3.40) and can write the Hamiltonian during a probe pulse on-resonant with transition kl as

$$\mathcal{H}_{pp}^{(kl)} = \Omega_S S_z + \omega_{12} S^{\alpha} I_z + \omega_{34} S^{\beta} I_z + \omega_1 f(\eta) S_x^{(kl)}, \quad (3.53)$$

where $f(\eta)=\cos\eta$ for allowed transitions and $f(\eta)=\sin\eta$ for forbidden transitions. This Hamiltonian can be diagonalized by the unitary transformation $U_{kl}\mathcal{H}_{pp}U_{kl}^{-1}$ with

$$U_{kl} = \exp(-i\theta_{kl}S_y^{(kl)}), \quad (3.54)$$

where

$$S_y^{(13, 24)} = S_y I^{\alpha/\beta}, \quad (3.55a)$$

$$S_y^{(14, 23)} = \frac{1}{2}(S_x I_y \pm S_y I_x), \quad (3.55b)$$

and

$$\theta_{kl} = \frac{-\omega_1 f(\eta)}{\Omega_S^{(kl)}}. \quad (3.56)$$

In the frame, where the product basis is its eigenbasis, the effective Hamiltonian during the probe pulse is given by

$$\tilde{\mathcal{H}}_{pp}^{(kl)} = \Omega_{\text{eff}}^{(kl)} S_z + \omega_{I, \text{eff}}^{(kl)} I_z + A_{\text{eff}}^{(kl)} S_z I_z . \quad (3.57)$$

The values of $\Omega_{\text{eff}}^{(kl)}$, $\omega_{I, \text{eff}}^{(kl)}$, and $A_{\text{eff}}^{(kl)}$ are given in Tab. 3-2. This description of non-ideal selective pulses has been applied to the two-pulse CRB experiment [44]. It has been found that in the range of ω_1' in which the mw irradiation does not perturb the observed nuclear frequencies significantly, this approach is in good agreement with numerical simulations based on exact diagonalization of the Hamiltonian. In [44], it has also been discussed how the approach can be modified if either the condition (3.38b) or the condition (3.38c) is violated. Whenever relation (3.38a) does not hold, one of the approaches discussed in §3.2.6 or §3.2.7 should be applied.

Table 3-2 Parameters of the effective Hamiltonian during an mw probe pulse (see Eq.(3.57))

Transition (kl)	$\Omega_{\text{eff}}^{(kl)}$	$\omega_{r,\text{eff}}^{(kl)}$	$A_{\text{eff}}^{(kl)}$
(13)	$-\frac{1}{2}[\omega_{\text{HF}} - (1 + \cos\theta_{13})\Omega_S^{(13)} + \omega_1' \cos\eta \sin\theta_{13}]$	$\frac{1}{2}\omega_{\text{NZ}}$	$\omega_{\text{HF}} - (1 - \cos\theta_{13})\Omega_S^{(13)} - \omega_1' \cos\eta \sin\theta_{13}$
(24)	$\frac{1}{2}[\omega_{\text{HF}} + (1 + \cos\theta_{24})\Omega_S^{(24)} - \omega_1' \cos\eta \sin\theta_{24}]$	$\frac{1}{2}\omega_{\text{NZ}}$	$\omega_{\text{HF}} + (1 - \cos\theta_{24})\Omega_S^{(24)} + \omega_1' \cos\eta \sin\theta_{24}$
(14)	$-\frac{1}{2}[\omega_{\text{NZ}} - (1 + \cos\theta_{14})\Omega_S^{(14)} - \omega_1' \sin\eta \sin\theta_{14}]$	$\omega_{\text{NZ}} - (1 - \cos\theta_{14})\Omega_S^{(14)} + \omega_1' \cos\eta \sin\theta_{14}$	ω_{HF}
(23)	$\frac{1}{2}[\omega_{\text{NZ}} + (1 + \cos\theta_{23})\Omega_S^{(23)} + \omega_1' \sin\eta \sin\theta_{23}]$	$\omega_{\text{NZ}} + (1 - \cos\theta_{23})\Omega_S^{(23)} - \omega_1' \cos\eta \sin\theta_{23}$	ω_{HF}

3.2.6 Non-ideal semi-selective microwave pulses

We have seen in §3.2.4 that the description of excitation by the concept of ideal semi-selective mw pulses fails if the fourth level takes part in the experiment. The reason for this is that \mathcal{H}_{ss} in Eq. (3.48) does not contain information on the energy of this level. As long as condition (3.46) holds, this can be remedied by writing the extended Hamiltonian

$$\mathcal{H}'_{ss} = \omega_1' (\cos \eta S_x^{(13)} + \sin \eta S_x^{(14)}) + (\omega_{12} - \omega_{34}/2) S^\alpha I^\beta, \quad (3.58)$$

with a matrix representation that differs from the one of \mathcal{H}_{ss} in Eq. (3.49) only by replacing the value zero in the lower left corner by $(\omega_{12} - \omega_{34}/2)$. The situation is depicted in Fig. 3-4.

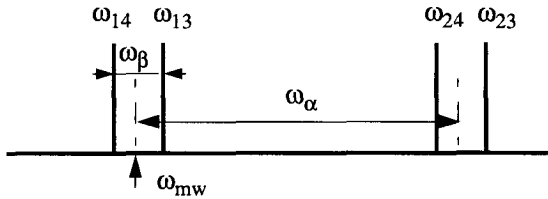


Fig. 3-4 ESR spectrum in a situation where the description by semi-selective pulses is appropriate.

\mathcal{H}'_{ss} can be diagonalized by the same unitary transformation as \mathcal{H}_{ss} , in the resulting diagonal matrix (cf. Eq.(3.51)), the value zero in the lower left corner has to be replaced also by $(\omega_{12} - \omega_{34}/2)$. This treatment is still restricted, since it cannot handle irradiation that is off-resonant from the center of the two excited transitions. As already mentioned in §3.2.2, the behaviour of the spin system during a pulse sequence can be explained at least qualitatively in spite of this and the deviations can be discussed in terms of a dependence of the nominal flip angle on Ω_S .

One can show that an ideal semi-selective mw pulse creates NC on *one* of the two nuclear transitions and that maximum coherence is obtained for a nominal flip angle of π

[47]. The same result is obtained with the approach presented here, for the expectation value of the NC created by a semi-selective pulse of duration t_p we find

$$\langle S^{\beta} I_x \rangle = \sin \eta \cos \eta [1 - \cos(\omega_1' t_p)] , \quad (3.59)$$

while $\langle S^{\beta} I_y \rangle = 0$. However, this is no longer true if the condition (3.46) is violated. As an example, we have calculated $\langle S^{\beta} I_x \rangle$ for $\omega_{\beta}/(2\pi) = 2$ MHz and $\omega_1'/(2\pi) = 10$ MHz by integrating the quantum mechanical master equation (2.14) for the three-level system numerically with the program Mathematica. This nuclear frequency, mw field strength and the used relaxation times of 1 μ s for EC, of 100 μ s for the NC and for electron polarization, and of 10 ms for nuclear polarization are typical for experiments on protons. Cross-relaxation has been neglected. From the result shown in Fig. 3-5 one can conclude that in practice flip angles larger than 2π may be needed to obtain maximum NC even in a situation where the transition probabilities of all four electron spin transitions are equal ($\eta = \pi/2$).

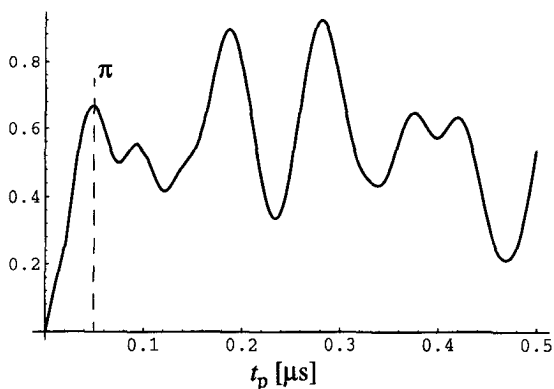


Fig. 3-5 Expectation value of $\langle S^{\beta} I_x \rangle$ after a semi-selective pulse ($\omega_1'/(2\pi) = 10$ MHz) of duration t_p acting on a system in Boltzmann equilibrium (numerical simulation). Other parameters are $\omega_{\beta} = 2$ MHz, $T_{2e} = 1$ μ s, $T_{2n} = 100$ μ s, $T_{1e} = 100$ μ s, $T_{1n} = 10$ ms. The mw frequency corresponds to the center of the two excited electron spin transitions, the transition probabilities of the two excited transitions are assumed to be equal.

3.2.7 Non-ideal pulses of arbitrary strength and duration

The finding that there is an optimum flip angle larger than 2π for the generation of NC by a semi-selective pulse shows that a description of mw pulses of arbitrary duration is required. In addition, it has been found experimentally that the nuclear modulations in a signal obtained with a *non-selective* probe pulse are maximum for $\omega_1' \approx \omega_I'$ [52], so that the required description should also allow for arbitrary field strengths of the mw pulse. In principle, it is possible to diagonalize any 4×4 matrix analytically, i.e., the eigenvalues of \mathcal{H}_{ex} can be calculated. This has been done for the matrix representation of \mathcal{H}_{ex} in Eq. (3.34) using the program Mathematica; the result is given in Appendix A. A similar result for an electron spin $S=1/2$ instead of a fictitious spin $S'=1/2$ has been published elsewhere [53]. Though these analytical expressions can be used for computationally efficient numerical calculations and to derive simpler formulas for limiting cases, they are too extensive to yield much physical insight. For that reason, no attempt has been made to calculate the eigenvectors.

Instead of using the brute force approach of exact diagonalization, one can try to find a basis in which all off-diagonal elements are small and then truncate the Hamiltonian. This method has been used for instance in NMR spectroscopy to describe coherence transfer in heteronuclear double irradiation experiments in solution [54]. Since in this case also a resonance condition exists for optimum coherence transfer¹, it seems appropriate to exploit the analogy. The complete Hamiltonian is given in the eigenbasis of its static part by

$$\tilde{\mathcal{H}}_{\text{ex}} = \Omega_S S_z + \omega_{12} S_z^\alpha I_z + \omega_{34} S_z^\beta I_z + \omega_1' \cos \eta S_x + \omega_1' \sin \eta S_y I_y, \quad (3.60)$$

1. This is the famous Hartmann-Hahn matching condition $\gamma_I B_{1I} = \gamma_S B_{1S}$ [12]. In fact, Hartmann-Hahn coherence transfer is a special case of coherence transfer in the vicinity of an avoided level crossing. At an avoided level crossing, states of different spins are completely mixed and two of the resulting states are nearly degenerate. A very small off-diagonal element X between these states is then sufficient to provide complete coherence transfer on a time scale of $2\pi/X$. Avoided level crossings can be attained by applying an appropriate external perturbation, e.g., setting the static or periodic external magnetic field to a certain value, rotating the sample with a certain speed or using an electric field of a certain strength.

according to Eqs. (3.20 and 3.39). In a large majority of cases, the transition moment of the forbidden transitions is much smaller than the one of the allowed transitions, i.e., $\sin \eta \ll \cos \eta$. Therefore, only small off-diagonal elements remain in the eigenbasis of the Hamiltonian that consists of only the static part and the excitation term $\omega_1' \cos \eta S_x$ corresponding to the allowed transitions. The unitary transformation that leads to the tilted frame where the product basis is this eigenbasis, is given by $U_a \tilde{\mathcal{H}}_{\text{ex}} U_a^{-1}$ with

$$U_a = \exp \{-i(\theta_\alpha S_y I^\alpha + \theta_\beta S_y I^\beta)\} , \quad (3.61)$$

and

$$\theta_{\alpha, \beta} = \text{atan} \left(\frac{-\omega_1' \cos \eta}{\omega_{\text{HF}}/2 \pm \Omega_S} \right) . \quad (3.62)$$

This transformation is completely analogous to the diagonalization of the static Hamiltonian (see Eq. (3.12-3.14)), and we can define the effective electron frequencies

$$\omega_{13, 24}^{\text{eff}} = \cos \theta_{\alpha, \beta} \left(\Omega_S \pm \frac{A'}{2} \right) - \omega_1' \sin \theta_{\alpha, \beta} \cos \eta , \quad (3.63)$$

the effective electron Zeeman frequency

$$\Omega_S^{\text{eff}} = (\omega_{13}^{\text{eff}} + \omega_{24}^{\text{eff}})/2 , \quad (3.64a)$$

and the effective hyperfine coupling

$$A^{\text{eff}} = (\omega_{13}^{\text{eff}} - \omega_{24}^{\text{eff}})/2 . \quad (3.64b)$$

In a first approximation, the hyperfine coupling is scaled by the decoupling factor

$$f_{\text{dec}} \approx \frac{\omega_{\text{HF}}}{2\omega_1' \cos \eta} \quad (3.65)$$

for small Ω_S . The *complete* Hamiltonian in the tilted frame can be written as

$$\begin{aligned} \mathcal{H}_{\text{ex}}^{\text{eff}} = & \Omega_S^{\text{eff}} S_z + (\omega_{\text{NZ}}/2) I_z + A^{\text{eff}} S_z I_z \\ & + \frac{1}{2} \omega_1' \sin \eta \cos \theta (S^+ I^- + S^- I^+) \\ & - \omega_1' \sin \eta \sin \theta I_x \\ & - \frac{1}{2} \omega_1' \sin \eta \cos \theta (S^+ I^+ + S^- I^-) \end{aligned} \quad (3.66)$$

where

$$\theta = (\theta_\alpha - \theta_\beta)/2, \quad (3.67a)$$

and

$$-45^\circ < \theta \leq 45^\circ. \quad (3.67b)$$

Eq. (3.67b) ensures that in the tilted frame, the first, second, and third off-diagonal term on the right-hand side of Eq. (3.66) correspond to zero-quantum, single-quantum, and double-quantum coherence, respectively. The single- and double-quantum terms are small off-diagonal elements that connect diagonal elements with a comparatively large energy difference as long as

$$\omega_1' \sin \eta \ll \omega_{\text{NZ}}/2, \quad (3.68)$$

so that they can be neglected. The remaining truncated Hamiltonian is diagonal in a frame defined by an unitary transformation with

$$U_{\text{tr}} = \exp \left\{ \frac{\xi}{2} (S^+ I^- - S^- I^+) \right\}, \quad (3.69)$$

and

$$\xi = \text{atan} \left(\frac{\omega_1' \sin \eta \cos \theta}{\Omega_S^{\text{eff}} - \omega_{\text{NZ}}/2} \right), \quad (3.70)$$

and can be written in this frame as

$$\mathcal{H}^{\text{tr}} = \Omega_S^{\text{tr}} S_z + \omega_I^{\text{tr}} I_z + A^{\text{eff}} S_z I_z, \quad (3.71)$$

with

$$\Omega_S^{\text{tr}} = \Omega_S^{\text{eff}} \cos^2\left(\frac{\xi}{2}\right) + \frac{\omega_{\text{NZ}}}{2} \sin^2\left(\frac{\xi}{2}\right) + \frac{1}{2}\omega_1' \sin\eta \cos\theta \sin\xi, \quad (3.72a)$$

and

$$\omega_I^{\text{tr}} = \frac{\omega_{\text{NZ}}}{2} \cos^2\left(\frac{\xi}{2}\right) + \Omega_S^{\text{eff}} \sin^2\left(\frac{\xi}{2}\right) - \frac{1}{2}\omega_1' \sin\eta \cos\theta \sin\xi. \quad (3.72b)$$

For $\xi = 90^\circ$ we have $\cos(\xi/2) = \sin(\xi/2) = \sqrt{2}/2$ and therefore complete mixing of electron and nuclear spin states. This condition is obviously fulfilled if $\Omega_S^{\text{eff}} = \omega_{\text{NZ}}/2$. By expressing Ω_S^{eff} with the help of Eqs. (3.62-3.64a) we obtain for the corresponding mw field strength

$$\omega_1^m = \frac{1}{|\omega_{\text{NZ}}/2| \cos\eta} \left[\omega_{12} \omega_{34} \left(\frac{\omega_{\text{NZ}}^2}{4} - \Omega_S^2 \right) \right]^{1/2}. \quad (3.73)$$

In the following we refer to this condition as a Hartmann-Hahn match [12] and to ω_1^m as the matching field, since the situation is analogous to a double resonance experiment. The difference is that in double resonance the effective fields for two spins in a *doubly rotating* frame must be matched, while in our case the effective field for the electron spin in the rotating frame matches the *static Zeeman* field for the nuclear spin. The irradiation of the nuclear spins is formally replaced by the pseudo-secular parts of the hyperfine coupling and the effective nuclear Zeeman interaction ($B' S_z I_x - \omega_{I_x}' I_x$). It has been shown earlier that the opposite replacement of a pseudo-secular hyperfine coupling by irradiation on-resonant with the nuclear spins is also feasible [42]. Alternatively, the matching can be explained in a dressed state picture. The electron spin dressed by the mw field has the same transition frequency as the nuclear spin in the static field, so that a small oscillating interaction between the two spins leads to energy-conserving flip-flop transitions.

For a group of spins with the same Ω_S , magnetization transfer processes between the electrons and nuclei take place on a time scale defined by $2\pi/\omega_1^m \sin\eta \cos\theta$. For

$\cos\theta \approx 0$, which is fulfilled in the case of small HFI for spin packets that are on-resonant, nearly complete transfer can be achieved as long as

$$\sin\eta > \frac{2\pi}{\omega_1^m T_2^m}, \quad (3.74)$$

where T_2^m is the transverse relaxation time at the matching, which is of the order of a few μs ¹.

The effect on the spin system of a non-ideal mw pulse of any strength satisfying the condition (3.68) can be described in the eigenbasis of the static Hamiltonian by the density operator equation

$$\sigma_1 = U_a^{-1} U_{\text{tr}}^{-1} \exp(-i \mathcal{H}^{\text{tr}} t_p) U_{\text{tr}} U_a \sigma_0 U_a^{-1} U_{\text{tr}}^{-1} \exp(i \mathcal{H}^{\text{tr}} t_p) U_{\text{tr}} U_a, \quad (3.75)$$

that can be simplified by using the superoperator notation

$$\hat{R}\sigma_0 = U_{\text{tr}} U_a \sigma_0 U_a^{-1} U_{\text{tr}}^{-1}, \quad (3.76)$$

where \hat{R} is a unitary transformation superoperator of Liouville space dimension 16. The matrix representation of \hat{R} has been given in [55]. It is now straightforward though tedious to calculate the effect of a non-ideal pulse on any state of the spin system. We find that such a pulse can effect transfers between two *arbitrary* elements of the density operator. These transfers are classified in Tab. 3-3. Forbidden transfers are enhanced by fulfilling the Hartmann-Hahn condition Eq. (3.73), correspondingly allowed transfers are weakened. It is therefore promising to insert matched pulses of sufficient duration into pulse sequences whenever a forbidden transfer is needed, while for allowed transfers, non-selective or selective pulses should be used with mw field strengths far from the Hartmann-Hahn condition.

1. Under conditions of complete mixing, there are no separate relaxation times for electron and nuclear spins.

Table 3-3 Classification of density operator single element transfers in an $S^z=1/2, I=1/2$ system.

Transfer	Single operator description	Type
Polarization \leftrightarrow allowed EC	$S^{\alpha}I^{\alpha}, S^{\alpha}\beta, S^{\beta}I^{\alpha}, S^{\beta}\beta \leftrightarrow S^+I^{\alpha}, S^-I^{\alpha}, S^+I^{\beta}, S^-I^{\beta}$	allowed
Polarization \leftrightarrow forbidden EC	$S^{\alpha}I^{\alpha}, S^{\alpha}\beta, S^{\beta}I^{\alpha}, S^{\beta}\beta \leftrightarrow S^+I, S^-I, S^+I^+, S^-I^+$	forbidden
Polarization \leftrightarrow NC	$S^{\alpha}I^{\alpha}, S^{\alpha}\beta, S^{\beta}I^{\alpha}, S^{\beta}\beta \leftrightarrow S^{\alpha}I^+, S^{\alpha}I^-, S^{\beta}I^+, S^{\beta}I^-$	forbidden
allowed EC \leftrightarrow forbidden EC	$S^+I^{\alpha}, S^-I^{\alpha}, S^+I^{\beta}, S^-I^{\beta} \leftrightarrow S^+I, S^-I, S^+I^+, S^-I^+$	forbidden
allowed EC \leftrightarrow NC	$S^+I^{\alpha}, S^-I^{\alpha}, S^+I^{\beta}, S^-I^{\beta} \leftrightarrow S^{\alpha}I^+, S^{\alpha}I^-, S^{\beta}I^+, S^{\beta}I^-$	forbidden
forbidden EC \leftrightarrow NC	$S^+I, S^-I, S^+I^+, S^-I^+ \leftrightarrow S^{\alpha}I^+, S^{\alpha}I^-, S^{\beta}I^+, S^{\beta}I^-$	allowed
forbidden EC interchange	$S^+I, S^-I^+ \leftrightarrow S^-I, S^+I^+$	allowed
allowed EC phase inversion	$S^+I^{\alpha} \leftrightarrow S^-I^{\alpha}, S^+I^{\beta} \leftrightarrow S^-I^{\beta}$	allowed
forbidden EC phase inversion	$S^+I \leftrightarrow S^-I^+, S^+I^+ \leftrightarrow S^-I$	strongly forbidden
NC phase inversion	$S^{\alpha}I^+ \leftrightarrow S^{\alpha}I^-, S^{\beta}I^+ \leftrightarrow S^{\beta}I^-$	strongly forbidden
allowed EC interchange	$S^+I^{\alpha}, S^-I^{\alpha} \leftrightarrow S^+I^{\beta}, S^-I^{\beta}$	strongly forbidden
NC interchange	$S^{\alpha}I^+, S^{\alpha}I^- \leftrightarrow S^{\beta}I^+, S^{\beta}I^-$	allowed

Of particular interest are the generation of NC from Boltzmann equilibrium (electron spin polarization) and the transfer between EC and NC, since the generation and detection of NC is the basis of most of the high-resolution experiments in solid-state ESR (see Chapter 4). A Hartmann-Hahn match of the form $\omega_1' = |\omega_j|^{-1}$ for optimum generation of NC by a single mw pulse has been suggested by Bowman for the case of very small hyperfine interactions $A' \ll \omega_j'$ [48]. Indeed, Eq. (3.73) reduces to this condition for a vanishing offset Ω_S under the assumptions used by Bowman. Note however, that the approach used in [48] leads to the erroneous result of an optimum flip angle of 109.47° (twice the magic angle), since it is valid only in the limit of small flip angles. In contrast, Fig. 3-6 shows that the pulse duration for optimum transfer depends on the strength of the forbidden transitions ($\sin\eta = 0.129$ in Fig. 3-6a, $\sin\eta = 0.012$ in Fig. 3-6b,c) and is much larger than the one of a π pulse for systems with typical parameters. It is also obvious, that in practice complete transfer cannot be achieved for very weak forbidden transitions, since the build-up competes with transverse relaxation. Nevertheless it can be concluded that pulse matching opens up a great potential for sensitivity enhancement in particular for very weak forbidden transitions.

For practical applications, further points have to be considered. First, the build-up of NC is oscillatory with a frequency $\omega_1^m/2$, local maxima are found close to nominal flip angles of $n\pi$, where n is a positive integer. Second, mw field inhomogeneities lead to destructive interference between spins in different regions of the resonator, this mechanism may cause an apparent decrease of T_2^m . More significantly, ω_1^m also depends on Ω_S , so that there is also destructive interference between spins with different resonance offsets. Simulations show that the last mechanism imposes the limit for the forbidden transfer efficiency of matched pulses. One can conclude that matched pulses are particularly promising for experiments that observe only spins with a small distribution in Ω_S , for instance coherent Raman beat experiments [48-52]. In addition, sensitivity enhancements should be large when *strongly* forbidden transfers are needed as for the creation of nuclear echoes solely with mw pulses [47]. In Chapter 5 it is shown that substantial

1. This can also be written in the more familiar form $\gamma_S B_1 = |\gamma_I B_0|$.

enhancements can even be obtained in two-pulse ESEEM where destructive interference is assumed to be important.

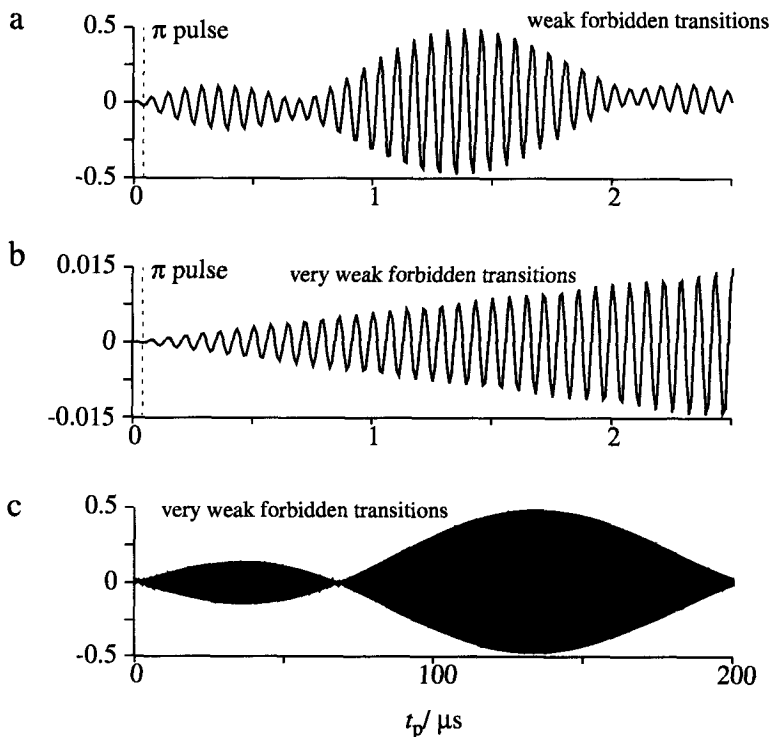


Fig. 3-6 Build-up of nuclear coherence during a non-ideal microwave pulse of duration t_p acting on a state of Boltzmann equilibrium. Numerical simulations of $\langle S^\alpha I_y \rangle(t_p)$ for a single spin packet are plotted. Parameters: a) $\omega_1'/2\pi = -14$ MHz, $A'/2\pi = 6.43$ MHz, $B'/2\pi = 3.43$ MHz, $\Omega_S/2\pi = 3.19$ MHz, $\omega_1/2\pi = 13.50$ MHz; b) $\omega_1'/2\pi = -14$ MHz, $A'/2\pi = 0.643$ MHz, $B'/2\pi = 0.343$ MHz, $\Omega_S/2\pi = 3.19$ MHz, $\omega_1/2\pi = 13.995$ MHz. The systems are typical for protons in transition metal complexes or in free radicals at X-band frequencies. Relaxation has been neglected.

It has already been mentioned before that we cannot assume that the partition into single-nucleus subsystems is a good approximation for non-ideal pulses. In the derivation above, this partition *can* be made for the static Hamiltonian which takes the form

$$\mathcal{H}_{0,N} = \Omega_S S_z + \sum_j^N [(\omega_{NZ,j}/2)I_{zj} + \omega_{HF,j} S_z I_{zj}] , \quad (3.77)$$

while the mw part is given by

$$\mathcal{H}_{mw,N} = \omega_1 S(k) \prod_j^N (\cos \eta_j + i I_{yj} \sin \eta_j) , \quad (3.78)$$

where the spin operator $S(k)$ depends on the number k of I_{yj} factors in the expansion of the product. It is given by S_x in terms with even k and by $-iS_y$ in terms with odd k . The Hamiltonian

$$\mathcal{H}_{a,N} = \mathcal{H}_{0,N} + S_x \prod_j^N \cos \eta_j , \quad (3.79)$$

can be diagonalized by the unitary transformation with

$$U_{a,N} = \prod_j^N U_{a,j} , \quad (3.80)$$

since $[S^\alpha I_{yj} + S^\beta I_{yj}, S^\alpha I_{yk} + S^\beta I_{yk}] = 0$ for arbitrary k, j , i.e., up to this point the whole tensor space can still be factorized. It can be shown however, that in the tilted frame the remaining off-diagonal elements for the different spins do not commute, for instance

$$[S^+ I_j^- + S^- I_j^+, S^+ I_k^- + S^- I_k^+] = -2S_z (I_j^+ I_k^- - I_j^- I_k^+) . \quad (3.81)$$

Therefore, the product rule breaks down if pulse non-ideality has to be considered; for a more detailed discussion see [55]. This is illustrated in Fig. 3-7 for two-pulse ESEEM with typical hard pulses on a system consisting of an electron spin and two nuclear spins that cause deep echo modulations. Though the absolute deviations are small, there are large relative deviations for the combination peaks that involve frequencies of both nuclei. Even larger deviations are found for matched pulses with high flip angle.

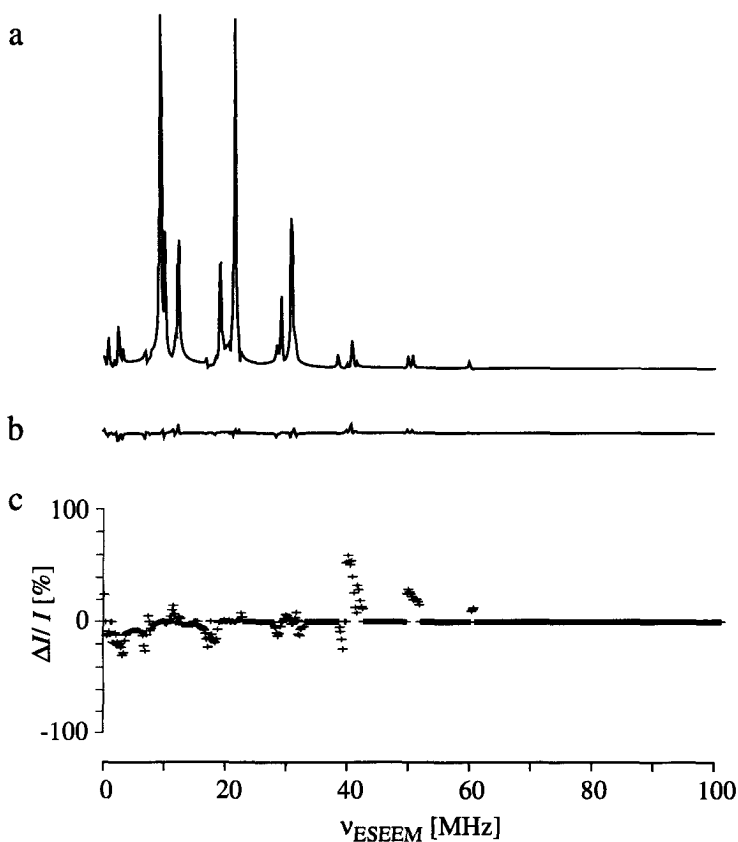


Fig. 3-7 Deviation of a two-pulse ESEEM spectrum from the product rule [28] in the case of deep modulations. Parameters: Mw pulses of duration 10 (flip angle $\pi/2$) and 20 ns (flip angle π), $\omega_{11}'/2\pi = \omega_{12}'/2\pi = 14$ MHz, $A_1'/2\pi = 13.43$ MHz, $B_1'/2\pi = 11.43$ MHz, $A_2'/2\pi = 9.43$ MHz, $B_2'/2\pi = 7.43$ MHz, a) Numerical simulation by exact matrix diagonalization. b) Difference between the spectrum in (a) and a spectrum calculated by using the product rule after diagonalization of submatrices corresponding to the single nuclei. c) Relative deviation of the spectrum calculated by the product rule.

A possibility for a partial reduction in dimensionality of the problem is discussed in [55]. Note also, that only the intensities but not the frequencies are affected by the breakdown of the product rule and that in most experimental situations no combination lines between different nuclei are observed. However, in schemes where the modulation depth is used to extract structural information, the effect may be important.

3.2.8 Selective radio frequency pulses

Consider the case of isotropic HFI and isotropic g matrix¹. In a frame rotating with frequency ω_{mw} about the S_z axis, the effective Hamiltonian during rf irradiation is given by

$$\begin{aligned} \mathcal{H}'_{\text{rf}}(t) = & \Omega_S S_z - \omega_I' I_z + a(S_x I_x + S_y I_y + S_z I_z) - 2\omega_2 \cos(\omega_{\text{rf}} t) I_x \\ & + \omega_{2S} \{ \cos[(\omega_{\text{rf}} + \omega_{\text{mw}})t] + \cos[(\omega_{\text{rf}} - \omega_{\text{mw}})t] \} S_x \\ & + \omega_{2S} \{ \sin[(\omega_{\text{rf}} + \omega_{\text{mw}})t] - \sin[(\omega_{\text{rf}} - \omega_{\text{mw}})t] \} S_y, \end{aligned} \quad (3.82)$$

with $\omega_2 = 2\pi g_n \beta_n B_2 / h$, $\omega_{2S} = 2\pi g_e \beta_e B_2 / h$. B_2 is the rf field strength, and the terms in the second and third line on the right hand side of Eq. (3.82) arise from the off-resonant interaction of this field with the electron spin. Note that we cannot neglect here the terms $aS_x I_x$ and $aS_y I_y$, for reasons that become apparent below. By introducing a rotation of the frame with frequency ω_{rf} about the I_z axis, we obtain a Hamiltonian $\mathcal{H}'_{\text{rf}}(t)$ in another interaction representation in which the term $-2\omega_2 \cos(\omega_{\text{rf}} t) I_x$ is replaced by $-\omega_2 I_x$ and ω_I' by

$$\Omega_I = \omega_I' - \omega_{\text{rf}}, \quad (3.83)$$

(see §3.2.1)². We can now calculate an average Hamiltonian by applying the Magnus expansion [56] up to first order

$$\bar{\mathcal{H}}_{\text{rf}}^{(0)} = \frac{1}{t_c} \int_0^{t_c} \mathcal{H}'_{\text{rf}}(t_1) dt_1, \quad (3.84a)$$

$$\bar{\mathcal{H}}_{\text{rf}}^{(1)} = \frac{-i}{2t_c} \int_0^{t_c} dt_2 \int_0^{t_2} [\mathcal{H}'_{\text{rf}}(t_2), \mathcal{H}'_{\text{rf}}(t_1)] dt_1, \quad (3.84b)$$

where t_c is the cycle time (period) of the time-dependent Hamiltonian. Strictly speaking, average Hamiltonian theory can only be applied to stroboscopic observation with period

-
1. The condition of an isotropic g matrix can be relaxed analogously to the treatment in §3.2.1.
 2. Being isotropic, the hyperfine coupling is invariant under rotations.

t_c . It is also a good approximation if the system evolves under the Hamiltonian for a time $t \gg t_c$. The application to the description of rf pulses with $t < t_c$ can be justified for the following reasons: (a) We will not use the approximation to describe the interaction of the rf field with EC (see below); (b) The interaction of the rf field with polarization or NC on a *single* nuclear transition can be described by a nutation with frequency ω_2' about an effective field; (c) The nutation frequency ω_2' can be determined with stroboscopic observation at least for $\omega_{\text{rf}} > 2\omega_2'$.¹

With Eqs. (3.84a,b) and using $\omega_{\text{mw}} \gg \omega_{\text{rf}}$ we find

$$\bar{\mathcal{H}}_{\text{rf}}^{(0)} = \Omega_S S_z - \Omega_I I_z + a S_z I_z - \omega_2 I_x, \quad (3.85a)$$

$$\bar{\mathcal{H}}_{\text{rf}}^{(1)} = \frac{B_2}{B_0} (-\omega_{2s} S_z - \Omega_S S_x - a S_x I_z + a S_z I_x). \quad (3.85b)$$

The first term on the right hand side of Eq. (3.85b) is the so-called Bloch-Siegert shift [57] of the electron spin transition frequencies. Note that the sign of this term is wrong in [42], while the sign found here is in agreement with the one in [58]. The second and third term can usually be neglected as they are small with respect to the time scale of the experiments. Finally, the fourth term is the so-called hyperfine enhancement [60] which is caused by a modulation of the hyperfine field with frequency ω_{rf} that results from the interaction of the electron spin with the rf field. This effect depends on the HFI in the xy -plane, which is the reason why the corresponding terms in the static Hamiltonian cannot be neglected in this case. *After* calculating the average Hamiltonian it is however permitted to drop these terms as has been done in Eq. (3.85a).

The average Hamiltonian during an rf pulse can thus be written as

$$\bar{\mathcal{H}}_{\text{rf}} = \left(\Omega_S - \frac{B_2}{B_0} \omega_{2s} \right) S_z - \Omega_I I_z + a S_z I_z - \omega_2 I_x + \frac{a}{2\omega_I} \omega_2 S_z I_x, \quad (3.86)$$

1. Since $\omega_{\text{mw}} \gg \omega_{\text{rf}}$, stroboscopic observation at a period $2\pi/\omega_{\text{rf}}$ is a good approximation.

where we have used $B_2/B_0 = \omega_2/\omega_I$ and discarded the insignificant terms. $\bar{\mathcal{H}}_{\text{rf}}$ is formally equivalent with the static Hamiltonian of the $S'=1/2, I=1/2$ system with *anisotropic* HFI (cf. Eq.(3.23)). This fact has been used to design an ESEEM experiment for systems with purely isotropic HFI [42]. To analyse the excitation by selective rf pulses, it is more convenient to write $\bar{\mathcal{H}}_{\text{rf}}$ in the form

$$\begin{aligned} \bar{\mathcal{H}}_{\text{rf}} = & \Omega_S' S_z + \left(\frac{a}{2} - \Omega_I\right) S^\alpha I_z - \left(1 - \frac{a}{2\omega_I}\right) \omega_2 S^\alpha I_x \\ & - \left(\frac{a}{2} + \Omega_I\right) S^\beta I_z - \left(1 + \frac{a}{2\omega_I}\right) \omega_2 S^\beta I_x \end{aligned} \quad (3.87)$$

where $\Omega_S' = \Omega_S - B_2\omega_{2s}/B_0$. With Eq. (3.83), we obtain the resonance frequencies $\omega_{\text{rf}}^\alpha = \omega_I' - a/2$ and $\omega_{\text{rf}}^\beta = \omega_I' + a/2$ and it becomes obvious that the nuclear spin nutation frequency for a given g_n is proportional to the nuclear transition frequency for $\omega_I' = \omega_I$.¹

The diagonalization of $\bar{\mathcal{H}}_{\text{rf}}$ is completely analogous to the one of the static Hamiltonian, so that the evolution of the system can be described as easily as the evolution of the unperturbed system with anisotropic HFI, the second column in Tab. 3-1 can be used accordingly. Note however, that it is usually not efficient to manipulate EC with rf pulses, since already the duration of rf $\pi/2$ pulses is often longer than the transverse relaxation time of the electron spins. Furthermore, it is not technically feasible to apply non-selective rectangular rf pulses, a remedy for this problem is described in §3.2.9.

The derivation given above is complicated considerably if we allow for an anisotropic hyperfine coupling. In this case we have to start from the laboratory frame and must consider the time-dependence of the anisotropic part of the HFI-matrix in the doubly rotating frame. This does not lead to qualitative changes, though to more complicated formulas for the hyperfine enhancement. In addition, we have to consider that the rf field is no longer perpendicular to the quantization axis of the nuclear spin, actually there are

1. This is true only when measurements at the *same external field* are compared.

two different quantization axes in the two electron spin manifolds. In a rough approximation, this can be considered by scaling ω_2 by factors $\cos\eta_\alpha$ and $\cos\eta_\beta$ in the two manifolds (cf. Eq.(3.13)). This means that for $I=1/2$ the ENDOR transition moment becomes zero in one of the manifolds at the exact cancellation condition. ENDOR transition moments can also vanish for $I>1/2$ in unfavourable cases. Under these conditions, modulation depths in ESEEM are normally large while they are zero for $\cos\eta_\alpha = \cos\eta_\beta = 1$, so that ENDOR and ESEEM methods complement each other. The problem of ENDOR transition moments in this more complicated case has been treated by using Fermi's golden rule and applying perturbation theory in the calculation of the state functions in [61].

3.2.9 Radio frequency chirp pulses

Even with state-of-the-art ENDOR equipment, one obtains only excitation bandwidths of about 1 MHz with rectangular rf pulses. This problem has hindered the development and application of time-domain ENDOR techniques after the first proposal to perform such experiments [62]. On the other hand, there is a growing number of time-domain experiments based on ESEEM techniques [29,31,33,34] which suffer from small modulation depths for nuclei with largely isotropic HFI, at fields where one is far from exact cancellation, and at the canonical orientations of the HFI matrix. For these reasons it is of large interest to combine the sensitivity of ENDOR with the resolution and potential for spin manipulation inherent in time-domain techniques.

To do this, one has to realise that rectangular pulses are actually a poor device for broadband excitation. The reasons for this can be seen immediately from the excitation profile shown in Fig. 3-8a. First, the excitation profile of a rectangular pulse is not smooth, there are excitation blind spots. Second, the excitation bandwidth is determined by the pulse length, with zero crossings at $\nu_{\text{rf}} \pm 1/t_p$. The latter point is particularly awkward, since it implies that pulse lengths of less than 100 ns had to be used to cover the band of approximately 20 MHz that is needed for proton ENDOR. This time is not sufficient to pump enough energy into the system since the rf field strength is limited. On the other hand, the relaxation of NC is slow enough to allow for much longer pulses, so that the problem can be solved by severing the link between excitation bandwidth and

pulse length. The optimum solution for this is a linear frequency sweep (chirp) over the needed band during the available time, as it has been used in Fourier-transform mass spectroscopy [63,64] and NMR spectroscopy [65]. The excitation profile of such a chirp pulse is much smoother and broader than for a rectangular pulse (see Fig. 3-8b). If necessary, this profile can be further smoothed by apodising the pulse flanks albeit at the cost of some bandwidth as is shown in Fig. 3-8c.

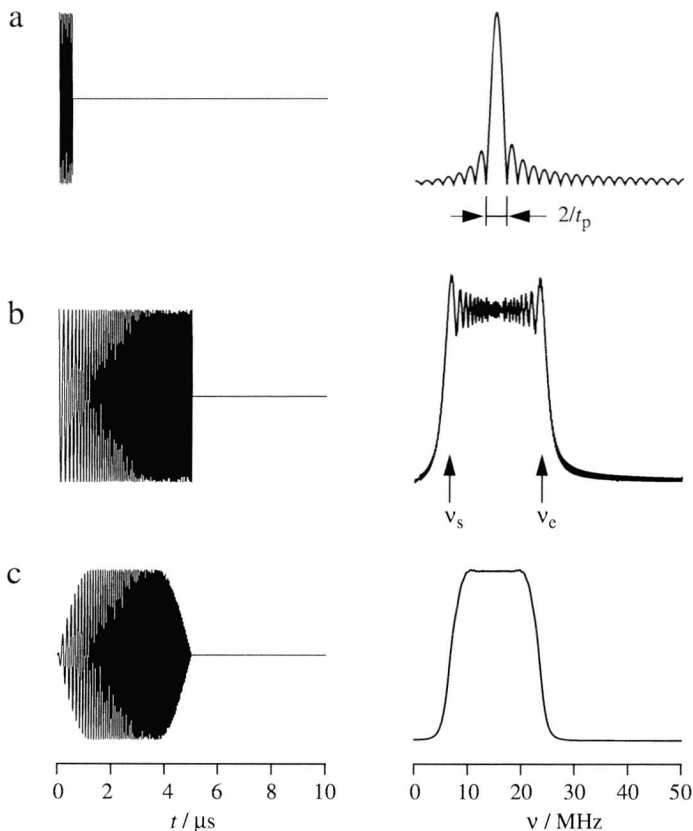


Fig. 3-8 Pulse shapes (right) and corresponding excitation profiles (left) obtained by magnitude Fourier transform (numerical simulations). Intensity units are arbitrary, but the same for all pulses. a) Rectangular monochromatic pulse, $\nu_{\text{rf}}=15$ MHz, $t_p=500$ ns. b) Linear frequency chirp from $\nu_s=5$ MHz to $\nu_e=25$ MHz, $t_p=5$ μs . c) Linear frequency chirp as in (b), but apodized with sine quarterwaves in the first and last quarter of the pulse.

A simple model for the description of fast linear frequency sweeps (rapid passage) has been given by Feretti and Ernst [66]. They show that the sweep can be considered as a sequence of selective pulses with frequency-dependent phase that act on a particular transition only at the time of passage through the corresponding resonance line. The effect of a chirp pulse on a system of n nuclear spins $I=1/2$ coupled to an electron spin (or fictitious spin) $S=1/2$ can then be described by applying the product operator formalism. For simplicity we assume that the chirp pulse has the same flip angle β_{ch} for all nuclear transitions, i.e., we neglect hyperfine enhancement (see §3.2.8). For the flip angle we obtain

$$\beta_{\text{ch}} = -\frac{\pi}{2} \frac{\omega_2}{\sqrt{3.01\alpha/2\pi}}, \quad (3.88)$$

where the sweep rate α is given by $\alpha=(\omega_c-\omega_s)/t_p$, and ω_s and ω_c are the start and end frequency of the chirp, respectively. Furthermore, we do not discuss the effect of an rf chirp pulse on EC, so that we can treat the two m_S manifolds separately. The selective pulse acting on a single transition can then be described by the product operator equation

$$I^\alpha \xrightarrow{\beta_{\text{ch}} I_\phi} \frac{1}{2}(1 + \cos\beta_{\text{ch}})I^\alpha + \frac{1}{2}(1 - \cos\beta_{\text{ch}})I^\beta + \sin\beta_{\text{ch}}(\sin\phi I_x - \cos\phi I_y), \quad (3.89)$$

where the arrow notation

$$A \xrightarrow{\beta B} C \quad (3.90a)$$

is shorthand for

$$C = \exp(-i\beta B)A \exp(i\beta B), \quad (3.90b)$$

and I_ϕ denotes a selective rf pulse with arbitrary phase ($I_\phi=I_x$ for $\phi=0$, $I_\phi=I_y$ for $\phi=\pi/2$).

In ENDOR, one uses the large polarization of the electron spin for the sensitive detection of nuclear spins. While the full polarization can be used for a single nuclear spin with selective excitation, this means that the electron spin polarization is distributed over the n nuclear spins in non-selective excitation. Therefore, one expects that in chirp time-domain ENDOR the signal intensity for a single transition depends on n . With Eq. (3.89)

and after some transformations, one finds indeed that the signal intensity obtained in a time-domain ENDOR scheme is given by

$$S_{\text{ch}} = C_{\text{ch}} \frac{1}{2^{n-1}} \sin^2 \beta_{\text{ch}} (1 + \cos^2 \beta_{\text{ch}})^{n-1}, \quad (3.91)$$

where C_{ch} is a constant factor [67]. The cosine in Eq. (3.91) accounts for the loss in signal intensity that arises from the excitation of multiple-quantum coherences by the chirp pulse. This loss is inevitable and can be easily understood in the picture of Feretti and Ernst, since a selective pulse that acts on a transition of the nuclear spin k transfers NC on a transition of spin j (that has been passed earlier) to double-quantum coherence. This implies that the optimum flip angle β_{ch} for the chirp pulse is smaller than $\pi/2$. The maximum signal and optimum flip angle can be obtained easily from Eq. (3.91), they are given by

$$S_{\text{ch,max}} = 2C_{\text{ch}} \frac{1}{n} \left(\frac{n-1}{n} \right)^{n-1}, \quad (3.92a)$$

and

$$\beta_{\text{ch,opt}} = \text{atan} \left(\sqrt{\frac{2}{n-2}} \right), \quad (3.92b)$$

for $n > 2$, $\beta_{\text{ch,opt}} = \pi/2$ for $n=1, 2$. In Eq. (3.92a), the factor $1/n$ reflects the distribution of the electron spin polarization to the n nuclear spins and the remaining n -dependent factor the loss to multiple quantum coherences. This factor decreases monotonically with increasing n and approaches $1/e$ for $n \rightarrow \infty$, where e is Euler's constant. The dependence of $\beta_{\text{ch,opt}}$ on n is shown in Fig. 3-9.

In experiments like time-domain ENDOR, where the observation of *single*-quantum coherences is intended, one can eliminate the multiple-quantum coherences by phase cycling [67]. Usually a four-step phase cycle $[0,0]-[0,\pi]-[\pi,0]+[\pi,\pi]$ applied to the two chirp pulses that generate and detect NC is sufficient, since coherences of an order higher than two are not significant. However, in some cases it may be interesting to *use* double-

quantum transfers (see Chapter 4). The efficiency of *one* double-quantum transfer by a chirp pulse is characterized by

$$F_{DQ} = \frac{1}{2^{(n-2)/2}} \sin^2 \beta_{ch} (1 + \cos^2 \beta_{ch})^{(n-2)/2}, \quad (3.93)$$

for $n > 1$. With that, we find the maximum efficiency factor and optimum flip angle for double-quantum transfers

$$F_{DQ,max} = \frac{4}{n} \left(\frac{n-2}{n} \right)^{(n-2)/2}, \quad (3.94a)$$

and

$$\beta_{ch,DQ} = \text{atan} \left(\sqrt{\frac{4}{n-4}} \right), \quad (3.94b)$$

for $n > 4$, $\beta_{ch,DQ} = \pi/2$ for $n=2, 3, 4$.

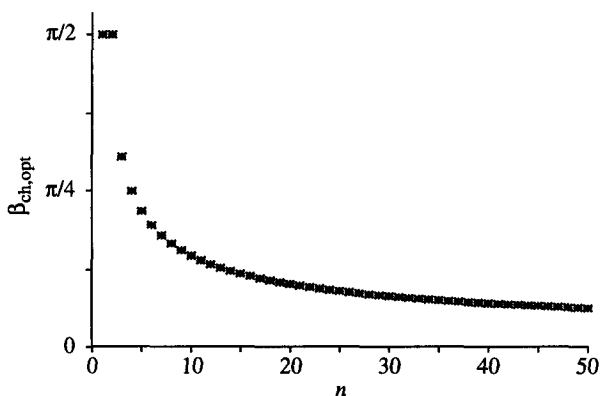


Fig. 3-9 Dependence of the optimum flip angle $\beta_{ch,opt}$ of a chirp pulse on the number n of nuclei coupled to the electron spin.

As can be seen in Fig. 3-8c, an apodized chirp pulse can provide an exactly tailored excitation profile. It is therefore possible to exclude spectral regions from excitation, for instance the matrix line. This may be advantageous, since it corresponds to a lowering of n and this in turn corresponds to an increase in sensitivity according to Eq. (3.92a). The instrumental and software requirements for the application of chirp pulses are described

in Appendix B. Here we mention only that the optimum flip angle given by Eq. (3.92b) can be achieved with conventional rf amplifiers and pulse ENDOR probeheads [68] for typical systems.

3.2.10 Combined microwave and radio frequency excitation

We have seen in §3.2.8 that the presence of an rf field can formally substitute for pseudo-secular hyperfine terms in the Hamiltonian. This suggests that combined rf and weak mw excitation leads to similar phenomena in systems without forbidden transitions as weak mw irradiation alone does in systems with forbidden transitions. In particular, one may expect that a combined rf/mw probe pulse can be used to detect NC. This would be trivial for NC on a transition that is on-resonant with the rf frequency, but interesting for NC on other transitions.

We start here with the Hamiltonian during rf irradiation in the doubly-rotating frame (Eq. (3.87)), that should at least qualitatively account for the behaviour of the spin system during rf irradiation even in cases where the detection is not stroboscopic.¹ This Hamiltonian can be diagonalized by the unitary transformation $U_{\text{rf}} \overline{\mathcal{H}}_{\text{rf}} U_{\text{rf}}^{-1}$ with

$$U_{\text{rf}} = \exp\{-i(\eta_{\alpha}^{\text{rf}} S^{\alpha} I_y + \eta_{\beta}^{\text{rf}} S^{\beta} I_y)\}, \quad (3.95a)$$

and

$$\eta_{\alpha, \beta}^{\text{rf}} = \text{atan} \left[\frac{\omega_2 \left(1 \mp \frac{a}{2\omega_I} \right)}{a/2 \mp \Omega_I} \right]. \quad (3.95b)$$

The perturbation by mw irradiation takes the form

$$\mathcal{H}_{\text{mw}}^{\text{rf}} = \omega_1' \cos \eta^{\text{rf}} (S_x^{(13)} + S_x^{(24)}) + \omega_1' \sin \eta^{\text{rf}} (S_x^{(14)} + S_x^{(23)}), \quad (3.96)$$

1. All perturbations not included in $\overline{\mathcal{H}}_{\text{rf}}$ are periodic with frequency ω_{rf} or a multiple thereof, since stroboscopic observation with period $2\pi/\omega_{\text{rf}}$ is a good approximation and hence additional perturbations must cancel for this kind of observation.

where $\eta^{rf} = (\eta_{\alpha}^{rf} - \eta_{\beta}^{rf})/2$ (cf. Eq. (3.19,3.40)). In the following we write ω_1 instead of ω_1' . It is convenient to define

$$\Omega_I' = \left(\sqrt{\left(\frac{a}{2} + \Omega_I\right)^2 + \omega_2^2} - \sqrt{\left(\frac{a}{2} - \Omega_I\right)^2 + \omega_2^2} \right) / 2, \quad (3.97a)$$

and

$$a' = \sqrt{\left(\frac{a}{2} + \Omega_I\right)^2 + \omega_2^2} + \sqrt{\left(\frac{a}{2} - \Omega_I\right)^2 + \omega_2^2}, \quad (3.97b)$$

and to write the Hamiltonian in the frame where it is diagonal as

$$\tilde{\mathcal{H}}_{rf} = \Omega_S S_z - \Omega_I' I_z + a' S_z I_z. \quad (3.97c)$$

For weak mw irradiation we need only to consider terms that are close to resonance. Nevertheless the problem becomes more involved than the description of non-ideal selective mw pulses in §3.2.5, since for rf that is on-resonant with one of the nuclear transitions, one allowed and one forbidden electron spin transition become degenerate.¹ In the following, we consider only the case where the rf is on-resonant or nearly on-resonant with one of the nuclear transitions, since we can conclude from Eq. (3.95b) that otherwise $\eta_{\alpha,\beta}^{rf} \approx 0$, $\eta^{rf} \approx 0$. The problem is then analogous to the one of non-ideal semi-selective pulses (cf. §3.2.6). Assume that ω_{mw} is set to the center of the nearly degenerate allowed and forbidden transitions (see Fig. 3-4 on page 68). This corresponds to $\Omega_S = -\Omega_I'/2 - a'/4$. By adding the energy $\Omega_I'/4 + a'/8$ to all levels of the system, we obtain the new Hamiltonian

$$\mathcal{H}_{rf}' = \Delta S^{\alpha} I_z + \tilde{a} S^{\alpha} I^{\beta}, \quad (3.98a)$$

with

$$\Delta = a'/2 - \Omega_I', \quad (3.98b)$$

1. This is a formal degeneracy that occurs since we are in a doubly rotating frame and the apparent energies depend on ω_{rf} . Alternatively, we may say that the transitions are degenerate indeed in a dressed states picture.

and

$$\tilde{a} = a'/2 + \Omega_I', \quad (3.98c)$$

and in particular, for on-resonant rf irradiation $\Delta = \omega_2$ and $\tilde{a} = \sqrt{a^2 + \omega_2^2}$ (in Fig. 3-4, ω_B must be replaced by the splitting Δ and ω_α by \tilde{a}). In the following we assume for simplicity that the rf is exactly on-resonant ($\Omega_I = a/2$), we then have $\cos\eta^{\text{rf}} = \sin\eta^{\text{rf}} = \sqrt{2}/2$. The complete Hamiltonian including the mw terms on the two excited transitions can then be written as

$$\mathcal{H}_{\text{rf,mw}} = \cos\theta\omega_{\text{eff}} S^\alpha I_z + \tilde{a} S^\alpha I^\beta + \frac{\sqrt{2}}{2} \sin\theta\omega_{\text{eff}} (S_x I^\alpha + S_x I_x + S_y I_y), \quad (3.99a)$$

with

$$\omega_{\text{eff}} = \sqrt{\omega_1^2 + \omega_2^2}, \quad (3.99b)$$

and

$$\theta = \text{atan}\left(\frac{\omega_1}{\omega_2}\right). \quad (3.99c)$$

The Hamiltonian $\mathcal{H}_{\text{rf,mw}}$ can be diagonalized by a unitary transformation with

$$U_{\text{rf,mw}} = \begin{bmatrix} \frac{\sqrt{2}}{2} \cot\frac{\theta}{2} & \frac{\sqrt{2}}{2} \tan\frac{\theta}{2} & 1 & 0 \\ -\frac{\sqrt{2}}{2} \tan\theta & \frac{\sqrt{2}}{2} \tan\theta & 1 & 0 \\ -\frac{\sqrt{2}}{2} \tan\frac{\theta}{2} & -\frac{\sqrt{2}}{2} \cot\frac{\theta}{2} & 1 & 0 \\ 0 & 0 & 0 & 1 \end{bmatrix}, \quad (3.100)$$

and we obtain the eigenvalues $\omega_{\text{eff}}/2, 0, -\omega_{\text{eff}}/2, \tilde{a}$. We are now in a position to calculate the transformation of an arbitrary density operator by the combined rf/mw probe

pulse. In particular, we obtain for the detection of NC in the α manifold of the electron spin ($\sigma_0 = S^\alpha I_x$), i.e., on a transition that is far off-resonant with respect to the rf

$$\langle S_x \rangle(t) = \frac{\omega_1 \omega_2}{2\omega_{\text{eff}}} \left\{ \cos(\tilde{a}t) - \frac{1}{2} \cos \left[\left(\tilde{a} - \frac{\omega_{\text{eff}}}{2} \right) t \right] - \frac{1}{2} \cos \left[\left(\tilde{a} + \frac{\omega_{\text{eff}}}{2} \right) t \right] \right\}, \quad (3.101a)$$

and

$$\langle S_y \rangle(t) = \frac{\omega_1 \omega_2}{2\omega_{\text{eff}}} \left\{ \sin(\tilde{a}t) - \frac{1}{2} \sin \left[\left(\tilde{a} - \frac{\omega_{\text{eff}}}{2} \right) t \right] - \frac{1}{2} \sin \left[\left(\tilde{a} + \frac{\omega_{\text{eff}}}{2} \right) t \right] \right\}, \quad (3.101b)$$

where we have made use of the relation $\sin 2\theta = 2\omega_1 \omega_2 / \omega_{\text{eff}}$. Obviously, the signal is zero when the mw field or the rf field are absent.¹ For a given mw or rf field, the signal is maximum for $\omega_1 = \omega_2$, or

$$g_e \beta_e B_1 = g_n \beta_n B_2. \quad (3.102)$$

As might have been expected for a double resonance phenomenon, we have thus arrived at a Hartmann-Hahn match [12]. For $\omega_2 \ll a$, we have $\sqrt{a^2 + \omega_2^2} \approx a$, and the Fourier transform of the signal leads to a line at the hyperfine frequency with two sidebands that are split by ω_{eff} and have opposite phase with respect to the centerband. To observe the signal, one needs field strengths so that $\omega_{\text{eff}} > 2\pi/T_{2n}$, where T_{2n} is a (phenomenological) transverse relaxation time of the nuclear spins. This condition can be fulfilled together with the Hartmann-Hahn condition Eq. (3.102) with hardware as it is usually applied in coherent Raman beat and ENDOR experiments [40,68] and without introducing strong shifts of the hyperfine frequencies. In the design of experiments, the Bloch-Siegert shift has to be taken into account. The use of combined mw/rf probe pulses in a pulse sequence for hyperfine spectroscopy is discussed in Chapter 7.

1. It is of course also zero, if both fields are absent. In this case, the sum in the curly brackets is zero.

Manipulation of nuclear coherence

4.1 Nuclear coherence generators

The generation, manipulation, and detection of NC is the basis of those solid-state pulse ESR experiments that feature the best resolution. The reason for this is the fact that usually nuclear spin relaxation is much slower than electron spin relaxation. This does not only lead to narrower lines, it also presents opportunities to do correlation experiments [3] and to use more elaborate refocusing schemes [36]. In the following we extend an earlier systematic overview [71] of the concepts that allow for the design of pulse sequences which make use of these opportunities. The advantages and disadvantages of the described NC generators are surveyed in Tab. 4-2.

4.1.1 SENSE generator

Though the Mims generator (see §4.1.2) was introduced much earlier [28], the SENSE (SElective/ Non-SElective pulse pair) generator [72] is easier to understand and will be treated first. NC generation by mw pulses can be seen as a task that requires two steps, namely the creation of a large population difference between the levels of a nuclear transition, and the induction of nuclear spin flips. In the SENSE generator, these steps are clearly separated. The first, selective mw pulse creates a state of two-spin order, $-2S_zI_z$, from Boltzmann equilibrium, $-S_z$ (see Fig. 4-1). Two-spin order can be considered as a superposition of nuclear polarization with different sign in the two electron spin mani-

folds ($-2S_z I_z = S^\beta I_z - S^\alpha I_z$). To eliminate EC that arises from flip angle imperfections, one can apply a phase cycle $[0]+[\pi]$ to the selective mw pulse. Alternatively, one can wait for the EC to decay in a time t_{ip} that is long compared to the phase memory time T_m of the electron spins but short compared to T_{1e} . Finally, the two-spin order is transferred to NC, $\sin(2\eta)I_x$, and two-spin order with inverted sign, $\cos(2\eta)2S_z I_z$, by the non-selective π pulse. Flip angle imperfections of this pulse also lead to the creation of EC, so that a phase cycle $[0]+[\pi]$ has to be applied to this pulse. Hence the complete phase cycle to eliminate EC can be written as $[0,0]+[\pi,0]+[0,\pi]+[\pi,\pi]$. In Fig. 4-1b, the two-spin order after the non-selective pulse has been neglected. However, it should be kept in mind that it exists, since part of it is transferred to NC by each subsequent non-selective pulse. Since it is impossible to separate NC and polarisation by phase cycling of mw pulses [43], the latter transfers may give rise to artefacts in experiments.

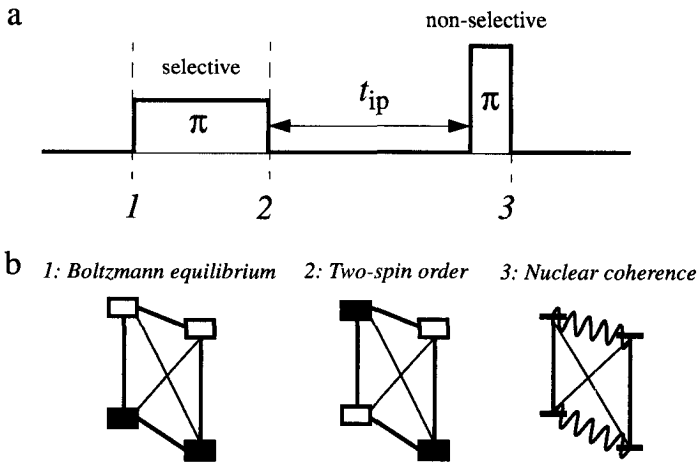


Fig. 4-1 Nuclear coherence generation by the SENSE generator. a) SENSE subsequence. b) Level diagrams for an $S=1/2$, $I=1/2$ spin system.

Up to now we have assumed that the mw is on-resonant with transition 24. For an analytical description one has to consider that there are spin packets with different Ω_S so that the selective mw pulse can be on-resonant with each of the four electron spin transitions, though only with one transition in a given spin packet. In addition, one usually assumes

that the selective mw pulse has *nominal* flip angle π , i.e., flip angles $\pi \cos \eta$ and $\pi \sin \eta$ for the allowed and forbidden electron spin transitions, respectively. With that we find

$$\sigma_{\text{NC}}^{(13, 24)} = \mp \sin(2\eta) \sin^2\left(\frac{\pi}{2} \cos \eta\right) I_x, \quad (4.1a)$$

and

$$\sigma_{\text{NC}}^{(14, 23)} = \pm \sin(2\eta) \sin^2\left(\frac{\pi}{2} \sin \eta\right) 2S_z I_x, \quad (4.1b)$$

where $\sigma_{\text{NC}}^{(jk)}$ is the NC part of the density operator after the SENSE subsequence with mw irradiation on-resonant with transition (jk) . Note that the four situations have to be treated separately throughout the *whole* pulse sequence: There is *no net NC* after the SENSE subsequence [72]. However, since the same sign comes in during NC detection, the single contributions add up and there is a *net signal*.

Eqs. (4.1a,b) reveal that the phase of the NC does not depend on the spin Hamiltonian parameters and that the NC amplitude depends only on η ; there are no blind spots. In addition, we may see that we obtain NC with the same phase in both electron spin manifolds if the mw is on-resonant with an allowed transition ($I_x = S^\alpha I_x + S^\beta I_x$), while opposite phase in the two manifolds is observed if the mw is on-resonant with a forbidden transition ($2S_z I_x = S^\alpha I_x - S^\beta I_x$).

While the absence of a phase dispersion and of blind spots are advantages of the SENSE generator, it is a disadvantage that a smaller number of spin packets takes part in the experiment than with the non-selective Mims generator. It is therefore important to adjust the power of the first mw pulse carefully. As a rule of thumb, two-spin order can be created by an mw π pulse if

$$t_p > \frac{2\pi}{\omega_{\text{HF}}}. \quad (4.2)$$

This condition describes hyperfine contrast selectivity [72-74], i.e., with a short pulse one can suppress peaks that are due to nuclei with small hyperfine coupling. If one is only interested in nuclei that have at least moderate coupling (as opposed to matrix

nuclei), one may thus use a comparatively short “selective” pulse in the SENSE generator and enhance sensitivity.

The generation of NC by the SENSE subsequence can also be understood in a classical picture. For that, consider the fields acting on the nuclear spin in the two electron spin manifolds (see Fig. 4-2). In the β manifold, the nuclear Zeeman and secular hyperfine field add up and the pseudo-secular hyperfine field is directed along the positive x axis. On the other hand, in the α manifold, the nuclear Zeeman field and secular hyperfine field partially cancel and the pseudo-secular hyperfine field has opposite direction. Accordingly, the directions of the *effective* fields $\omega_{\text{eff}}^{\alpha, \beta}$ at the nucleus are different in the two manifolds, the angle between the effective field axes is 2η . Assume now that we have created polarization on the nuclear transition in the β manifold. This corresponds to magnetization directed along the $\omega_{\text{eff}}^{\beta}$ axis. A non-selective π pulse changes the electron spin state suddenly, so that the effective field is now along the $\omega_{\text{eff}}^{\alpha}$ axis, while the nuclear spins and hence the direction of the magnetization are unaffected. At this instant we have transverse nuclear magnetization that begins to precess about the new effective field. It can be seen immediately that the amount of transverse magnetization is given by $\sin(2\eta)$ and the amount of remaining longitudinal magnetization by $\cos(2\eta)$. The scheme can be easily adapted to situations with different signs or relative magnitudes of the interactions.

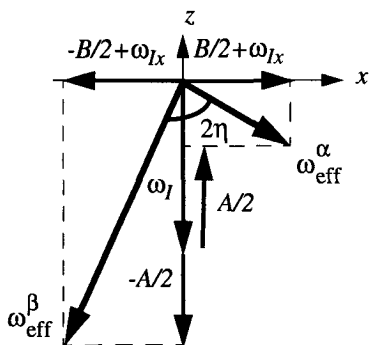


Fig. 4-2 Effective fields acting on the nuclear spin in the two electron spin manifolds of an $S=1/2$, $I=1/2$ system. The situation corresponds to positive secular and pseudo-secular hyperfine coupling, positive g_n and $B/2 > \omega_{Ix}$. Primes on the symbols have been omitted.

4.1.2 Mims generator

The first ESEEM experiments involving NC (three-pulse ESEEM) have been performed by Mims with a subsequence $\pi/2$ - τ - $\pi/2$ of non-selective mw pulses [28,75] as a generator. The NC after this subsequence is given by

$$\begin{aligned} \sigma_{\text{NC}} = \sqrt{\frac{k}{4}} \sin(\Omega_S \tau) & \left[\sin\left(\frac{\omega_{\text{HF}} \tau}{2}\right) I_x - \sin\left(\frac{\omega_{\text{NZ}} \tau}{2}\right) 2S_z I_x \right. \\ & \left. + 2 \sin\left(\frac{\omega_\alpha \tau}{2}\right) \sin\left(\frac{\omega_\beta \tau}{2}\right) 2S_z I_y \right] \end{aligned} \quad (4.3)$$

where

$$k = 4 \sin^2 \eta \cos^2 \eta = \sin^2(2\eta) \quad (4.4)$$

is the modulation depth parameter. Eq. (4.3) is equivalent to an expression given in [76], except for the sign of the $2S_z I_y$ term. The modulation of the NC with $\sin(\Omega_S \tau)$ may lead to spin diffusion, in turn faster decay of the NC and line broadening can result. Obviously, the phase of the NC now depends on the parameters in the spin Hamiltonian and is different in the two electron spin manifolds. One can show easily from Eq. (4.3), that there is no NC in the electron spin α manifold if $\tau = 2\pi k / \omega_\beta$ and no NC in the β manifold if $\tau = 2\pi k / \omega_\alpha$, where k is an integer. This is the blind spot behaviour of the Mims generator. In order to ensure that all nuclear frequencies are detected, one has to perform the experiments at different τ values, whenever one cannot ensure that

$$\tau < \frac{2\pi}{\omega_\alpha}, \frac{2\pi}{\omega_\beta} \quad (4.5)$$

This is important if the Mims generator is combined with another $\pi/2$ pulse as NC detector in three-pulse ESEEM. The contributions of all spin packets are refocused at time τ after the third mw pulse, so that τ must be larger than the instrumental dead time. For X-band spectrometers this usually prevents one from fulfilling condition (4.5).

The Mims generator creates a polarization pattern that cannot be separated from the NC by phase cycling. The FID that follows the application of a $\pi/2$ pulse to this polarization pattern leads to a refocusing of the magnetization at time τ after this pulse; this signal is called a stimulated echo. The superposition of the signal due to NC evolution with

the stimulated echo can cause problems in the detection if the latter part is much larger. In addition, the unmodulated stimulated echo contribution has to be removed before the Fourier-transform. If either of these difficulties is significant, it may be advantageous to apply the three-pulse generator (see §4.1.6). To prevent EC generation by the Mims generator, a phase cycle $[0,0]-[0,\pi]-[\pi,0]+[\pi,\pi]$ has to be applied to the two mw pulses.

4.1.3 Single microwave pulse

It has already been discussed in §3.2.4, §3.2.6 and §3.2.7 that a single mw pulse can create NC. In the limiting case of a semi-selective pulse, NC is only generated in the electron spin manifold with the smaller nuclear frequency. The phase of the NC does not depend on the spin Hamiltonian parameters and there are no blind spots (cf. Eq. (3.59)). However, if this limit can be reached is not in the hand of the experimenter. In the more general case of a non-ideal mw pulse, it has been shown in §3.2.7 that the amplitude of the NC can be maximized by matching the mw field to the nuclear Zeeman field and using flip angles larger than π . The NC created by a single, non-ideal mw pulse is described by coefficients C^P of single transition operators $P = S^{\alpha, \beta} I_{x,y}$,

$$\begin{aligned}
 C^P = \sin \xi C_0^P \{ & C_{13}^P \cos[(\Omega_S^{tr} + A^{eff}/2)t_p] + C_{24}^P \cos[(\Omega_S^{tr} - A^{eff}/2)t_p] \\
 & + C_{12}^P \cos[(\omega_I^{tr} + A^{eff}/2)t_p] + C_{34}^P \cos[(\omega_I^{tr} - A^{eff}/2)t_p] \\
 & + C_{23}^P \cos[(\Omega_S^{tr} - \omega_I^{tr})t_p] - C_{23}^P \} , \quad (4.6)
 \end{aligned}$$

in the product operator decomposition of the density matrix in the eigenbasis of the unperturbed Hamiltonian. The coefficients C_{kl}^P in Eq. (4.6) correspond to different transfer pathways *during* the mw pulse, they are given in Tab. 4-1. This equation has been derived and discussed in some detail in [53].

To eliminate EC, a phase cycle $[0]+[\pi]$ has to be applied to the pulse. In general, there is also polarization after a single mw pulse. However, if high turning angles are involved as they are needed for optimum NC creation, any contributions due to polarization are largely suppressed by saturation effects throughout a broad band. Another possibility to suppress such contributions is the use of a flip angle 2π or a multiple thereof.

Table 4-1 Coefficients in Eq. (4.6) describing the contribution of different pathways during the nuclear coherence generation by a single, non-ideal microwave pulse.

P	C_0^P	C_{13}^P	C_{24}^P	C_{12}^P	C_{34}^P	C_{23}^P
$S^\alpha I_x$	$\frac{\theta_\alpha \cos \frac{\theta_\beta}{2}}{\sin \frac{\theta_\alpha}{2} \cos \frac{\theta_\beta}{2}}$	$(1 + \cos \theta_\alpha)$	$-(1 - \cos \theta_\beta)$	$-(1 + \cos \theta_\alpha)$	$(1 - \cos \theta_\beta)$	$\cos \xi (\cos \theta_\alpha + \cos \theta_\beta)$
$S^\alpha I_y$	$\frac{\theta_\alpha \theta_\beta}{\sin \frac{\theta_\alpha}{2} \cos \frac{\theta_\beta}{2}}$	$(1 + \cos \theta_\alpha)$	$(1 - \cos \theta_\beta)$	$-(1 + \cos \theta_\alpha)$	$-(1 - \cos \theta_\beta)$	$\cos \theta_\alpha + \cos \theta_\beta$
$S^\beta I_x$	$\frac{\theta_\alpha \sin \frac{\theta_\beta}{2}}{\cos \frac{\theta_\alpha}{2} \sin \frac{\theta_\beta}{2}}$	$(1 - \cos \theta_\alpha)$	$-(1 + \cos \theta_\beta)$	$-(1 - \cos \theta_\alpha)$	$(1 + \cos \theta_\beta)$	$-\cos \xi (\cos \theta_\alpha + \cos \theta_\beta)$
$S^\beta I_y$	$\frac{\theta_\alpha \theta_\beta}{\cos \frac{\theta_\alpha}{2} \sin \frac{\theta_\beta}{2}}$	$(1 - \cos \theta_\alpha)$	$(1 + \cos \theta_\beta)$	$-(1 - \cos \theta_\alpha)$	$-(1 + \cos \theta_\beta)$	$-(\cos \theta_\alpha + \cos \theta_\beta)$

4.1.4 Monochromatic radio frequency pulse

All NC generators considered so far depend on forbidden transitions, hence they cannot be used if the HFI is isotropic or if one is close to a canonical orientation of the HFI matrix. A remedy for this is the use of rf pulses.¹ The most simple generator of this type consists of a selective mw π pulse that creates two-spin order (see §4.1.1), followed by a monochromatic rf $\pi/2$ pulse that transfers the polarization on a *single* transition to NC. This generator is subject to hyperfine contrast selectivity, i.e., Eq. (4.2) has to be fulfilled for the selective mw π pulse. However, in spite of the use of a selective mw pulse, there are usually no serious sensitivity problems with this generator since the polarization on a nuclear transition is transferred virtually completely to NC. It is possible to eliminate EC by a phase cycle $[0]+[\pi]$ applied to the mw pulse, however, it is advantageous to phase cycle the rf pulse instead ($[0]-[\pi]$), since the latter cycle also eliminates contributions to the signal by polarization.

Instead of using a selective mw pulse to create the polarization on a nuclear transition, one can also use a $\pi/2-\tau-\pi/2$ subsequence of non-selective mw pulses [77]. Since in this case more spin packets take part in the experiment, sensitivity is enhanced. The polarization on the two nuclear transitions after the $\pi/2-\tau-\pi/2$ subsequence is given by

$$\sigma_{\text{pol}}^{\alpha, \beta} = \mp \sin(\Omega_S \tau) \left[\cos^2 \eta \sin\left(\frac{\omega_{\text{HF}}}{2} \tau\right) \mp \sin^2 \eta \sin\left(\frac{\omega_{\text{NZ}}}{2} \tau\right) \right] S^{\alpha, \beta} I_z, \quad (4.7)$$

so that there are blind spots for certain values of τ . The NC generated by this subsequence before the rf pulse does not interfere, since it is eliminated by rf phase cycling. For an isotropic HFI $aS_z I_z$, one easily finds from Eq. (4.7) the blind spot condition for Mims ENDOR [78]

$$\tau = \frac{2\pi k}{a}. \quad (4.8)$$

1. As discussed in [42] and §3.2.8, one can also use continuous rf irradiation to create the equivalent of a pseudo-secular hyperfine term. To avoid problems with the Bloch-Siegert shift, one then applies the rf irradiation during the whole pulse sequence and can employ all NC generators discussed in this Chapter that depend on forbidden transitions. Note that the rf coil has to be adjusted carefully, since an rf field along the z -axis modulates the electron spin energy levels and prevents or diminishes EC refocusing.

For small hyperfine couplings it is necessary to use a very long interpulse delay τ to create a sufficient amount of polarization. Since during time τ the EC decays with the phase memory time T_m of the electron spins, it may be difficult to detect lines that correspond to very small hyperfine couplings with *either* of the nuclear polarization generators. To distinguish between the two types of preparation of the nuclear polarization, we term the combination of a $\pi/2$ - τ - $\pi/2$ subsequence with an rf pulse a Mims-type generator and the combination of a selective mw pulse with an rf pulse a Davies-type generator¹ henceforth (see Fig. 4-3).

Though monochromatic rf pulses usually cannot excite a very broad frequency band, it is possible to use them for the observation of nuclear FIDs and echoes on single transitions and to extract information on the relaxation of NC [58,62].

4.1.5 Chirp generators

More versatile NC generators are obtained with an rf chirp pulse instead of monochromatic irradiation (see §3.2.9, [67]). With respect to phase cycling, hyperfine contrast selectivity of the Davies-type generator, and blind spot behaviour of the Mims-type generator, there are no differences to the case of monochromatic rf pulses, see §4.1.4.

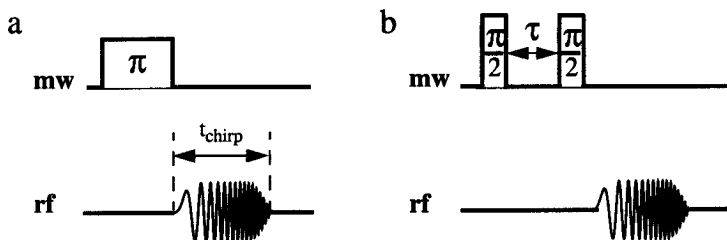


Fig. 4-3 Davies-type (a) and Mims-type (b) NC generators based on radio frequency chirp pulses. For selective excitation of the nuclear transitions, the chirp pulses can be replaced by rectangular monochromatic radio frequency pulses.

1. This combination is part of the Davies-ENDOR sequence [79].

While effectively eliminating nuclear polarization and therefore artefacts, the chirp generators also create a comparatively large amount of NC, since they do not depend on forbidden transitions. The disadvantage is that there is a dead time t_{chirp} for the (indirect) detection of the NC. According to the model of Feretti and Ernst [66], the NC on a particular transition is created at the moment when the chirp passes the frequency of this transition. If another chirp pulse is used for detection, there is at least a delay t_{chirp} before the same frequency is passed during the second chirp. This is usually no problem if the lines in the nuclear spectra are only homogeneously¹ broadened, i.e., if Ω_S is the only parameter in the static Hamiltonian that has a distribution for different spin packets. T_{2n} is usually sufficiently longer than the achievable t_{chirp} . On the other hand, it is not possible to apply chirp generators to disordered systems where linewidths are much larger than $1/t_{\text{chirp}}$. This problem can be overcome by refocusing the NC as discussed in §4.3.1 and §4.3.2.

The dead time also results in a phase dispersion of the NC on different transitions. In our model of the chirp pulse (see §3.2.9), the dependence of the phase on the transition frequency is linear, since the phase of the chirp pulse depends quadratically and its frequency linearly on t (cf. Eq. (B.1a) in Appendix B). Therefore, it should be possible to find a time t_0 at which all the frequency components are in phase and to eliminate the phase dispersion by use of the shift theorem of Fourier transformation

$$\mathcal{F}\{s(t-t_0)\} = S(\omega)\exp(-it_0\omega), \quad (4.9)$$

where $S(\omega) = \mathcal{F}\{s(t)\}$ is the desired pure-phase spectrum. However, we have found that a phase correction according to this equation did not produce pure-phase spectra from our experimental time-domain traces. This is probably due to the creation of harmonics by the rf amplifiers and due to deviations of the chirp pulse from the idealized model used in §3.2.9.

1. In fact, this use of the term homogeneous broadening is somewhat loose. These lines are inhomogeneously broadened by nuclear-nuclear interactions, but we may safely neglect this fact in our discussion as long as we do not attempt to resolve nuclear-nuclear interactions.

4.1.6 Three-pulse generator

In §4.1.2 it has been found that the amplitude of the NC created by the Mims generator is limited by the factor \sqrt{k} (cf. Eq. (4.3)). This is not the case for a single matched mw pulse with high turning angle (see §3.2.7 and §4.1.3), but in this case the conditions for optimum NC generation may differ among the nuclear transitions and destructive interference may limit the gain in NC amplitude for experiments with broad band excitation and detection. An NC generator that improves on the modulation depth of the Mims generator for a broad range of systems and is not hampered by destructive interference of different spin packets, is the three-pulse generator introduced by Gemperle et al. [76,80], see Fig. 4-4.

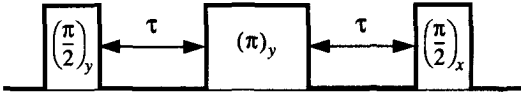


Fig. 4-4 Three-pulse nuclear coherence generator introduced by Gemperle et. al. [80]. All pulses are considered to be ideal (non-selective).

The NC created by this generator can be given in the same form as for the Mims generator, cf. Eq. (4.3),

$$\begin{aligned}
 \sigma_{\text{NC}}^{(3p)} = & \sqrt{\frac{k}{4}} \left\{ 2 \sin^2 \eta \sin\left(\frac{\omega_{\text{HF}}}{2} \tau\right) \left[\cos\left(\frac{\omega_{\text{NZ}}}{2} \tau\right) - \cos\left(\frac{\omega_{\text{HF}}}{2} \tau\right) \right] I_x \right. \\
 & + 2 \cos^2 \eta \sin\left(\frac{\omega_{\text{NZ}}}{2} \tau\right) \left[\cos\left(\frac{\omega_{\text{HF}}}{2} \tau\right) - \cos\left(\frac{\omega_{\text{NZ}}}{2} \tau\right) \right] 2S_z I_x \\
 & + \cos(2\eta) [\cos(\omega_\alpha \tau) + \cos(\omega_\beta \tau) - 1] 2S_z I_y \\
 & \left. + [\sin^2 \eta \cos(\omega_{\text{HF}} \tau) - \cos^2 \eta \cos(\omega_{\text{NF}} \tau)] 2S_z I_y \right\}. \tag{4.10}
 \end{aligned}$$

This expression is equivalent with a result in [76] except for the sign of the $2S_z I_y$ term. Since the Ω_S inhomogeneity is refocused at the time where the third pulse is applied, the result *does not depend* on Ω_S . As a consequence, there should be no contribution of spin diffusion to the relaxation of the NC in contrast to the Mims generator. In addition, one can show that the amount of polarization left over after the three pulses is weighted by

$\sin^2\eta$ and is thus very small for weak forbidden transitions [76,80]. Similarly, few polarization contributes to the signal if the corresponding NC detector (see §4.2.2) is used. This means that the unmodulated contribution to the signal is very small and also that artefacts in experiments using additional mw pulses should be much weaker with this generator than with the Mims generator. Finally, it has been shown that for weak forbidden transitions a factor $\sqrt{8}$ can be gained in NC generation as compared to the Mims generator and the same factor can be gained in detection [76,80]. This gain can be traced back to the refocusing of the EC that leads to a situation where all electron spins are directed along the y axis at the moment when the third pulse with phase y is applied, while one has a phase distribution of the allowed EC in the case of the Mims generator. From Tab. 3-1 one can infer that a pulse with phase ϕ transfers only allowed EC of phase ϕ to NC.

The imperfections of the three-pulse generator result mainly from the fact that refocusing is not complete, since the refocusing of forbidden EC requires a forbidden transfer (see Tab. 3-3). This leads to non-vanishing polarization as well as to the fact that the gain in sensitivity becomes smaller if the transition probability of the forbidden transitions becomes larger. Nevertheless, this generator is probably superior to the Mims generator for most systems of interest, the only disadvantage being its more complicated blind spot behaviour.¹

4.1.7 ELDOR generator

If an NC generator depends on forbidden transitions, it can be shown that in one spin system both an allowed and a forbidden electron spin transition must be excited to create NC. Since any pair of such transitions is separated by one of the nuclear frequencies ω_α or ω_β , this prevents NC generation if

$$\omega_1 \ll \omega_\alpha, \omega_\beta . \quad (4.11)$$

1. Since τ is of no significance for the detection, values $\tau < \tau_D$ can be chosen, so that the blind spot problem for this generator may be rendered harmless.

For state-of-the-art pulse spectrometers at X-band this problem is hardly relevant since firstly the excitation bandwidth is close to the width of the resonator mode for Q-values where sensitive detection is still possible, and secondly, there are few systems that fulfil relation (4.11) and have significant probabilities of forbidden transitions.¹ This is no longer true for high-field, high-frequency ESR, where resonator bandwidths tend to be much larger, the mw fields smaller, and where ESEEM effects become observable for larger HFI since the nuclear Zeeman interaction is also larger. It may then be necessary to work with two mw sources to excite a forbidden and an allowed transition. Such a method has been introduced by Husted et al. and termed soft ESEEM [81].² It can be considered as an electron electron double resonance (ELDOR) experiment. The NC generator can be written in short notation as $(\pi/2)[\omega_{mw}^{(1)}] - \tau - (\pi)[\omega_{mw}^{(2)}]$, see Fig. 4-5.

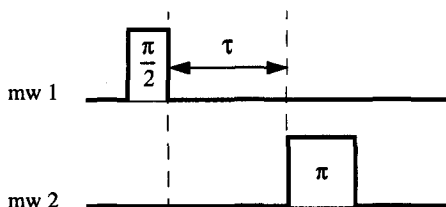


Fig. 4-5 ELDOR nuclear coherence generator used in the stimulated soft ESEEM experiment [81].

Without losing generality we use for the description of this generator the same pair of an allowed and a forbidden transition as in the description of semi-selective mw pulses (see §3.2.4). Assume that the first pulse is on-resonant with the allowed transition (13)

1. In fact, only protons with very large HFI qualify. This concerns a few defect centers, since even for α -protons in organic radicals $\omega_\alpha/(2\pi)$ or $\omega_\beta/(2\pi) < 60$ MHz and since $\omega_1/(2\pi) \approx 50$ MHz can be achieved.
2. Alternatively, one can shift the second electron spin transition closer to resonance by changing the magnetic field [29]. However, field jumps larger than 4 mT corresponding to 112 MHz can be hardly achieved. This may still be smaller than the resonator bandwidth. Fast field jumps also pose larger technical problems than double irradiation. The theoretical description of both experiments is very similar.

and the second pulse with the forbidden transition (14) (cf. Fig. 3-2 on page 47). The NC after the second mw pulse is then given by

$$\sigma_{\text{NC}}^{(13, 14)} = \cos\left[\left(\frac{\omega_{\text{HF}}}{2} + \Omega_S\right)\tau\right] S^\beta I_x - \sin\left[\left(\frac{\omega_{\text{HF}}}{2} + \Omega_S\right)\tau\right] S^\beta I_y . \quad (4.12)$$

For the case $(\pi/2)[\omega_{\text{mw}}^{(14)}] - \tau - (\pi)[\omega_{\text{mw}}^{(13)}]$ that is realized in other spin packets if the inhomogeneous line broadening is much larger than ω_α and ω_β , we find that the sign of the $S^\beta I_y$ term changes. Note however that it is usually not possible to adjust the flip angles for both cases at the same time. The optimum condition is given by

$$\frac{B_1^{(13)}}{B_1^{(14)}} = \frac{\sin \eta}{\cos \eta} , \quad (4.13)$$

alternatively one could use different pulse lengths. If $\sin \eta \ll \cos \eta$ as is usually the case, it is straightforward to adhere to condition (4.13) and thus to use only half of the spin packets. This still leads to a considerable gain in NC amplitude as compared to the other generators that depend on forbidden transitions, since the modulation depth parameter k is not involved in Eq. (4.12). Note that there is no need to perform experiments of this type with low-power pulses as the term soft ESEEM might suggest, only condition (4.11) has to be fulfilled. For application purposes it is interesting that nevertheless only one of the mw sources has to provide high power pulses, namely the one that is used to drive the forbidden transitions. If condition (4.13) cannot be fulfilled, one should apply the low power source for the π pulse and the high power source for the $\pi/2$ pulse if $\cos \eta B_1^{(13)} > \sin \eta B_1^{(14)}$ and *vice versa* to limit losses by relaxation during the pulses.

The disadvantage of the ELDOR generator is that the difference between the two mw frequencies varies for the nuclear transitions so that the second mw source has to be swept and that no additional information is obtained by this sweep. However, a slight modification of the experiment does allow one to obtain correlation information in the inevitable frequency sweep in many cases (see §4.3.1).

Table 4-2 Overview of advantages (+) and disadvantages (-) of nuclear coherence generators. The column on overall sensitivity should be used cautiously, since this parameter may depend strongly on the system under consideration and may change at different ESR frequencies. Details on this are discussed in the text.

Generator	Blind spot free	Modulation depth	Low nuclear spin diffusion	Broad band excitation ^a	Overall sensitivity at X-band frequencies	Description
SENSE	+	-	O	+	-	§4.1.1
Mims	-	-	-	+	O	§4.1.2
Single mw pulse	O ^b	O	O	+	O	§4.1.3
Three-pulse	-	O	+	+	+	§4.1.6
ELDOR	+	+	-	+++ ^c	+ ^d	§4.1.7
Monochromatic rf, Davies-type	+	++	O	-	O ^d	§4.1.4
Chirp, Davies-type	+	+	O	+	++	§4.1.5
Monochromatic rf, Mims-type	-	++	-	-	O ^d	§4.1.4
Chirp, Mims-type	-	+	-	+	++	§4.1.5

a. Refers to nuclear frequencies.
 b. No complete blind spots, but NC amplitude may vary significantly with pulse length, and global maxima may differ for different transitions.
 c. In fact, two very narrow bands are used, but an mw sweep provides a broader band than is possible with any of the other generators.
 d. Takes into account the requirement to sweep the frequency of one pulse.

4.2 Nuclear coherence detectors

NC detection in an ESR experiment is indirect detection that involves *excitation* of electron and nuclear spins to transfer the NC to EC. The basics for the description of NC detectors in the following paragraphs are provided in §3.2. An overview on the compatibility of NC generators and detectors is given in Table 4-3 on page 115.

4.2.1 FID detection

Since NC is transferred to allowed and forbidden EC by a non-selective mw pulse (cf. Tab. 3-1), it is feasible to use the FID following a single mw pulse for NC detection. The FID after application of a sufficiently non-selective mw pulse usually decays during the dead time τ_D at X-band frequencies, but this is no longer true at W-band frequencies of about 95 GHz where $\tau_D \approx 10$ ns can be achieved. Apart from this, FID detection of NC can be used if the NC is prepared in such a way that the EC generated by a single mw pulse refocuses at a time τ after that pulse ($\tau > \tau_D$). This is the case if the NC amplitude is modulated with $\sin(\Omega_S \tau)$ as for the Mims generator. It can be inferred from Tab. 3-1 that the optimum nominal flip angle for the transfer of NC to EC is $\pi/2$. The combination of the Mims generator with a non-selective mw $\pi/2$ pulse leads to the well known three-pulse ESEEM experiment.

For the ELDOR generator, the NC amplitude is modulated with $\sin(\Omega_S \tau)$ and $\cos(\Omega_S \tau)$, it also refocuses at a time τ after an mw pulse. In this case, the optimum flip angle for the *selective* pulse is π [81]. This pulse has to be on-resonant with the forbidden electron spin transition to create EC on the allowed transition. Such EC is detected with higher efficiency than EC on forbidden transitions, so that the stronger mw source should be used for the detection pulse.

Alternatively, one may transfer the NC to polarization with a non-selective mw pulse (optimum flip angle π) and detect the polarization *via* an FID following a selective mw $\pi/2$ pulse [72]. This detection method makes only sense if the NC was also created using a selective mw pulse, e.g. with the SENSE generator, since one loses signal otherwise.

Note however that a sequence of *several* non-selective pulses has a smaller bandwidth than a single non-selective pulse, so that the losses may be small if τ_D is small enough.

Finally, it should be feasible to detect NC *via* the oscillatory FID [82,83] following a matched high-turning angle pulse (see §3.2.7). However, experiments indicate that echo detection of the EC created by such a pulse is superior with respect to sensitivity at least for the typical $\tau_D \approx 100$ ns at X-band frequencies.

4.2.2 Echo detection

The defocusing of the EC during the dead time τ_D can be reversed in an echo experiment. The optimum detection sequence of mw pulses is then $\pi/2-\tau_2-\pi-\tau_2$ -echo. It has to be used if the NC is not amplitude modulated, as for instance if it was created by a single mw pulse [84] or by the three-pulse generator [80]. The general expression for the detection of NC by this sequence can be calculated easily with the help of Tab. 3-1, by computing the transformation of the density operator at the time of echo formation to the rotating frame by applying the unitary transformation $\sigma_{\text{echo}}^{(\text{rot})} = U^{-1} \sigma_{\text{echo}} U$, and extracting the coefficients of S_x and S_y from the product operator expression. For pulses with phase x we find that $\langle S_y \rangle(t = 2\tau) = 0$, i.e., the signal is *in phase* with the detection sequence. The complete expression for the expectation value of S_x is rather extensive and is not reproduced here. We note only that this type of detection leads to a τ_2 -dependent blind spot behaviour. Echo detection may fail if some nuclei in the system give rise to very deep modulations [85].

The first pulse in the echo sequence can be replaced by a matched high-turning angle pulse to optimize the transfer. Further work is needed to assess if experiments of this type are more sensitive than the conventional ESEEM methods.

4.2.3 Remote echo detection

It has been mentioned above that dead times at X-band frequencies usually prevent one from fulfilling Eq. (4.5) for the Mims generator if FID detection is used. This problem can be solved with remote echo detection which has first been introduced for two-

pulse ESEEM [86] and has later been applied to the HYSORE experiment [87]. Instead of observing the echo at time τ after the $\pi/2$ pulse, the magnetization is stored along the z -direction by applying another $\pi/2$ pulse with the same phase (see Fig. 4-6). After a waiting time t_w that is short with respect to T_{1e} , the longitudinal magnetization is detected with an echo sequence with $\tau_2 > \tau_D$. If $T_m \ll T_{1e}$, one can use $t_w \gg T_m$ and no additional phase cycling is necessary. Otherwise one can choose values of t_w and τ_2 for which there is no echo overlapping at time $\tau + t_w + 2\tau_2$. Note that remote echo detection can also be applied to echo detection. The part $\pi/2 - \tau$ has to be replaced then by $\pi/2 - \tau_1 - \pi - \tau_1$. Such a detection scheme is necessary to solve the blind spot problem for the three-pulse NC generator (see §4.1.6).

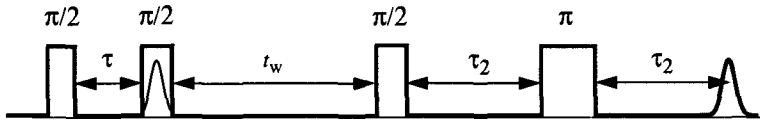


Fig. 4-6 Subsequence for remote echo detection of nuclear coherence.

4.2.4 Coherent Raman beat detection

One disadvantage of indirect NC detection is that a single data point must be sampled for each value of the evolution time: There is no multiplex advantage. This problem is particularly disturbing when large data matrices have to be sampled in 2D or 3D experiments. A remedy for this problem has been proposed by Bowman [37,48] and termed coherent Raman beat (CRB) detection of NC. In addition, this detection method is less sensitive to instantaneous diffusion. The method observes the signal during a weak mw probe pulse. In the original work, it has been suggested that the probe pulse field should be in the linear response region. Alternative descriptions for such a probe pulse have been given later by different authors [40,50,51]. A description that is valid beyond the linear response region has been discussed in §3.2.5.

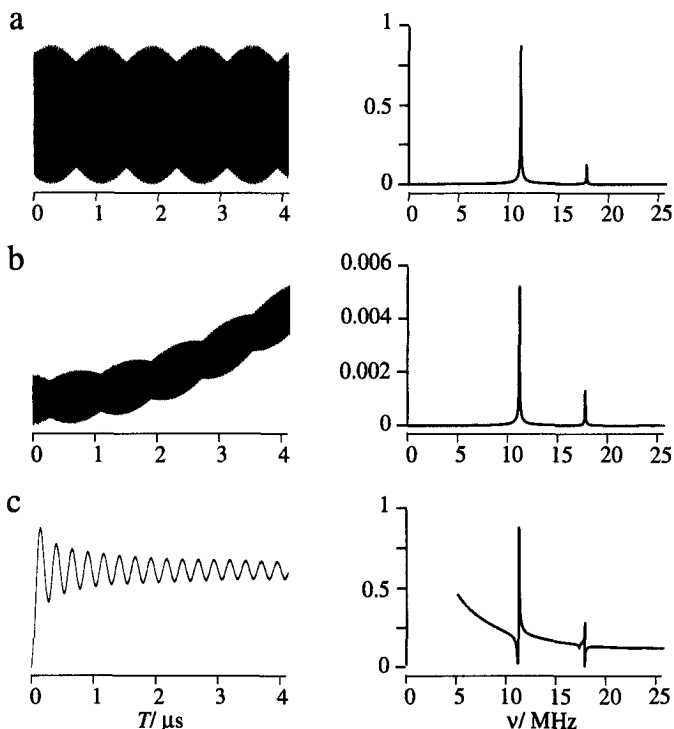


Fig. 4-7 Comparison of the signal-to-noise ratio in three-pulse ESEEM and two-pulse CRB measurements. Simulations have been performed with GAMMA [89], mw pulse non-ideality has been considered. An inhomogeneous line with Gaussian shape and FWHH of 20 MHz has been assumed. The parameters are $\omega_1'/2\pi = -14$ MHz, $A'/2\pi = 6.43$ MHz, $B'/2\pi = 3.43$ MHz. Time-domain traces (left) are not to scale. Intensity units are arbitrary but the same for all spectra (right). a) Three-pulse ESEEM. b) Two-pulse CRB with total flip angle 30° ($\omega_{1,CRB}/(2\pi) = 0.001$ MHz) corresponding to the limit of the linear response region. The spectrum has been multiplied by 64 (see text). c) CRB trace with $\omega_{1,CRB}/(2\pi) = 0.2$ MHz. The slow modulations are due to electron spin nutation [44]. The spectrum has been multiplied by 64.

Though line broadening by spectral diffusion and instantaneous diffusion may begin to appear in this case, it may be necessary to use mw probe pulses that violate the linear approximation in order to achieve sufficient sensitivity. This is illustrated in Fig. 4-7. To compare the signal-to-noise ratio of three-pulse ESEEM and the equivalent two-pulse CRB experiment that uses the Mims generator and probe pulse detection, we have assumed that the mw irradiation does not add to the noise. Thus, both experiments sample the same noise. In the time where a data trace of N points can be measured with

three-pulse ESEEM, N accumulations of the CRB experiment can be performed, thus improving on the signal-to-noise ratio of a single CRB trace by a factor \sqrt{N} . The signal-to-noise ratios of the two experiments can then be compared by plotting the CRB trace multiplied by \sqrt{N} and the three-pulse ESEEM trace. Besides the additional noise created by mw irradiation, this approach also neglects signal losses due to instantaneous diffusion during the last mw pulse in the three-pulse ESEEM experiment. Note here that in the two-pulse CRB approach, spin diffusion is also significant since the NC amplitude is also modulated by $\sin(\Omega_s\tau)$. For proton lines, a Nyquist frequency of 80 MHz and a resolution of 20 kHz are sufficient, so that $N=4096$ can be used. Obviously, CRB in the linear response region is much less sensitive than three-pulse ESEEM. This can be explained by the fact that due to the selectivity of the probe pulse much fewer spin packets take part in the former experiment and that the *whole* probe pulse transfers less NC to EC than a hard mw pulse as the former has a smaller total flip angle.

In contrast to these results, Burghaus and Klein found an improvement in resolution and a significant increase in signal-to-noise ratio in an experimental study that compared three-pulse ESEEM and *one-pulse* CRB [88]. The resolution improvement is most probably due to their different choice of the NC *generator* for the CRB experiment which suppresses spin diffusion. As for the increase in signal-to-noise ratio, the Figures 1 and 3 in their paper suggest that the CRB experiments were performed outside the linear response region though not far beyond it. In addition, a rather large value of $\tau=352$ ns has been used in the Mims generator, no data are given on T_m , and different devices were used to sample the ESEEM and CRB data. Nevertheless, the enhancement in signal-to-noise ratio by a factor 40 is astonishing. The authors also supply the information that enhancement factors ranged from 3 to 80 for different samples which suggests that relaxation during τ may play a role. Further work to clarify the relative sensitivity of CRB detection with respect to FID or echo detection is needed.

It may be advantageous to apply CRB detection to acquire 2D or 3D spectra even in cases where the signal-to-noise ratio is worse than with FID or echo detection. The total measurement time of a spectrum has a lower limit given by the time needed to sample all data points at least once. For large data matrices this time may be longer than the one that

would be needed to achieve a sufficient signal-to-noise ratio. CRB detection reduces this time by a factor of N because of the multiplex advantage. A further advantage of CRB detection is that no lower limit on τ in the Mims generator is set by the dead time [40], so that condition (4.5) can nearly always be fulfilled.

4.2.5 Pulse train detection

CRB detection poses the technical problem of observation during mw irradiation. To overcome this, mw leakage has to be compensated for and the resonator mode must be very stable [40]. The problem becomes more serious as the mw field increases. In addition, it may be difficult to eliminate the nutation contribution to the signal by data processing as can be seen in Fig. 4-7c. It is possible to separate the irradiation from the observation and the nutation component from the NC component of the signal without losing the multiplex advantage by replacing the probe pulse by a train of equally spaced mw pulses with small flip angle [90], see Fig. 4-8. A further advantage of this scheme is that the short mw pulses have a larger excitation bandwidth than an mw probe pulse of the same mw field strength. For this reason, more spin packets take part in the experiment. A theoretical description using an explicit calculation of the echo after the n -th pulse has been given by Hoffmann [40].

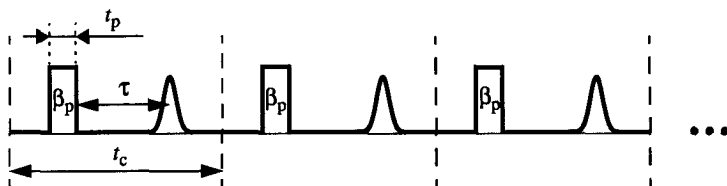


Fig. 4-8 Section from a pulse train that can be used for detection of nuclear coherence prepared with the Mims or ELDOR generator with an interpulse delay τ .

Pulse train detection of NC can be considered as repetitive FID detection, so that the considerations in §4.2.1 are also valid in this case. The additional problem to be solved in the calculation of the response to the n -th pulse is the influence of the $n-1$ previous pulses on the evolution of the NC. Since the Hamiltonian during this evolution is periodic with cycle time t_c (cf. Fig. 4-8) and the detection is stroboscopic, average Hamiltonian theory is well suited to this task. The calculation of the integrals on the right hand side of Eq.

(3.84a,b) becomes particularly simple, since in the rotating frame the Hamiltonian is piecewise constant during the pulse and during the remainder of t_c , with the Hamiltonians given by \mathcal{H}_{ex} in Eq. (3.34) and \mathcal{H}_0 in (3.23), respectively. We find

$$\bar{\mathcal{H}}_{\text{pt}}^{(0)} = \mathcal{H}_0 + \frac{t_p}{t_c} \omega_1 S_x, \quad (4.14a)$$

$$\bar{\mathcal{H}}_{\text{pt}}^{(1)} = 0, \quad (4.14b)$$

and it can be shown that all higher order terms in the Magnus expansion also become zero. The average Hamiltonian is thus of the same form as \mathcal{H}_{ex} and can be treated likewise. We can therefore apply the diagonalization of the Hamiltonian used for the description of non-ideal selective pulses to the spin packets for which the mw irradiation is on-resonant or nearly on-resonant with one of the electron spin transitions (see §3.2.5), and we can neglect the S_x term for all the other spin packets. If the scaled mw field $\bar{\omega}_1 = t_p \omega_1 / t_c$ becomes so large that condition (3.38a) breaks down, the approach to mw pulses of arbitrary strength and duration has to be used (see §3.2.7).

4.2.6 Radio frequency detection

Rf generation of NC should be combined with rf detection, since otherwise the advantages as independence on forbidden transitions and the possibility to eliminate contributions by polarization are lost. NC generated by a selective rf pulse can be transferred to polarization by another rf pulse and the polarization can be detected *via* an FID or an echo. Again, FID detection is possible if a Mims-type generator has been used or if the pulse length of the selective mw pulse in a Davies-type generator is considerably larger than τ_D .

Alternatively, NC can be detected by a combined mw/rf probe pulse (see §3.2.10). In this case the parameters in the NC generator have to be adjusted in a way that a sufficient amount of NC is created at $\Omega_S = -B_2 \omega_{2s} / B_0$, since this offset corresponds to the on-resonant position during the probe pulse considering the Bloch-Siegert shift (see §3.2.8).

Table 4-3 Compatibility of nuclear coherence generators and detectors. + compatible, - incompatible, o combination hardly useful.

Generator/ Detector	FID	Echo	Remote echo	CRB	Pulse train	Radio frequency	Mw/rf probe pulse	Generator description
SENSE	+	+	o	+	-	o	o	§4.1.1
Mims	+	-	+	+	+	o	o	§4.1.2
Single mw pulse	+	+	o	+	-	o	o	§4.1.3
Three-pulse	o	+	+	+	-	o	o	§4.1.6
ELDOR	+	-	o	+	+	o	o	§4.1.7
Monochromatic rf, Davies-type	+a	+a	o	o	o	+	+	§4.1.4
Chirp, Davies-type	+a	+a	o	+	o	+	+	§4.1.5
Monochromatic rf, Mims-type	+a	o	+a	o	o	+	+	§4.1.4
Chirp, Mims-type	+a	o	+a	o	o	+	+	§4.1.5
Detector description	§4.2.1	§4.2.2	§4.2.3	§4.2.4	§4.2.5	§4.2.6	§4.2.6,	§4.1.5

^a.Combined with radio frequency detection.

4.3 Manipulation of nuclear coherence

In many cases it is not sufficient to know just the set of nuclear frequencies of a given spin system, but it is necessary to establish correlations between frequencies to assign the peaks in a spectrum. In addition, NC may decay so fast in the presence of inhomogeneous broadening that detection becomes impossible. This problem is often encountered with disordered systems. Finally, the nuclear frequencies may not be sufficient to extract all parameters of the nuclear spin Hamiltonian even if their assignment is known. In this case it may be necessary to eliminate certain contributions to the Hamiltonian to simplify the problem. All these tasks require tools for the manipulation of NC as they are described in the following paragraphs. A whole chapter (Chapter 6) is devoted to hyperfine decoupling which can also be considered as manipulation of NC.

4.3.1 Sublevel transfer by a microwave π pulse

By applying a non-selective mw π pulse, one can change m_S by unity and thus achieve a transfer of NC between different m_S manifolds. The actual transfer is somewhat more complicated, since part of the NC is transferred to polarization by forbidden transitions.¹ With the NC in the α manifold before the π pulse given by

$$\sigma_{\text{NC}}^{\alpha}(\pi_{-}) = C_{+}^{\alpha} 2S^{\alpha}I_{+} + C_{-}^{\alpha} 2S^{\alpha}I_{-} , \quad (4.15a)$$

we find

$$\begin{aligned} \sigma(\pi_{+}) &= P_{\pi} \sigma_{\text{NC}}^{\alpha}(\pi_{-}) P_{\pi}^{-1} = [\cos^2 \eta C_{+}^{\alpha} - \sin^2 \eta C_{-}^{\alpha}] 2S^{\beta}I_{+} \\ &\quad + [\cos^2 \eta C_{-}^{\alpha} - \sin^2 \eta C_{+}^{\alpha}] 2S^{\beta}I_{-} \\ &\quad + \sin(2\eta)(C_{+}^{\alpha} + C_{-}^{\alpha}) 2S^{\beta}I_z , \end{aligned} \quad (4.15b)$$

where $P_{\pi} = U \exp(-i\pi S_x) U^{-1}$ is the propagator for an ideal mw π pulse. Eq. (4.15b) does not depend on the phase of the mw pulse. An analogous equation holds for NC that is in the β manifold before the pulse. It becomes obvious that the π pulse does not only transfer NC between manifolds but also changes its phase if $\eta \neq 0$. In particular, Eq.

1. Correspondingly, polarization is transferred to NC.

(4.15b) shows that a negatively rotating component is created from a positively rotating one and *vice versa*.

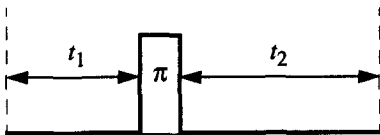


Fig. 4-9 Building block for hyperfine sublevel coherence transfer experiments.

Consider now the building block $t_1\text{-}\pi\text{-}t_2$ for hyperfine sublevel coherence transfer experiments (see Fig. 4-9). If the NC at the beginning of this building block is described by

$$\sigma_0 = C_+^\alpha 2S^\alpha I_+ + C_-^\alpha 2S^\alpha I_- + C_+^\beta 2S^\beta I_+ + C_-^\beta 2S^\beta I_- , \quad (4.16)$$

one can describe the contribution to the signal detected after the building block and any other parts of the pulse sequence by

$$\begin{aligned} I_{\text{NC}} = & \\ & C^\alpha D^\beta [\cos^2\eta \cos(\omega_{12}t_1 + \omega_{34}t_2 + \psi_1) + \sin^2\eta \cos(\omega_{12}t_1 - \omega_{34}t_2 + \psi_2)] \\ & + C^\beta D^\alpha [\cos^2\eta \cos(\omega_{34}t_1 + \omega_{12}t_2 + \psi_3) + \sin^2\eta \cos(\omega_{34}t_1 - \omega_{12}t_2 + \psi_4)] \\ & + \sin^2\eta [C^\alpha D^\beta \cos(\omega_{12}t_1 + \psi_5) + C^\beta D^\alpha \cos(\omega_{34}t_1 + \psi_6)] , \end{aligned} \quad (4.17)$$

where the ψ_i are phases that are of no further interest if a magnitude spectrum is calculated.¹ The $D^{\alpha\beta}$ are weighting coefficients for the detection of NC in the α and β manifold, respectively; they may also contain further time evolutions after the considered building block. Similarly, the $C^{\alpha\beta}$ are weighting coefficients for the generation of NC and may contain time evolution before the considered building block. In the following we refer to terms weighted by $\sin^2\eta$ as artefacts and to terms weighted by $\cos^2\eta$ as the wanted contribution.

1. Actually, phases are of interest as far as destructive interference between contributions of different spin packets is concerned. However, expressions for the phases can become tedious and we will not discuss such effects here.

We recall here that $\omega_{\text{HF}} = \omega_{12} - \omega_{34}$ and $\omega_{\text{NZ}} = \omega_{12} + \omega_{34}$ with the nuclear frequencies ω_{12} and ω_{34} given by Eq. (3.15a,b). By expressing ω_{HF} and ω_{NZ} in a power expansion with respect to B and neglecting terms higher than quadratic, we obtain

$$\omega_{\text{HF}} = A (m_S^{(\alpha)} - m_S^{(\beta)}) + B^2 \left[\frac{(m_S^{(\alpha)})^2}{2(A m_S^{(\alpha)} - \omega_I)} - \frac{(m_S^{(\beta)})^2}{2(A m_S^{(\beta)} - \omega_I)} \right], \quad (4.18a)$$

and

$$\omega_{\text{NZ}} = 2\omega_I - A(m_S^{(\alpha)} + m_S^{(\beta)}) - B^2 \left[\frac{(m_S^{(\alpha)})^2}{2(A m_S^{(\alpha)} - \omega_I)} + \frac{(m_S^{(\beta)})^2}{2(A m_S^{(\beta)} - \omega_I)} \right]. \quad (4.18b)$$

For $S=1/2$, we have $m_S^{(\alpha)} = 1/2$ and $m_S^{(\beta)} = -1/2$ and the formulas boil down to

$$\omega_{\text{HF}}^{(S=1/2)} = A - B^2 \frac{\omega_I}{4\omega_I^2 - A^2}, \quad (4.19a)$$

$$\omega_{\text{NZ}}^{(S=1/2)} = 2\omega_I + B^2 \frac{A}{2(4\omega_I^2 - A^2)}. \quad (4.19b)$$

For small hyperfine couplings, we thus have $\omega_{\text{HF}}^{(S=1/2)} \approx A$ and $\omega_{\text{NZ}}^{(S=1/2)} \approx 2\omega_I$. The latter result is of particular interest, since there is no distribution of ω_I in disordered systems. This means, that for $S=1/2$, $I=1/2$ systems, the building block $t_1-\pi-t_2$ leads to a refocusing at $t=t_1=t_2$ where the evolution of the wanted contributions is described by a factor $\cos(\omega_{\text{NZ}}t)$.¹ The second order term in Eq. (4.19b) can be used to distinguish nuclei of the same isotope with a different anisotropy of the HFI in an experiment where t_1 and t_2 are incremented at the same time [31,92]. The refocusing can also be used to

1. This is not the case for $S>1/2$ as can be inferred from Eq. (4.18b). For $I>1/2$, nuclear frequencies contain a nuclear quadrupole contribution that is also not refocused by an mw π pulse. The only exception are $-1/2 \leftrightarrow 1/2$ transitions of half-integer nuclear spins.

generate a nuclear coherence transfer echo that allows one to recover broad lines in ESEEM spectra in the DEFENCE method [36].

On the other hand, the wanted contribution is modulated with $\cos(\omega_{\text{HF}}t)$ if t_1 is incremented and t_2 decremented by the same time difference. Such methods are termed hyperfine spectroscopy and are treated in more detail in Chapter 7. As long as the high-field approximation for the electron spin holds, we always have $m_S^{(\alpha)} - m_S^{(\beta)} = 1$ and, apart from a second order contribution, $\omega_{\text{HF}} \approx A$ for any allowed transition even in a $S > 1/2$ system. One can show that there is also only a second order contribution to ω_{HF} by the nuclear quadrupole interaction for $I > 1/2$. The separation of interactions in ω_{HF} and ω_{NZ} makes it attractive to measure these frequencies instead of ω_α and ω_β .

It is also of large interest to correlate the ω_α and ω_β of a given nucleus. This can be done by incrementing t_1 and t_2 independently in the 2D HYSORE experiment [3]. In fact, it is possible to correlate any two frequencies out of the set (ω_α , ω_β , ω_{HF} and ω_{NZ}) of a given nucleus [91]. Though all these correlation methods yield *in principle the same information*, they differ in the opportunities to suppress artefacts by data post-processing, in the resolution that can be obtained for a given size of the time-domain data matrix, and in sensitivity for disordered systems. The possible incrementation schemes for the building block $t_1 - \pi - t_2$ are summarized in Tab. 4-4.

Eq. (4.17) shows, that two types of artefacts have to be considered. Firstly, there are terms modulated with respect to both t_1 and t_2 and weighted with $\sin^2\eta$. They introduce peaks at ω_{HF} (ω_{NZ}) in spectra where the wanted contribution is ω_{NZ} (ω_{HF}), and cross peaks in a different quadrant in HYSORE spectra. Usually, these artefacts are much weaker than the wanted contributions, since $\sin^2\eta \ll \cos^2\eta$. The second type of artefacts is described by the term in the last line on the right hand side of Eq. (4.17). The asymmetry between t_1 and t_2 arises, since we did not consider nuclear polarization in σ_0 . Though these artefacts are also weighted by $\sin^2\eta$, they are not necessarily weak. For instance, nuclear polarization is created and detected much more efficiently than NC by

the Mims generator with FID detection, and since the efficiency ratio is $\cos^2\eta/\sin^2\eta$, artefacts and wanted contributions are of the same magnitude. In HYSORE, these artefacts are situated on the axes and can be removed easily by data post-processing. In the measurement of ω_{NZ} and in hyperfine spectroscopy they lead to peaks at the nuclear frequencies ω_α and ω_β . In the former case one has $|\omega_{\text{NZ}}| > 2|\omega_I|$ and in the weak coupling case $\omega_\alpha, \omega_\beta < 2|\omega_I|$, so that artefacts and wanted contributions can be safely distinguished. In the latter case, artefact suppression is mandatory. Since this is not possible with phase cycling [43], NC generator-detector pairs have to be used that can either eliminate (see §4.1.5) or strongly suppress (see §4.1.3, §4.1.6, §4.1.7) contributions by polarization.

Another type of artefacts is not accounted for in Eq. (4.17), which has been calculated under the assumption of an ideal mw π pulse. Normally we have $\omega_1 < \Gamma$, where Γ is the inhomogeneous ESR linewidth, so that there are spin packets for which the flip angle is smaller than π . In this case, part of the NC is not transferred to the other electron spin manifold and evolves with the same frequency before and after the mw π pulse. This leads to diagonal peaks in HYSORE spectra and artefacts at $2\omega_\alpha$ and $2\omega_\beta$ in the measurement of ω_{NZ} . No artefacts occur in hyperfine spectroscopy, since the contribution of this pathway to the signal is constant and can be removed by baseline correction. These artefacts cannot be suppressed by phase cycling. They can be partially suppressed by using a stronger mw field for the π pulse than for the “non-selective” pulses in the NC generator and detector. This approach decreases sensitivity, since fewer spin packets take part in the experiment. It has been found that suppression as compared to the original HYSORE experiment is possible without sacrificing sensitivity by using the three-pulse generator [93]. The artefacts are weak in all approaches that use selective mw pulses in the NC generator or detector. In 2D experiments, they can be removed completely by a baseline correction in time domain if ω_{HF} is chosen as one dimension [90].

Table 4-4 Incrementation schemes for the times t_1 and t_2 to obtain different one-dimensional representations and two-dimensional correlation spectra with the building block shown in Fig. 4-9. t_{10} and t_{20} are constant starting values.

Experiment	$t_1(i,j)$	$t_2(i,j)$	Frequencies	References
Sumpeak	$t_{10} + i\Delta t$	$t_{20} + i\Delta t$	$\omega_{\text{NZ}} (1\text{D})$	[31],[92]
DEFENCE	t_{10}	$t_{20} + iD t$	$\omega_\alpha, \omega_\beta (1\text{D})^a$	[36]
Hyperfine	$t_{10} + i\Delta t^b$	$t_{20} - i\Delta t$	$\omega_{\text{HF}} (1\text{D})$	[91]
HYSORE	$t_{10} + i\Delta d_1$	$t_{20} + j\Delta d_1$	$(\omega_{\alpha,\beta}; \omega_{\beta,\alpha}) (2\text{D})$	[3]
CF-NF	$t_{10} + i\Delta d_1$	$t_{20} + i\Delta d_1 + j\Delta d_2$	$(\omega_{\text{NZ}}; \omega_{\alpha,\beta}) (2\text{D})$	[91]
HF-NF	$t_{10} + i\Delta d_1$	$t_{20} - i\Delta d_1 + j\Delta d_1$	$(\omega_{\text{HF}}; \omega_{\alpha,\beta}) (2\text{D})$	[91]
HF-CF	$t_{10} - i\Delta d_1 + j\Delta d_2^c$	$t_{20} - i\Delta d_1 + j\Delta d_2$		[91]

a. Nuclear coherence transfer echo detection, secular hyperfine contributions are refocused.

b. $t_{10} > N\Delta t$

c. $t_{10} > N_1\Delta d_1$

If either $\omega_{\text{NZ}} \gg \omega_1$ or $\omega_{\text{HF}} \gg \omega_1$ ¹, a non-selective π pulse can no longer be applied. Nevertheless, hyperfine sublevel transfer is still possible, if in the first case $\omega_1 > \omega_{\text{HF}}$, and in the second case $\omega_1 > \omega_{\text{NF}}$ can be fulfilled. In the first case, the transfer leads to only the wanted contribution. In the second case, with flip angle π for the *forbidden* transitions, only the terms with factor $\sin^2\eta$ in the first and second line on the right hand side of Eq. (4.17) are produced. In this case, the sign for the incrementation of t_2 has to be inverted in Tab. 4-4, e.g., the incrementation schemes for sumpeak and hyperfine spectroscopy change places.

In systems with more than one spin $I=1/2$ or with spins $I>1/2$, the mw π pulse usually correlates transitions with the same nuclear magnetic quantum numbers m_{Ik} of all spins. However, since m_{Ik} can be changed by forbidden transitions, combination peaks can also occur that then have by a factor $\sin\eta_k/\cos\eta_k$ smaller intensity than the allowed correla-

1. These cases and $\omega_{\text{NZ}}, \omega_{\text{HF}} \gg \omega_1$ can only occur, if the NC has been created with the ELDOR generator (§4.1.7) or by radio frequency excitation.

tion peaks. These peaks can be used to determine relative signs of hyperfine couplings [43].

4.3.2 Refocusing by a radio frequency π pulse

In the preceding paragraph we have seen that NC refocusing schemes based on an mw π pulse fail, if $S > 1/2$ or if nuclear spin transitions other than $-1/2 \leftrightarrow 1/2$ are concerned. A more versatile method of refocusing NC is an rf π pulse [94], the effect of which can be described for $I=1/2$ spins or for a *single* transition of an $I > 1/2$ spin by

$$C_+ I_+ + C_- I_- \xrightarrow{(\pi)_{\text{rf}}} C_- I_+ + C_+ I_- \quad (4.20)$$

Since only the rotation sense but not the frequency of the NC changes, any broadening is refocused in the primary nuclear spin echo created by such a pulse, the only condition being that the pulse is sufficiently non-selective. With monochromatic π pulses, nuclear echoes can usually be created only on single transitions that are broadened by a small anisotropy of the hyperfine coupling or of the nuclear quadrupole interaction.

It should also be possible to create primary nuclear spin echoes with rf chirp pulses. For that, consider the subsequence shown in Fig. 4-10. NC at frequency ω_x is created at time $t_{\text{chirp}}(\omega_x - \omega_s)/(\omega_e - \omega_s)$ after the begin of the first chirp pulse (point 1), its rotation sense is inverted at the same time after the begin of the second chirp pulse (point 2), and finally it is detected at the same time after the begin of the third chirp pulse (point 3). Independently of ω_x , the NC thus evolves for time $\tau_1 = t_{\text{ip1}} + t_{\text{chirp}}$ with one sense of rotation and for time $\tau_2 = t_{\text{ip2}} + t_{\text{chirp}}$ with the other sense, where the t_{ip} are the inter-pulse delays between the chirp pulses. Refocusing occurs for $t_{\text{ip1}} = t_{\text{ip2}}$. Note that the second chirp pulse should have larger amplitude than the other two, but equal duration. The feasibility of this approach depends of the validity of the Feretti-Ernst-model, i.e., on the question if the transition at frequency ω_x is excited only at the time when the chirp passes this frequency. For this reason, harmonics generation by the rf amplifier has to be prevented. No experiments with this subsequence have been performed so far.

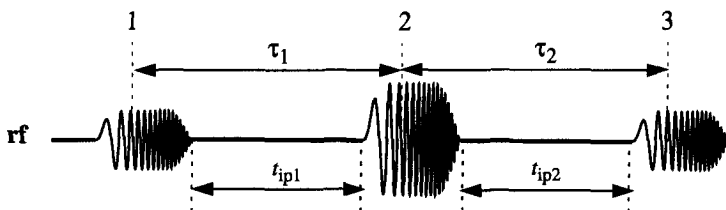


Fig. 4-10 Subsequence for primary nuclear echo creation with a chirp pulse.

For an $I=1$ system, refocusing with the subsequence shown in Fig. 4-10 does not work, but it should be possible to use the solid-echo sequence [95] instead, that translates for indirect detection with chirp pulses to $(\text{chirp})_x-t_{ip1}-(\text{chirp})_y-t_{ip2}-(\text{chirp})_x$ with 90° phase-shifted chirp pulses. The echo is also formed at $t_{ip1} = t_{ip2}$, and the optimum flip angle for all chirp pulses is given by Eq. (3.92b). In NMR spectroscopy, it has been shown that the solid echo sequence refocuses the first order contribution of the nuclear quadrupole interaction [96]. To refocus the anisotropic hyperfine coupling at the same time, the more elaborate subsequence $(\text{chirp})_x-\tau_1/2-(\text{CHIRP})-\tau_1/2-(\text{chirp})_y-\tau_2/2-(\text{CHIRP})-\tau_2/2-(\text{chirp})_x$ has to be used, where the symbol (CHIRP) denotes a chirp pulse of larger amplitude, and where the refocusing occurs at $\tau_1=\tau_2$.¹ Note however that the use of five chirp pulses leads to a comparatively long subsequence and that sensitivity is diminished further by the inevitable creation of multiple quantum coherences (see §3.2.9). On the other hand, chirp time-domain ENDOR with two chirp pulses features much higher sensitivity than ESEEM methods. It remains to be explored, if this approach to refocusing the nuclear quadrupole interaction is feasible.

4.3.3 Refocusing by microwave excitation

Inversion of the sense of rotation of NC can be also achieved by mw excitation as has been shown by Hoffmann et al. [47]. The authors have demonstrated that either a semi-selective mw 2π pulse or the subsequence $\pi-t_{\text{mix}}-\pi$ of non-selective mw pulses can

1. Refocusing of the secular part of the HFI can also be accomplished by using mw π pulses instead of the (CHIRP) pulses.

accomplish this transfer. For the effect of a non-ideal semi-selective pulse of nominal flip angle 2π on NC we find

$$C_+ S^\beta I_+ \xrightarrow{(2\pi)_{ss}} C_+ \sin^2(2\eta) (S^\beta I_+ + S^\beta I_-) - C_+ S^\beta I_- \quad (4.21)$$

i.e., the efficiency of the phase inversion transfer is given by $\sin^2(2\eta) = k/4$ ¹. This is a *strongly forbidden* transfer (cf. Table 3-3 on page 75), usual forbidden transfers are weighted with $\sqrt{k}/2$. It is therefore expected that the use of matched pulses (see §3.2.7) can enhance this transfer strongly. For the subsequence π - t_{mix} - π , the expressions become rather extensive and blind spots are introduced; the inversion transfer is also weighted with $k/4$ [47]. Since no phase shift can be introduced in the indirect excitation of nuclear spins by mw pulses, this kind of refocusing fails for $I=1$ systems with significant nuclear quadrupole broadening.

4.3.4 Correlation within the same electron spin manifold

The hyperfine sublevel correlation experiment [3] correlates nuclear transitions that differ by unity in m_S . However, except for the case where the weak combination peaks with a change in m_{Ik} can be seen, it does not provide any information which transitions belong to the *same* m_S manifold. This information is of interest for the determination of relative signs of the hyperfine coupling- if a peak with $\omega_\alpha > |\omega_{I1}|$ is correlated to a peak with $\omega_\beta > |\omega_{I2}|$, the respective signs of A must differ.² The classical experiment that provides this information is TRIPLE resonance, which is an extension of ENDOR that uses two radio frequencies [97]. The pulse ENDOR version [58,98] makes use of the fact that in a Davies-ENDOR experiment only one level in a given manifold has non-equilibrium population. If this level belongs to a transition that is on-resonant with the first rf π pulse, its equilibrium population is restored, and the second rf pulse at another frequency has no effect if it is on-resonant with a transition in the *same* manifold. However, if the second rf pulse is on-resonant with a transition in the *other* manifold, it changes the non-

-
1. The last term on the right hand side of Eq. (4.21) is not refocused, since the sign change of the term and the inversion of the rotation sense cancel each other.
 2. This is true if ω_{I1} and ω_{I2} have the same sign, otherwise the respective signs of A must be the same.

equilibrium population of the second level that belongs to the ESR observer transition. Usually, the effect is not that clear cut, since the first rf pulse is not an ideal π pulse. However, if two spectra are measured with and without application of a second rf pulse that is on-resonant with a known ENDOR transition, only peaks appear in the difference of the spectra that belong to the same m_S manifold as this transition¹. This version of the pulse TRIPLE experiment does not involve manipulation of NC but only of nuclear polarization.

It is often sufficient to perform TRIPLE experiments only for a few selected frequencies of the second rf pulse instead of performing a 2D experiment, since there are only two m_S manifolds. This situation changes if signals from several paramagnetic centers or different sites overlap at the ESR observer position and TRIPLE is used to assign ENDOR signals to the different centers [100]. Furthermore, difference TRIPLE spectra have usually low intensities and need so many accumulations that a measurement of a 2D spectrum can be performed in the same time. A 2D spectrum can be obtained by using the property of the chirp pulse to induce several nuclear transitions after each other. Consider NC on a transition with nuclear frequency ω_{x1} during a first chirp pulse. Part of it will be transferred back to polarization at time $t_{\text{chirp}}(\omega_{x1} - \omega_s)/(\omega_e - \omega_s)$ during a second chirp pulse and this polarization is modulated with $\cos(\omega_{x1} t_{\text{ip1}})$ where t_{ip1} is the interpulse delay between the two chirp pulses. Whenever the chirp pulse now passes a nuclear transition with frequency ω_{x2} in the same m_S manifold, a part of the polarization is transferred to NC on this nuclear transition. After another interpulse delay t_{ip2} , the NC can be detected by a third chirp pulse. A 2D Fourier transform with respect to t_{ip1} and t_{ip2} will then yield the desired correlation spectrum. The method will also produce correlation peaks for $\omega_{x1} > \omega_{x2}$, since in this case part of the NC is transferred to double quantum coherence when ω_{x2} is passed and back to single quantum coherence when ω_{x1} is passed. This experiment is explained in some more detail in §4.4.3.

1. In low-temperature measurements, the second rf pulse should be applied also in the first experiment, but after the echo observation. This is necessary, since otherwise the purely thermic difference between the two sequences may cause spurious peaks [99].

4.4 Chirp time-domain ENDOR spectroscopy

The following paragraphs illustrate the concepts of NC manipulation by example of the chirp time-domain ENDOR experiment and provide some experimental illustrations.

4.4.1 One-dimensional time-domain ENDOR

The most simple experiment that can be performed after generation of NC is the observation of its evolution, i.e., a measurement of the basic nuclear frequencies. In Davies-type chirp ENDOR (see Fig. 4-11a), nuclear polarization is created by the selective mw π pulse, transferred to NC by the chirp pulse, the NC evolves for time T , is transferred back to nuclear polarization by the second rf chirp pulse, and the polarization is finally detected by a two-pulse echo with selective mw pulses. The Mims-type experiment (see Fig. 4-11b) differs only in the generation and detection of the nuclear polarization.

The properties of both pulse sequences have been tested by experiments on the bis(glycinato)copper(II) complex in a single crystal of glycine [67]. The known structure of the complex is shown in the inset of Fig. 4-12a. Strong hyperfine couplings are expected for the nitrogen ligands (20-40 MHz), intermediate couplings for the amino protons (5-15 MHz), and small couplings for the CH₂ protons. In addition, for spins $I=1$ with inversion symmetry, a small second order splitting (50-150 kHz) is anticipated [101]. This second order splitting is not well resolved in the Davies-ENDOR spectrum (see Fig. 4-12b) due to power broadening while it can be evaluated with fairly high precision from the Davies-type chirp time-domain ENDOR spectrum (see Fig. 4-12a and detail plots). The slightly larger deviation of the splitting of the leftmost line is caused by superposition with an amino proton line (see §4.4.2). Furthermore, the peaks of the amino protons can be found in the Davies-type chirp ENDOR spectrum while the peaks of the weakly coupled CH₂ protons are suppressed. A similar suppression effect has been found for time-domain ENDOR with monochromatic rf pulses by Höfer (cf. Fig. 3.35 in [58]). It can be rationalized by a stronger effect of hyperfine contrast selectivity on time-domain ENDOR than on polarization based methods.

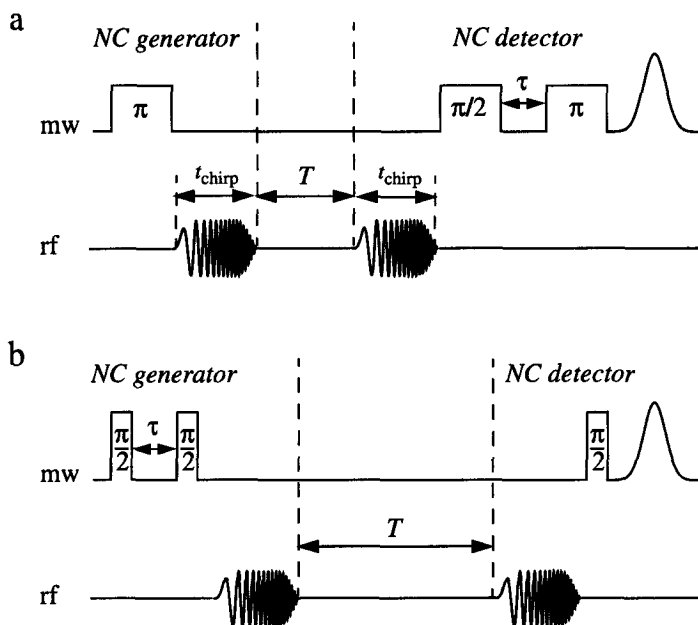


Fig. 4-11 Pulse sequences for Davies-type (a) and Mims-type (b) chirp time-domain ENDOR.

This suppression of peaks of weakly coupled nuclei can be overcome by applying Mims-type chirp time-domain ENDOR (see Fig. 4-12c). Note however, that Mims-type experiments feature blind spots and that the resolution may be smaller because of spin diffusion that leads to a decay of the Ω_S -dependent amplitude modulation of the NC. This effect can be clearly seen in Fig. 4-12c. Although power broadening is absent, the second order splittings of the nitrogen peaks are no longer resolved.

The experiments discussed in this paragraph have been performed at a temperature of 17 K on a home-built spectrometer [68] with the ENDOR probehead described in [70]. The measurement time per frequency-domain data point was the same in all spectra. For chirp ENDOR, a two-step phase cycle $[0]-[\pi]$ has been applied to the first chirp pulse. Further experimental parameters are given in [67].

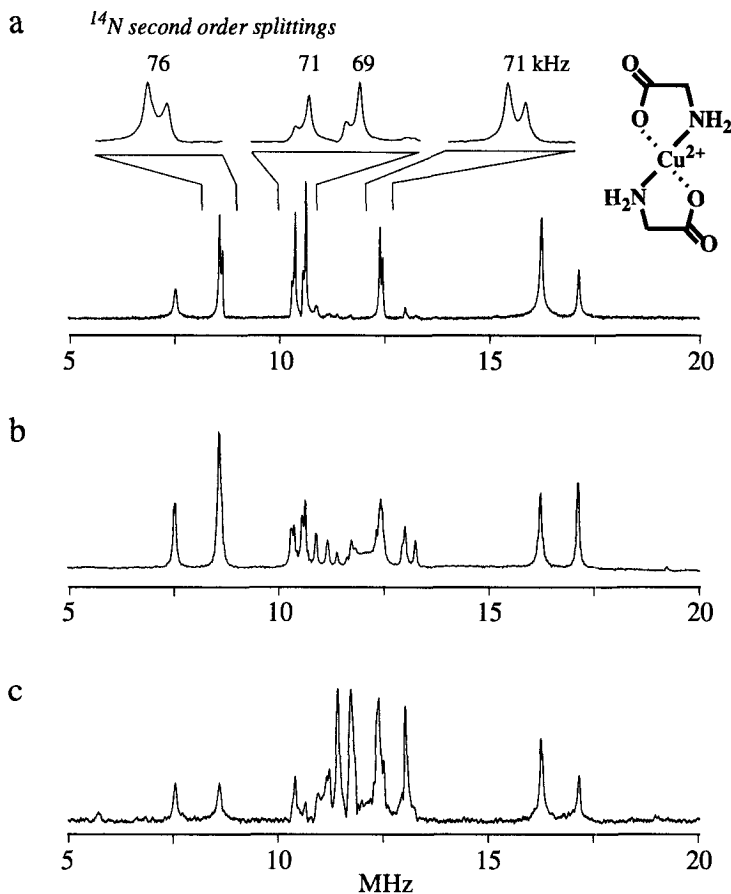


Fig. 4-12 Chirp time-domain ENDOR on the bis(glycinato)copper(II) complex in a single crystal of glycine at arbitrary orientation. a) Davies-type chirm ENDOR with resolved second order splittings of the ^{14}N lines. b) Davies-ENDOR with the same rf pulse length for comparison. c) Mims-type chirm ENDOR.

4.4.2 HYSORE-type correlation experiment

The overlapping proton and nitrogen lines in the ENDOR spectrum can be resolved if a second dimension is introduced in a HYSORE-type correlation experiment (see §4.3.1). For that, the evolution time T (cf. Fig. 4-11) has to be substituted by the building block for hyperfine sublevel coherence transfer (see Fig. 4-9), and the times t_1 and t_2 have to be incremented independently. A Davies-type chirm ENDOR HYSORE on the

bis(glycinato)copper(II) complex reveals two cross peaks in different quadrants for the ENDOR line at 8.5 MHz (see Fig. 4-13). The effect that cross peaks in the weak coupling case ($|A'| < 2|\omega_I'|$) appear in the first quadrant and cross peaks for the strong coupling case ($|A'| > 2|\omega_I'|$) in the second quadrant, is well known in HYSCORE [102]. The reason is that for an $S=1/2$ system in the strong coupling case ω_{12} and ω_{34} have different sign, while they have the same sign in the weak coupling case (see Eqs. (3.15a,b)). The inner nitrogen lines at about 10.5 MHz are not resolved in the 2D spectrum (128×128 data points). It is however possible to acquire a 1024×1024 data matrix with a four-step phase cycle within a few hours of measurement time as will be demonstrated in later Chapters. The other experimental parameters for the spectrum shown in Fig. 4-13 are the same as for the Davies-type chirp ENDOR spectrum discussed in §4.4.2.

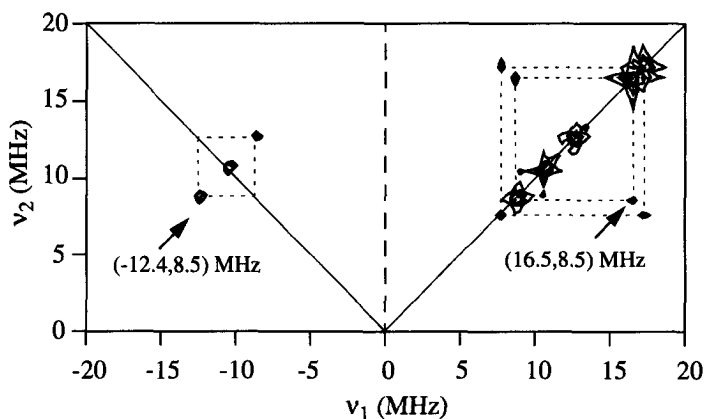


Fig. 4-13 Chirp ENDOR HYSCORE spectrum of the bis(glycinato)copper(II) complex in a single crystal of glycine at the same orientation as for the spectra in Fig. 4-12 on page 128. Cross peaks in the first quadrant (right) correspond to protons (weak coupling case) and cross peaks in the second quadrant to the nitrogen ligands (strong coupling case).

4.4.3 TRIPLE-type correlation experiment

For correlating nuclear frequencies within the same electron spin manifold, the pulse sequence in Fig. 4-14 or its Mims-type equivalent can be used. The optimum flip angle for the first and third chirp pulse is given by Eq. (3.92b) and the one for the second chirp pulse by Eq. (3.94b). Depending on the required information, more or less elaborate phase cycling has to be used. In the most simple case, only the two step phase cycle [0]–

$[\pi]$ is applied to the first rf chirp pulse as in the 1D experiments. Besides the wanted cross peaks, one obtains diagonal peaks from coherence transfer pathways (CTPs) in which the NC is *not* influenced by the second chirp pulse, axial peaks from CTPs where the NC is converted to polarization by the second chirp pulse and not influenced by the third chirp pulse, and finally cross peaks where double-quantum nuclear coherence evolves during the second evolution period and is detected by the third chirp pulse. The first and second type of additional peaks can be easily distinguished from the desired cross peaks, while the third type should be removed by phase cycling. This can be done by applying a phase cycle $[0]+[\pi]$ to the second chirp pulse, so that the complete phase cycle for the first and second chirp pulse is now $[0,0]-[\pi,0]+[0,\pi]-[\pi,\pi]$. This may still leave weak artefacts that arise from the creation of triple-quantum NC from single quantum NC by the second chirp pulse (which is equally efficient as the wanted transfer) and the detection of this triple quantum coherence by the third chirp pulse.¹ If these artefacts are significant, four phases are needed for the second chirp pulse to prevent changes in the coherence order by ± 2 . The phase cycle for the second pulse in this case is $[0]+[\pi/2]+[\pi]+[3\pi/2]$. If necessary, the axial peaks can be removed by a phase cycle $[0]-[\pi]$ applied to the last chirp pulse.² A memory-saving approach to programming the complete phase cycle on an arbitrary function generator is described in Appendix B. No experiments with the sequence in Fig. 4-14 have been performed so far.

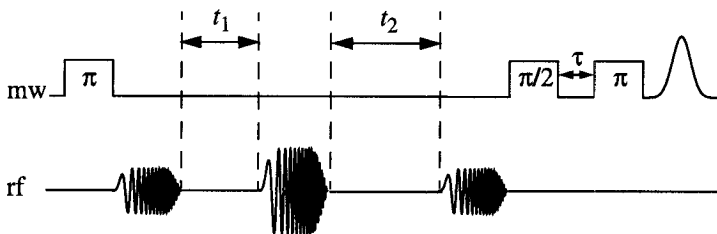


Fig. 4-14 Pulse sequence for a TRIPLE-type correlation experiment with chirp pulses. The second chirp pulse has higher amplitude since its flip angle must be optimized for two spin flips instead of one.

1. Transfers with a nuclear coherence order change by two for *one* spin can be neglected since the flip angle is small.
2. This may be necessary if cross peaks at small frequencies are observed.

Matched two-pulse ESEEM

5.1 Features of two-pulse ESEEM

5.1.1 Practical considerations

The most simple experiment for the measurement of nuclear frequencies is two-pulse ESEEM [28] which is based on the manipulation of EC. The line widths in two-pulse ESEEM spectra are determined by *half* the phase memory time T_m of the electron spins, usual values are 1 MHz as compared to about 100 kHz for methods that are based on the manipulation of NC. The slower decay of the signal governed by T_{2n} in the latter methods can also lead to higher sensitivity. However, these disadvantages of two-pulse ESEEM are no longer borne out if *inhomogeneous* broadening in disordered systems leads to line widths larger than $2/T_m$. In this case, dead time considerations become paramount. Three-pulse ESEEM has a dead time of $T_0+2\tau$, and two-pulse echo modulation only a dead time of τ_0 .¹ As a result, observation of inhomogeneously broadened lines requires refocusing schemes in three-pulse ESEEM, while they can often be detected without refocusing by the two-pulse ESEEM experiment.

1. The reason for the latter fact is that two-pulse ESEEM measures nuclear frequencies as difference frequencies and the modulation is with $\cos(\omega_{\alpha\beta}\tau)$, instead of $\cos(2\omega_{\alpha\beta}\tau)$.

Another advantage of two-pulse ESEEM is that lines at ω_{NZ} are contained in the spectrum while they have to be introduced by an additional π pulse in methods that are based on NC manipulation. These lines are often the only well resolved ones for disordered systems.¹ The introduction of additional pulses into the NC-based experiments for refocusing or introduction of additional frequencies leads to signal losses. In addition, though the *modulation depth* is the same in two-pulse and three-pulse ESEEM, the two-pulse echo is by a factor of two larger. Two-pulse ESEEM features no blind spots and can be performed on spectrometers with only one mw channel, since no phase cycling is necessary. The sensitivity advantage for some disordered systems together with the simplicity of use have made this experiment very popular [29,33,103-108].

Nevertheless, two-pulse ESEEM normally uses only a few percent of the echo amplitude, since forbidden transition probabilities and hence modulation depths are small. We have seen in Chapter 4 that modulation depth limits can be overcome. Furthermore, the presence of ω_{NZ} and ω_{HF} can also be a problem, because it is often difficult to assign peaks to the different types of frequencies. It is possible to improve two-pulse ESEEM on these two counts without giving up its inherent advantages as will be shown in this Chapter.

5.1.2 Coherence transfer echo description

Two-pulse ESEEM is usually considered as amplitude modulation of the Hahn echo ($\pi/2$ - τ - π - τ -echo) with respect to τ . For theoretical considerations it is more convenient to analyse the experiment in terms of coherence transfer pathways. First, there is the primary electron spin echo (Hahn echo) on the allowed transitions, which results from a phase inversion of allowed EC. This echo is not modulated. The refocusing of the magnetization occurs along the -y direction if the phase of the mw pulses is zero (x-pulses), i.e., the echo is out-of-phase. Second, another primary echo is formed on the forbidden transitions, but note that the phase inversion of forbidden EC requires a complete flip of the nuclear spins, so that the necessary transfer is strongly forbidden (cf. Table 3-3 on

1. Note however that NC-based observation of ω_{NZ} is superior with respect to resolution if the narrowing of these lines is large enough for the line widths to be governed by the relaxation times.

page 75). This echo is very weak and also unmodulated. Third, the π pulse can transfer EC from an allowed to a forbidden transition and *vice versa* (forbidden transfers), between the two allowed transitions (strongly forbidden transfer), or between the two forbidden transitions (allowed transfer). If the phase of the EC is inverted at the same time, these transfers also lead to refocusing of the off-resonances Ω_S at time 2τ . On the other hand, the contribution of the hyperfine coupling and nuclear Zeeman interaction is different in the two periods of free evolution for these coherence transfer echoes (CTEs). Therefore, the refocusing of the magnetization does not occur along the $-y$ axis, but along an axis in the xy -plane that makes an angle $\phi = \Delta\omega \tau$ with the $-y$ axis, where $\Delta\omega$ is the difference of the evolution frequencies in the periods after and before the π pulse. With the observer along the $-y$ -axis, this corresponds to an oscillation of the CTE amplitudes described by $\cos(\Delta\omega \tau)$. Such a CTE description of two-pulse ESEEM has first been given by Ponti and Schweiger [35]. The six possible CTEs are summarized in Tab. 5-1.

Table 5-1 Coherence transfer echoes in two-pulse ESEEM. The type of electron coherence during the two evolution periods is expressed by product operators. Transfer pathways without detection bottleneck are emphasized.

#	Excitation	First evolution	Coherence transfer	Second evolution	Detection	Oscillation frequency $\Delta\omega$
1	allowed	$S^+I^{\alpha/\beta}, S^-I^{\omega/\beta}$	strongly forbidden	$S^-I^{\beta/\alpha}, S^+I^{\beta/\alpha}$	allowed	ω_{HF}
2	forbidden	$S^+I^{+/-}, S^-I^{+/-}$	allowed	$S^-I^{+/-}, S^+I^{+/-}$	forbidden	ω_{NZ}
3	forbidden	$S^+I^{+/-}, S^-I^{+/-}$	forbidden	$S^-I^{\beta/\alpha}, S^+I^{\beta/\alpha}$	allowed	ω_{α}
4	forbidden	$S^+I^{+/-}, S^-I^{+/-}$	forbidden	$S^-I^{\omega/\beta}, S^+I^{\omega/\beta}$	allowed	ω_{β}
5	allowed	$S^+I^{\alpha/\beta}, S^-I^{\omega/\beta}$	forbidden	$S^-I^{+/-}, S^+I^{+/-}$	forbidden	ω_{α}
6	allowed	$S^+I^{\omega/\beta}, S^-I^{\omega/\beta}$	forbidden	$S^-I^{+/-}, S^+I^{+/-}$	forbidden	ω_{β}

5.2 Sensitivity improvement and peak discrimination

5.2.1 Theoretical considerations

With Tab. 5-1 and the description of non-ideal mw pulses (see §3.2.7) it is now straightforward to design two-pulse ESEEM experiments that enhance individual CTEs. Forbidden transfers are optimized by using matched high-turning angle (HTA) pulses instead of the $\pi/2$ or π pulse, while allowed transfers are diminished by this procedure. Each forbidden transfer contributes a factor $\sqrt{k}/2$ to the original CTE amplitude, a strongly forbidden transfer contributes a factor $k/4$.¹ Matching can now increase these factors. All CTEs that involve forbidden *detection* contribute a factor $\sqrt{k}/2$ that cannot be increased by pulse matching; we call this a detection bottleneck. Such a detection bottleneck is encountered in the only pathway that leads to ω_{NZ} and in one of the two pathways that lead to ω_{α} (ω_{β}). Hence it is expected that the sensitivity gain in matched ESEEM is largest for hyperfine peaks and lowest for peaks at the nuclear Zeeman splitting.

Furthermore, the experiment that enhances hyperfine peaks does only enhance the pathways leading to ω_{α} and ω_{β} that feature a detection bottleneck, so that the intensity gain is much higher for the hyperfine peaks. It is then possible to distinguish between both types of peaks by comparing a conventional two-pulse ESEEM spectrum with a hyperfine-frequency enhanced ESEEM spectrum (the π pulse is substituted by a matched HTA pulse, see Fig. 5-1a). Similarly, peaks at ω_{NZ} can be recognized, since their intensity is decreased rather than increased with this experiment. An analogous reasoning shows that it is possible to distinguish between ω_{α} and ω_{β} on the one hand and ω_{NZ} on the other hand by comparing a conventional two-pulse ESEEM spectrum with a nuclear-frequency enhanced ESEEM spectrum (both the $\pi/2$ pulse and the π pulse are substituted by HTA pulses, see Fig. 5-1c).

The optimum length of the matched HTA pulses cannot be predicted exactly from theory, since it depends on the transition probability of the forbidden transitions (which is

1. Detection has to be counted as a transfer here.

not known before the experiment), on the relaxation times in the rotating frame, and on destructive interference between different spin packets. As a rule of thumb, the $\pi/2$ pulse should be substituted by a matched pulse with a flip angle $(2l+1)\pi/2$ and the π pulse by a matched pulse with flip angle $(l+1)\pi$, where l is a positive integer. This ensures that the pulse lengths in nuclear-frequency enhanced ESEEM differ only by a small amount (18 ns for protons at X-band frequencies) and the influence of relaxation and destructive interference during both pulses is similar.

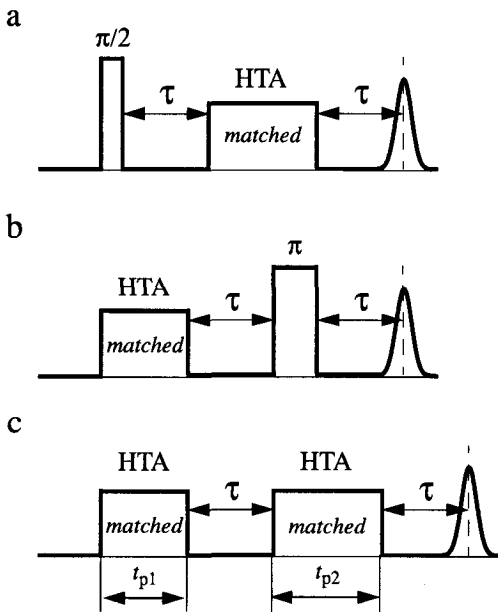


Fig. 5-1 Pulse sequences for matched two-pulse ESEEM experiments that employ high turning angle (HTA) pulses. a) Hyperfine-frequency enhanced ESEEM. b) Nuclear-Zeeman-splitting enhanced ESEEM. c) Nuclear-frequency enhanced ESEEM.

HTA pulses can also introduce unwanted contributions to the signal. For instance, the oscillatory FID after a HTA pulse of length t_p has also duration t_p [35,82], so that it contributes to the signal if $t_{p2} > \tau$ or $t_{p1} > 2\tau + t_{p2}$. If necessary, the contribution can be eliminated in the first case by applying a phase cycle $[0] + [\pi]$ to the second pulse, and in the second case by applying a phase cycle $[0] - [\pi/2] + [\pi] - [3\pi/2]$ also to the *second* pulse. Furthermore, flip angle imperfections of the π pulse can lead to formation of a notched

echo [35,109] in nuclear-Zeeman-splitting enhanced ESEEM, and to formation of an analogous type of echo in nuclear-frequency enhanced ESEEM. These contributions can also be eliminated by the phase cycle $[0]+[\pi]$ for the second pulse as well as by the four-step phase cycle. Finally, edge echoes [110] can occur at time $t < t_p$ after a pulse if the ESR line is excited off-center or has an asymmetric shape [35]. The remedy is again the above mentioned two-step phase cycle for the edge echo of the second pulse and the four-step phase cycle applied to the second pulse for the edge echo of the first pulse.

5.2.2 Simulations

As a first test of the considerations in the preceding paragraph we have performed simulations for the three pulse sequences shown in Fig. 5-1 on a spin system typical for protons at X-band frequencies (parameters: see Fig. 4-7 on page 111, $T_m=1 \mu\text{s}$, $\tau=300 \text{ ns}$, $\omega_1=\omega_I$). In agreement with the expectations, the intensity gain is particularly large for the peak at ω_{HF} in hyperfine-frequency enhanced ESEEM (factor 20, see Fig. 5-2a) and particularly small for the peak at ω_{NZ} in nuclear-Zeeman-splitting enhanced ESEEM (factor 2, Fig. 5-2b). The first trace in these figures corresponds to pulse sequences $\pi/2-\tau-\pi$ that feature only small enhancements even if the pulses for the forbidden transfers are matched. Therefore, these traces have similar intensities as conventional two-pulse ESEEM spectra. Significant enhancements are also found for nuclear-frequency enhanced ESEEM (factor 3... 5, Fig. 5-2c,d). No noticeable distortions due to the oscillatory FID are recognized in the simulation of hyperfine-frequency enhanced ESEEM even if the length of the second pulse becomes much longer than τ . On the other hand, there are distortions due to the notched echo in nuclear-frequency enhanced ESEEM as can be seen in Fig. 5-2c. These distortions are even stronger in nuclear-Zeeman-splitting enhanced ESEEM; the result without phase cycling is not displayed in this case.

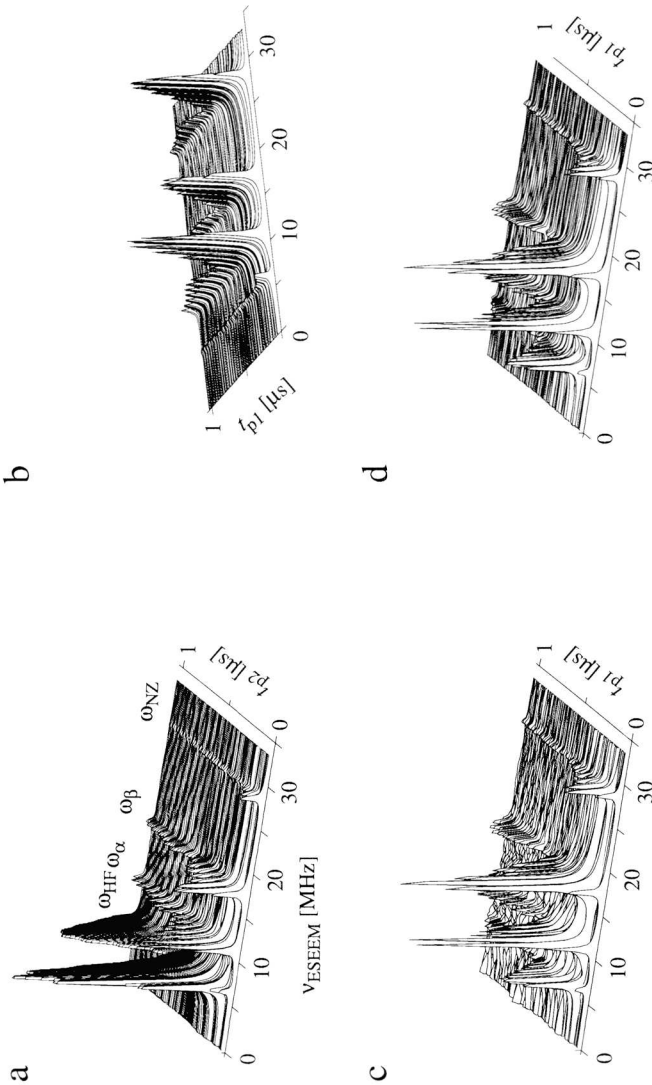


Fig. 5-2 Simulations of matched two-pulse ESEEM experiments for a spin system typical for protons at X-band frequencies. a) Hyperfine-frequency enhanced ESEEM without phase-cycling. b) Nuclear-Zeeman-splitting enhanced ESEEM, with two-step phase cycle $[0]-[\pi]$ for the second pulse. c) Nuclear-frequency enhanced ESEEM without phase cycle. d) Nuclear-frequency enhanced ESEEM with the same phase cycle as in b).

The simulations show that the optimum enhancement occurs at a flip angle larger than 2π of the second pulse in hyperfine-frequency enhanced ESEEM, but at flip angles of approximately $3\pi/2$ and 2π in nuclear-frequency enhanced ESEEM. The reason for the losses at larger flip angles is destructive interference between spin packets with different Ω_S . For smaller transition probabilities of the forbidden transitions, it is nevertheless possible that the maximum gain occurs at larger flip angles. On the other hand, B_1 -field inhomogeneities that can decrease the sensitivity gain and lead to smaller optimum flip angles are not considered in the simulations.

5.3 Experimental examples

5.3.1 Nuclear-frequency enhanced ESEEM

The performance of the nuclear-frequency enhanced ESEEM sequence has been studied experimentally with a spin-label doped polymer sample. Spin labels are widely used in investigations of polymer dynamics, so that it is of interest to characterize the interaction of the spin label with the polymer. In particular, it should be known if spin density is transferred from the label to atoms in the polymer and how close the radical center is to the polymer chain. Hyperfine interactions are well suited for this task, but it is not possible to distinguish proton hyperfine interactions with polymer atoms from intramolecular proton hyperfine interactions in the spin label compound. One way to overcome this problem is to use a polymer with a heteroatom that does not occur in the spin label. This approach is discussed in Chapter 7. On the other hand, one can use a completely deuterated spin label, so that proton hyperfine interactions can only originate from the polymer chain. The problem is then detection of the shallow proton modulations in the presence of deep deuterium modulations.

This problem is illustrated in Fig. 5-3a for a sample of poly(isobutene) doped with $^{15}\text{N}, \text{d}_{18}$ -4-hydroxy-2,2,6,6-tetramethyl-piperidin-1-oxyl (TEMPOL). Though there is some indication for a proton peak at $\omega_{\text{NZ}}/(2\pi) = 29$ MHz, one cannot find a peak at the corresponding basic frequency of 14.5 MHz. The reason for this is a small modulation depth for the protons together with the strong deuterium signal that may have different

phase. The interference of both signals leads to an uncharacteristic bump close to 14.5 MHz that does not allow for any conclusions on the proton hyperfine coupling.

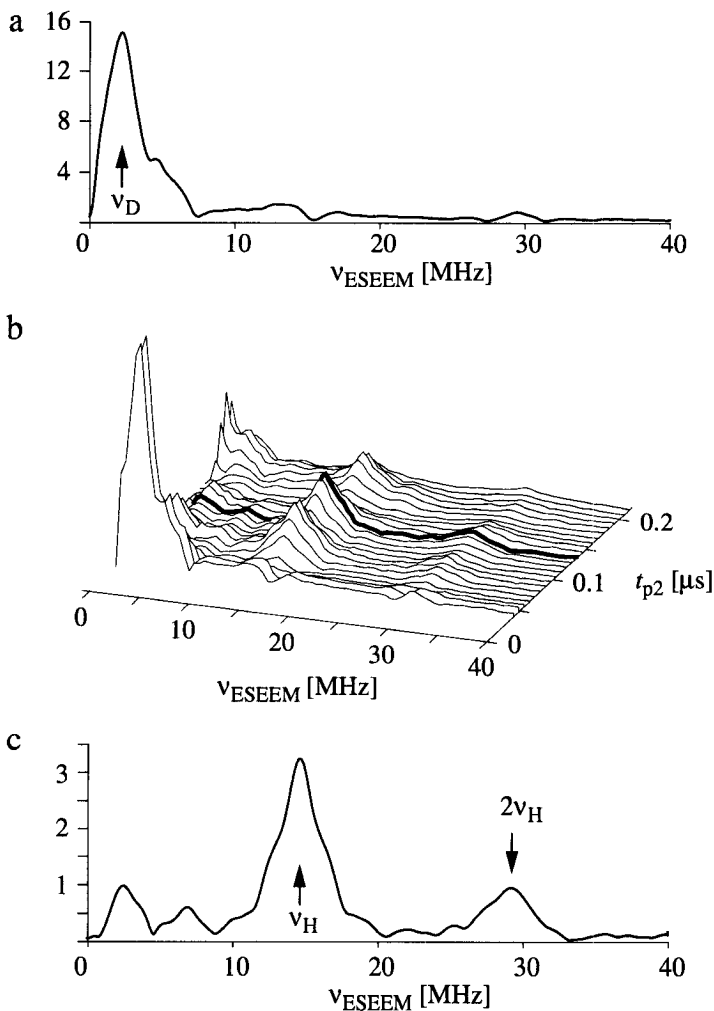


Fig. 5-3 Detection of proton peaks in the presence of deuterium by matched ESEEM in poly(isobutene) doped with ^{15}N -labelled, perdeuterated TEMPOL. a) Conventional ESEEM spectrum. b) Nuclear-frequency enhanced ESEEM for different lengths $t_{p1}=t_{p2}-24$ ns and t_{p2} of the two matched microwave pulses. c) Nuclear-frequency enhanced ESEEM spectrum for $t_{p1}=112$ ns, $t_{p2}=136$ ns corresponding to flip angles of approximately 3.1π and 3.8π . This spectrum is emphasized in b).

On the other hand, it can be seen in Fig. 5-3b that matching and prolonging the two mw pulses leads to enhancement of the proton peaks by at least a factor of three as well as to suppression of the disturbing deuterium signal by nearly a factor of ten. The latter effect is explained by the fact that the mw field is not matched for deuterium and that there is thus no compensation for destructive interference.

In the nuclear-frequency enhanced ESEEM spectrum with optimized pulse lengths (Fig. 5-3c), the proton line can be recognized easily. Its peculiar form with shoulders and sidebands is most likely due to significant contributions by deuterium combination lines at $\omega_H \pm \omega_D$ and $\omega_H \pm 2\omega_D$. The derivation of an estimate for the proton hyperfine coupling would therefore require a measurement of T_m and a simulation of the lineshape which considers the combination lines. This task is beyond the scope of the present work.

The experiment was performed at a temperature of 30 K on a Bruker ESP 380 spectrometer where pulse lengths are restricted to multiples of 8 ns. The matching was adjusted by maximizing the echo for a sequence of two pulse with lengths 16 and 40 ns, respectively. This corresponds to $\omega_1/2\pi \approx 13.9$ MHz, while $\omega_f/2\pi = 14.6$ MHz at $B_0 = 342.7$ mT where the measurement was performed. A Bruker ER 4118 probe head was employed. We found that no phase cycling was necessary in the experiments, i.e., no difference could be detected between spectra measured with and without phase cycling. This can be explained by the oscillatory shape of the notched echo which leads to partial cancellation if the signal is integrated over a finite gate width. This gate width was 24 ns in the experiments, while no integration was assumed in the simulations in §5.2.2. We emphasize here that the experiment can be performed on a single-channel spectrometer and that nearly optimum enhancement can be achieved with the "standard" flip angles of $3\pi/2$ and 2π . This standard version of nuclear-frequency enhanced ESEEM combines the simplicity of use of conventional two-pulse ESEEM with the advantages of matched ESEEM and has been found to provide significant sensitivity gains for all samples investigated so far. A nuclear-frequency enhanced ESEEM experiment on an ordered system has been described in [55].

5.3.2 Hyperfine-frequency enhanced ESEEM

Larger sensitivity gains than a factor of three are expected for hyperfine-frequency enhanced ESEEM, in particular, if the modulation depth for individual lines is very small. This is demonstrated in an experiment on the $[\text{VO}(\text{H}_2\text{O})_5]^{2+}$ complex in a single crystal of $\text{Mg}(\text{NH}_4)_2(\text{SO}_4)_2 \cdot 6 \text{H}_2\text{O}$. The experimental parameters are the same as in §5.3.1, except for the static field $B_0 = 418.9 \text{ mT}$ and for the mw power of the $\pi/2$ pulse that was adjusted with a two-pulse sequence with pulse lengths of 8 and 16 ns. We find that all observable hyperfine peaks of the water ligand protons are enhanced in the spectrum that is obtained by matching the second mw pulse and increasing its length (see white part of the contour plot in Fig. 5-4a). In particular, there is again a standard sequence, $\pi/2 - \tau - 2\pi$, that provides a sensitivity gain for all peaks (see Fig. 5-4bcd), though not necessarily the optimum gain for each single peak. The latter point is most obvious for the hyperfine peak at 2.4 MHz that cannot even be detected with a matched π pulse as second pulse or with conventional two-pulse ESEEM. It corresponds to a very small modulation depth and the optimum enhancement of at least a factor of 12 is obtained for $t_{p2} = 256 \text{ ns}$ (nominal flip angle of about 6.7π). The authenticity of the hyperfine peaks is confirmed by the occurrence of the corresponding nuclear frequencies (shadowed part of the contour plot in Fig. 5-4a).

In agreement with the simulation we found that no phase cycling was necessary to obtain artefact-free spectra. Substitution of the hard $\pi/2$ pulse by a $\pi/2$ pulse of 16 ns length in the same mw channel as the matched pulse was found to have only small influence on the spectrum (less than 10% signal loss). Hyperfine-frequency enhanced ESEEM is thus also as simple to use as conventional two-pulse ESEEM. Significant enhancement of hyperfine peaks has also been found for most of the other samples investigated so far [55,111].¹ On the other hand, sensitivity gains are small for nuclear-Zeeman-splitting enhanced ESEEM, in no case we have observed a factor larger than two, in

1. The only exception was the spin-label doped polymer sample discussed in §5.3.1. Possibly the hyperfine frequency is too small in this case to be safely distinguished from the constant contribution to the echo and is removed by the inevitable baseline correction.

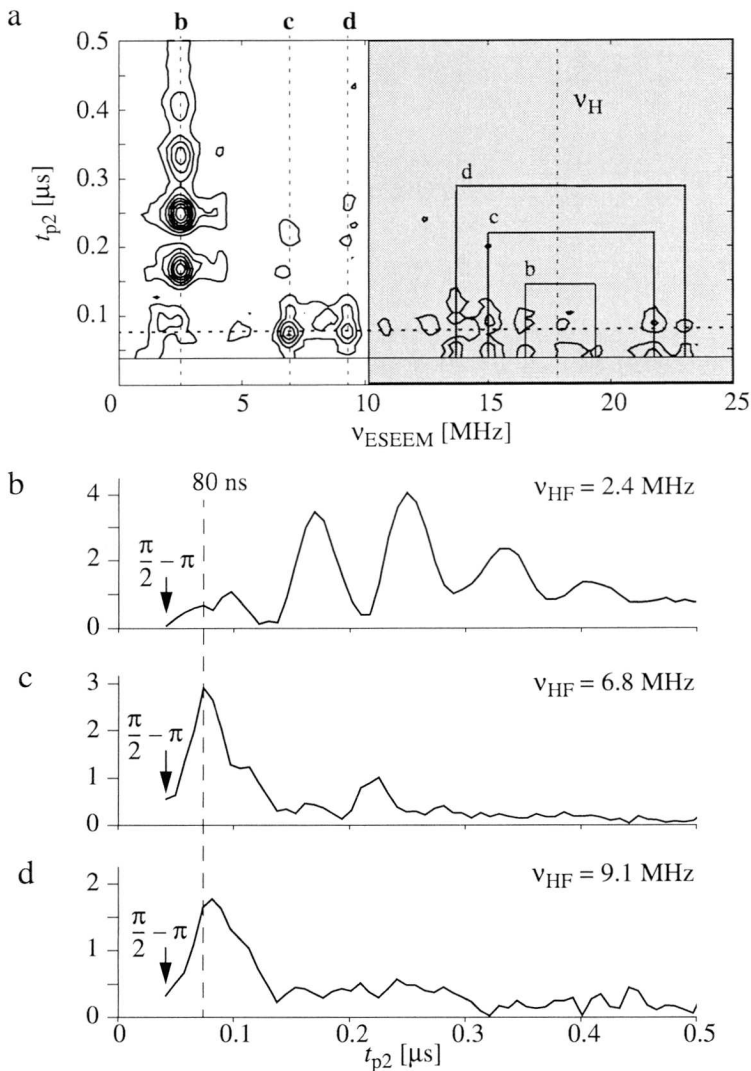


Fig. 5-4 Hyperfine-frequency enhanced ESEEM on the $[\text{VO}(\text{H}_2\text{O})_5]^{2+}$ complex in a single crystal of $\text{Mg}(\text{NH}_4)_2(\text{SO}_4)_2 \cdot 6 \text{H}_2\text{O}$. a) Contour plot of the dependence of the spectrum on the length of the second mw pulse. The shadowed part contains basic nuclear frequencies. b,c,d) Single traces for three hyperfine peaks showing the dependence of the peak intensity on the length t_{p2} of the second microwave pulse. The dashed line at 80 ns corresponds to a $\pi/2-\tau-2\pi$ standard sequence for hyperfine-frequency enhanced ESEEM.

a number of cases no visible gain was observed at all. Hence, matched ESEEM is most useful for the observation of ω_α , ω_β , and ω_{HF} .

6.1 Basics

6.1.1 Decoupling in solid-state ESR

Nuclear frequencies are determined by three significant interactions, namely the nuclear Zeeman interaction, the hyperfine coupling and the nuclear quadrupole coupling. The anisotropy of the latter two interactions is significant in our context. Furthermore, all interactions are of similar magnitude (see Fig. 2-1 on page 29) and either of them may be the dominant one, so that line assignment and evaluation of parameters are often difficult. Ambiguities can arise, since more than one parameter set may fit the observed frequencies. If two interactions are of the same order of magnitude (strong mixing situation), second order effects become large, additional lines can occur, and spectrum analysis requires simulations. Strong mixing situations can be overcome by going to higher magnetic fields, but this does not apply if the hyperfine coupling and the nuclear quadrupole coupling are of the same order of magnitude. In disordered systems, resolution is often not sufficient to find the correct parameter set even in the absence of strong mixing.

Low resolution and assignment difficulties can be remedied by eliminating or refocusing one or several interactions. Such methods are particularly useful if the resulting simplified spectrum can be correlated to the original spectrum in a 2D experiment. Refocusing techniques are discussed in §4.3 and in more detail in Chapter 7. For decou-

pling, it is of significance that the gyromagnetic ratios γ_i of the electron and nuclear spin differ by more than two orders of magnitude. Since the condition $\gamma_i B_{1i} \gg A$, B has to be fulfilled for complete decoupling, one immediately recognizes that decoupling the nuclear spins by irradiation on the electron spins is comparatively easy, while the opposite task is nearly impossible to accomplish, except for very small couplings.¹ The case of nuclear-nuclear decoupling is similar to NMR, since the bulk of the nuclei that contribute to dipolar broadening are matrix nuclei with weak hyperfine couplings, mostly protons. Their resonance frequency is close to the nuclear Zeeman frequency ω_i , so that ENDOR line widths of strongly coupled nuclei can be reduced by strong irradiation at ω_i [112].

For nuclear spins $I=1/2$ coupled to an electron spin $S=1/2$, hyperfine decoupling can be used to assign ESEEM or ENDOR lines to certain elements (isotopes) and to find out the elements and number of nuclei that contribute to ESEEM combination lines in the case of large modulation depths. For $I>1/2$, hyperfine decoupling enables one to separate the hyperfine and nuclear quadrupole interaction, and finally for $S>1/2$, it can aid line assignments and allows for conclusions on the electron spin states of the ESR observer transition.

The first experiment that observed nuclear frequencies during strong irradiation on the electron spins was proposed as an alternative to existing ESEEM methods [113]. It has been realized soon that this experiment leads to hyperfine decoupling [114]. The underlying theory and more sophisticated experiments are described in the rest of this Chapter.

6.1.2 Theory

Decoupling by strong mw fields cannot be described by the approach in §3.2.7, since condition (3.68) may be violated. Instead, we make use of the exact analytical solutions for the eigenvalues of the $S'=1/2, I=1/2$ system given in Appendix A. One can check easily that the nuclear frequencies for large ω_1 are given by $\omega_{12}^{\text{dec}} = \epsilon_1 - \epsilon_2$ and

1. Dipolar couplings contain the product of the two gyromagnetic ratios, $\gamma_e \gamma_n$, see Eq. (2.7).

$\omega_{34}^{\text{dec}} = \varepsilon_3 - \varepsilon_4$ with the ε_i given by Eq.(A.2a-d). The expressions can be expanded in a Taylor series and terms of higher than second order can be neglected. For the residual splitting between the two lines we find

$$A_{\text{res}} = \omega_{12}^{\text{dec}} - \omega_{34}^{\text{dec}} \approx \frac{A'\omega_I' + B'\omega_{I_x}'}{\sqrt{\omega_I'^2 + \omega_{I_x}'^2}} \frac{\Omega_S}{\omega_1}. \quad (6.1)$$

For an electron spin $S=1/2$ instead of a fictitious spin S' , the expression simplifies to $A\Omega_S/\omega_1$ [53]. The decoupled nuclear frequency is given by

$$\omega_{\text{dec}} = \left| \frac{\omega_{12}^{\text{dec}} + \omega_{34}^{\text{dec}}}{2} \right| = \sqrt{\omega_I'^2 + \omega_{I_x}'^2} + \frac{(A'\omega_{I_x}' - B'\omega_I')^2 (\omega_I'^2 + \omega_{I_x}'^2 - \Omega_S^2)}{8\omega_1^2 (\omega_I'^2 + \omega_{I_x}'^2)^{3/2}}, \quad (6.2)$$

the simplified expression for $S=1/2$ can be obtained by substituting ω_{I_x}' by zero. Only spin packets with $\Omega_S \ll \omega_1$ lead to narrow features in the spectrum, other spin packets contribute to broad feet of the lines. For the former spin packets, we can neglect the hyperfine splitting in the calculation of the *eigenstates* and treat the electron and nuclear spin separately. The Hamiltonian during decoupling is then given by

$$\mathcal{H}_{\text{dec}} = \Omega_S S_z + \omega_1 S_x + \omega_I' I_z + \omega_{I_x}' I_x, \quad (6.3)$$

and can be diagonalized by a unitary transformation $U_{\text{dec}} \mathcal{H}_{\text{dec}} U_{\text{dec}}^{-1}$ with

$$U_{\text{dec}} = \exp\{-i(\theta_{\text{dec}} S_y + \eta_{\text{dec}} I_y)\}, \quad (6.4a)$$

where

$$\theta_{\text{dec}} = \text{atan}\left(\frac{\omega_1}{\Omega_S}\right), \quad (6.4b)$$

and

$$\eta_{\text{dec}} = -\text{atan}\left(\frac{\omega_{I_x}'}{\omega_I'}\right). \quad (6.4c)$$

Note that ω_I' contains a contribution from the secular hyperfine coupling, see Eq. (3.24c), and that ω_{I_x}' is part of the pseudo-secular hyperfine coupling, see Eq. (3.24d). The term “hyperfine decoupling” is therefore in some sense a misnomer for electron

spins $S > 1/2$. In fact, strong irradiation on an S spin transition mixes the two states that are involved in this transition, and decoupling arises only for $1/2 \leftrightarrow -1/2$ transitions where the energy contribution by the coupling has equal amplitude and different sign in the two states. As we have done in Chapter 3, one can however define an *effective* nuclear Zeeman interaction and *effective* secular and pseudo-secular parts of the hyperfine interaction, so that a fictitious spin $1/2$ can be treated analogously to an electron spin $1/2$. One should be aware in such a treatment that the *effective* nuclear Zeeman interaction can be *anisotropic*.

For nuclear spins $I > 1/2$, the residual hyperfine splittings and second order shifts for the single transitions can be obtained in an analogous way as for $I = 1/2$, since a *strong* mw field does no longer mix different nuclear spin states. We can then apply a fictitious spin $1/2$ treatment also to the *nuclear* spins and obtain effective values ω_I'' , ω_{I_x}'' , ω_{I_y}'' , A'' , B_x'' , and B_y'' for the single transitions.¹ The residual hyperfine splitting and the decoupled nuclear frequency for this Hamiltonian are given in Appendix C. The derivation of the fictitious spin Hamiltonian involves a diagonalization of *only the quadrupole part* of the nuclear spin Hamiltonian (corresponding to a zero-field situation in nuclear quadrupole resonance, see [8]), so that analytical expressions for the frequencies during decoupling can be found for $I \leq 2$. Note however, that for the calculation of transition moments, a diagonalization of the complete nuclear Hamiltonian is needed, which can be performed analytically only for $I \leq 3/2$ (see §3.1.3).

6.2 Pulse sequences

6.2.1 Spin-locked ESEEM

The most simple sequence for the measurement of nuclear frequencies during strong mw irradiation is the spin-locked ESEEM sequence [113,114], see Fig. 6-1. The $\pi/2$ pulse creates EC which evolves during time τ and is partially transferred to NC in the eigenbasis of the Hamiltonian that describes strong mw irradiation. The NC evolves dur-

1. It is no longer possible to choose the x -axis along the projection of the effective hyperfine field onto the xy -plane if the nuclear quadrupole interaction does not have axial symmetry.

ing time T under decoupling conditions, and part of it is transferred to EC when the mw field is switched off. The EC refocusses during the second period of free evolution and forms an echo at time $T+2\tau$.

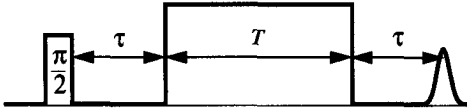


Fig. 6-1 Pulse sequence for spin-locked ESEEM.

The 2D version of the experiment can be performed by incrementing τ and T ; it correlates the two-pulse ESEEM spectrum to the decoupled ESEEM spectrum. For simplicity, we assume an $S=1/2$, $I=1/2$ system for the calculation of an analytical formula. For the echo modulation $E_M(\tau, T)$ we find

$$\begin{aligned}
 E_M(\tau, T) = C_d \left\{ k \left[\frac{\omega_{34}^{(0)} + \omega_{34}}{2\omega_I} \cos(\omega_{12}\tau + \omega_I T) + \frac{\omega_{34}^{(0)} - \omega_{34}}{2\omega_I} \cos(\omega_{12}\tau - \omega_I T) \right. \right. \\
 \left. \left. + \frac{\omega_{12}^{(0)} + \omega_{12}}{2\omega_I} \cos(\omega_{34}\tau + \omega_I T) + \frac{\omega_{12}^{(0)} - \omega_{12}}{2\omega_I} \cos(\omega_{34}\tau - \omega_I T) \right] \right. \\
 + \cos^2 \eta \left[\frac{(\omega_{12}^{(0)} + \omega_{12})(\omega_{34}^{(0)} - \omega_{34})}{4\omega_{12}\omega_{34}} \cos(\omega_{HF}\tau + \omega_I T) \right. \\
 \left. + \frac{(\omega_{12}^{(0)} - \omega_{12})(\omega_{34}^{(0)} + \omega_{34})}{4\omega_{12}\omega_{34}} \cos(\omega_{HF}\tau - \omega_I T) \right] \quad (6.5) \\
 \left. + \sin^2 \eta \left[\frac{(\omega_{12}^{(0)} + \omega_{12})(\omega_{34}^{(0)} + \omega_{34})}{4\omega_{12}\omega_{34}} \cos(\omega_{SC}\tau + \omega_I T) \right. \right. \\
 \left. \left. + \frac{(\omega_{12}^{(0)} - \omega_{12})(\omega_{34}^{(0)} - \omega_{34})}{4\omega_{12}\omega_{34}} \cos(\omega_{SC}\tau - \omega_I T) \right] \right\},
 \end{aligned}$$

with

$$\omega_{12}^{(0)} = \omega_I + A/2, \quad (6.6a)$$

$$\omega_{34}^{(0)} = \omega_I - A/2, \quad (6.6b)$$

where C_d is a constant that depends on ω_1 and on the lineshape function $G(\Omega_S)$ of the ESR line,

$$C_d = -\frac{1}{16} \int \sin^2 \theta_{\text{dec}} \cos^2(\Omega_S \tau) G(\Omega_S) d\Omega_S. \quad (6.7)$$

Note that we have made the assumption of complete decoupling for *all* spin packets which may not be fulfilled in many practical cases. Therefore, Eq. (6.5) should be considered as a description that allows for a qualitative understanding of the experiment rather than as the basis for the analysis of experimental data. Nevertheless, we can conclude that cross peaks between the basic nuclear frequencies and the nuclear Zeeman splitting on the one side and the decoupled nuclear frequency on the other side are stronger in the first quadrant than in the second quadrant ($\omega_{\alpha, \beta}^{(0)} + \omega_{\alpha, \beta} \gg \omega_{\alpha, \beta}^{(0)} - \omega_{\alpha, \beta}$), while cross peaks between the hyperfine splitting and the decoupled nuclear frequency have similar intensity in both quadrants.

The large number of cross peaks and the comparatively fast decay of the EC during the two free evolution periods lead to poor resolution in this experiment, in particular for disordered systems. On the other hand, the experiment is free of blind spots, has a small inherent dead time (see §5.1.1), and only one mw channel is needed. The pulse sequence can also be employed for a 1D experiment by using a fixed delay τ and incrementing T . In this case, the intensity of the peaks depends on the choice of τ . However, numerical simulations show that there are no blind spots.

6.2.2 DECENT

The resolution problems in spin-locked ESEEM can be overcome if the decoupled spectrum is correlated with the three-pulse ESEEM spectrum instead of the two-pulse ESEEM spectrum, see Fig. 6-2.

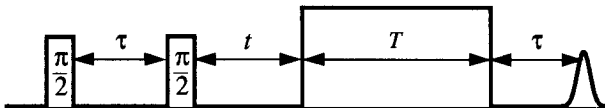


Fig. 6-2 Pulse sequence for the DECENT experiment.

In the DECENT (decoupled ESEEM correlated to nuclear transition frequencies) experiment, NC is created by the Mims-generator (see §4.1.2), evolves for time t , a part of it remains NC during the decoupling pulse of duration T and is transferred to EC when the mw is switched off. The experiment leads to the same blind spots with respect to the nuclear frequencies as three-pulse ESEEM. The four-step phase cycle $[0,0]-[\pi,0]-[0,\pi]-[\pi,\pi]$ can be applied to the first two mw pulses to eliminate interference by echo crossings.

A complete formula for the echo modulation in dependence on the times t and T becomes rather extensive and few insight can be gained from it. The only significant difference to three-pulse ESEEM is the requirement that NC exists during the decoupling pulse, which leads to an additional factor $\sin\theta_{\text{dec}}\cos\theta_{\text{dec}}$ in the modulation amplitude. This means that on-resonant spin packets do not contribute to the signal, since $\cos\theta_{\text{dec}}=0$ for $\Omega_S=0$.¹ Accordingly, the peaks should be broader in the decoupled dimension than in spin-locked ESEEM, where the completely decoupled on-resonant spin packets contribute and where off-resonant spin packets are more strongly suppressed by the factor $\sin^2\theta_{\text{dec}}$. In practice, we found that this is of no particular importance in 2D experiments, since for ordered systems the linewidth is determined by the size of the data matrix that can be sampled in a reasonable measurement time and by the maximum length of the time increment (i.e., by the Nyquist frequency), and for disordered systems by the anisotropy of the nuclear quadrupole interaction. Cross peaks in DECENT correlate ω_{dec} with ω_α and ω_β , they appear in the first quadrant in the weak coupling case and in the second quadrant in the strong coupling case.

6.2.3 Hyperfine-decoupled ENDOR

In cases where the transition probability of the forbidden transitions is small, hyperfine-decoupled ENDOR is needed. The most simple pulse sequence can be based on the ENDOR effect imposed on the spin-locked echo, see Fig. 6-3a. In this sequence, allowed

1. Note also that the Mims-generator does not create NC for $\Omega_S=0$, see Eq. (4.3). Nevertheless, the factor $\cos\theta_{\text{dec}}$ is significant, since one can replace the Mims-generator by another NC generator.

EC is created by the $\pi/2$ pulse and evolves with frequency ω_{13} (ω_{24}), if the nuclear spin is in its α state (β state). When the mw field along x is turned on at time τ , the part of the EC in this direction is spin-locked. If the rf irradiation is on-resonant with the nuclear spin, an rf π pulse interchanges the α and β states of the nuclear spin. In the free evolution period following the decoupling pulse, the EC evolves now with ω_{24} (ω_{13}) and does no longer refocus.

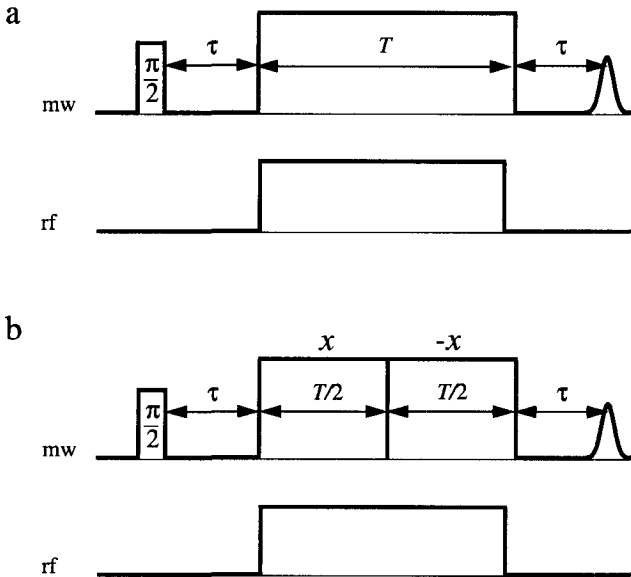


Fig. 6-3 Pulse sequences for hyperfine-decoupled ENDOR. a) Spin-locked ENDOR. b) PEANUT-ENDOR.

For a quantitative description, we restrict ourselves to a two-spin system with purely isotropic hyperfine coupling. The unperturbed Hamiltonian is given by

$$\mathcal{H}_{\text{iso}} = \Omega_S S_z + a S_z I_z + \omega_I I_z, \quad (6.8)$$

and we obtain for the echo signal (along the y -axis) in the absence of rf irradiation

$$E_0 = -\sin \theta_{\text{dec}} \left[\cos^2 \left(\frac{a\tau}{2} \right) \sin^2 (\Omega_S \tau) + \sin^2 \left(\frac{a\tau}{2} \right) \cos^2 (\Omega_S \tau) \right], \quad (6.9a)$$

while we have for on-resonant rf irradiation

$$E_{\text{rf}} = -\sin\theta_{\text{dec}} \left[\cos^2\left(\frac{a\tau}{2}\right) \sin^2(\Omega_S\tau) - \sin^2\left(\frac{a\tau}{2}\right) \cos^2(\Omega_S\tau) \right]. \quad (6.9b)$$

Obviously, the ENDOR effect vanishes for $\tau = \frac{k\pi}{a}$, which is a *similar* blind spot behaviour as observed in Mims-ENDOR, see Eq. (4.8). In practice, the echo is cancelled by the ENDOR effect for any τ if the rf is on-resonant with ω_I , since there are usually matrix nuclei with a broad distribution of a values. However, the blind spot behaviour can play a role if $I > 1/2$ or $S > 1/2$.

A disadvantage of spin-locked ENDOR is that only the spin-locked magnetization is used. There is also EC that nutates during time T and defocusses comparatively fast because of a broad distribution of the nutation frequencies. This magnetization can be observed in an echo-detected rotary echo, where it is refocussed by an inversion of the mw field direction in the middle of the decoupling pulse, see Fig. 6-3b. Since the mw field direction in the middle of the decoupling pulse, see Fig. 6-3b. Since the mw part of this pulse sequence is the PEANUT sequence (see Chapter 9), we refer to the experiment as PEANUT-ENDOR. This experiment allows one to gain a factor of two in signal intensity in favourable cases.

Up to now we have not considered the interaction of the rf field with the *electron* spins. The Bloch-Siegert shift can be neglected, since it does not influence the behaviour of spin-locked magnetization and is refocussed for nutating magnetization in the PEANUT sequence. One has to be aware however, that the transition frequencies of the electron spins in the presence of a strong mw field are in the radio frequency region. This can be rationalized by calculating level energies for the rotating frame Hamiltonian (interaction representation) or considering the electron spins as being dressed by the mw field (dressed states picture). The frequencies for the allowed and forbidden electron spin transitions¹ become [114],

$$\omega_a = \omega_{1,\text{eff}} = \sqrt{\omega_I^2 + \Omega_S^2}, \quad (6.10a)$$

$$\omega_f = \omega_{1,\text{eff}} \pm \omega_I. \quad (6.10b)$$

1. In the presence of mw *and* rf irradiation, all transitions in the system are actually allowed.

Therefore, to avoid detection of the peaks due to electron spin transitions in the ENDOR spectrum, the condition

$$\omega_1 > \omega_{\max} + |\omega_j| + w_{\text{nut}} , \quad (6.11)$$

must be fulfilled, where ω_{\max} is the maximum frequency of the ENDOR spectrum and w_{nut} is the width of the nutation lines in angular frequency units. Note that the nutation frequency can be observed in spin-locked ENDOR in spite of the fact that nutating magnetization does not contribute to the echo.

6.3 Experimental examples

6.3.1 Nuclear spin $I=1$ in an ordered system

In a number of metalloproteins, information on weakly coupled nitrogen nuclei is needed for structure determination. Such nitrogen nuclei often belong to histidines in the protein backbone or to a substituted porphyrine. At X-band frequencies, all three interactions of the nuclear spin are of the same order of magnitude, and irrespective of the ESR frequency there is strong mixing of hyperfine and nuclear quadrupole interactions. Hyperfine decoupling is a promising method for the simplification of the resulting spectra.

The principle of the DECENT experiment is first demonstrated for the organic radical that is formed by γ -irradiation (10 kGy) of dichloroacetamide at ambient temperature. The radical decays with a time constant of a few hours at ambient temperature and is virtually stable at liquid nitrogen temperature. Its structure as inferred from ESR measurements [115] is shown in the inset in Fig. 6-4a. The experiments were performed at a Bruker ESP 380 spectrometer with an EN 4118 probe head at a temperature of 80 K, $\nu_{\text{mw}} = 9.7411$ GHz, and $B_0 = 343.4$ mT. The phase cycle $[0,0]-[\pi,0]-[0,\pi]-[\pi,\pi]$ was applied to the first two mw pulses in all experiments.

The three-pulse ESEEM spectrum (see Fig. 6-4a) consists of nitrogen peaks in the region between 0 and 6 MHz and weak proton peaks around 15 MHz (not shown). It is dominated by the peak at twice the nitrogen Larmor frequency of 1.057 MHz ($\Delta m_f = 2$

transition) as it is characteristic for a strong mixing situation. No chlorine peaks are observed because of the strong hyperfine coupling of $A_{\text{Cl}} \approx 38$ MHz.

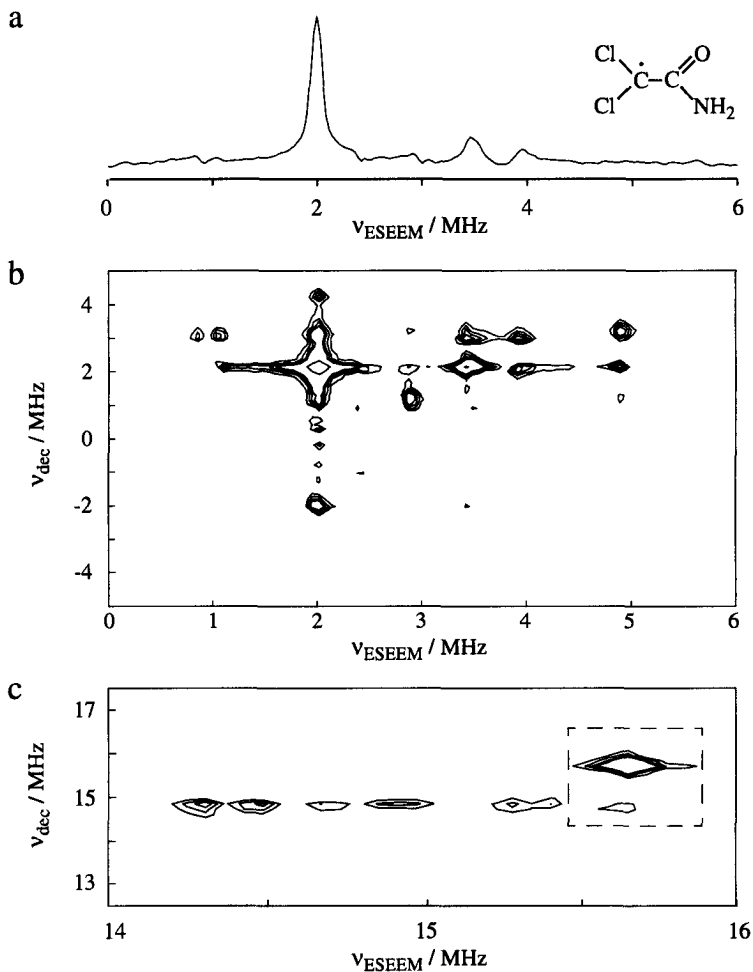


Fig. 6-4 Decoupled ESEEM of the radical produced by γ -irradiation of a dichloroacetamide single crystal (the elongated axis of the crystal is approximately perpendicular to the external field). a) Three-pulse ESEEM spectrum. The inset shows the structure of the radical. b) Contour plot of the nitrogen region of the DECENT spectrum. c) Contour plot of the proton region of the DECENT spectrum. The peaks in the dashed box are spurious peaks introduced by the spectrometer.

The DECENT spectrum ($t_{\pi/2}=8$ ns, $\tau=152$ ns, $t_0=400$ ns, $T_0=8$ ns, $\Delta t=16$ ns, $\Delta T=8$ ns, 1024×1024 data points) is also dominated by the peak at $(2|\omega_{\text{N}}|, 2|\omega_{\text{N}}|)$, but a number of cross peaks can be observed in addition (see Fig. 6-4b). Besides the peak at $2\omega_{\text{N}}$, six nitrogen frequencies are found in the ESEEM dimension while only three frequencies occur in the decoupled dimension. The decoupled spectrum is centered at 2.14 MHz and the splitting between the two outer frequencies is 2 MHz, i.e., close to $2\omega_{\text{N}}$. If we assume that the nuclear quadrupole tensor has axial symmetry, this suggests that $P \approx 1.33$ and that the nuclear quadrupole tensor is nearly coaxial with the external magnetic field in the chosen orientation. The number of peaks in the ESEEM dimension indicates that a small deviation from this special orientation causes the two sites in the crystal to be slightly inequivalent.

The proton region of the spectrum reveals six ESEEM frequencies that are all correlated with the proton Larmor frequency (14.62 MHz) in the decoupled dimension. The two larger couplings have the same order of magnitude as the nitrogen couplings, which is in agreement with a result in [115]. The smallest coupling may be due to intermolecular hyperfine interactions (matrix protons). A more detailed analysis of the data would require the measurement of the spectrum at different crystal orientations.

6.3.2 Nuclear spin $I=1$ in a disordered system

In many cases, metalloproteins cannot be obtained as single crystals of a sufficient size for ESR experiments, so that the measurements have to be performed with frozen solutions. As a model compound for such proteins with histidine ligands of the metal center, we have used 1% of the copper(II)tetraimidazol complex in a water-glycerol solution (equal volumes). The ESEEM spectra of this compound have been studied in a seminal paper by Mims and Peisach [116], the HFI of the remote nitrogens is largely isotropic.¹ The analogous complex with 2-methylimidazole as the ligand has been used as a model compound for the copper binding site in phenylalanine hydroxylase from *Chromobacterium violaceum* [117]. Our measurements were performed at a Bruker ESP 380 spectrometer with an EN 4118 probe head at a temperature of 14 K, $\nu_{\text{mw}}=9.707$

1. The directly coordinated nitrogens do not give rise to ESEEM signals.

GHz, and $B_0 = 339.2$ mT (corresponding to g_{\perp}). The other parameters in the DECENT experiment were $t_{\pi/2} = 8$ ns, $\tau = 136$ ns, $t_0 = 112$ ns, $T_0 = 16$ ns, $\Delta t = 16$ ns, $\Delta T = 8$ ns, and 1024×512 data points. The phase cycle $[0,0] - [\pi,0] - [0,\pi] - [\pi,\pi]$ was applied to the first two mw pulses in all experiments.

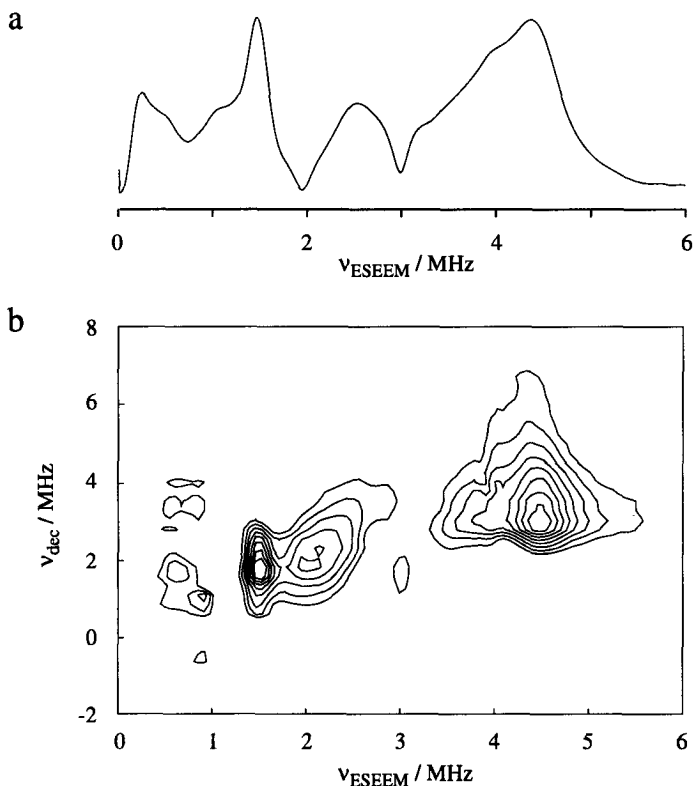


Fig. 6-5 Hyperfine decoupling for copper(II) tetraimidazol in frozen solution (mixture of equal volumes of water and glycerol). Only the nitrogen region of the spectra is shown. a) Three-pulse ESEEM spectrum. b) DECENT spectrum.

The nitrogen region of the ESEEM magnitude spectrum shown in Fig. 6-5a features a number of broad and only weakly structured peaks. In particular, it may be suspected that the “holes” at 0.6-0.9, at about 2, and at about 3 MHz are actually peaks with a phase that is different from the one of the broad background. This is confirmed by the DECENT spectrum shown in Fig. 6-5b, which features cross peaks at these ESEEM fre-

quencies. In addition, one may conclude that the sharp cross peaks at (0.92, 1.6) and at (1.53, 1.8) MHz belong to the β manifold which is closer to exact cancellation and the broad cross peaks at (2.02, 1.8) and (4.46, 3.1) MHz belong to the α manifold of the electron spin. These results are in agreement with the level scheme in Fig. 9 and the simulated ENDOR spectrum in Fig. 10 of [116]. The weak additional cross peaks at (0.61, 1.8) and (2.99, 1.8) MHz are most probably combination peaks that arise from the presence of several imidazole ligands ($0.61 = 1.53 - 0.92$, $2.99 \approx 2 \times 1.53$).¹ Similarly, the feature at about (0.7, 3.3) MHz may be a broad combination cross peak from the α manifold. The cross peak at (1.53, 1.8) MHz is broader in the decoupled dimension than in the ESEEM dimension since the decoupling prevents cancellation of the nuclear Zeeman and hyperfine field in the β manifold, so that one does no longer observe the zero-field nuclear quadrupole frequencies and ν_0 and ν_+ become different.

6.3.3 Electron spin $S > 1/2$

For electron spins $S > 1/2$, line assignment becomes complicated in ENDOR and ESEEM spectra whenever the ESR observer transition is not an $m_S = -1/2 \leftrightarrow 1/2$ transition. The reason for this is the contribution of the hyperfine coupling to the effective nuclear Zeeman frequency which leads to a first order shift of the multiplet centers away from the Larmor frequency of the nucleus. On the other hand, this shift enhances resolution for small couplings, since the corresponding multiplets no longer overlap. With respect to this it is of particular interest that the *sign of the hyperfine coupling* determines the sign of the first order shift, so that even signals of very weakly coupled nuclei may be resolved if their couplings differ in sign. Furthermore, if the peaks can be assigned to a particular isotope so that the Larmor frequency is known, the shift can also be used to determine the relative sign of the hyperfine coupling with respect to the zero-field splitting. Since the absolute sign of the latter interaction is often known, one can thus determine signs of hyperfine couplings in contrast to the case where the ESR observer transition is an $m_S = -1/2 \leftrightarrow 1/2$ transition.

1. The resolution in the two dimensions is 0.06 resp. 0.24 MHz/point.

In principle, line assignment in such cases can be done by HYSORE spectroscopy or by two-dimensional Mims-ENDOR [118]. However, both methods run into problems if small splittings are concerned. In HYSORE spectroscopy, peaks corresponding to small splittings are very close to the artefact peaks on the diagonal. The use of a hyperfine dimension (see §4.3.1) may not solve this problem if splittings of less than about 0.5 MHz are concerned, since these may be masked by baseline imperfections of the time domain data in the hyperfine dimension. Two-dimensional Mims-ENDOR uses the blind spot behaviour of the nuclear polarization generator (see §4.1.4) to introduce a second spectral dimension by incrementing the interpulse delay τ . Since EC evolves during time τ , the resolution in the second dimension is limited by T_m , so that it is usually too low to resolve small hyperfine couplings. In addition, the second dimension is also a hyperfine dimension and the baseline correction problem becomes even more serious in this case, since a decay of the unmodulated part of the stimulated echo is superimposed on the signal. Hyperfine decoupling techniques solve this resolution problem. They feature the additional advantages discussed above, if nuclear spins $I > 1/2$ are coupled to the electron spin.

We demonstrate hyperfine decoupling for an $S > 1/2$ case on the complex $[\text{Mn}(\text{H}_2\text{O})_6]^{2+}$ in a single crystal of $\text{La}_2\text{Mg}_3(\text{NO}_3)_{12} \cdot 24 \text{H}_2\text{O}$ doped with 1% Mn(II). In this double nitrate there are two Mn-sites with different symmetry. Site I features trigonal and inversion symmetry and has been investigated in [119], while site II features only trigonal symmetry.¹ Our measurements were performed at a Bruker ESP 380 spectrometer with an EN 4118 probe head and a DICE ENDOR system at a temperature of 15 K, $\nu_{\text{mw}} = 9.721$ GHz, and $B_0 = 408.0$ mT. This field setting corresponds to an ESR observer transition with $|m_S| = 3/2 \leftrightarrow 5/2$, where only one site contributes to the signal. This assignment can be verified by the experimental results (see below). The other parameters for the DECENT experiment were $t_{\text{pw}2} = 8$ ns, $\tau = 96$ ns, $t_0 = 304$ ns, $T_0 = 16$ ns, $\Delta t = 8$ ns, $\Delta T = 8$ ns, and 1024×1024 data points. The phase cycle $[0,0] - [\pi,0] - [0,\pi] - [\pi,\pi]$ was applied to the first two mw pulses in the three-pulse ESEEM and in the DECENT experiment. In spin-locked ENDOR, a decoupling pulse of 7 μs and an rf pulse of 5 μs duration were

1. Mn^{2+} substitutes for Mg^{2+} ; the crystal structure of the isomorphous salt $\text{Ce}_2\text{Mg}_3(\text{NO}_3)_{12} \cdot 24 \text{H}_2\text{O}$ has been determined by X-ray diffraction [120].

used, the interpulse delay τ was also 96 ns and $t_{\pi/2} = 8$ ns, the rf increment was 20 kHz. The full mw power of the spectrometer was used for the decoupling pulses in DECENT and spin-locked ENDOR, while the $\pi/2$ pulse of 8 ns duration corresponded to an attenuation of 13 dB.

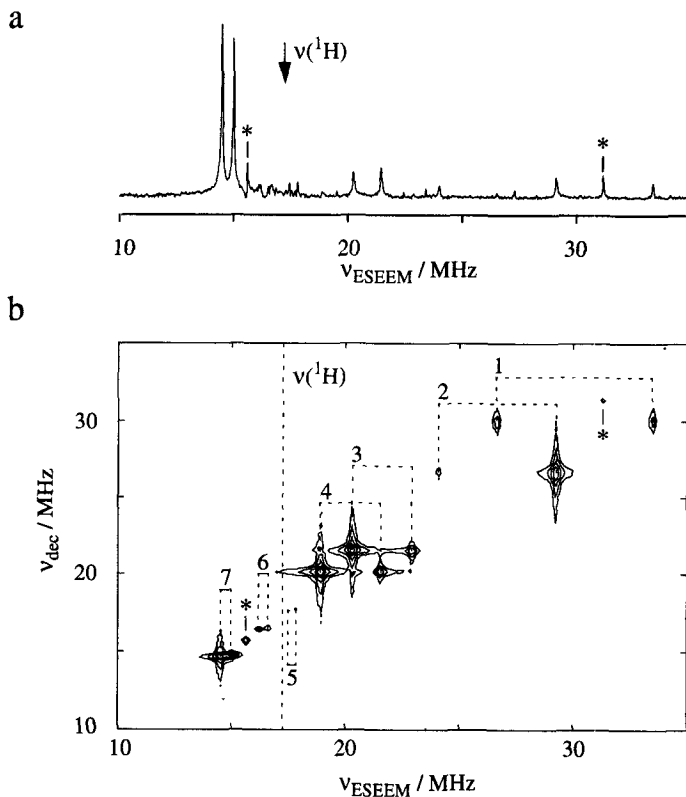


Fig. 6-6 Hyperfine decoupling of the complex $[\text{Mn}(\text{H}_2\text{O})_6]^{2+}$ in a Mn(II)-doped single crystal of $\text{La}_2\text{Mg}_3(\text{NO}_3)_{12} \cdot 24 \text{H}_2\text{O}$. The peaks labelled with an asterisk are spurious frequencies introduced by the spectrometer. a) Three-pulse ESEEM spectrum. b) Contour plot of the DECENT spectrum (logarithmic levels).

The assignment problems involved in ESEEM for $S > 1/2$ nuclei become apparent in Fig. 6-6a. Note that it is usually not possible to use peak intensities as an aid to the assignment, since the blind spot behaviour may lead to strongly different intensities for the peaks belonging to the same multiplet. On the other hand, the hyperfine splittings and

center frequencies of the doublets can be easily inferred from the DECENT spectrum shown in Fig. 6-6b. Together with the spin-locked ENDOR results they are summarized in Tab. 6-1.

Table 6-1 Proton hyperfine splittings ν_{HF} and multiplet center frequencies ν_c for the complex $[\text{Mn}(\text{H}_2\text{O})_6]^{2+}$ in a Mn(II)-doped single crystal of $\text{La}_2\text{Mg}_3(\text{NO}_3)_{12} \cdot 24 \text{H}_2\text{O}$.

#	ν_{HF} /MHz	ν_c /MHz	$\frac{\nu_c - \nu(^1\text{H})}{\nu_{\text{HF}}}$
1	6.86	29.98	1.8
2	5.14	26.54	1.8
3	2.64	21.48	1.6
4	2.60	20.08	1.0
5 ^a	0.37	17.72	0.94
6	0.44	16.40	-2.2
7	0.49	14.62	-5.6
8 ^b	0.98	15.40	-2.0
9 ^b	2.78	11.82	-2.0

a. Observed only with the DECENT experiment.

b. Observed only with spin-locked ENDOR.

The magnitude of the quantity $\Delta M = [\nu_c - \nu(^1\text{H})]/\nu_{\text{HF}}$ given in Tab. 6-1 characterizes the ESR observer transition, and its sign is the relative sign of the hyperfine coupling with respect to the zero-field splitting. As a first order approximation, we find

$$\Delta M \approx \text{sgn}(A)(m_S^{(-)} + 1/2), \quad (6.12)$$

where $m_S^{(-)}$ is the magnetic quantum number of the electron spin in the lower state of the ESR observer transition, so that we expect $|\Delta M| \approx 2$ in the case at hand. The deviations for the protons #4, #5, and #7 in Tab. 6-1 are most probably due to the pseudo-secular part of the hyperfine interaction. The fact that $|\Delta M| < 2$ for the transitions where the secular part of the hyperfine interaction dominates, can be explained by a mixing of electron

spin states by the zero-field splitting. The results indicate that our observer transition is (approximately) $m_S = -3/2 \leftrightarrow -5/2$ and not $m_S = 3/2 \leftrightarrow 5/2$, since the isotropic part of the HFI is positive for water protons and the possibly negative dipolar part cannot have a magnitude large enough as to provide $A/(2\pi) \approx -6.85$ MHz for proton #1. ¹ On the other hand, we could determine the exact states of the observer transition from the known ESR parameters of the paramagnetic center [119] and hence the precise magnitude and absolute sign of A , if we would use a known orientation of the crystal.

While spin-locked ENDOR has low sensitivity if the frequencies during hyperfine decoupling become lower than about 2 MHz and strong mixing situations are encountered, we expect a high sensitivity in cases like the present one. This is confirmed by the spin-locked ENDOR spectrum shown in Fig. 6-7 together with a Mims-ENDOR spectrum. The assignment of the peaks becomes straightforward if both these spectra are known, since the decoupled frequency is to a very good approximation the center frequency of the corresponding doublet. Therefore, it is not necessary in this case to acquire a 2D spectrum. The total measurement time for the two spectra shown in Fig. 6-7 is by a factor 20 smaller than the one needed for the DECENT spectrum shown in Fig. 6-6b. It seems to be feasible to apply spin-locked ENDOR routinely during a crystal rotation, while DECENT may be restricted to checks at a few selected orientations. In the spin-locked ENDOR spectrum, two additional protons (#8 and #9) are detected that probably escape detection in DECENT because of a small modulation depth and/or blind spots. On the other hand, the weakly coupled proton #5 cannot be detected in the ENDOR spectra.

Because of the trigonal symmetry of Mn^{2+} at site II, there are only two non-equivalent water ligands. Since the proton positions in each of the ligands are again non-equivalent, ² we expect four *geometrically* non-equivalent protons. However, an external magnetic field introduces a symmetry breaking so that all twelve protons can be *magnetically*

1. This would imply $A_{\parallel}/(2\pi) \geq 13.7$ MHz in contrast to expectations from the internuclear distance and to earlier results for the $[Mn(H_2O)_6]^{2+}$ complex in frozen solutions [121].
2. The hydrogen positions are determined within 20 pm by X-ray diffraction at ambient temperature [120].

non-equivalent in a measurement at a particular orientation. The occurrence of only nine signals could be explained if one assumes that in three of the six water molecules the two hydrogen atoms become equivalent through a dynamic process. To substantiate this assumption, measurements at different orientations would be necessary.

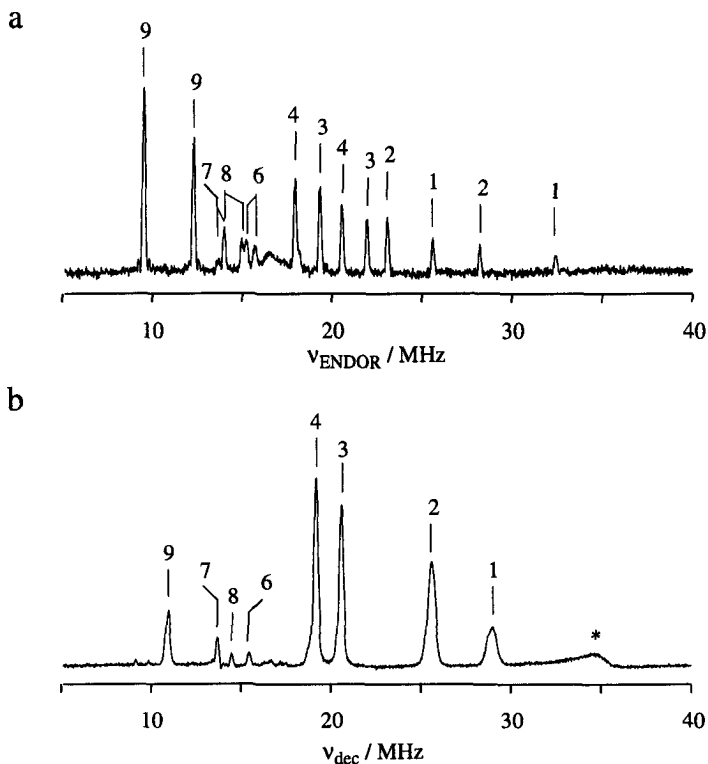


Fig. 6-7 ENDOR spectra of the complex $[\text{Mn}(\text{H}_2\text{O})_6]^{2+}$ in a Mn(II)-doped single crystal of $\text{La}_2\text{Mg}_3(\text{NO}_3)_{12} \cdot 24 \text{H}_2\text{O}$. The orientation is the same as for the spectra shown in Fig. 6-6. a) Mims-ENDOR spectrum. b) Spin-locked ENDOR spectrum featuring hyperfine decoupling. The peak designated with an asterisk is due to excitation of electron spin transitions.

Note also that the Mims-ENDOR intensity decreases as the ENDOR frequency increases (see Fig. 6-7a). This is a consequence of the nearly linear decrease of the rf field with frequency in the Bruker ENDOR system. For $m_S = -1/2 \leftrightarrow 1/2$ transitions, this linear decrease is roughly compensated by the hyperfine enhancement (see §3.2.8), while this is no longer true in the case at hand.

Hyperfine spectroscopy

7.1 Basics

7.1.1 General approach

Hyperfine couplings provide valuable structure information, since the isotropic part characterizes the spin density of the unpaired electron in the s -orbital of a given nucleus and the anisotropic part the dipole-dipole interactions between the electron and nuclear spin.¹ To obtain this information, it is necessary to extract the hyperfine couplings from spectra that depend also on the nuclear Zeeman and nuclear quadrupole interaction. This process may be cumbersome even for ordered systems and may fail altogether for disordered systems because of insufficient resolution. For these reasons, spectroscopic methods are required for the separation of the hyperfine coupling from the other interactions.

The general approach to this task can be derived from considerations on first order frequencies. The hyperfine coupling term is unique, since it is the only first order contribution that depends on m_I in ESR spectra and the only first order contribution that depends on m_S in nuclear spectra. A change of m_I (m_S) by unity, which can be achieved by an rf (mw) π pulse, thus changes the frequency in the ESR (nuclear frequency) spectrum by the hyperfine splitting. Such a π pulse combined with a method to measure fre-

1. The anisotropic part may include spin density in other orbitals of a given nucleus. On the other hand, if the point-dipole approximation is valid, the anisotropic part depends only on the distance between the electron spin and the nucleus and on the angle between the external magnetic field and electron-nuclear axis, see Eq. (2.7).

quency differences can then be used to obtain spectra that contain only peaks at the hyperfine frequencies ω_{HF} . We designate this spectroscopic method as hyperfine spectroscopy. A hyperfine spectroscopy experiment that uses rf π pulses to shift a spectral hole by the hyperfine frequency and measures the frequency difference *via* an FID has been proposed earlier [68,122]. With monochromatic π pulses this method is inherently two-dimensional, since the rf must be swept. In addition, artefacts that arise from forbidden transitions cannot be eliminated in EC-based methods, and the resolution is significantly worse than in NC-based methods. In the following, we therefore restrict ourselves to experiments that use mw π pulses for the transfer of NC and measure the difference frequencies of nuclear transitions.

One of the advantages of hyperfine spectroscopy is a reduction of the number of spectral lines. For a system consisting of an electron spin S and n nuclear spins I_i , the number of spectral lines in an ESR spectrum is given by

$$N_{\text{ESR}} = 2S \prod_{i=1}^n (2I_i + 1) . \quad (7.1)$$

In ESEEM and ENDOR methods, the number of lines reduces to

$$N_{\text{ENDOR}} = 2(2S + 1) \sum_{i=1}^n I_i , \quad (7.2)$$

since nuclear-nuclear interactions are not resolved. Eq. (7.2) is still true if we consider n groups of equivalent nuclear spins, while the multiplicity in ESR increases if equivalent nuclei are added. Together with the smaller linewidth, this tremendous reduction leads to a resolution improvement by about two or even three orders of magnitude in going from ESR to ENDOR spectra. It is a result of the topology of the spin system as shown in Fig. 3-1 on page 41. If the electron spin transitions in the absence of hyperfine interactions are well resolved and a fictitious spin description is possible, the number of ENDOR lines reduces by another factor $(2S+1)/2$. In hyperfine spectroscopy, we have

$$N_{\text{HS}} = n , \quad (7.3)$$

irrespective of the question if one or several transitions of the electron spin are on-resonant and act as observer transitions. Eq. (7.3) is also valid for n groups of equivalent

nuclear spins. Since the linewidth is twice as large in hyperfine spectroscopy as compared to ENDOR or ESEEM spectroscopy, this reduction of the number of lines translates into improved resolution, if there are nuclei with $I > 1/2$ or if more than one transition of the same electron spin is on-resonant.

The simplification of the parameter extraction and reduction of the line number in hyperfine spectroscopy are achieved at the expense of a loss of information on the nuclear Zeeman and quadrupole interaction. This information can be reintroduced in 2D methods that correlate the hyperfine spectrum to the ESEEM or ENDOR spectrum. 2D experiments can actually be easier to perform, since requirements on broad band excitation and artefact suppression are not as stringent as in 1D methods. In principle, 2D hyperfine spectroscopy provides the same information as HYSORE-type experiments; however, it may be advantageous with respect to resolution for a given size of the data matrix and with respect to artefact suppression (see §4.3.1, [91]).

7.1.2 Second order effects

The considerations in §7.1.1 are strictly valid only in the absence of any second order effects. Such effects can introduce additional splittings of hyperfine lines, and the mw π pulse can then induce forbidden transfers which in turn introduce artefact peaks into the spectra. As long as second order effects are small, the advantages of hyperfine spectroscopy are retained, since the additional splittings are small and the artefacts are weak and can at least partially be suppressed. On the other hand, strong mixing situations may require hyperfine decoupling for spectrum simplification, the hyperfine coupling can then be obtained by fitting 2D DECENT spectra (see §6.2.2) after the nuclear Zeeman and nuclear quadrupole interaction have been determined from the decoupled spectrum.

The first kind of second order effects arises from the pseudo-secular part of the hyperfine interaction. For simplicity, we restrict our discussion to a system consisting of a fictitious spin $S = 1/2$ and a nuclear spin $I = 1/2$. Analytical expressions for ω_{HF} and ω_{NZ} in situations where the second order effects are small have been derived in Chapter 4 (see Eq. (4.18a,b)). The pseudo-secular hyperfine term introduces no splitting but only a shift of the hyperfine frequency that is negative in the weak coupling case and positive in the strong coupling case. Since the shift depends on the observer transition, line broadening

or splitting arises if the mw is on-resonance with more than one transition of the same electron spin.

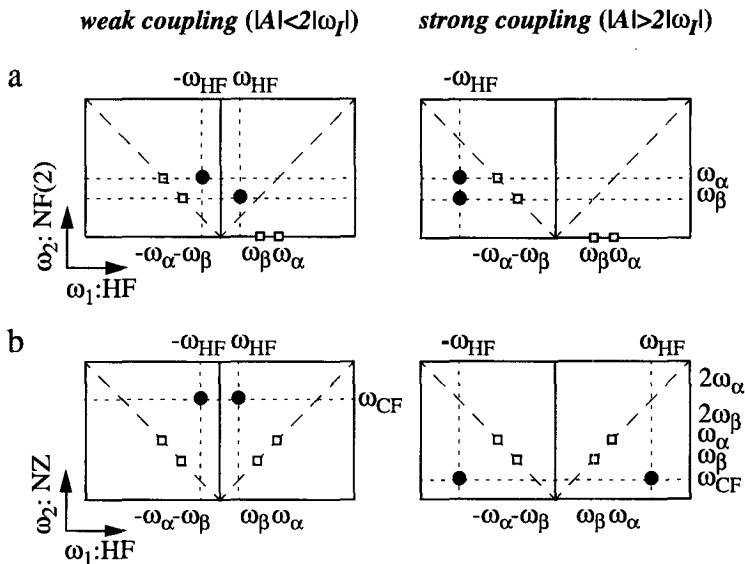


Fig. 7-1 Location of cross peaks (filled circles) and artefacts (hollow squares) in 2D hyperfine spectroscopy. a) Nuclear-frequency correlated hyperfine spectroscopy. b) Nuclear-Zeeman-splitting correlated hyperfine spectroscopy.

Furthermore, the mw π pulse can transfer NC to nuclear polarization and polarization to NC in the presence of a pseudo-secular hyperfine term. This leads to artefacts at the basic nuclear frequencies in the hyperfine spectrum (or hyperfine dimension), if the generation and detection of nuclear polarization cannot be prevented. The artefacts are by a factor of at least $\sin\eta/\cos\eta$ weaker than the hyperfine peaks if the NC is generated and detected by rf pulses, they can be eliminated completely in this case by rf phase cycling. In ESEEM methods, NC generators and detectors should be used that suppress contributions by polarization, for instance the three-pulse generator (see §4.1.6) combined with echo detection (see §4.2.2). An exception from this arises for disordered systems, where a nuclear coherence transfer echo [36] can be used in the detection of hyperfine frequencies [91]. Artefacts are then suppressed since they are not refocused, so that any NC generator/detector pair may be used. In 2D experiments, it is usually possible to distinguish this type of artefacts from the wanted peaks by their location. This is illustrated in

Fig. 7-1. The artefact peaks (hollow squares) are located either along the diagonals or along the axes of the 2D plot, while the hyperfine cross peaks can never have such locations.

Second order effects can be put to use in disordered systems for the resolution of peaks that correspond to nuclei of the same isotope but feature different hyperfine matrices. Such peaks overlap in ESEEM and ENDOR spectra as well as in hyperfine spectra, whenever there are orientations where the secular hyperfine coupling A is the same for the different nuclei. This case is usually encountered for protons in organic radicals and in ligands of transition metal complexes. In a 2D hyperfine spectrum, the corresponding cross peaks may be resolved due to the second order shifts. Schematic contour plots of HYEND spectra (see §7.2.3) for a system of four protons at X-band and S-band frequencies are shown in Fig. 7-2. All hyperfine matrices are of axial symmetry, the hyperfine couplings a_{\perp} and a_{\parallel} ¹ are given in the figure caption. No orientation selection has been assumed. Obviously, the resolution of the different protons becomes much better in the strong mixing situation encountered at S-band frequencies where the second order effects are larger. The use of second order hyperfine effects for parameter determination in HYSCORE spectra has been suggested recently by several authors [87,123,124].

For $I > 1/2$, second order effects of the nuclear quadrupole interaction must be considered. In general, second order shifts are the same for hyperfine frequencies of the $m_I \leftrightarrow m_I + 1$ and $-m_I - 1 \leftrightarrow -m_I$ transitions. Thus, there is no broadening or additional splitting in the hyperfine spectra for $I=1$, while the multiplicity of a hyperfine line becomes two for $I=3/2$ and $I=2$ and three for $I=5/2$ and $I=3$. The splittings are small if the nuclear quadrupole and hyperfine interaction differ strongly in magnitude.

1. In agreement with common usage, we give hyperfine couplings a_{iso} , a_{\perp} , and a_{\parallel} in frequency units instead of angular frequency units.

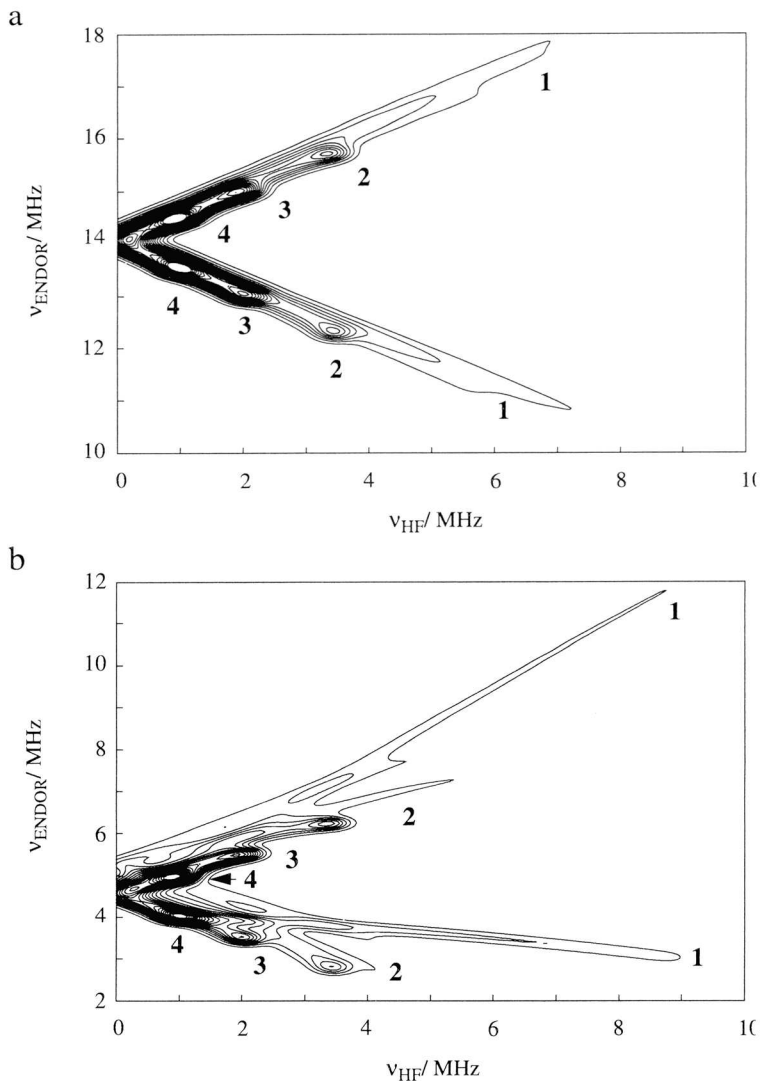


Fig. 7-2 Resolution of protons with different hyperfine matrices in 2D hyperfine spectroscopy due to second order effects (HYEND simulations). The parameters are: $a_{\perp 1} = 15$, $a_{\parallel 1} = 1$, $a_{\perp 2} = 8.5$, $a_{\parallel 2} = -3.5$, $a_{\perp 3} = 5.8$, $a_{\parallel 3} = -2.1$, $a_{\perp 4} = 2.1$, $a_{\parallel 4} = -1.0$ MHz. ENDOR line widths of 100 kHz have been assumed. a) Contour plot of the spectrum at X-band frequencies ($\omega/2\pi = 14$ MHz). b) Contour plot of the spectrum at S-band frequencies ($\omega/2\pi = 4.5$ MHz).

Finally for $I > 1/2$, second order effects can also arise from large isotropic hyperfine couplings a_{iso} . The second order shift of the ENDOR frequencies is given by [125]

$$\delta\omega_{\text{ENDOR}}(m_I \leftrightarrow m_I + 1) \approx \frac{-2\pi^2 a_{\text{iso}}^2 (m_I + m_S + 1/2)}{\omega_S}, \quad (7.4)$$

so that the shift of the hyperfine frequency becomes

$$\delta\omega_{\text{HF}}(m_I \leftrightarrow m_I + 1) \approx \frac{-2\pi^2 a_{\text{iso}}^2 (m_I + 1/2)}{\omega_S}. \quad (7.5)$$

This shift obviously vanishes for the $m_I = -1/2 \leftrightarrow 1/2$ transition and leads to a multiplicity of the hyperfine line of $2I$ with equal splittings $2\pi^2 a_{\text{iso}}^2 / \omega_{\text{mw}}$ between the components of the multiplet.¹

7.2 Pulse sequences

7.2.1 ESEEM hyperfine spectroscopy

ESEEM hyperfine spectroscopy can be performed by combining the building block for hyperfine sublevel coherence transfer (see Fig. 4-9 on page 117) with ESEEM-type NC generators and detectors and using the incrementation scheme $t_1 = t$, $t_2 = T - t$ to measure the difference between the nuclear frequencies before and after application of the π pulse. Two possible pulse sequences are shown in Fig. 7-3. The experiment based on the original HYSORE sequence (Fig. 7-3a) requires only two mw channels if it is performed with a $[0,0] - [0,\pi] - [\pi,0] + [\pi,\pi]$ phase cycle on the first two mw pulses and only one mw channel if phase cycling can be substituted by a choice of τ , t_0 and T that separates the unwanted echoes from the wanted echoes in time. For hyperfine spectroscopy, such a separation can easily be achieved since T is much longer than τ . If one ensures that $t > 2\tau$ and $T - t > 2\tau$ for all data points, phase cycling is not necessary.² On the other hand, the six-pulse sequence based on the three-pulse NC generator (see Fig. 7-3b) leads

1. ω_S can be replaced by ω_{mw} since $\Omega_S \ll \omega_S$.

2. The additional assumption $T \gg T_m$ has been made, which is usually fulfilled.

to weaker artefact peaks, since much less nuclear polarization is created and detected (see §4.1.6). The latter sequence has first been introduced for HYSORE experiments by Song et al. in [126].

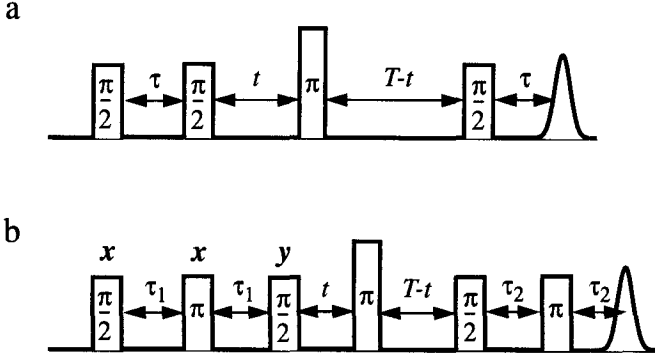


Fig. 7-3 Pulse sequences for ESEEM hyperfine spectroscopy. Pulses without phase label may all have the same phase. a) Four-pulse sequence. b) Six-pulse sequence.

For 1D hyperfine spectroscopy with the four-pulse sequence and incrementation of t , the echo modulation is described by

$$\begin{aligned}
 E(t; T, \tau) = 1 - \frac{k}{4} \bigg\{ & C_0 + 2C_c \left[\cos^2 \eta \cos \left(\omega_{\text{NZ}} \left(T + \frac{\tau}{2} \right) \right) \cos \left(\omega_{\text{HF}} t - \omega_{\text{HF}} \frac{T}{2} \right) \right. \\
 & \left. - \sin^2 \eta \cos \left(\omega_{\text{HF}} \frac{T}{2} \right) \cos \left(\omega_{\text{NZ}} t - \omega_{\text{NZ}} \frac{T}{2} + \omega_{\text{HF}} \frac{\tau}{2} \right) \right] \\
 & + 2C_\alpha \cos \left(\omega_\alpha \left(T + \frac{\tau}{2} \right) \right) \cos \left(\omega_\alpha t - \omega_\alpha \frac{T}{2} \right) \\
 & \left. + 2C_\beta \cos \left(\omega_\beta \left(T + \frac{\tau}{2} \right) \right) \cos \left(\omega_\beta t - \omega_\beta \frac{T}{2} \right) \right\}, \quad (7.6)
 \end{aligned}$$

where the amplitude factors C_0 , C_c , C_α , and C_β are given by

$$C_0 = 3 - \cos(\omega_\alpha \tau) - \cos(\omega_\beta \tau) - \sin^2 \eta \cos(\omega_+ \tau) - \cos^2 \eta \cos(\omega_- \tau), \quad (7.7a)$$

$$C_c = -2 \sin \left(\frac{\omega_\alpha \tau}{2} \right) \sin \left(\frac{\omega_\beta \tau}{2} \right), \quad (7.7b)$$

$$C_{\alpha} = \cos^2 \eta \cos\left(\omega_{\beta} \tau - \frac{\omega_{\alpha} \tau}{2}\right) + \sin^2 \eta \cos\left(\omega_{\beta} \tau + \frac{\omega_{\alpha} \tau}{2}\right) - \cos\left(\frac{\omega_{\alpha} \tau}{2}\right), \quad (7.7c)$$

$$C_{\beta} = \cos^2 \eta \cos\left(\omega_{\alpha} \tau - \frac{\omega_{\beta} \tau}{2}\right) + \sin^2 \eta \cos\left(\omega_{\alpha} \tau + \frac{\omega_{\beta} \tau}{2}\right) - \cos\left(\frac{\omega_{\beta} \tau}{2}\right). \quad (7.7d)$$

This formula can be derived by a few trigonometric transformations from the HYSORE formula [43] considering a sign correction given by Tyryshkin et al. [127]. By replacing t_1 by t and t_2 by $T-t$ in the HYSORE formula, an expression is obtained which is more convenient for the description of 2D ESEEM hyperfine spectroscopy where also T is incremented.

The hyperfine peaks are described by the last term in the first line of Eq. (7.6), their intensity is weighted with $\cos^2 \eta$ and blind spots occur with respect to τ , cf. Eq. (7.7b), and T . The latter blind spots are comparatively dense since T is large. Therefore, it is necessary to perform the experiment for a few different values of T and add the resulting spectra. Artefacts at ω_{NZ} are weighted with $\sin^2 \eta$, they are usually too weak to be detected and can be distinguished easily from hyperfine peaks since their frequency is close to $2\omega_I$. However, the artefacts at ω_{α} and ω_{β} pose a problem, since C_{α} and C_{β} are of the same order of magnitude as C_c . For disordered systems, only the hyperfine peaks are refocussed at $t=T/2$, since among the constant factors in front of the modulation cosines, $\cos[\omega_{\text{NZ}}(T + \tau/2)]$ is the only one that does not vanish in an integration over an anisotropic hyperfine line.¹ For ordered systems, six-pulse ESEEM hyperfine spectroscopy should be preferred where the equivalents of C_{α} and C_{β} are much smaller than C_c . Note that the latter experiment in addition features higher modulation depths. If the artefacts are still too strong or if the modulation depth is still too small, chirp hyperfine spectroscopy is the method of choice.

A peculiarity of hyperfine spectroscopy based on the building block $t - \pi_{\text{mw}} - T - t$ is the fixed length of the pulse sequence, i.e., there is no decay of the modulation when t is incremented. A trade-off between resolution and sensitivity then becomes straightfor-

1. ω_{NZ} is broadened only due to the second order effects of the pseudo-secular hyperfine term.

ward: T is selected according to the required resolution, and the necessary number of accumulations is determined by the signal that is left over after relaxation during time T . On the other hand, the sensitivity of such experiments is worse than the one of the corresponding ESEEM and ENDOR experiments which start with small interpulse delays, since the signal decay is roughly exponential. However, the difference is not large since similar line widths in the spectra can be obtained for $T \approx T_{2n}$ where the signal loss is not dramatic.

7.2.2 Chirp hyperfine spectroscopy

The pulse sequence for Davies-type chirp hyperfine spectroscopy is obtained from the ESEEM hyperfine spectroscopy sequences by exchanging the NC generator and detector, see Fig. 7-4. The corresponding sequence for the Mims-type experiment can be inferred from Fig. 4-11 on page 127. A phase cycle $[0,0]-[0,\pi]-[\pi,0]+[\pi,\pi]$ is applied to the rf chirp pulses in both cases, no mw phase cycling is performed.

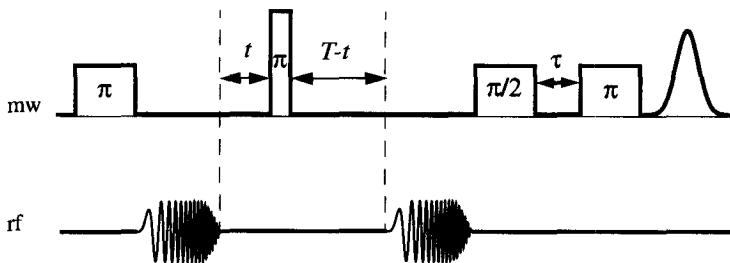


Fig. 7-4 Pulse sequence for Davies-type chirp hyperfine spectroscopy.

The echo modulation in Davies-type chirp ENDOR is described by an expression similar to Eq. (7.6), where the constant part of the echo vanishes, where $C_{\alpha}=C_{\beta}=0$ as a result of rf phase cycling, and where C_c does no longer depend on time τ , i.e., there are only blind spots with respect to T . An expression for C_c and the phases of the hyperfine peaks for a system with purely isotropic hyperfine coupling has been given in [128]. In Mims-type chirp hyperfine spectroscopy, τ -dependent blind spots occur; they are described by Eq. (4.8). In general, Mims-type chirp hyperfine spectroscopy is better suited for the observation of small hyperfine couplings which are suppressed by hyperfine contrast selectivity in the Davies-type experiment, while the latter experiment is bet-

ter suited for the observation of large hyperfine couplings. It should be noted, that the NC in Mims-type experiments is amplitude modulated with respect to Ω_S , so that these experiments are susceptible to line broadening and signal loss by spin diffusion.

7.2.3 HYEND

For ENDOR-based 2D hyperfine spectroscopy, broad band rf excitation is not necessary, since one of the dimensions is an ENDOR dimension which can also be obtained *via* an rf sweep. The advantage of such an approach is that standard ENDOR equipment can be used for the experiment. Furthermore, in disordered systems selective rf excitation affects only spins within a small distribution of hyperfine frequencies if either $I=1/2$ or if the quadrupole interaction is small as for instance for 2D ($I=1$). In the former case, the width of the distribution is determined by the pseudo-secular part of the hyperfine interaction. Since a narrow distribution means slow decay of the corresponding NC, in many cases refocusing is not needed if selective excitation can be used. Broad distributions of the nuclear quadrupole interaction are also narrowed since the experiment involves double orientation selection. The first orientation selection occurs if the excitation bandwidth of the selective mw pulses is small with respect to the ESR frequency spread caused by the g -anisotropy [129]. The second orientation selection is possible if the excitation bandwidth of the selective rf pulses is small with respect to the NMR frequency spread caused by the anisotropy of the hyperfine interaction. HYEND is therefore better suited to detect hyperfine peaks for broad distributions of the nuclear quadrupole interaction than ESEEM-based methods, since these involve only the first kind of orientation selection. It should also be possible to refocus the NC in HYEND experiments, such an approach is discussed in §7.4.2.

With a narrow-band rf source, excitation and detection of the NC have to take place at the same nuclear transition, so that a second mw π pulse is needed for the back transfer. The complete pulse sequence for such an **H**yperfine correlated **E**NDOR (HYEND) experiment is shown in Fig. 7-5 together with four-level schemes that symbolize five states of the spin system during the experiment. The first selective mw pulse creates a state of two-spin order (state I), in which polarization exists on both nuclear transitions. The rf $\pi/2$ pulse which is on-resonant with one of the two transitions, creates NC on this

transition with frequency ω_{12} (II) which is immediately transferred to the other nuclear transition by a non-selective mw π pulse (III). The NC evolves there for a time T with frequency ω_{34} , is transferred back to the first nuclear transition by another non-selective mw π pulse (IV) and converted to nuclear polarization by a second rf $\pi/2$ pulse (V). This leads to a population of level 1 that depends on the phase which the NC has gained *with respect to the rf source* during time T . The population change is finally detected by an echo created by two selective mw pulses. The echo is modulated with $\sin[(\omega_{34} - \omega_{\text{rf}})T]$, and since the on-resonance condition is $\omega_{\text{rf}} = \omega_{12}$, the peak appears at frequency ω_{HF} after a Fourier-transform with respect to T . The cases where the mw frequency or the rf frequency or both are on-resonant with other transitions are completely analogous.

The phase cycle $[0,0]-[0,\pi]-[\pi,0]+[\pi,\pi]$ is applied to the rf pulses; phase cycling of the mw is usually not necessary. The latter point has been discussed in more detail in [130]. Note that in HYEND direct excitation and detection of NC is necessary in only one electron spin manifold, so that the hyperfine frequency can also be measured if the transition probability of one of the two ENDOR transitions is zero.

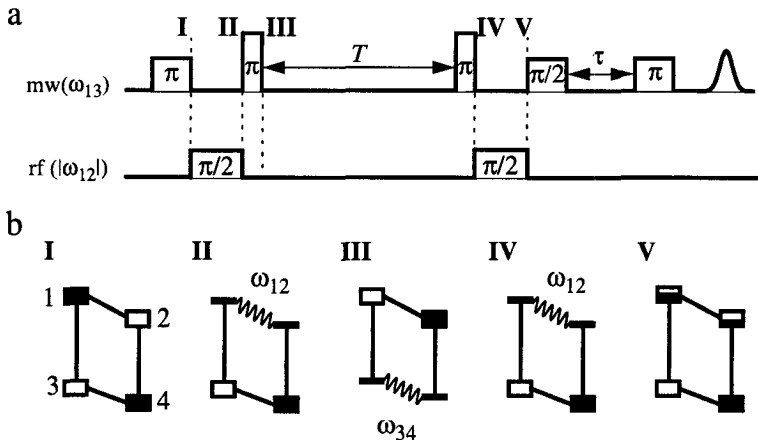


Fig. 7-5 Pulse sequence for the HYEND experiment (a) and four-level schemes symbolizing the inner working (b).

In deriving a formula for the echo modulation for an $S^z=1/2$, $I=1/2$ spin system, we must explicitly take into account the phase of the rf pulse, since the x axis of the I spin subspace has already been defined in Eq. (3.7). An rf pulse of arbitrary phase ϕ with flip angle β_{rf} can be described by the unitary transformation for a composite rotation

$$U_{\text{rf}} = \exp\{-i\phi I_z\} \exp\{-i\beta_{\text{rf}} S^{\alpha, \beta} I_x\} \exp\{i\phi I_z\}. \quad (7.8)$$

With the transformations given in Table 3-1 on page 50 and a few simplifications, we find the signal $E^{\alpha, \beta}$ for rf pulses on-resonant with ω_{α} , ω_{β} ,

$$\begin{aligned} E^{\alpha, \beta}(T, \phi) = & C_{\text{HF}}^{\alpha, \beta} \sin(\omega_{\text{HF}} T + \phi_{\text{HF}}^{\alpha, \beta}) + C_{\text{NZ}}^{\alpha, \beta} \sin(\omega_{\text{NZ}} T + \phi_{\text{NZ}}^{\alpha, \beta}) \\ & + C_0^{\alpha, \beta} \sin(\omega_{\alpha, \beta} T + \phi) \end{aligned}, \quad (7.9)$$

with the amplitudes

$$C_{\text{HF}}^{\alpha, \beta} = \pm \operatorname{sgn}(2\omega_I + A) \left[\sqrt{1-k} + \frac{\omega_{\alpha, \beta}^{(0)}}{\omega_{\alpha/\beta}} \right] C_0^{\alpha, \beta}, \quad (7.10a)$$

$$C_{\text{NZ}}^{\alpha, \beta} = -\operatorname{sgn}(2\omega_I + A) \left[\sqrt{1-k} - \frac{\omega_{\alpha, \beta}^{(0)}}{\omega_{\alpha/\beta}} \right] C_0^{\alpha, \beta}, \quad (7.10b)$$

$$C_0^{\alpha, \beta} = \frac{1}{2\sqrt{2}} \left(1 + (1-2k) \sin^2 \phi + \cos^2 \phi \frac{(\omega_{\alpha, \beta}^{(0)})^2 - B^2/4}{(\omega_{\alpha, \beta}^{(0)})^2 + B^2/4} \right)^{1/2}, \quad (7.10c)$$

$$C^{\alpha, \beta} = -k \sin \phi, \quad (7.10d)$$

and phases

$$\phi_{\text{HF}}^{\alpha, \beta} = \operatorname{atan} \left(\frac{\tan(\phi) \sqrt{1-k} + \cot(\phi) \omega_{\beta, \alpha}^{(0)} / \omega_{\beta, \alpha}}{2 \left[\omega_{\beta, \alpha}^{(0)} / \omega_{\beta, \alpha} - \sqrt{1-k} \right]} \right), \quad (7.11a)$$

$$\phi_{\text{NZ}}^{\alpha, \beta} = \operatorname{atan} \left(\frac{\tan(\phi) \sqrt{1-k} - \cot(\phi) \omega_{\beta, \alpha}^{(0)} / \omega_{\beta, \alpha}}{2 \left[\omega_{\beta, \alpha}^{(0)} / \omega_{\beta, \alpha} + \sqrt{1-k} \right]} \right). \quad (7.11b)$$

The $\omega_{\alpha, \beta}^{(0)}$ have been defined in Eq. (6.6a,b). In addition to the hyperfine peaks, there are two types of artefacts. Except for strong mixing situations, we have $k \ll 1$ and $\omega_{\alpha, \beta}^{(0)}/\omega_{\alpha, \beta} \approx 1$, so that the intensity of the artefacts is much smaller than the intensity of the hyperfine peaks. Furthermore, the artefacts are easily recognized, since $\omega_{NZ} \approx 2\omega_I$ and the second type of artefacts is located on the diagonal where no cross peaks can be situated.

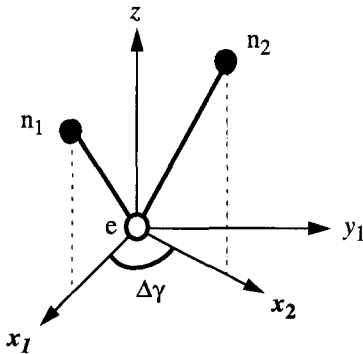


Fig. 7-6 Definition of the I spin subspace x axes for different nuclei. Validity of the point-dipole approximation is assumed.

The intensity factor $C_0^{\alpha, \beta}$ of the second type of artefacts depends on the phase ϕ , which is in turn related to the orientation of the hyperfine interaction matrix with respect to the rf field. If the point-dipole approximation is valid, the x axis is along the projection of the electron-nuclear axis on the plane perpendicular to the external magnetic field. This means that the x axis is *different for different nuclei* (see Fig. 7-6), and thus, the phase dependence of the artefact line intensity is also different. The angle $\Delta\gamma$ between the two projections can be determined by measuring the dependence of the intensity of the artefact lines on the rf phase, since $\Delta\gamma$ is just the phase difference between the intensity maxima. Note that such measurements require an rf phase lock, since the lines of different nuclei are on-resonant at different frequencies. For the same reason, the phase shift has to be taken into account that is caused by the cable length between source and ENDOR coil. For ordered systems, it may thus be easier to use a crystal rotation which

even yields more information. For disordered systems, the artefact usually becomes too weak for detection since nuclei with different orientation can have the same secular hyperfine coupling and there is destructive interference because of the variation of ϕ .

7.3 Experimental examples

7.3.1 Ordered systems

Line overlapping and assignment ambiguities in ENDOR spectra usually do not pose large problems for ordered systems, since a large number of spectra can be obtained at different crystal orientations, and the resulting patterns often allow for an unequivocal determination of the parameters. Nevertheless, if the number of nuclei is large and in particular if quadrupole nuclei are involved, it may be difficult to obtain starting values for the analysis of the patterns without being able to assign at least the spectra at a few orientations. The acquisition of a few 2D hyperfine spectra does not considerably increase the measurement time for a crystal rotation. Furthermore, a 1D hyperfine spectrum can be acquired in the same time as an ENDOR spectrum, so that it is feasible to obtain the much more simple pattern for the orientation dependence of the hyperfine spectrum along with the more complicated ENDOR pattern.

The spectrum simplification inherent in 1D hyperfine spectroscopy shall be demonstrated here on the example of the bis(glycinato)copper(II) complex in a Cu(II)-doped triglycine sulfate single crystal. The structure of this complex has been investigated earlier by both ESR [131] and ENDOR [132] methods, it is shown in the inset of Fig. 7-7b. The experiments have been performed with a home-built ESR spectrometer [68] and the chirp ENDOR setup described in Appendix B. The detailed experimental parameters are given in [128]. Six traces with $\Delta T = 25$ ns were acquired and the resulting spectra added to obtain a blind-spot free hyperfine spectrum.

One expects a large hyperfine coupling (20–40 MHz) for the directly coordinated nitrogen nuclei and a hyperfine coupling of 5–15 MHz for the amino protons, while only small hyperfine couplings are anticipated for the CH_2 protons (see also §4.4.2). While there may be overlapping of the nitrogen and proton ENDOR lines, the hyperfine spectra should be well resolved.

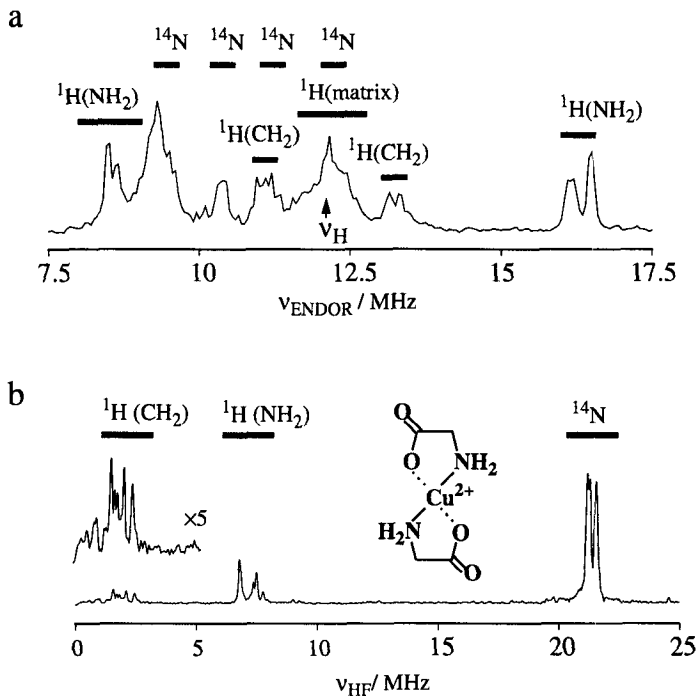


Fig. 7-7 Davies-ENDOR (a) and chirp hyperfine (b) spectrum of the complex bis(glycinato)-copper(II) in a Cu-doped single crystal of triglycine sulfate. Labels designate the assignment of spectral regions to the ligand nuclei. The inset in (b) shows the structure of the complex.

This is confirmed by the experimental spectra shown in Fig. 7-7. The Davies-ENDOR spectrum in the given orientation is difficult to assign, and in particular, no precise values for the peak frequencies can be obtained because of severe peak overlapping. On the other hand, the hyperfine spectrum is nicely resolved and it can be inferred immediately that the two glycine ligands are not equivalent in Cu(II)-doped TGS.¹ One of the two nitrogen peaks shows an additional splitting that is in good agreement with the expected value of 50 kHz for the second order splitting according to Eq. (7.5).

1. This slight non-equivalence is also the reason for the comparatively poor resolution of the ENDOR spectrum.

The peaks of the CH_2 protons are rather weak because of the suppression due to hyperfine contrast selectivity. However, they can still be detected easily (see enlarged detail in Fig. 7-7b), so that it was not necessary to perform a Mims-type experiment to increase their intensities.

For the demonstration of 2D hyperfine spectroscopy on an ordered sample, we use a copper complex with two equivalent ligands and inversion symmetry with respect to the copper ion, namely copper(II) α -picolinate doped into zinc(II) α -picolinate. The Davies-ENDOR spectrum in Fig. 7-8a is much better resolved in this case than for the bis(glycinato) complex, nevertheless, some of the proton and nitrogen lines overlap. This overlapping is eliminated in the HYEND spectrum shown in Fig. 7-8b. Note that the nitrogen cross peaks are weaker than the proton cross peaks, while the opposite relation was observed for the hyperfine peaks in chirp hyperfine spectroscopy of the bis(glycinato) copper(II) complex. The reason is the larger nitrogen hyperfine coupling which is close to the excitation bandwidth of the "non-selective" mw π pulses together with the need for two of these mw π pulses in HYEND. The pulses do no longer achieve a complete transfer of the nitrogen NC between the two electron spin manifolds and signal losses occur. A version of HYEND that uses only one mw π pulse is proposed in §7.4.1.

Cross peaks belonging to six protons are resolved in the HYEND spectrum (see detail plot in Fig. 7-8c), four of them probably belong to the phenyl protons and two of them to the protons of the axially coordinated water molecules. Matrix protons of zinc picolinate are expected to have even smaller couplings. Note that the suppression of peaks belonging to small hyperfine couplings is not so drastic as in Davies-type chirp hyperfine spectroscopy. Nevertheless, it is stronger than in Davies-ENDOR itself.

The nitrogen lines feature an additional splitting that is too large to be explained by a second order contribution of the predominantly isotropic hyperfine coupling. This splitting is typical for a group spin $F=2$ of two magnetically equivalent nitrogen nuclei [133,134]. The HYEND pattern contains additional correlation information on the eight nitrogen lines that is not inherent in the ENDOR spectrum. In agreement with theory, the whole four-line pattern is split and the second order splitting behaves like a difference in the hyperfine splittings of the two nuclei.

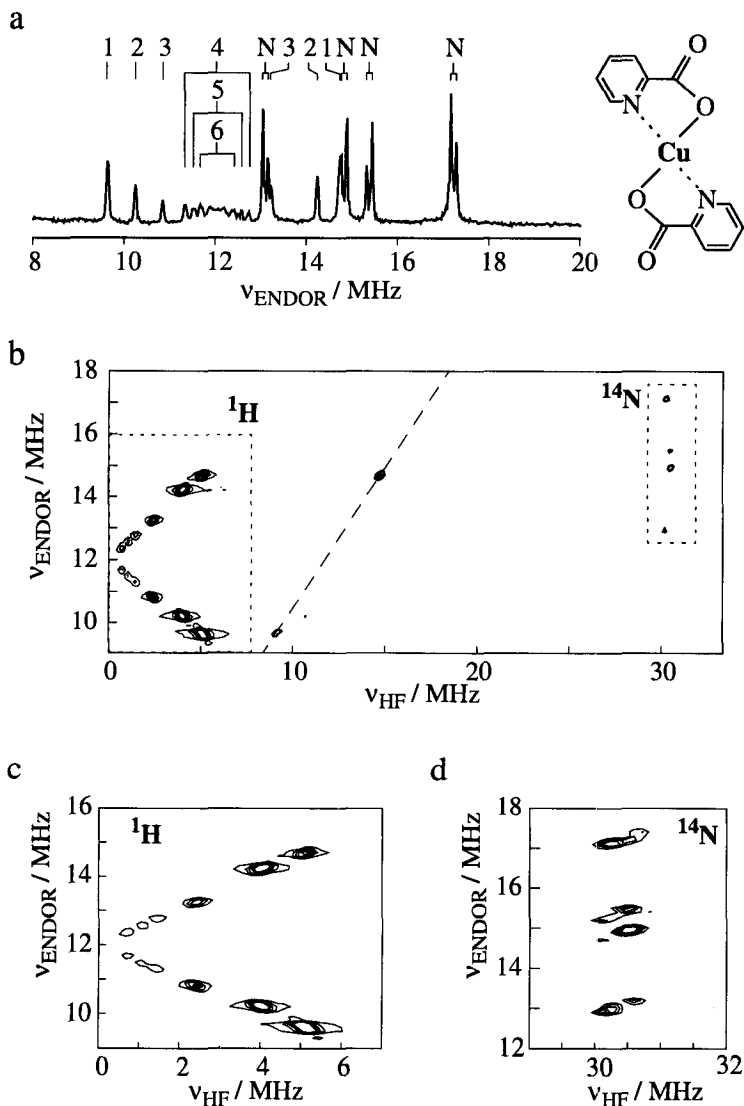


Fig. 7-8 Davies-ENDOR spectrum (a) and contour plot of the HYEND spectrum (b) of copper(II) α -picolinate in a Cu(II)-doped single crystal of zinc α -picolinate at arbitrary orientation. The structure of the complex is shown in the inset in (a). Detail plots of the proton region (c) and nitrogen region (d) of the HYEND spectrum are also shown.

The prediction by Eqs. (7.9,7.10a-d) of a dependence of the peak intensities on the rf phase was tested for one of the proton lines in a slightly different orientation of the

Cu(II)-doped zinc picolinate crystal. In agreement with theory, the artefact at $\omega_{\beta}/(2\pi)=13.85$ MHz vanishes at a certain phase (see Fig. 7-9). The peak intensities are periodic for a 180° phase shift since magnitude spectra have been calculated.¹

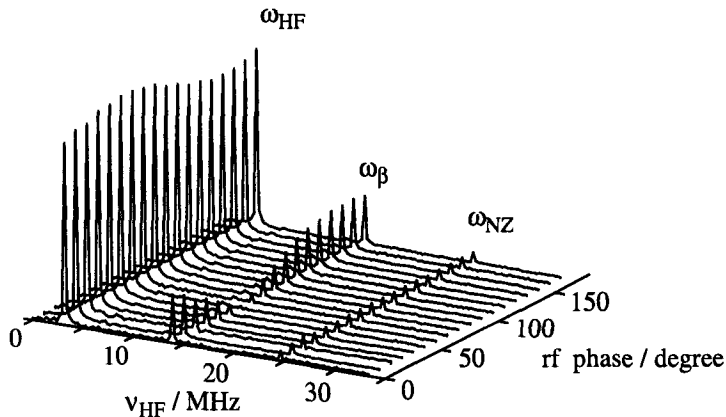


Fig. 7-9 Dependence of the intensities of the hyperfine peak and the artefact peaks on the phase of the radio frequency excitation. The sample is the same crystal as in Fig. 7-8 in a slightly different orientation.

7.3.2 Disordered systems

In disordered systems, strong overlapping of ENDOR and ESEEM peaks is commonplace and tools for resolution enhancement are needed in a number of cases to extract any useful information from the spectra. This is demonstrated below on the example of proton and fluorine hyperfine interactions in a sample of poly(vinylidene)fluoride doped with 0.5% 4-oxo-2,2,6,6-tetramethyl-piperidin-1-oxyl (TEMPO). As a model sample for the comparison of different hyperfine spectroscopy experiments, we employ the sandwich complex bis(η_6 -benzene)vanadium(0). All experiments have been performed on a home-built spectrometer [68], for chirp hyperfine spectroscopy and HYEND experiments, the ENDOR setup described in Appendix B was used.

1. The complicated expressions for the phases of the peaks at ω_{HF} and ω_{NZ} , see Eq. (7.11a,b), preclude a simple phase correction.

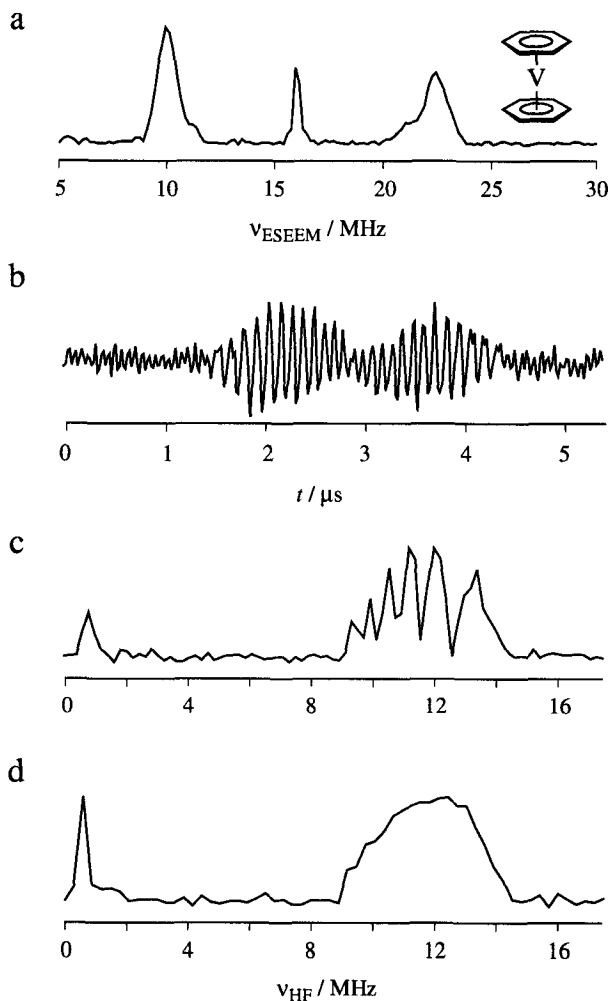


Fig. 7-10 1D ESEEM hyperfine spectroscopy on bis(η_6 -benzene)vanadium(0) doped into polycrystalline ferrocene. a) ESEEM spectrum obtained by the DEFENCE method [36]. The inset shows the structure of the complex. b) Nuclear coherence transfer echo obtained in a 1D ESEEM hyperfine spectroscopy experiment. c) Magnitude spectrum corresponding to the time-domain data shown in (b). d) Blind-spot free 1D hyperfine spectrum obtained by adding eight spectra obtained with different fixed delays T .

The ESEEM spectrum of bis(η_6 -benzene)vanadium(0) doped into polycrystalline ferrocene is shown in Fig. 7-10a; it was obtained with the DEFENCE experiment [36] at an

observer position that mainly selects orientations in the benzene ring plane. Apart from the peak at $\nu(^1\text{H}) = 15.9$ MHz due to weakly coupled matrix protons, there are broader peaks corresponding to the twelve benzene protons which differ only slightly in their hyperfine interactions (mean values in the ferrocene matrix: $\bar{a}_{11} = 9.2$ MHz, $\bar{a}_{22} = 7.1$ MHz, $\bar{a}_{33} = 17.0$ MHz, [135,136]). A nuclear coherence transfer echo centered at $t = T/2$ is observed in the 1D ESEEM hyperfine spectroscopy experiment because of refocusing of the hyperfine frequencies (see Fig. 7-10b). In agreement with Eq. (7.6), blind spots occur in the magnitude spectrum calculated by a Fourier transform from the hyperfine echo (see Fig. 7-10c), they can be removed by adding spectra acquired with different values of the fixed interpulse delay T . The blind spot free spectrum in Fig. 7-10d has been obtained from a series of eight spectra with an increment $\Delta T = 20$ ns. The interpulse delay $\tau = 205$ ns has been chosen to suppress τ -dependent blind spots as far as possible. Further experimental parameters are given in [91]. The hyperfine spectrum features a peak close to $\omega_{\text{HF}} = 0$ corresponding to the matrix protons, and a hyperfine peak extending from about 9 to 14.5 MHz corresponding to the benzene ring protons. This can be compared to the range of 7 to 17 MHz expected from the hyperfine matrix principal values. The differences are partially due to τ -dependent blind spots, but for the upper limit mainly due to orientation selection (see [36]) and for the lower limit mainly due to the fact that modulation depths become zero at the canonical orientations of the hyperfine matrix. Therefore, 1D ESEEM methods are not well suited to obtain the principal values for disordered systems, while 2D methods have the potential to recover the information *via* second order effects on the cross peak shape [87,123,124]. However, in most cases it may be easier to use ENDOR methods which do not rely on orientation dependent modulation depths.

The 1D chirp hyperfine spectrum of the same sample is shown in Fig. 7-11. Again, eight traces with an increment $\Delta T = 20$ ns have been acquired and the resulting spectra added to avoid blind spots. The pulse lengths of the first selective mw π pulse, the non-selective π pulse, the selective $\pi/2$ pulse and the last selective π pulse, were 100, 10, 100, and 200 ns, respectively. The rf was swept in a time of 5 μs from 3 to 27 MHz during the chirp pulse with an apodized envelope (see Appendix B). The measurement has been performed at a temperature of 16.5 K with $\nu_{\text{mw}} = 9.244$ GHz and $B_0 = 3277$ G. Obviously,

the refocusing is much worse in chirp hyperfine spectroscopy than in ESEEM hyperfine spectroscopy and the spectrum does not extend up to the expected maximum hyperfine coupling in the benzene ring plane $\bar{a}_p = 14.4$ MHz. In addition, the sensitivity of the experiment is rather low as compared to chirp ENDOR experiments on ordered systems. Apart from the generation of harmonics by the rf amplifier, the reason is probably the dependence of the phase of the NC on the frequency which leads to destructive interference. Experiments on other disordered systems gave similar results. Chirp hyperfine spectroscopy may thus be restricted to samples with ENDOR linewidths not much larger than 1 MHz.

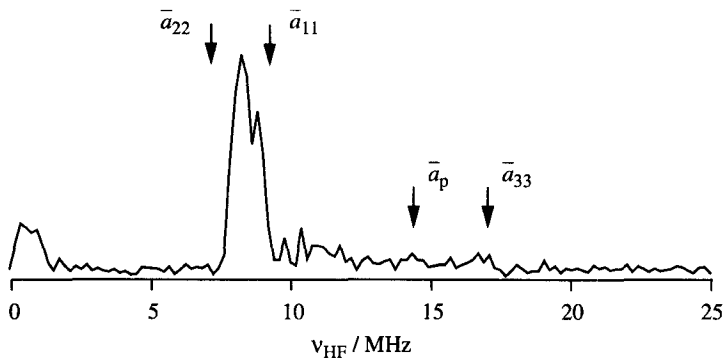


Fig. 7-11 Chirp hyperfine spectrum of bis(η_6 -benzene)vanadium(0) doped into polycrystalline ferrocene. The labels \bar{a}_{ii} designate the principal values of the hyperfine interaction matrix determined by earlier ENDOR work [136] and \bar{a}_p is the maximum hyperfine coupling in the benzene ring plane.

In contrast to chirp hyperfine spectroscopy, HYEND is well suited for measurements on disordered systems. The cross peak *intensity* resembles closely the shape expected for an ENDOR powder pattern and second order effects can be recognized clearly in the contour plot shown in Fig. 7-12a. Only the ω_α line has been measured, since the ω_β line is virtually the mirror-image with respect to $\omega_{NZ}/2$ in this case. For comparison, the HYEND spectrum was simulated with the HFI matrix principal values given in [136], the result is shown in Fig. 7-12b. The formulas for the calculation of A and B from \bar{a}_{11} , \bar{a}_{22} , and \bar{a}_{33} and the orientation of the external magnetic field with respect to the principal axes are given in Appendix D.

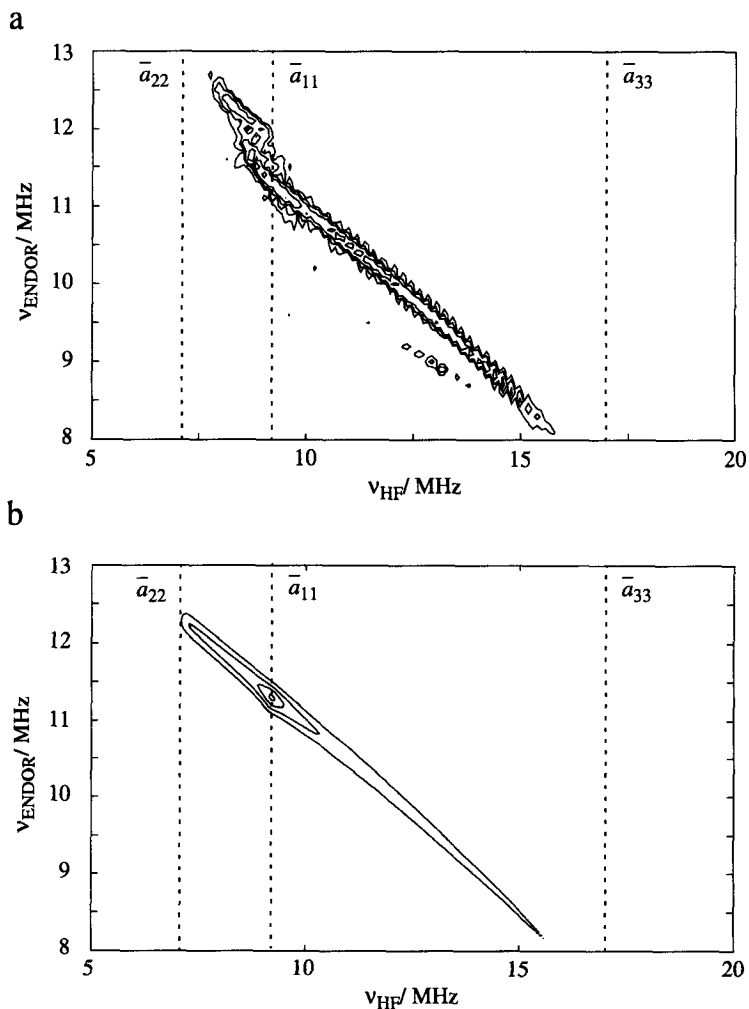


Fig. 7-12 HYEND spectrum of bis(η_6 -benzene)vanadium(0) doped into poly-crystalline ferrocene. a) Contour plot of the experimental spectrum. b) Contour plot of a spectrum simulated with the parameters given in [136].

Though the curvature of the cross peak in the simulated spectrum fits perfectly with the experimental spectrum between \bar{a}_{11} and \bar{a}_p , there are significant deviations between \bar{a}_{22} and \bar{a}_{11} which cannot be explained by effects of orientation selection. An analogous curvature has been observed in HYSORE spectra for this part of the cross peak [91]. It

seems to be impossible to fit the sharp bent close to \bar{a}_{11} with a single HFI matrix or even with a few similar HFI matrices as expected for the benzene ring protons from single crystal measurements [136]. At present, the reason for the peculiar cross peak shape is unknown.

As an application of HYEND for disordered systems we choose the characterization of the interaction between a spin label and a polymer. Such interactions are of interest, since spin labels are widely used to characterize polymer dynamics (see also §5.3.1). In a sample of 4-oxo-2,2,6,6-tetramethyl-piperidin-1-oxyl (TEMPO) in poly(vinylidene fluoride), fluorine HFI can only occur between the spin label and the polymer chain. Furthermore, fluorine is well suited for such investigations, since already very small spin densities in fluorine atomic orbitals lead to detectable hyperfine couplings. However, in an ENDOR spectrum, the fluorine peak is completely masked by the strong proton peak, since the difference in the nuclear Zeeman frequencies of the two nuclei is smaller than the ENDOR line width (see Fig. 7-13a). In the HYEND spectrum, the proton and fluorine cross peaks are nicely resolved (see Fig. 7-13b), and ENDOR spectra for the single isotopes can be obtained by projection of the respective ridges onto the ENDOR axis (see Fig. 7-13c,d). Note, that the latter procedure may lead to spurious points in the ENDOR spectra where the different ridges cross. In the present example, this effect is barely visible. The holes in the ENDOR lines at ν_H and ν_F are suppression effects due to hyperfine contrast selectivity.

From the HYEND spectrum, one can infer that the largest fluorine hyperfine coupling is about 2.2 MHz. Since no fluorine correlation peaks were found in a HYSORE spectrum and no peaks close to $2|\nu_F|$ with four-pulse ESEEM spectroscopy, we assume that the coupling is predominantly isotropic. Even in this case, the $2s$ spin density of the unpaired electron of TEMPO in ^{19}F atomic orbitals is as small as 4.5×10^{-5} . Spin density the same magnitude in *proton* $1s$ -orbitals would lead to an isotropic coupling of only 70 kHz. Valence shell atomic-orbital couplings for these calculations have been taken from [17].

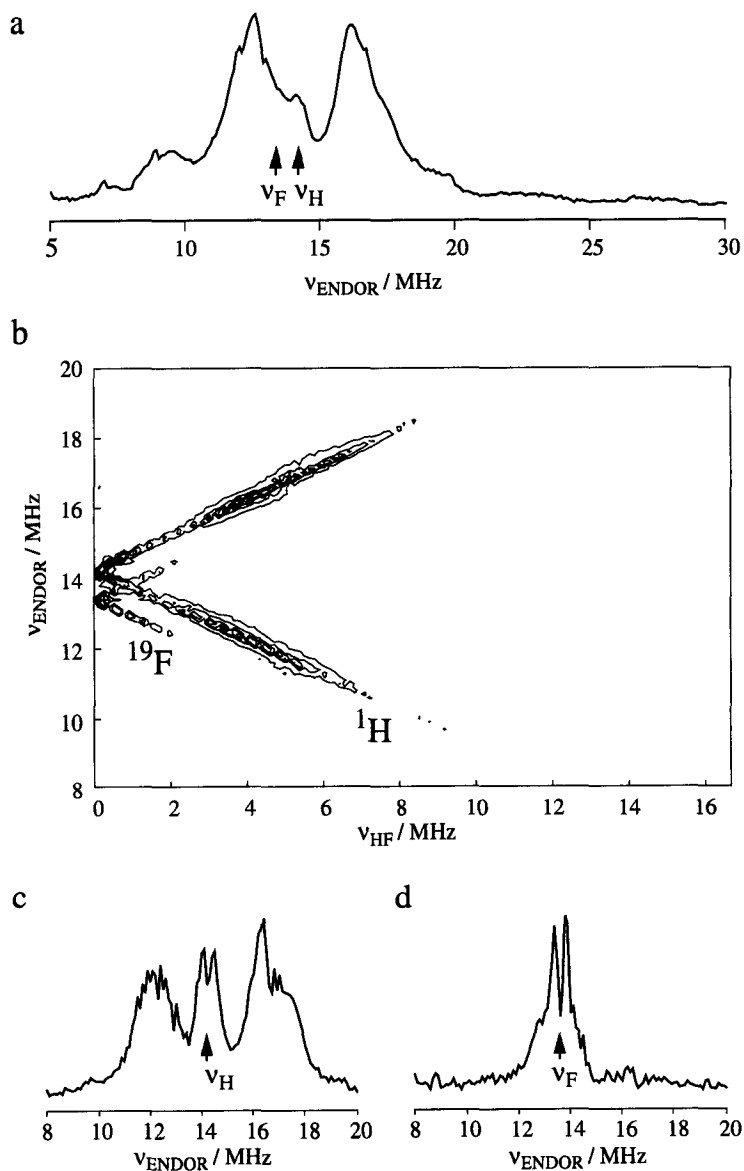


Fig. 7-13 Separation of fluorine and proton ENDOR lines in poly(vinylidene)fluoride doped with TEMPN spin label. a) Davies-ENDOR spectrum. b) Contour plot of the HYEND spectrum. c) Proton ENDOR spectrum obtained by projection of the proton ridge in the HYEND spectrum. d) Fluorine ENDOR spectrum obtained by the same procedure.

In the proton region of the HYEND spectrum, second order splittings due to the pseudo-secular part of the HFI are partially resolved, see Fig. 7-14. However, the splittings are too small to determine the HFI matrices of the different protons in TEMPON. As discussed in §7.1.2, larger splittings and better resolution might be obtained at S-band frequencies. The experimental details for the measurement on the polymer sample are given in [130].

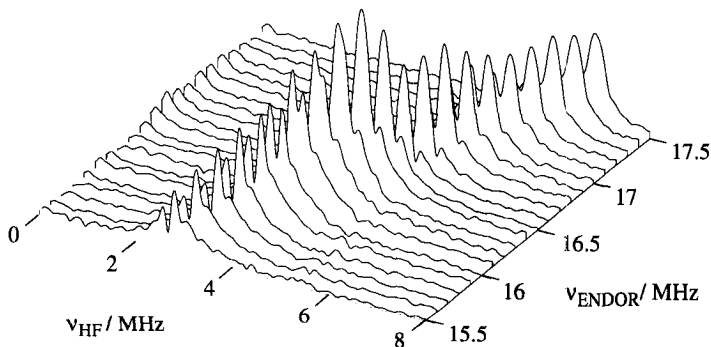


Fig. 7-14 Second order splittings in the hyperfine dimension. The stack plot is a detail of the HYEND spectrum of poly(vinylidene)fluoride doped with TEMPON spin label.

7.4 Proposed experiments

7.4.1 Probe-pulse detected HYEND

The acquisition of highly resolved 2D spectra can be very time-consuming. Consider a HYEND data matrix of 1024×1024 points, acquired with a four-step phase cycle and a repetition rate of 1000 Hz. Even with only one accumulation per point and phase cycle step, 70 minutes are needed to obtain the whole data matrix. Particularly for single crystals, such a long measurement time is not needed to achieve a sufficient signal-to-noise ratio. The measurement time can be reduced if one of the dimensions is acquired with a multiplex advantage. It has been shown in §3.2.10 that a combined mw/rf probe pulse can be used to measure hyperfine frequencies. For that, the spin system has to be prepared in a state where NC exists on a nuclear transition in the electron spin α (β) manifold, when the rf is on-resonant with the corresponding transition in the β (α) manifold.

This can easily be done by creating NC on a single transition with a selective rf $\pi/2$ pulse and transferring it to the other electron spin manifold by a non-selective mw π pulse. The whole sequence is shown in Fig. 7-15. It is also possible to create the nuclear polarization by a sequence of two non-selective mw $\pi/2$ pulses with an interpulse delay τ (Mims-type experiment).

For optimum sensitivity, the Hartmann-Hahn condition (3.102) should be fulfilled by the mw and rf field during the probe pulse. The maximum achievable rf field of $\omega_2/(2\pi) \approx 0.05 \dots 0.1$ MHz can be used in most cases, since this still leaves the hyperfine frequencies virtually unperturbed, see §3.2.10, and can be matched by the mw field without particular problems.

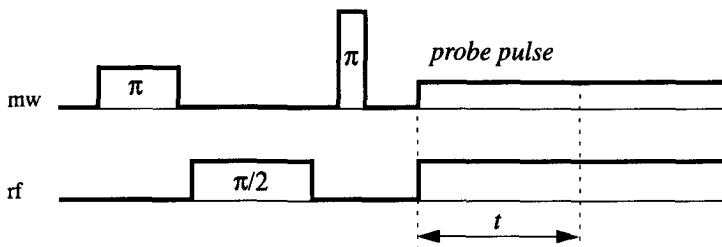


Fig. 7-15 Pulse sequence for probe-pulse detected HYEND.

In a Mims-type experiment, the ENDOR coil has to be adjusted carefully to be perpendicular to the external magnetic field, since EC refocusing is prevented otherwise (see Footnote on page 100). However, this is not required for the Davies-type sequence in Fig. 7-15, since in this case the NC is transferred to EC which is detected instantaneously.

An additional advantage of probe-pulse detected HYEND is that only one transfer to the other electron spin manifold by a non-selective mw π pulse is needed. Sensitivity losses for large hyperfine frequencies because of insufficient excitation bandwidth are thus minimized. No experiments have been performed so far with this pulse sequence.

7.4.2 Refocussed HYEND

In some disordered systems, double orientation selection may not be sufficient to narrow the lines in the hyperfine dimension sufficiently to detect them in $I > 1/2$ systems with large nuclear quadrupole couplings. The reason is that interference effects of the two non-selective π pulses occur if they are too close together¹ and thus there is a dead time between the creation and detection of NC. The full modulation could be recovered by creating an echo on the nuclear transition. This is difficult to do on the transition where the NC evolves during the HYEND experiment, since there is a frequency distribution over several MHz and usually only selective rf pulses on-resonant with the other transition are available. The refocusing can then be achieved by applying an rf π pulse to NC that was transferred back to the original electron spin manifold. The complete pulse sequence is shown in Fig. 7-16, refocusing occurs for $t = t_0$.

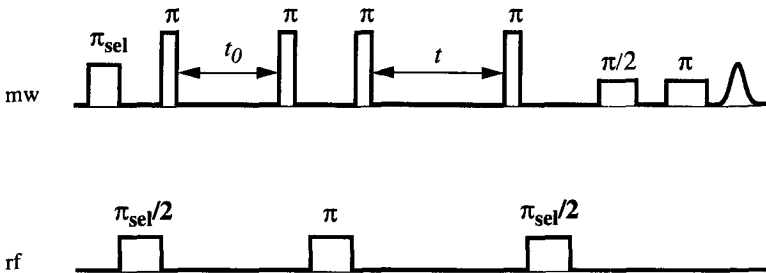


Fig. 7-16 Pulse sequence for refocussed HYEND.

The use of four mw π pulses may lead to excitation bandwidth problems for large hyperfine frequencies, but it should be possible to use this method for instance for remote nitrogen atoms and for the majority of quadrupole nuclei that feature hyperfine couplings smaller than about 10 MHz. No experiments with this sequence have been performed so far.

1. In our experiments, interpulse delays smaller than 40 ns lead to spurious signals.

Zero-field ESEEM and ENDOR

8.1 Theory

8.1.1 Basics of zero-field ESR

The most important complication in magnetic resonance spectroscopy of disordered solids is orientational broadening. The external magnetic field removes the isotropy of space, hence the resonance frequency depends on the relative orientation between the magnetic field axis and the structure element that carries the spin. Since all possible orientations occur in a disordered solid, this usually leads to severe line broadening and a tremendous loss in resolution.

The isotropy of space is restored and narrow spectral lines are re-established in zero external magnetic field. If the Zeeman interaction is the only term in the Hamiltonian that can provide sufficiently large level splittings and population differences for a magnetic resonance experiment, this method of resolution enhancement cannot be used since the Zeeman interaction vanishes in zero field, cf. Eq. (2.1) and (2.8).¹ On the other hand,

1. This problem can be overcome by either preparing the system at high field and measuring the frequencies at zero field [137] or by providing an *average* Hamiltonian during the measurement of the frequencies that corresponds to a zero-field situation [138,139]. The first method is technically demanding, particularly in ESR spectroscopy, since the field sweep must be fast as compared to the longitudinal relaxation times. In the second method, external perturbations must be provided that are of at least the same order of magnitude as the rotating frame frequencies of any transition in the system. This is usually impossible in the case of ESR spectroscopy.

one can infer from Fig. 2-1 on page 29 that the zero-field splitting and in extreme cases the hyperfine interaction can approach frequencies higher than 1 GHz. The population differences in zero field are then sufficient to detect paramagnetic species in roughly the same concentration range as in high-field experiments.

Nevertheless, zero-field ESR spectroscopy [140] is still technically demanding. ESR spectroscopy is usually performed by sweeping the magnetic field, since in a frequency sweep, ranges of more than octave band would have to be covered. Efficient microwave sources, wave guides, phase shifters, attenuators, circulators, and resonators can however be built only for restricted frequency bands. Though frequency-sweep spectrometers for zero-field ESR spectroscopy both without [143] and with use of resonators [144,145] have been described, it seems to be the general perception that the disadvantages of the method outweigh its advantages and comparatively few applications have been reported [140].

The technical requirements are drastically reduced for ENDOR and ESEEM experiments which are performed at a fixed ESR observer frequency. A usual pulse ESR spectrometer can be used whenever a suitable observer transition is available in its frequency range, and the problem boils down to tuning the resonator to the observer frequency. A tuning range of a few hundred MHz can be obtained easily by introducing dielectric materials into the region of a resonator where the electric fields are concentrated. By perturbing the fringe fields outside a dielectric resonator, a tuning range of up to $\pm 20\%$ of the unperturbed frequency can be achieved [146], so that one dielectric resonator could cover the X-band from 8-10 GHz. Whispering-gallery mode dielectric resonators feature a number of periodically spaced modes with different Q -factors over a broad frequency range [147]. A loop-gap (or split-ring) resonator that can be tuned over a range from 250-900 MHz by varying the gap width has also been described [148]. Finally, loop-gap resonators can be constructed for frequencies differing by up to one order of magnitude without large changes in resonator size. Thus it becomes possible to cover the whole frequency range between 1 and 10 GHz (L-band, S-band, C-band, and X-band frequencies) with the same probe head and a set of different loop-gap resonators [149]. A number of interesting samples feature zero-field resonances in this frequency range, e.g., Mn^{2+} complexes ($S=5/2$), Cu^{2+} dimers ($S=1$), and VO^{2+} complexes ($S=1/2$, $I=7/2$).

Among these, Mn^{2+} is of particular importance, since it is a metal cofactor in a number of metalloproteins and can furthermore be substituted for Mg^{2+} in Mg-dependent enzymes [150]. Note also that zero-field ESEEM and ENDOR do not require the compensation of the earth field, since the nuclear Zeeman interaction is smaller than ESEEM and ENDOR line widths in fields up to at least 1 mT. In fact, the experiments can be performed even in the residual field of modern ESR magnets.

The general spin Hamiltonian in zero field is given by

$$\mathcal{H}_{ZF} = \mathcal{H}_{ZFS} + \mathcal{H}_{HF} + \mathcal{H}_{NQ}, \quad (8.1)$$

cf. Eq. (2.11), where \mathcal{H}_{ZFS} vanishes for $S=1/2$ systems. The theoretical description of zero-field experiments differs considerably between non-Kramers systems with integer S and Kramers systems with half-integer S . Most non-Kramers systems are ESR silent, but if a quasi-degenerate non-Kramers doublet is split in zero field by an energy close to the energy of the mw quantum,¹ transitions can be observed at zero field as well as at high fields [16]. Only a small part of the ESR literature is concerned with such systems; however, recently there has been renewed interest in non-Kramers ions when it was recognized that they feature in a number of metalloproteins [151,152]. Only in one instance ENDOR and ESEEM experiments on a non-Kramers system have been reported [153], the corresponding theory was given by Hoffman [154]. For our purpose, the main conclusion from this theory is that the contribution of the hyperfine interaction to the nuclear frequencies vanishes at zero field. Accordingly, there is no longer mixing between electron and nuclear spin states and the ESEEM effect vanishes, too. The fact that the resonance condition depends on strain, leads to a considerable broadening of the lines in ENDOR and ESEEM spectra already at very low fields where the broadening due to the nuclear Zeeman interaction can still be neglected. The situation may differ somewhat for triplets, where two-pulse echo modulations in zero field have been observed with optical detection in two instances and tentatively assigned to neighbour nuclei [155,156]. In both cases, no determination of Hamiltonian parameters from the modulation frequencies was

1. In fact, this splitting Δ is due to strain and its average value $\bar{\Delta}$ must be close to the energy of the mw quantum.

attempted and no modulations were observed for the stimulated echo (three-pulse sequence).

On the other hand, small static fields contribute to line broadening in ENDOR and ESEEM spectra only in the $m_S = \pm 1/2$ manifolds for *Kramers ions* and the hyperfine interaction contributes to the nuclear frequencies at zero field. The $m_S = \pm 1/2$ manifolds are special, since the states $|+1/2, -m_I\rangle$ and $|-1/2, +m_I\rangle$ are degenerate in zero field and are thus *completely* mixed even by small off-diagonal terms in the Hamiltonian which connect them. For $m_I > 0$, such terms $A_{xx} S_x I_x$ and $A_{yy} S_y I_y$ are provided already by an isotropic hyperfine coupling.¹ In the following we refer to the states that result from this mixing as the $|+\rangle$ and $|-\rangle$ states. Neither m_S nor m_I is a good quantum number for the resulting states, so that the concept of an indirect observation of the nuclear spins *via* the electron spins breaks down for the $m_S = \pm 1/2$ manifolds. Though there are resonances in the frequency band that is usually covered by ESEEM and ENDOR techniques, the corresponding transitions are by no means nuclear spin transitions, in particular they should exhibit much shorter relaxation times and they are broadened even by small strain effects and small external fields. The $|+m_S, -m_I\rangle$ and $|-m_S, +m_I\rangle$ states with $m_S \neq 1/2$ are also degenerate at zero field, but there are no terms in the unperturbed Hamiltonian that connect them, so that no mixing occurs. Therefore, nuclear transitions can be observed in the $m_S \neq \pm 1/2$ manifolds, i.e., for half-integer electron spins $S \geq 3/2$.

8.1.2 Description of pulse experiments at zero magnetic field

For a theoretical description of pulse ESR experiments at zero magnetic field, the density operator at Boltzmann equilibrium must be derived and mw excitation must be treated under the consideration that degenerate transitions exist. The former problem is easily solved by substituting \mathcal{H}_{ZF} for \mathcal{H}_0 in Eq. (2.23). In this calculation, one can usually drop \mathcal{H}_{NQ} and the ligand hyperfine interactions, cf. Eq. (8.1), since these terms are much smaller than the zero-field splitting and the central ion hyperfine interaction. For the

1. These states are mixed whenever $A_{xx} + A_{yy} \neq 0$. For $m_I < 0$, the states are mixed if $A_{xx} - A_{yy} \neq 0$, which requires an anisotropic hyperfine coupling.

measurements at X-band frequencies described below, the zero-field splitting is by far the dominant interaction and the density operator at Boltzmann equilibrium can be written as

$$\sigma_0 = -S_z^2, \quad (8.2)$$

where we have dropped a constant factor since we are only concerned with relative intensities.

The problem of excitation is formally analogous to the one encountered in zero-field nuclear quadrupole resonance (NQR) spectroscopy. An insightful discussion is given in [8], two theoretical approaches have been provided by Bloom et al. [157] and Das and Saha [158]. The first of these approaches does not apply density operator formalism but makes use of a rotating frame description which leads to a tremendous simplification and much physical insight. The second approach is based on the density operator formalism together with a rather complicated calculation of the propagator for the excitation by explicit integration of the time-dependent Schrödinger equation. Here we follow basically the first approach, but reformulate it using the tools provided in Chapter 2. For the explanation we restrict ourselves to an $S=3/2$ system, the extension to larger S being straightforward.

The usual rotating frame approach runs into problems at zero field, since both circularly polarized components of the mw field interact with the electron spin, one of them with transitions $m_S \leftrightarrow m_S+1$, $m_S > 0$ and the other one with transitions $m_S-1 \leftrightarrow m_S$, $m_S < 0$.¹ However, we can use a counterclockwise rotating frame for the $m_S > 0$ subspace and a clockwise rotating frame for the $m_S < 0$ subspace, since the excitation does not mix the

1. The $-1/2 \leftrightarrow +1/2$ transition is not driven by the mw excitation. Note also, that this transition is not polarized if the density operator in Boltzmann equilibrium is given by Eq. (8.2).

two subspaces.¹ The application of the mw pulse can then be written as a unitary transformation with the propagator

$$U_{ZFP} = \exp\{-i\beta(S_x^{+1/2 \leftrightarrow +3/2} + S_x^{-3/2 \leftrightarrow -1/2})\}, \quad (8.3)$$

where $\beta = \cos(\theta)\omega_1 t_p$ is the flip angle, the $S_x^{m \leftrightarrow m+1}$ are single transition operators, and where we have neglected the static Hamiltonian \mathcal{H}_{ZF} during the pulse. The z -axis of the coordinate frame is the quantization axis of the electron spin and the x -axis is the projection of the direction of the linearly polarized mw field onto the xy -plane. The angle between the z -axis and the mw field direction is θ . For an ideal pulse of zero duration, no subspace rotation actually takes place and the resulting density operator is correct. It is necessary however to consider the finite pulse length, since the subsequent description of the evolution is not done in the rotating frame. We must then backrotate the two subspaces after the application of the pulse. The backrotation corresponds to the application of a unitary transformation with the propagator

$$U_{BR} = \exp\{-i\omega_{mw} t_p S_z^2\}. \quad (8.4)$$

For on-resonant excitation, it can be shown easily that the product $U_{BR}U_{ZFP}$ is the same propagator as calculated by Das and Saha by explicit integration of the time-dependent Schrödinger equation [158].

In contrast to the case of a fictitious spin 1/2 at high field, it is not feasible here to describe the *free evolution* of the system in the rotating frame, since the two subspaces $m_S > 0$ and $m_S < 0$ are usually mixed by \mathcal{H}_{ZF} and can no longer be rotated independently of each other. Instead, the evolution can be conveniently calculated in the eigenbasis of \mathcal{H}_{ZF} . The detection is then described by Eq. (2.26) with

$$M_x(t) = C_{\text{det}} \text{trace}\{\sigma(t) (S_x^{+1/2 \leftrightarrow +3/2} + S_x^{-3/2 \leftrightarrow -1/2})\}. \quad (8.5)$$

With this approach, the results for the NQR two-pulse echo signal and modulation in zero and weak magnetic fields [157,158] can be easily reproduced.

1. The senses of rotation are given here for a positive zero-field splitting. As long as one uses linearly polarized mw fields, they are of no further interest.

8.1.3 Conditions for the observation of echo modulations

As we have seen above, the states $|+1/2, -m_I\rangle$ and $|-1/2, +m_I\rangle$ are degenerate in zero field and are completely mixed by an isotropic hyperfine coupling ($m_I > 0$). This suggests that mw irradiation on-resonant with transitions between the $|+\rangle$ and $|-\rangle$ states and the $|+3/2\rangle$, $|-3/2\rangle$ states can create electron-nuclear zero and double quantum coherences. This is indeed the case, however, as long as the symmetry between the $m_S > 0$ and $m_S < 0$ subspaces is retained, all coherence transfer echoes cancel and no two-pulse echo modulation is observed. The symmetry under consideration is between $|m_S, m_I\rangle$ and $| -m_S, -m_I\rangle$ states and cannot be broken by hyperfine interactions that depend on the product of m_S and m_I . On the other hand, the symmetry is broken by the electron Zeeman interaction in a weak external field, and two-pulse ESEEM is then observed. The frequencies depend on both the external field and the hyperfine interaction and the modulation is expected to decay fast because of the orientational broadening connected with the electron Zeeman term.

As long as there is only isotropic hyperfine coupling, no NC can be created by mw pulses in zero field. For an $S=3/2$, $I=1/2$ system this can be seen easily by partitioning the original spin states into two groups $\{|+3/2, +1/2\rangle, |+1/2, +1/2\rangle, |-1/2, -1/2\rangle, |-3/2, -3/2\rangle\}$ and $\{|+3/2, -1/2\rangle, |+1/2, -1/2\rangle, |-1/2, +1/2\rangle, |-3/2, +3/2\rangle\}$. Mw excitation or the isotropic hyperfine interaction can mix only states within the two groups, while NC is a coherent superposition of states belonging to different groups. Note that the two groups are mixed in a weak field that is not parallel to the quantization axis of the electron spins or if the hyperfine interaction is anisotropic.

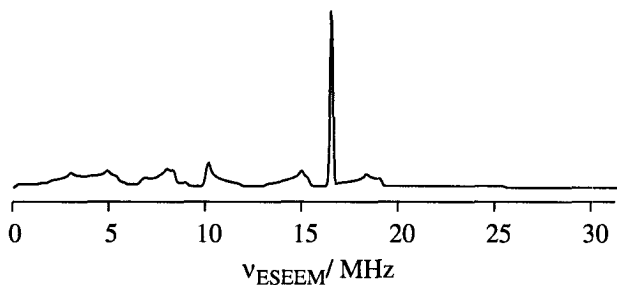


Fig. 8-1 Three-pulse ESEEM powder spectrum of an $S=3/2$, $I=1/2$ model system with purely anisotropic hyperfine coupling in a field of about 0.1 mT (simulation, see text for parameters).

Analytical calculations become too involved if the effects of nuclear quadrupole interactions and/or weak external fields have to be considered. Therefore, numerical simulations of three-pulse ESEEM experiments based on the approach discussed in §8.1.2 were performed using the program GAMMA [89]. For $I=1/2$, we found that the stimulated echo is unmodulated for a purely isotropic hyperfine interaction in both zero field and weak fields, and for an anisotropic hyperfine interaction in zero field. In the case of anisotropic hyperfine coupling in a weak external field, an ESEEM effect is found, and integration over the possible orientations between the external field and the ZFS tensor axis reveals that only one narrow line appears in the spectrum (see Fig. 8-1). A system with purely anisotropic hyperfine coupling of axial symmetry has been assumed, corresponding to a case where the point-dipole approximation is valid. The parameters were $\Delta a/2\pi=6.43$ MHz, $\omega_S/2\pi=3$ MHz, $\theta_{\text{HF}}=37^\circ$, where Δa is the anisotropic hyperfine coupling, ω_S the electron Zeeman interaction in angular frequency units, and θ_{HF} the angle between the electron-nuclear axis and the z -axis of the ZFS tensor which was assumed to be of axial symmetry with $D/2\pi=4.5$ GHz (see Fig. 8-2). Spiral sampling [159] with 28657 points was used for the integration over the angles θ_S and ϕ_S that characterize the orientation of the external field with respect to the molecular coordinate system. A homogeneous linewidth of 100 kHz has been assumed for the ESEEM lines. The nuclear Zeeman interaction can be neglected in fields up to about 10 mT and has not been included in the simulation.

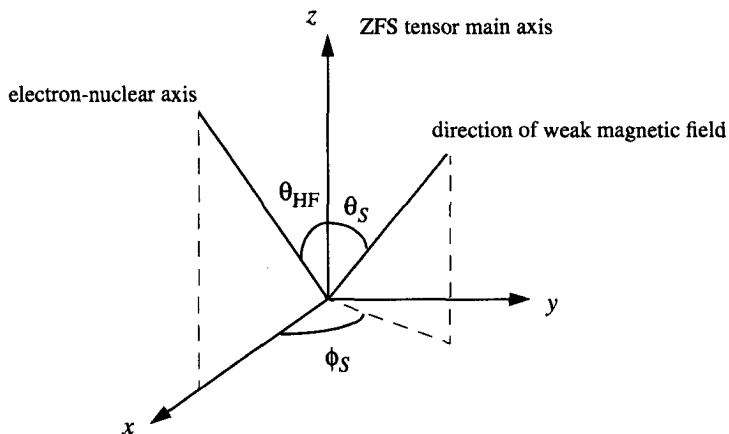


Fig. 8-2 Definition of angles for the simulation of three-pulse ESEEM on an $S=3/2$, $I=1/2$ model system (cf. Fig. 8-1).

The single narrow line can be traced back to the common nuclear frequency in the $m_S=\pm 3/2$ manifolds which does not depend on the electron Zeeman interaction. We find for the frequency of this line $\omega_{\pm 3/2} = \frac{3}{4}\sqrt{10 + 6\cos(2\theta_{\text{HF}})}\Delta a$ and with the given parameters $\omega_{\pm 3/2}/2\pi = 16.46$ MHz. From the simulated spectrum we obtain $\omega_{\pm 3/2}/2\pi = (16.48 \pm 0.03)$ MHz in good agreement with the expected value. This example shows that the resolution advantage of zero-field ESEEM is retained in weak fields for the measurement of nuclear frequencies except for the $m_S=\pm 1/2$ manifolds.

For $I>1/2$ with nuclear quadrupole interaction and anisotropic hyperfine interaction our simulations show that an ESEEM effect occurs both in zero field and in weak fields, *irrespective* of the mutual orientation between the ZFS tensor, nuclear quadrupole tensor, and the hyperfine interaction matrix. An example is treated in §8.2.2.

8.2 Experimental

8.2.1 Two-pulse ESEEM

As a model system for zero-field ESEEM and ENDOR we have used the $[\text{MnCl}_4(\text{H}_2\text{O})_2]^{2-}$ center in polycrystalline Mn(II)-doped ammonium chloride. The Mn^{2+} -ion occupies an interstitial site in the lattice and two of the neighbour ammonium ions are replaced by water molecules for charge compensation (see Fig. 8-3). The structure of the Mn-center has been established by X-ray diffraction for Mn-rich phases [160], for small Mn concentrations only indirect ESR evidence was obtained earlier from conclusions on the symmetry of the environment of the Mn^{2+} ion [161]. No chlorine or proton hyperfine splittings are resolved in the ESR spectra. The zero-field ESR spectrum of this center has been measured by Bramley and Strach [162].

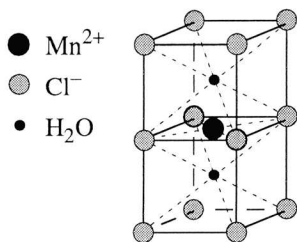


Fig. 8-3 Structure of the $[\text{MnCl}_4(\text{H}_2\text{O})_2]^{2-}$ center in polycrystalline Mn(II)-doped ammonium chloride.

A sample of ammonium chloride doped with 0.08 Mol% of manganese(II)chloride has been prepared according to Ref. [162], the same procedure was used for the preparation of a deuterated sample from anhydrous MnCl_2 , D_2O and NDCl_4 . All measurements have been performed at a temperature of 15 K on a Bruker ESP 380E spectrometer equipped with a DICE ENDOR system and a Bruker EN 4118 ENDOR probe head. Experiments at the earth field (20 μT) were performed with the probe head placed sufficiently far away from the magnet. In two-pulse and three-pulse ESEEM experiments and in HYSORE and Mims-ENDOR, nominal pulse lengths of 8 ns ($\pi/2$ pulse) and 16 ns (π pulse) were used. The minimum interpulse delay τ_0 in two-pulse ESEEM as well as the interpulse delay τ between the first two pulses in three-pulse ESEEM, HYSORE,

and Mims-ENDOR was 88 ns. The rf pulse length was 5 μ s for Mims-ENDOR and 10 μ s in the Davies-ENDOR and TRIPLE experiments, a selective mw inversion pulse of 192 ns duration was used in the latter two experiments, where the ENDOR effect was detected via the FID following a 400 ns mw read-out pulse of flip angle π . The mw frequency was in the range between 9.689 GHz and 9.723 GHz in all experiments, no significant changes of the two-pulse and three-pulse ESEEM spectra were observed in this frequency region. From the zero-field ESR measurements at room temperature, one obtains a theoretical frequency for the transition at $2D+5A_{Mn}/2$ of 9.639 GHz, all other transitions are much farther apart from the frequencies used by us. Note that D may depend slightly on temperature. Two observer transitions overlap at $2D+5A_{Mn}/2$, each of them shows twofold degeneracy. The states contributing to the transitions can be specified by $|m_S, m_{Mn}\rangle$, where m_{Mn} is the magnetic quantum number of the manganese nuclear spin. One of the observer transitions is the one between the $|\pm 1/2, \pm 5/2\rangle$ and the $|\pm 3/2, \pm 5/2\rangle$ states, for the other one, only the upper state can be characterized ($|\pm 3/2, \mp 3/2\rangle$), the lower states being a mixed states due to the largely isotropic manganese hyperfine coupling.

The two-pulse ESEEM signal decays fast even in measurements at the earth field of 20 μ T (see Fig. 8-4a), so that only a few periods of the modulation can be observed. Accordingly, the resolution in two-pulse ESEEM spectra is poor. In agreement with theory, the two-pulse ESEEM signal depends strongly on the external field (Fig. 8-4b-d), so that at magnetic fields larger than 20 mT the two-pulse echo decays within the dead time of the spectrometer. No attempt has been made to compensate the earth field for a "true" zero-field measurement, since the resolution limits due to fast relaxation of the EC would preclude the use of two-pulse ESEEM as a spectroscopic tool for structure determination on this sample even if there was no influence of the external field.

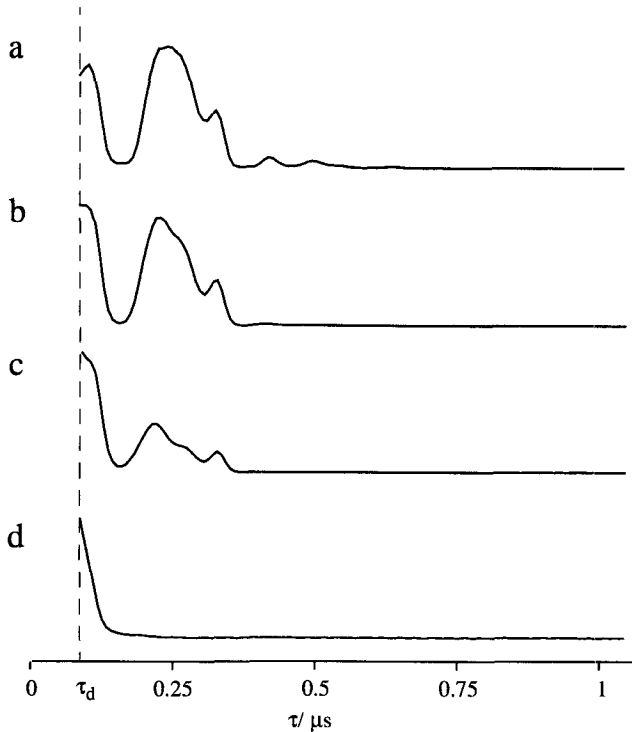


Fig. 8-4 Two-pulse ESEEM time-domain traces of the $[\text{MnCl}_4(\text{H}_2\text{O})_2]^{2-}$ center in Mn(II)-doped polycrystalline ammonium chloride at different magnetic fields. τ_d is the dead time. a) Earth field ($20 \mu\text{T}$). b) Residual field of the magnet ($150 \mu\text{T}$). c) 2.5 mT . d) 10 mT .

8.2.2 Three-pulse ESEEM

In contrast to the fast decay of the two-pulse ESEEM signal, the three-pulse echo envelope modulation persists for several microseconds (see Fig. 8-5). The modulation depth is close to unity. In addition, the time-domain pattern does not depend significantly on the magnetic field below about 2.5 mT , only a loss in sensitivity is observed.

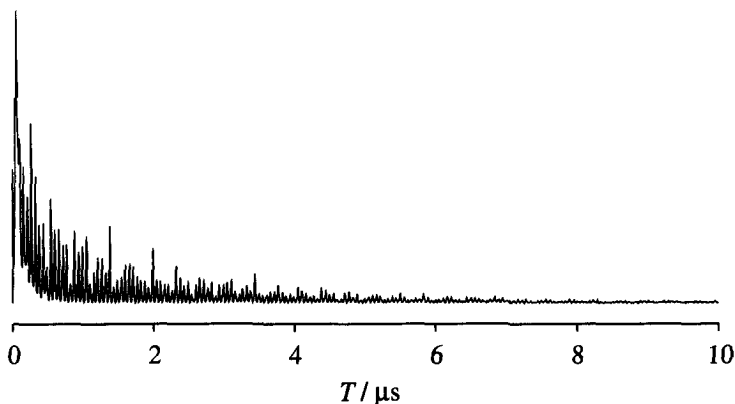


Fig. 8-5 Three-pulse ESEEM time-domain trace of the $[\text{MnCl}_4(\text{H}_2\text{O})_2]^{2-}$ center in Mn(II)-doped polycrystalline ammonium chloride at earth field ($20 \mu\text{T}$).

The corresponding spectrum is characterized by a large number of peaks (see Fig. 8-6). This can be rationalized by the fact, that in a strong mixing situation as it is encountered here, each of the two chlorine isotopes may give rise to peaks at six nuclear basic frequencies in a given electron spin manifold and that combination peaks have significant intensities because of the large modulation depth. On the other hand, the four nearest chlorine neighbours are magnetically equivalent in a zero-field situation for the structure shown in Fig. 8-3, narrow lines are expected only in the $m_S = \pm 3/2$ manifolds, and the nuclear frequencies do not depend on the sign of m_S . For $m_S \neq \pm 1/2$, a nuclear spin Hamiltonian can be defined that is given in zero field by

$$\mathcal{H}_n(m_S) = P \left[3I_z^2 - I(I+1) + \frac{1}{2}\eta(I_+^2 + I_-^2) \right] + 2m_S(AI_z + B_xI_x + B_yI_y), \quad (8.6)$$

which simplifies for an axial nuclear quadrupole tensor ($\eta=0$) to

$$\tilde{\mathcal{H}}_n(m_S) = P[3I_z^2 - I(I+1)] + 2m_S(AI_z + BI_x). \quad (8.7)$$

To determine parameters sets in Eq. (8.6) or (8.7) that are in agreement with the experimental spectrum, one has to recognize the nuclear basic frequencies. This has been done by searching the peak list of the experimental spectrum for frequencies that are sums or differences of other frequencies and for peak pairs that feature a frequency ratio between

0.7871 (ratio of the nuclear quadrupole moments of ^{37}Cl and ^{35}Cl) and 0.8324 (ratio of the corresponding nuclear g -values). Furthermore, the intensity ratio between peaks at a ^{35}Cl and ^{37}Cl basic frequency should be approximately 3:1, since the natural abundances are 75.77% and 24.23%, respectively,¹ and combination peaks should have a lower intensity than the peaks at the contributing basic frequencies. With these informations at hand, it was possible to identify five pairs of basic nuclear frequencies, they are labelled in Fig. 8-6a.

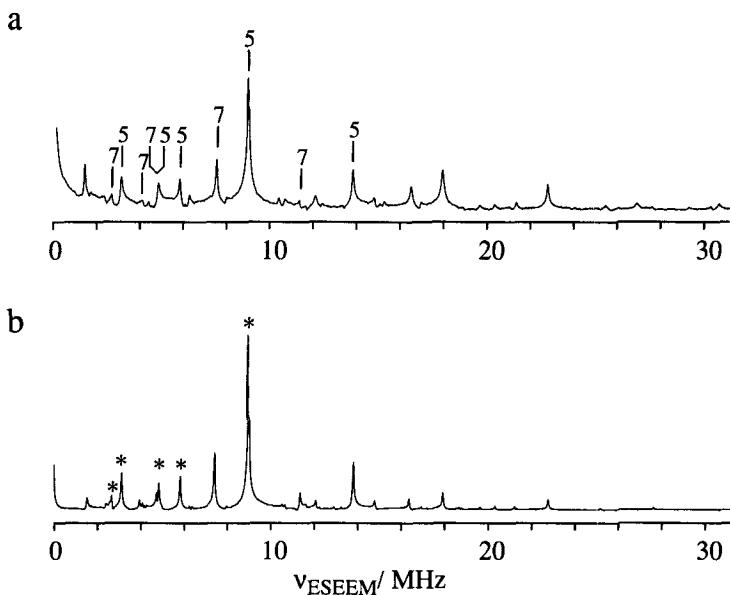


Fig. 8-6 Three-pulse ESEEM spectrum of the $[\text{MnCl}_4(\text{H}_2\text{O})_2]^{2-}$ center in Mn(II)-doped polycrystalline ammonium chloride at earth field (20 μT). a) Experimental spectrum. The labels designate ^{35}Cl (5) and ^{37}Cl (7) basic frequencies. b) Simulated spectrum (see text). The asterisks designate peaks that have also been found in the ENDOR spectrum.

The basic frequencies for each of the two isotopes can be expressed as sums and differences of only three independent parameters, suggesting that the nuclear quadrupole tensor is axial within the experimental error limits. Therefore, Eq. (8.7) was used for fur-

1. This relation is only approximate, since the blind spot behaviour may differ for the two related lines.

ther parameter evaluation. A grid search was performed for the region $0 < P, A, B < 2\pi \cdot 10$ MHz, the parameter sets that fit the five ^{35}Cl basic frequencies within experimental error are summarized in Tab. 8-1 together with the missing sixth basic frequency and the quality of the fit of the ^{37}Cl basic frequencies. The parameters for ^{37}Cl can be calculated from the ^{35}Cl parameters using the known ratios of the nuclear quadrupole moments and of the nuclear g values. Only two parameter sets lead to the sixth basic frequency that is found in the ENDOR spectra (see §8.2.3), while only one of them fits all *ten basic frequencies of both isotopes* in the ESEEM spectrum within experimental error.

Table 8-1 Parameter sets fitting the five ^{35}Cl nuclear basic frequencies in the ESEEM spectrum displayed in Fig. 8-6a, calculated value for the missing sixth basic frequency, and quality of the fit of the corresponding ^{37}Cl frequencies. P : nuclear quadrupole coupling, A : secular hyperfine coupling, B : pseudo-secular hyperfine coupling.

$P/(2\pi \text{ MHz})$	$A/(2\pi \text{ MHz})$	$B/(2\pi \text{ MHz})$	$\nu_6 / \text{ MHz}$	^{37}Cl fit quality
2.110	0.902	1.017	7.99	within experimental error
3.56	0.70	0.79	7.99	larger than experimental error
4.36	0.37	0.83	10.72	larger than experimental error
4.78	0.55	0.45	10.72	larger than experimental error

A complete simulation of the three-pulse ESEEM spectrum *at earth field* would require a powder integration, since the *intensities* depend on the orientation of the center with respect to the earth field. This problem arises because of the involvement of EC in the $|+\rangle$ and $|-\rangle$ manifolds in the preparation of the NC. Even at zero field, strain might play a role. We have therefore taken the intensities of the five peaks at the ^{35}Cl basic frequencies from the experimental spectrum and assumed that the cumulative modulation depth is unity. It is then possible to calculate the modulation pattern including the combination lines by applying the product rule to all possible isotope combinations and computing the weighted sum (32.96% centers with four nearest neighbour ^{35}Cl , 42.16% with three ^{35}Cl , 20.22% with two ^{35}Cl , 4.31% with one ^{35}Cl , and 0.35% with only ^{37}Cl). The result of the simulation is shown in Fig. 8-6b. The simulated spectrum fits the frequencies of all the observed ESEEM lines nicely, though there are significant deviations in the relative intensities. These deviations may result from two reasons. First, the blind spot

behaviour is not the same for ^{35}Cl and ^{37}Cl as is implicitly assumed in our approach and second, the modulation depth may be slightly smaller than unity. Nevertheless, the simulation confirms the conclusions that the four nearest chlorine neighbours are magnetically equivalent in zero field, that the nuclear quadrupole tensor is axial and that no peaks with significant intensity in the ESEEM spectrum are caused by other nuclei. The last point is also supported by the fact that no changes in the three-pulse ESEEM spectrum are observed on complete deuteration of the sample.

8.2.3 ENDOR

Zero-field cw ENDOR has been performed earlier by Ishchenko et al. on Gd^{3+} centers ($S=7/2$) in GaSe, using an $m_S=\pm 5/2 \leftrightarrow \pm 7/2$ transition at 8.646 GHz as the observer transition [163]. The spectrum was due to Ga nuclei ($I=3/2$) and was explained by the Hamiltonian given in Eq. (8.6), where the nuclear quadrupole part was written in terms of irreducible tensor operators. In addition, zero-field ENDOR has been observed optically in a number of cases, usually in $S=1$ systems (triplet states), see for instance [164,165]. The following examples represent the first zero-field pulse ENDOR spectra.

Mims-ENDOR (see Fig. 8-7a) has normally a sensitivity advantage as compared to Davies-ENDOR since it uses non-selective excitation. In the case at hand, the large modulation depth cancels this advantage; the ENDOR effect can only be observed for the part of the echo that still persists after the time which is needed for an rf pulse and for the ringing in the rf circuit to decay to a level where it does not perturb ESR detection. To obtain sufficient sensitivity, we were therefore forced to use rf pulses of only 5 μs duration (cf. Fig. 8-5) while pulses of twice this duration could be used in Davies-ENDOR (see Fig. 8-7b-d). The relative line intensities in Mims-ENDOR did not strongly depend on the interpulse delay τ between the first two mw pulses. The same frequencies appear in the Mims- and Davies-ENDOR spectra, compare Fig. 8-7a and b, albeit with different relative intensities of the peaks. Three of the ENDOR lines disappear on deuteration of the sample, compare Fig. 8-7b and c, while the Davies-ENDOR spectrum does not change strongly in a field of 2 mT, only its intensity decreases, see Fig. 8-7d.

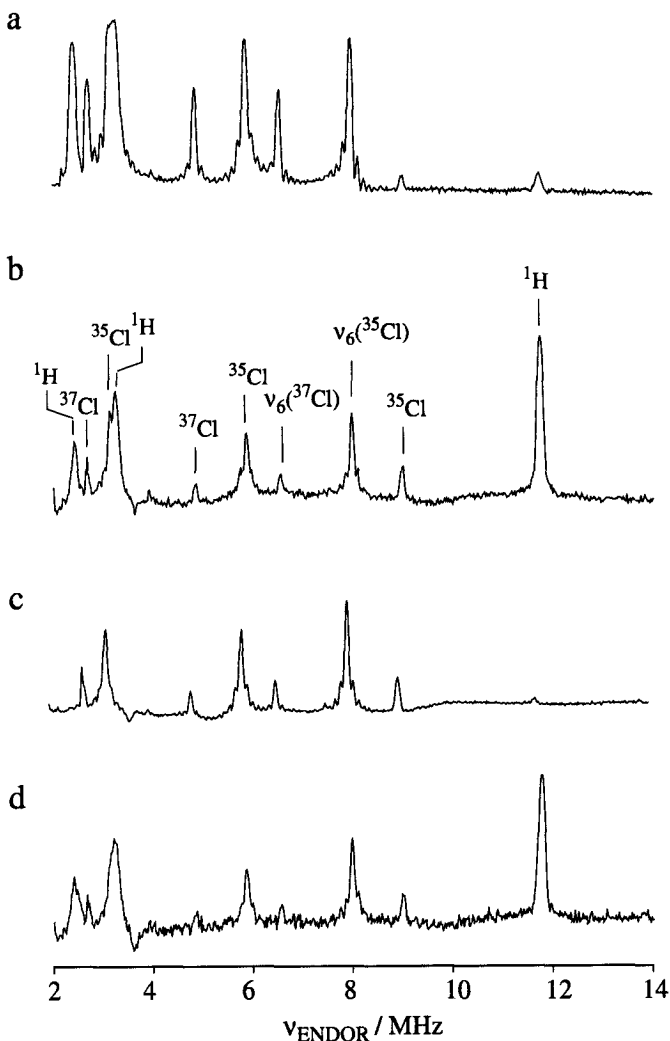


Fig. 8-7 ENDOR spectra of the $[\text{MnCl}_4(\text{H}_2\text{O})_2]^{2-}$ center in Mn(II)-doped polycrystalline ammonium chloride. a) Mims-ENDOR at earth field (20 μT). b) Davies-ENDOR at earth field. Labels designate the line assignment. ν_6 is the basic nuclear frequency missing in the ESEEM spectra. c) Davies-ENDOR at earth field of the $[\text{MnCl}_4(\text{D}_2\text{O})_2]^{2-}$ center in a completely deuterated sample. d) Davies-ENDOR at 2 mT.

Except for the three peaks that disappear on deuteration, all ENDOR signals can be explained by the basic nuclear frequencies of the nearest neighbour ^{35}Cl and ^{37}Cl nuclei

as they were found in the three-pulse ESEEM spectrum and by the missing sixth basic nuclear frequencies for the two isotopes. The information on this sixth frequency excludes two of the four parameter sets given in Tab. 8-1. Of the remaining three proton lines, the one at 11.74 MHz corresponding to $\sqrt{A^2 + B^2}/(2\pi) = 7.83$ MHz can be assigned to the water protons. The assignment of the lines at 2.42 and 3.24 MHz is less obvious, they might be due to ammonium protons.

8.2.4 Correlation experiments

To check the theoretical prediction that all spectral lines belong to the $m_S = \pm 3/2$ manifolds, correlation experiments have been performed. In a HYSORE experiment, the mw π pulse would correlate peaks in the $m_S = \pm 3/2$ manifolds with peaks in the $m_S = \pm 1/2$ manifolds. In agreement with theory, no cross peaks have been found in the HYSORE spectrum. On the other hand, a TRIPLE experiment correlates frequencies within the *same* electron spin manifold. We found that the pulse difference TRIPLE spectrum (see Fig. 8-8) contains all frequencies that occur in the Davies-ENDOR spectrum (see Fig. 8-7b), again in agreement with theory. This result did not depend on the ENDOR transition on which the fixed-frequency rf “pump” pulse was applied.

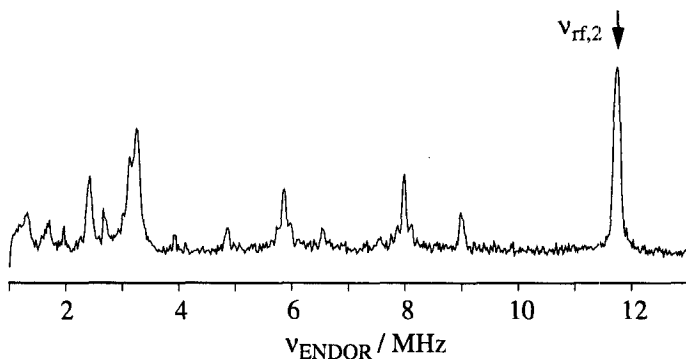


Fig. 8-8 Pulse difference TRIPLE spectrum of the $[\text{MnCl}_4(\text{H}_2\text{O})_2]^{2-}$ center in Mn(II)-doped polycrystalline ammonium chloride at earth field. The label $\nu_{\text{rf},2}$ designates the fixed “pump” frequency.

Thus, both HYSCORE and difference TRIPLE spectra do not contain any information beyond the one found in three-pulse ESEEM and ENDOR spectra, once it is established that there are indeed no peaks originating from the $m_S = \pm 1/2$ manifolds. These experiments may be useful however, when the character of the ESR observer transition is unknown. This may be the case if the zero-field splitting is not much larger than the hyperfine interaction, as for the large number of Mn^{2+} complexes with zero-field transitions at S-band frequencies.

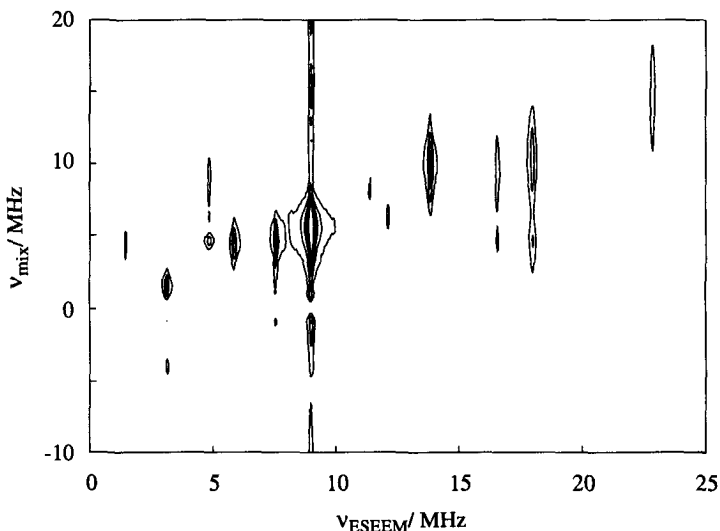


Fig. 8-9 DECENT spectrum of the $[MnCl_4(H_2O)_2]^{2-}$ center in Mn(II)-doped polycrystalline ammonium chloride in earth field.

Information beyond the three-pulse ESEEM frequencies is obtained with the DECENT experiment, see Fig. 8-9. The frequencies in the second dimension result from a mixing of $m_S = \pm 3/2$ states with $m_S = \pm 1/2$ states, the resolution in this dimension is much higher than in two-pulse ESEEM but lower than in three-pulse ESEEM. However, further work is needed to explain the frequencies in the mixing dimension *quantitatively*, since the theory provided in §8.1.2 does not take into account the influence of the static Hamiltonian during excitation.

Transient electron spin nutation

9.1 Resolution and assignment in ESR spectra

In the preceding chapters, we have dealt almost exclusively with improvements in resolution, information content, and sensitivity in the indirect detection of *nuclear* frequencies *via* the electron spin. As mentioned in the introduction, the direct measurement of *electron* spin transition frequencies has largely remained a domain of cw techniques mainly because of sensitivity considerations. However, there are cases where cw ESR spectra are not sufficiently resolved to obtain all relevant parameters of the spin Hamiltonian or where the observed patterns are so complicated that assignment problems arise in the spectrum analysis. It has proved difficult to overcome these problems with cw ESR methods while for a large part of the samples the sensitivity of pulse ESR is high enough. With increasing availability of pulse spectrometers, the bottleneck may now lie in the development of methods that improve on the resolution and information content of cw ESR spectra by using pulse ESR methodology.

Several approaches seem to be feasible to eliminate this bottleneck. Some of the methods developed for the indirect observation of nuclear frequencies can provide information on the ESR observer transition, as has been discussed in §6.3.3 for hyperfine decoupling and in §8.2.4 for zero-field *HYSORE* and *TRIPLE* experiments. On the other hand, such methods usually imply a severe sensitivity loss as compared to echo detection of the ESR spectrum and the additional information is limited. Dedicated methods for the direct observation of electron spin transitions can be designed by intro-

ducing a second dimension that differs from the ESR spectrum in its dependence on one or several spin Hamiltonian parameters. From a theoretical viewpoint, it is most satisfying to single out *one* parameter, as it is done in electron-Zeeman resolved ESR by the use of magnetic field steps, though this may be technically demanding [45,166]. Resolution enhancement can also be obtained by introducing “anisotropy” as a second dimension. This can be achieved by measuring the change in the resonance frequency of a spin caused by a slight reorientation that can in turn be effected by sample rotation about an axis which makes a right angle with the static magnetic field [45,166,167]. Again, hardware extensions are needed to perform the experiment. One could also devise ELDOR experiments using two mw frequencies to obtain correlation information on transitions in $S > 1/2$ systems. Such an experiment might be based on subsequent selective excitation of two transitions in a multi-level system to find out if these transitions share a common level. The theory is straightforward (see §10.3), but in many cases resonator bandwidth limitations prevent the application. This resonator bandwidth problem diminishes considerably in high-frequency ESR. Finally, one can introduce a second dimension in a way that does not require hardware extensions by observing the frequencies of Torrey oscillations [168] (nutation frequencies).

9.2 Nutation frequency

A Torrey oscillation or transient nutation of the magnetization is observed, if an mw field on-resonant or nearly on-resonant with an electron spin transition is suddenly switched on. For an electron spin or fictitious spin $S=1/2$ with the Hamiltonian $\mathcal{H}_0 = \Omega_S S_z$, the density operator in Boltzmann equilibrium $\sigma_0 = -S_z$, and the perturbation $\mathcal{H}_1 = \omega_1 S_x$ turned on at time $t=0$, we can diagonalize the Hamiltonian including the perturbation by the unitary transformation $U_{\text{nut}}(\mathcal{H}_0 + \mathcal{H}_1)U_{\text{nut}}^{-1}$ with

$$U_{\text{nut}} = \exp\{-i\theta_{\text{nut}}S_y\}, \quad (9.1)$$

and

$$\theta_{\text{nut}} = \text{atan}(-\omega_1/\Omega_S). \quad (9.2)$$

In its eigenbasis, the Hamiltonian takes the form

$$\mathcal{H}_{\text{nut}} = \omega_{\text{nut}} S_z, \quad (9.3)$$

with the nutation frequency

$$\omega_{\text{nut}} = \sqrt{\omega_1^2 + \Omega_S^2}. \quad (9.4)$$

The signal at time t is proportional to

$$M_y(t) = -\sin(\theta_{\text{nut}}) \sin(\omega_{\text{nut}} t). \quad (9.5)$$

Obviously, the nutation frequency increases and the signal intensity decreases with increasing resonance offset. This resonance offset broadening of nutation lines is inevitable if the nutation is observed directly after switching on the mw field, but can be reduced in an indirect observation of the nutation frequency by making either the preparation step or the detection of the experiment more selective.

Except for the resonance offset, the nutation frequency is determined by ω_1 . For an electron spin 1/2 this quantity has been derived in Eq. (3.33). For a fictitious spin, one has to take into account the fact that the matrix element of S_x for the transition between the states $|m_S\rangle$ and $|m_S + 1\rangle$ is given by

$$\langle m_S | S_x | m_S + 1 \rangle = \frac{1}{2} [S(S+1) - m_S(m_S + 1)]^{1/2}. \quad (9.6)$$

As long as m_S is a good quantum number, we have

$$\omega_1(m_S \leftrightarrow m_S + 1) = \frac{2\pi\beta_e}{\hbar} g_x B_1 [S(S+1) - m_S(m_S + 1)]^{1/2}, \quad (9.7)$$

where we have assumed that the mw field is perpendicular to the static field. The dependence of the nutation frequency on the effective spin S and on the type of transition opens up one possibility to disentangle complicated ESR spectra by introduction of a second dimension [6].

If m_S is no longer a good quantum number, one has to consider the transition probability for the particular transition. There is a conceptual difficulty in the fact that transition

probabilities are derived with disregard to coherence phenomena while a nutation can only come about because coherence exists [8]. Nevertheless, the nutation frequency for $\Omega_S=0$ and any perturbation strength¹ is proportional to the square root of the transition probability for a weak perturbation (the transition moment), where the latter one is calculated by Fermi's golden rule. The reason is that both quantities are related to the matrix element of the perturbation between the two states under consideration (see for instance [10]). The importance lies in the fact that a vast body of approaches to the calculation of transition probabilities does already exist [41].

The measurement of nutation frequencies thus opens up direct access to transition probabilities. In contrast, the intensities of cw ESR signals depend not only on transition probabilities but also on relaxation times, so that a quantitative analysis can be complicated or even impossible. In addition, overlapping lines can be separated in the nutation dimension if they belong to transitions with different transition probability that do not have a common level.

Eq. (9.7) shows that the nutation frequency also depends on the mw field B_1 and on the g -value in the direction of this field. Since most of the line broadening mechanisms in the nutation dimension lead to a linear increase of the linewidth with B_1 , the whole spectrum scales linearly with B_1 except for the contribution of relaxation to the linewidth which remains constant. To obtain ultimate resolution, B_1 should then be large enough to make relaxational broadening insignificant,

$$\omega_1 \gg \frac{2\pi}{T_2}. \quad (9.8)$$

This requirement often precludes direct observation of the nutation unless a bimodal resonator is used to isolate the detection channel from the excitation power. The dependence on B_1 also means that any inhomogeneity of the B_1 field over the sample leads to additional line broadening. The requirements on B_1 homogeneity to make this type of broadening insignificant depend strongly on the type of sample. For disordered systems,

1. The perturbation must not be strong enough, however, to excite another transition that shares a level with the transition under consideration. This case is discussed later on.

other broadening mechanisms are usually dominant so that normal sample volumes in any type of resonator can be used. With single crystals or with systems with largely isotropic g -matrices, particularly if there are few or none ligand interactions, one is either restricted to a small sample volume or has to use a resonator with a highly homogeneous magnetic field distribution if ultimate resolution is sought. This point has been investigated in more detail in [169].

In a single crystal, the value of g_x can be derived from the g -matrix and the orientation of the crystal with respect to the static field [16,41]. If ESR lines of different sites overlap, they can be separated in the nutation dimension whenever the g_x values of the two sites differ by a sufficient amount [6]. Furthermore, it is possible to determine very small g -values corresponding to very large resonance fields *via* a nutation experiment [170]. This is possible since the ESR observation can be performed at a small resonance field corresponding to the g -value in a direction perpendicular to the direction of the abnormally small g -matrix principal value. Obviously, large B_1 fields are needed to fulfil condition (9.8), and indirect observation becomes mandatory. Nevertheless, B_1 fields of the required magnitude are easier to achieve than the static fields needed to observe ESR signal at g -values below about 0.5.

In disordered systems, selective excitation chooses spin packets within a narrow band of g_z -values at least in the absence of large hyperfine couplings. This does however not necessarily lead to a narrow distribution of g_x -values. If the g -matrix is visualized by an ellipsoid, the resonance frequency and thus the g_z -value defines a sphere that cuts the ellipsoid in two curves. For a g -matrix with axial symmetry these curves are circles (see Fig. 9-1a), in a general case the curves do not lie in a plane. Each point on the cutting curves corresponds to a set of possible orientations. The direction of the static field (z -axis) is given by the radius that connects the center of the ellipsoid with a given point on a cutting curve. A plane perpendicular to this radius through the center of the ellipsoid characterizes the xy -plane that cuts the ellipsoid in another curve (cf. Fig. 9-1b). The set of the new cutting curves for all points on the two original cutting curves defines a segment of the g -matrix ellipsoid. Any radius in this segment of the ellipsoid is a possible g_x -value (cf. Fig. 9-1c). Obviously, the distribution of g_x -values and hence of nutation

frequencies can become rather broad for large g -anisotropies. An experiment for the measurement of nutation frequencies should be able to recover these broad distributions.

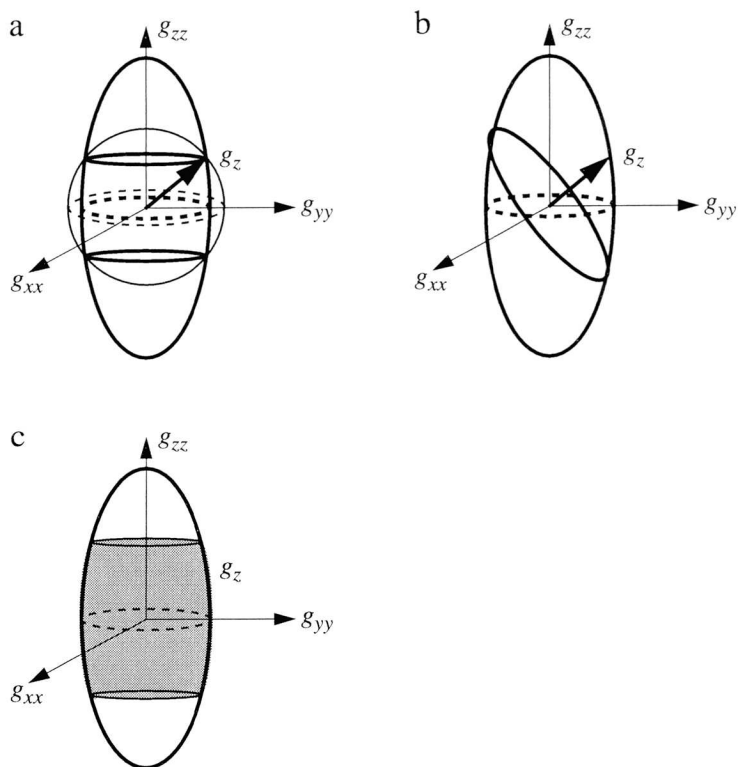


Fig. 9-1 Visualization of the distribution of g_x values for a given g_z value for a g -matrix with axial symmetry. a) A sphere with radius g_z (narrow outline) cuts the ellipsoid characterizing the g -matrix with principal values g_{xx} , g_{yy} , g_{zz} . Any point of the two cutting circles is related to orientations on-resonance. b) The radius from the center of the ellipsoid to a point on a cutting circle is along the static field direction. A plane through the center of the ellipsoid and perpendicular to this radius cuts the ellipsoid in an ellipse. c) The set of all possible cut ellipses determines a segment of the g -matrix ellipsoid (grey). Any radius connecting the center of the ellipsoid with a point on this segment is a possible g_x value.

Though the hyperfine coupling does not directly influence the nutation frequency, it may lead to indirect effects in several ways. If the high-field approximation is no longer fulfilled for the electron spin with large central ion couplings, there is an influence of the hyperfine coupling on the transition probability and forbidden transitions with small

transition probabilities can be observed. In addition, large hyperfine couplings can bring spin packets with significantly different g_z -values on resonance at the same field. This leads to additional broadening in the nutation dimension (indirect hyperfine broadening), or, in favourable cases, to the resolution of transitions belonging to different magnetic quantum numbers of the central ion nuclear spin.

Up to this point we have restricted our discussion to the excitation of a two-level sub-system, corresponding to the case where B_1 is small enough to allow for the selective excitation of only one electron spin transition. If two transitions are simultaneously excited that share a common level but are isolated from all other transitions, one has a three-level system that can be treated in the way described in §3.2.4. A more common case is the one of a fictitious spin coupled to nuclear spins of ligand nuclei. This leads to a group of transitions spread over a frequency band with the width $\Delta\omega$. As long as $\omega_1 \gg \Delta\omega$, where ω_1 corresponds to the fictitious spin disregarding all ligand couplings, there is no influence of the (completely decoupled) ligand nuclei on the nutation experiment whatsoever. A somewhat similar situation is encountered for a small ZFS interaction, i.e., when the mw perturbation term in the Hamiltonian is much larger than the ZFS term. In this case, all transitions in a $S > 1/2$ system are driven at the same time, and ω_1 is given by Eq. (3.33). This result may be surprising since the nutation frequency for each of the single transitions is larger, cf. Eq. (9.7), but it is an immediate consequence of the fact that spin operators are generators of rotations and that their commutation relations do not depend on S . There are no simple formulas for the nutation frequencies in the intermediate regime where the mw perturbation is of the same order of magnitude as the ZFS term.

On the other hand, if ω_1 is much smaller than the hyperfine couplings, one can define new fictitious spins corresponding to single electron spin transitions in the multilevel system. The transition moments of the single transitions can be calculated according to Eq. (3.11). For ligand nuclear spins $1/2$, the $\langle i_k | j_k \rangle$ reduce to the $\cos\eta_k$ and $\sin\eta_k$ that are given by Eqs. (3.13) and (3.19). This regime is encountered only for weak mw fields as used in direct detection experiments [6]. In the intermediate regime, where the excitation is neither transition-selective nor non-selective, a treatment of the full Hamiltonian

including the perturbation is needed. If the coupling is only to a single nucleus, the approach in §3.2.7 can be used. Generally, the mw field introduces additional state mixing in this regime, and the nutation frequencies are no longer proportional to the transition moments of the unperturbed system. Other Hamiltonian parameters, like the nuclear Zeeman interaction, ligand hyperfine interaction, and nuclear quadrupole interaction may have a strong effect on the frequencies that are observed in the nutation dimension, especially if ω_1 approximately matches the nuclear frequencies that would be observed in the absence of hyperfine coupling. For more than one ligand nucleus, this regime can no longer be described analytically since the product rule breaks down. It is advisable to avoid this strong mixing regime. At X-band frequencies and below, one can normally use $\omega_1 \gg \omega_I$ for all nuclei, and $\omega_1 \ll \omega_I$ can be used at W-band frequencies and above.

In conclusion, nutation frequencies can in some cases depend on many parameters and broad distributions can then lead to insufficient resolution for disordered systems. However, in most systems only a part of these parameters plays a role and a number of situations exists where only one of them is significant. In ordered systems, the resolution in the nutation dimension is usually sufficient if strong mixing situations for the ligand interactions are avoided. In particular, nutation spectroscopy is well suited to detect forbidden transitions that overlap with allowed transitions and to provide information on transition probabilities. A suitable pulse sequence should allow for a broad range of mw field strengths for adaptation to the system under investigation, hence it should facilitate indirect detection of the nutation. In addition, it should be able to recover broad distributions of nutation frequencies.

9.3 PEANUT sequence

Broad frequency distributions can be detected *via* an echo. The suitable echo for nutation frequencies is the rotary echo which was originally introduced to refocus rf field inhomogeneities in NMR experiments [171]. The phase inversion of the coherences in the rotating frame that is necessary for the refocusing is effected by a phase inversion of the driving field (see Fig. 9-2a) and the echo is superimposed on the strong mw irradiation which causes detection problems. Indirect observation can be achieved by echo detection of the rotary echo in the **Phase-inverted Echo-Amplitude detected NUTation**

(PEANUT) sequence (see Fig. 9-2b). The possibility to select spin packets with a narrow distribution of Ω_S by using an mw $\pi/2$ pulse of lower power is an additional advantage of this sequence.

The length of the whole sequence, $t_{\pi/2} + 2\tau + T$, remains constant during the experiment; the incrementation of t merely shifts the boundary between the two opposite phase parts of the high-turning angle (HTA) pulse. Therefore, relaxation does not directly contribute to the linewidth, though it must be taken into account in selecting an appropriate T value. The same phenomenon has been discussed in the context of 1D hyperfine spectroscopy (see §7.2.1).

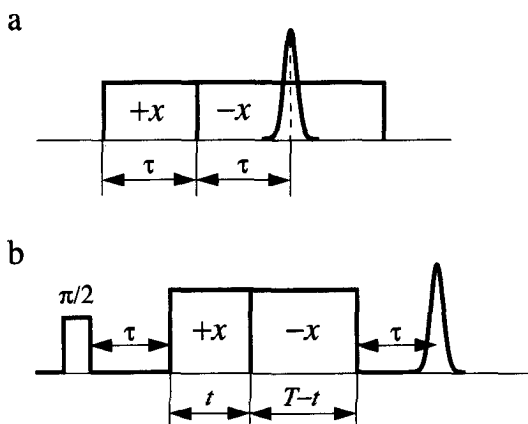


Fig. 9-2 Pulse sequences for the observation of nutation echoes. a) Rotary echo sequence [171]. b) PEANUT sequence. Time t is incremented, the echo is centered at $t = T/2$.

The echo is modulated with respect to t with *twice* the nutation frequency in the PEANUT experiment, since the magnetization nutates in one direction during the first part of the HTA pulse and in the opposite direction during the second part of it. In addition, there are contributions that are modulated with the nutation frequency for $t \rightarrow 0$ and $t \rightarrow T$. These components are not refocused; they originate from the transfer of EC to polarization and polarization to EC *in the rotating frame* at the phase boundary during the HTA pulse. These transfers take only place if $\theta_{\text{nut}} \neq \pi/2$, i.e., for off-resonance spin packets, or if the phases during the two parts of the HTA pulse do not differ exactly by π .

Finally, there is a contribution to the echo from a coherence transfer pathway where polarization in the rotating frame persists during the whole HTA pulse. This contribution is completely analogous to a spin-locked echo [172,173] and provides the unmodulated part of the PEANUT echo.

First experimental tests of the sequence have been performed with a home-built spectrometer [68] equipped with a bridged loop-gap resonator probe head on a sample of polycrystalline γ -irradiated calcium formate at room temperature, $\nu_{mw} = 9.003$ GHz, and with the Bruker ESP 380 equipped with an EN 4118 probe head (dielectric resonator) on a single crystal of $\text{La}_2\text{Mg}_3(\text{NO}_3)_{12} \cdot 24 \text{H}_2\text{O}$ doped with 1% Mn at 18 K, $\nu_{mw} = 9.728$ GHz.

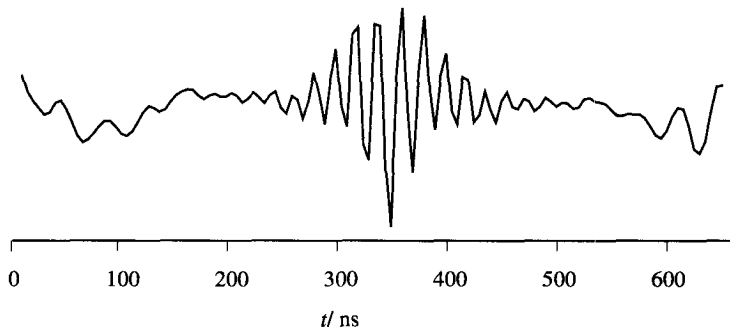


Fig. 9-3 Time-domain trace of a PEANUT experiment on polycrystalline γ -irradiated calcium formate.

In agreement with theory, the time-domain trace from the measurement on calcium formate consists of the nutation echo centered at $t \approx 345$ ns that is modulated with twice the nutation frequency and of the unrefocused contributions close to $t=0$ and $t=T=690$ ns that are modulated with the nutation frequency (see Fig. 9-3). The spin-locked echo contribution introduces only a constant offset.

A 2D PEANUT spectrum correlates the nutation frequencies to the electron spin transitions. In the example shown in Fig. 9-4, several groups of six allowed transitions as well as a group of five doublets corresponding to $\Delta m_{I, \text{Mn}} = 1$ forbidden transitions can be recognized. The multiplet splittings in the groups of allowed transitions correspond to

A_{Mn} ($I=5/2$); due to second order effects the splittings are not exactly equal within the groups. The dashed lines connecting the peaks within each group show clearly that the nutation frequency depends on the magnetic quantum number of the manganese nucleus, which is also a second order effect. At nutation frequencies below 2 MHz, forbidden transitions can be observed that coincide with allowed transitions in the ESR dimension. These transitions involve proton spin flips. More detailed studies of the PEANUT sequence and a number of application examples have been provided by Stoll [169].

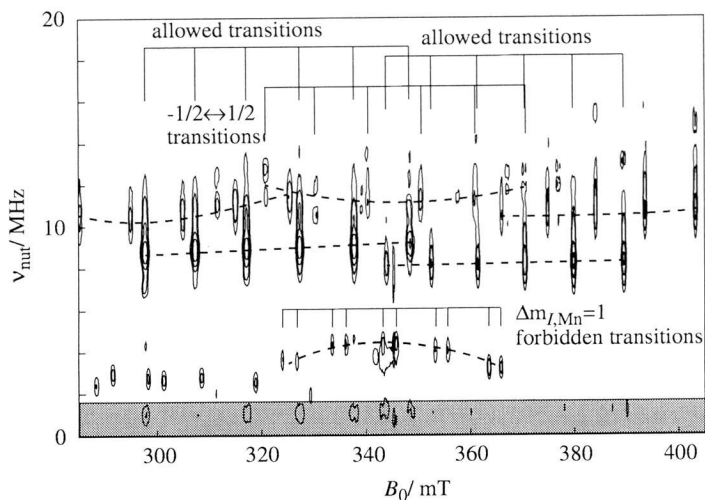


Fig. 9-4 Detail in the $g=2$ region of a PEANUT spectrum of the $[\text{Mn}(\text{H}_2\text{O})_6]^{2+}$ complex in a single crystal of $\text{Mn-doped La}_2\text{Mg}_3(\text{NO}_3)_{12} \cdot 24 \text{ H}_2\text{O}$ at arbitrary orientation. The shaded region corresponds to forbidden transitions involving proton spin flips. Only complete peak groups have been labelled.

10.1 High-field high-frequency ESR

High-field high-frequency pulse ESR spectrometers at W-Band frequencies (≈ 95 GHz) and above will become more widely available during the next few years and the focus in this field will shift from basic technical developments and feasibility studies to spectroscopic applications and method development. Arguably, this is the most important development in solid-state pulse ESR in the foreseeable future. High-field high-frequency ESR spectroscopy has a number of inherent advantages. First, the resolution of g -factor differences and anisotropies improves since the electron Zeeman interaction scales linearly with the field. This leads also to better orientation selection in ENDOR and ESEEM experiments, particularly for organic radicals. Second, relaxation times become longer for many systems at higher frequencies [174]. Third, the Boltzmann factor increases and the energy quanta become larger, so that a higher sensitivity arises. This statement has to be qualified however, since sample sizes as they are usual at X-band frequencies would exceed the wavelength in high-frequency ESR. The requirement to reduce the sample size roughly compensates for the sensitivity enhancement in going to higher fields and frequencies in ESR. However, the sensitivity advantage persists if only small quantities of the sample are available. This is often the case for biological samples, particularly, if single crystal studies of metalloproteins are intended. Fourth, systems with large zero-field splittings (>30 GHz) can be studied at higher frequencies while inaccessibly large magnetic fields may be required to observe *any* transitions of such sys-

tems at X-band frequency.¹ Fifth, it becomes possible at high frequencies to violate the high-temperature approximation with standard cryogenic systems. This can be used to gain information on the absolute sign of parameters of the spin Hamiltonian [175].

Drawbacks of high-field high-frequency ESR are mainly the higher cost of the equipment and the fact that a number of methods do no longer work that rely on the violation of the high-field approximation for the nuclei. In some cases, the resolution of hyperfine structure in the ESR spectrum becomes worse at higher fields, namely, when broadening due to g -strain limits this resolution. These drawbacks ensure that high-field high-frequency ESR will not completely supersede spectroscopy at lower frequencies and fields (e.g., at S-band and X-band frequencies). Nevertheless, the drawbacks are outweighed by the advantages to such an extent that high-field high-frequency methods will probably extend their share of applications to significantly more than 50% by the time when they are fully developed.

From the point of view of applications, the largest advantages of high-field high-frequency ESR are realized for organic radicals, where the resolution of g -factor differences and g -anisotropies is almost generally insufficient at X-band frequencies, and for quadrupole nuclei that are often in strong mixing situations at X-band frequencies (see §10.2). The largest disadvantages occur in studies of proton interactions, where ESEEM is a convenient tool at X-band frequencies but cannot be used at W-band frequencies and above because of too small modulation depths for all systems except α -protons in organic radicals and a few defect centers in crystals.

From a technical point of view, a limit of the quest for high frequencies is given by the availability of magnetic fields for the investigation of $g \approx 2$ systems. The frequency limit is then approximately 660 times the proton frequency of the latest high-resolution NMR spectrometer, i.e., 528 GHz at the moment of writing. The availability of mw components (or of far-infrared lasers at higher frequencies) is also a design criterion. Pulse ESR spectrometers have been built for W-band frequencies [176-178] and for F-Band frequencies (≈ 140 GHz) [179,180]. It has also been demonstrated that electron spin echoes

1. If the ZFS splitting for the $m_S = -1 \leftrightarrow m_S = 1$ transition is larger than the mw quant, it is already impossible to observe *all* ESR transitions of a system.

can be obtained with a pulsed far-infrared laser system at 604 GHz by using a resistive magnet [181], though this approach may be prohibitively expensive for routine application. Recently, a commercial W-band pulse spectrometer has become available from Bruker. The spectrometer is based on an intermediate frequency in the X-band, so that many components of the X-band pulse spectrometer can be used. It is probably possible to extend this concept to even higher frequencies.

The advent of high-field, high-frequency ESR will have a strong influence on ESR method development. Some, though not all resolution problems that require dedicated experiments at X-band frequencies can also be solved by going to higher fields and applying simpler pulse sequences. Some of the methods that were developed for spectroscopy in the X-band are not applicable at higher frequencies since they depend on the violation of the high-field approximation or require excitation bandwidths that cannot be provided with existing technology at higher frequencies. On the other hand, some of the technical problems of spectroscopy at X-band frequencies are not significant at W-band and higher frequencies, so that new opportunities exist. It will be necessary to exploit them, since whatever frequency and field can be achieved, there will always be spin systems for which the resolution of standard experiments does not suffice.

One of the more obvious trends in method development for high-field high-frequency ESR is the gain in significance of ENDOR approaches at the expense of ESEEM approaches. At W-band, the large majority of ligand nuclei in transition metal complexes or of nuclei in an organic radical have nuclear Zeeman interactions that are larger than the hyperfine coupling. In many cases, the ratio of the two interactions is so large that modulation depths in ESEEM become very small. At ESR frequencies corresponding to a 600 MHz NMR spectrometer, ESEEM effects are virtually absent for almost all samples. On the other hand, the situation for ENDOR experiments generally improves in going to higher fields since ENDOR frequencies increase and fewer ENDOR transitions lie in the region between 0 and 2 MHz where detection is rather insensitive. While modulation depths become smaller, ENDOR transition probabilities increase. In addition, the overlapping of ENDOR frequencies of different isotopes is more and more removed as fields become higher. Refocusing of interactions in ENDOR and correlation experiments

for disordered systems with $I > 1/2$ nuclei may become two of the important research topics in this field.

A second trend can be spotted by looking at the problem of excitation. At X-band, resonator bandwidths at reasonable Q -values, rise times of mw switches, and available mw power all lead to about the same limit for π pulse lengths of 10-20 ns. This is sufficient for hard-pulse ESEEM on most significant systems. For a given Q -value, the resonator bandwidth is proportional to the frequency, i.e., it increases by about one order of magnitude in going from X-band to W-band. Accordingly, the dead time decreases by about one order of magnitude. To achieve the necessary time resolution and resonator bandwidth, one can therefore use higher Q -values than at lower frequencies, so that the detection is more sensitive and less power is needed to achieve a certain mw field in the resonator. Nevertheless, the lack of suitable high-power amplifiers at high frequencies leads to the problem that pulses of a given flip angle are longer than at X-band frequencies. Typical values are 60-100 ns π pulse lengths with single-channel operation of the spectrometer [177,178,182], pulses become even longer if phase cycling is required. The excitation bandwidth is therefore considerably smaller than at X-band frequencies and by at least one order of magnitude smaller than the resonator bandwidth. This precludes hard-pulse ESEEM experiments in most cases even if the theoretical modulation depth is sufficient. To allow for ESEEM experiments and in particular to take advantage of the large resonator bandwidth in new pulse experiments, two-frequency operation of the spectrometer is needed. With two mw sources that can be tuned independently, one can use the soft ESEEM experiment [81], see also §4.1.7, and the simple correlation scheme for ESR transitions described in §10.3. Such a high-frequency high-field ELDOR spectrometer is not significantly more expensive than a single-frequency ESR spectrometer in the same frequency band, but much more versatile.

The lower powers involved in high-frequency ESR spectroscopy with high- Q resonators have the additional advantage that no device is necessary to protect the detector from serious overload, in fact, it can even be avoided that the detection systems is saturated during the pulses [174]. Any experiment using probe pulse detection as well as the direct detection of transient nutations can then be performed very conveniently.

10.2 Quadrupole nuclei

The present arsenal of pulse ESR methods for studying ligand interactions or nuclear frequencies in organic radicals is still deficient in suitable experiments for quadrupole nuclei ($I > 1/2$) in disordered systems. The only exception is ^2D ($I=1$) with its comparatively small quadrupole moment. In the other cases and in particular for ^{14}N which is important in many biomolecules, two problems have to be addressed. The first is the refocusing of the quadrupole interaction in time-domain experiments. Time-domain methods are required since the resolution of ENDOR spectra is usually not sufficient, so that 2D correlation experiments become mandatory. In the absence of suitable refocusing schemes, one is then restricted to narrow features in the spectra, namely the $\Delta m_F=2$ transitions in $I=1$ systems and the $-1/2 \leftrightarrow +1/2$ transitions of half-integer nuclei. In some cases it is possible to achieve exact cancellation ($|A|=2\omega_I$) in one of the electron spin manifolds and to observe narrow features at the zero-field NQR frequencies [46]. This method requires a nearly isotropic hyperfine matrix and may involve considerable effort since the static field value for the measurement is determined by the exact cancellation condition

$$B_0 = \left| \frac{a_{\text{iso}} h}{4\pi \beta_n g_n} \right|, \quad (10.1)$$

where a_{iso} is usually not known in advance. One has to perform ESEEM or ENDOR measurements at different B_0 values to find the static field where the lines become narrow, but this is only possible at mw frequencies for which condition (10.1) is fulfilled for an ESR transition. For application at an arbitrary sample this requires the capability to do the experiment at an arbitrary mw frequency. Zero-field ESEEM and ENDOR are even more restricted with respect to the samples for which the experiments can be done.

Theoretically possible refocusing schemes have been discussed in §4.3.2. It might also be possible to refocus the quadrupole contribution to the nuclear frequencies exclusively with mw pulses and a suitable incrementation scheme. To design and discuss such approaches, a more detailed version of the theory of $I=1$ systems sketched in §3.1.3 may be required.

The same more detailed theory with suitable approximations would be needed to solve the second problem, namely to achieve a better understanding of strong mixing situations where the nuclear quadrupole, hyperfine, and nuclear Zeeman interactions are of the same order of magnitude. This would be a prerequisite for the analysis of ESEEM, ENDOR, and 2D spectra in such situations that are quite common at X-band frequencies.

On the other hand, the problem of strong mixing situations can be solved by going to higher fields where the nuclear Zeeman interaction dominates. In many cases, W-band frequencies are sufficient, frequencies corresponding to the static field in a NMR spectrometer with a proton frequency of 600 MHz would virtually always do. This leaves only the problem of the nuclear quadrupole and hyperfine interaction being of the same order of magnitude which is somewhat easier to treat theoretically and which can be solved by hyperfine decoupling, provided that enough mw power is available.

10.3 ESR resolution

As discussed in §9.1, new spectroscopic tools are needed to improve on the resolution of ESR spectra, in particular for disordered systems. A very simple approach to this task is a 2D ELDOR method that correlates ESR transitions which share one level, the pulse sequence is shown in Fig. 10-1a. The experiment requires that the frequency difference $\Delta\omega=|\omega_{12}-\omega_{23}|$ of the two transitions is not larger than the bandwidth of the resonator, that two mw sources are available, and that one of them can be swept. Actually, it is not required that a π pulse can be created with the sweepable mw source 1, all that is needed is a detectable change in the polarization of transition 12. Any such change in polarization corresponds to a change in the population of the common level and in turn to a change of the polarization of the second transition that can be detected by an echo experiment. The signal is the difference between the echo intensity in experiments with and without the pulse of mw source 1.

Two situations must be distinguished that can lead to frequency differences within the resonator bandwidth between two ESR transitions with a common level. First, two *allowed* transitions $m_S-1 \leftrightarrow m_S$ and $m_S \leftrightarrow m_S+1$ in an $S > 1/2$ system have a small frequency difference if the zero-field splitting is small, for instance in cases where the devi-

ation from cubic symmetry is small. The first pulse then increases the polarization of transition 23 and the difference signal is positive (see Fig. 10-1bc). One can check easily that a positive difference signal results also in the case where the first pulse is on-resonant with transition 23 and the two-pulse echo with transition 12.

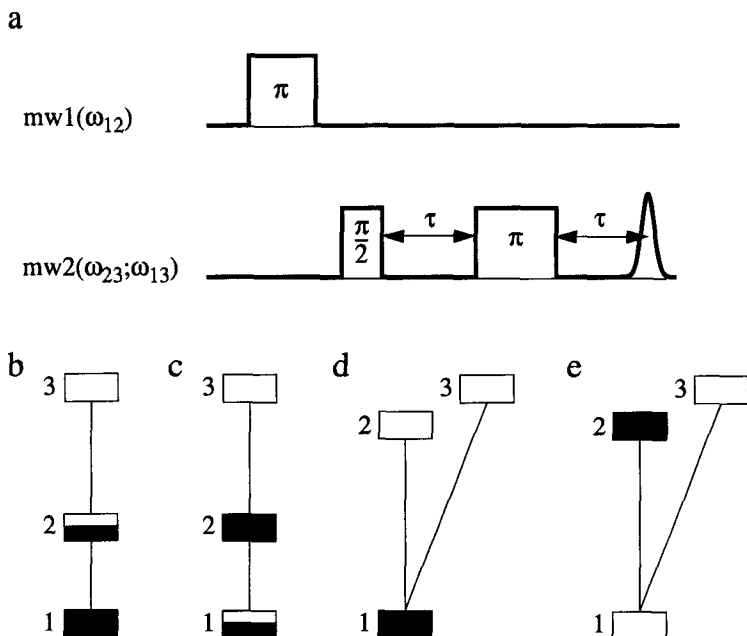


Fig. 10-1 Correlation of ESR transitions that share a level. a) Pulse sequence. In the two dimensions, the mw frequency 1 and the static field are swept. The π pulse lengths at the two mw frequencies are not necessarily the same. b) Boltzmann equilibrium for a three-level subsystem of two connected allowed transitions. c) Situation after the first π pulse at transition 12 for the subsystem of two allowed transitions. d) Boltzmann equilibrium for a subsystem of one allowed and one forbidden transition. e) Situation after the first π pulse at transition 12 for the subsystem of one allowed and one forbidden transition.

Second, an allowed and a forbidden $\Delta m_l = 1$ transition may have a frequency difference within the resonator bandwidth of a high-frequency ESR spectrometer even for the central ion nucleus in a transition metal complex. In addition, the transition probability of this forbidden transition becomes significant at high fields since the nuclear Zeeman frequency approaches the order of magnitude of a central ion hyperfine coupling. In this case, the first mw pulse changes the population of the common level 1 and thus the polar-

ization of transition 13. In contrast to the case of two allowed transitions, the polarisation is decreased here, so that a negative difference signal arises. Again this result does not depend on the order in which the two transitions are excited during the sequence. As a consequence, the two cases can be distinguished easily. Note also, that the latter case with ligands instead of the central ion is used in the closely related pulsed ELDOR detected NMR experiment [183]. The concept of FID-detected hole-burning used in this sequence optimizes the resolution of this type of correlation experiment at the expense of sensitivity.

Though this experiment may work for some samples at X-band frequencies, its potential is much higher in high-field high-frequency ESR spectroscopy, where larger resonator bandwidths can be achieved. Even then it may be impossible to access the complete correlation information, in particular for $S > 1/2$ systems with moderate ZFS. Nevertheless, in disordered systems there are always orientations for which the frequency difference of the allowed transitions approaches zero. Hence static field values exist in the vicinity of which positive correlation ridges should be observable. The curvature of these ridges and the static field at their zero crossings contain information on the magnitude of the ZFS and on the mutual orientation of the g -matrix and the ZFS tensor. Similarly, the central ion hyperfine matrix is characterized by the negative correlation ridges.

Since the resolution in the 2D spectrum is limited by the phase memory time T_m of the electron spins, it is interesting to note that an increase of more than one order of magnitude in T_m as compared to X-band has been observed in a 604 GHz pulse ESR experiment on a nitroxide spin label in a polymer sample [181]. Increases of T_m with respect to X-band frequencies have also been observed for other solid samples, see Table VII in [174].

10.4 Technical problems

The performance of a number of the existing pulse ESR methods is limited by technical problems rather than by spin physics. Most of these problems are related to the resonators. As has been discussed in §3.2.10 and §4.2.4, the sensitivity of probe pulse or coherent Raman beat detection increases with increasing mw field strength. However,

direct observation even during a probe pulse of moderate field strength presents several problems. The resonator must be carefully critically coupled and the inevitable mw leakage into the detection arm must be compensated to avoid saturation of the detector. Though it is usually no problem to establish these conditions initially, it may be difficult to maintain them during a long experiment. The problem could probably be diminished by using a bimodal resonator instead of the combination of a resonator with a circulator. Bimodal resonators with a sufficiently large isolation between the two modes could also be used to decrease the dead time at X-band and lower frequencies. Such a setup has been proposed recently for an S-band spectrometer; 70 dB isolation between the two modes has been achieved [184]. With a single-mode resonator and a circulator, the dead time is inextricably related to the Q -value of the resonator. Lowering the Q -value by overcoupling leads to shorter dead times but sacrifices sensitivity. Furthermore, reflections on several other mw elements or connections in the spectrometer can limit the success of overcoupling. Both problems would be overcome by a bimodal resonator.

Transient nutation experiments require homogeneous B_1 fields (see §9.2). It has been found that these can be provided by a BLGR, but that this resonator type exhibits break throughs at large B_1 fields during long pulses [169]. The susceptibility to break throughs could probably be decreased by small changes in the design and/or material of the BLGR. A second problem with the BLGR is encountered if Q -degradation by overcoupling is needed. The BLGR is inherently a low- Q resonator, but at least with the presently used types of coupling (loop and iris), the Q -value cannot be lowered much further by overcoupling. Accordingly, dead times are longer than for a strongly overcoupled dielectric resonator. On the other hand, for a number of experiments the BLGR has advantages beyond its superior B_1 -field homogeneity, mainly its transparency for rf fields and its small size which is only insignificantly larger than the filling volume. The best solution would be to improve the overcoupling capabilities of the BLGR by changing the coupling type and/or by optimizing the coupling element. If this is not successful, one could attempt to decrease the Q -value of the *critically* coupled resonator so far as to obtain dead times of 100 ns or below at X-band frequencies.

The performance of more advanced chirp ENDOR experiments (see for instance §4.3.2) depends on the opportunity to amplify rf chirp pulses to powers of at least 300 W

without significant creation of harmonics. When this becomes possible, refocusing in chirp 1D hyperfine spectroscopy should be re-examined (cf. §7.3.2).

10.5 Technical opportunities

A number of technical opportunities has arisen during the past few years that are not yet employed in ESR. Coherent Raman beat experiments as well as other experiments that use short mw pulses combined with probe pulse detection could gain significantly from using a Q -switch. While low- Q operation is needed to allow for sufficient excitation bandwidth in the preparation, high- Q operation is desirable during probe pulse detection to achieve both enhanced sensitivity and larger probe fields with a given mw power. Q -switching could be done at a time where only NC exists, so that no interference with the spin system would be expected. The design of a remote controlled Q -switch for a loop-gap resonator has been published recently [185]. The idea is to couple the resonator weakly to a loop of wire that contains a PIN diode. The resistance of the PIN diode leads to Q -spoiling, thus providing a Q -switch with rise times on a nanosecond time scale.

Digital attenuators with switching speeds of 200 ns, 8 bit resolution, and 0.25 dB attenuation step are available for X-band and S-band frequencies for instance from General Microwave. These elements could be used for introducing the B_1 field as a variable in experiments. The separation of transitions with different transition probability could then be achieved *via* a two-pulse echo B_0 sweep with B_1 incrementation as a second dimension [169]. Though the resolution might be worse than in a transient nutation experiment, one expects a larger sensitivity. 10 bit digital phase shifters with less than 25 ns switching time for X-band frequencies can also be obtained from General Microwave. These elements could probably enhance the performance of phase cycling since the pulses for different steps of the phase cycle would travel through the same mw channel. In addition, they would allow for more sophisticated excitation schemes that might also be used for the separation of ESR lines with different transition probabilities.

Arbitrary function generators or arbitrary waveform generators can now produce waveforms with 2.5 or even 1 ns time resolution and 8 bit vertical resolution (LeCroy, Tektronix). Waveform memories are as long as 1 MByte. These devices can provide tai-

lored rf excitation in ENDOR experiments. In connection with a mixer, they can be used for mw pulse shaping. Few work has been done so far on shaped pulses in solid-state ESR. Such approaches could probably be used to minimize off-resonance effects which are a source of problems in a number of experiments. Off-resonance effects could also be diminished by using composite pulses that are commonplace in NMR spectroscopy [9]. This development becomes possible since modern pulse-forming units on the ESR time scale allow for a practically unlimited number of pulses in a sequence [186].

In this work, a theoretical framework has been established for the description of pulse ESR experiments on systems with arbitrary (effective) electron spin S . Existing theoretical approaches to mw and rf excitation have been described systematically and care has been taken to define the conditions under which certain approaches are valid. New approaches have been introduced for non-ideal mw pulses of arbitrary strength and duration, for rf chirp pulses, and for combined mw/rf probe pulses. It has been shown that the product rule for the calculation of ESEEM patterns breaks down for non-ideal pulses.

The inner working of existing NC generators and detectors as well as their advantages and disadvantages have been discussed in some detail. A new, simple description has been given for the evolution of a spin system during a time where a train of weak mw pulses is applied. Tools for the manipulation of NC have been discussed under consideration of $S > 1/2$ and $I > 1/2$ systems. The new opportunities in NC manipulation that arise from broadband excitation by rf chirp pulses have been examined. Two broadband time-domain ENDOR experiments based on chirp pulses have been introduced that feature high sensitivity and better resolution than the existing pulse ENDOR techniques. Experimental examples have been provided and a HYSORE-type correlation experiment has been developed. A second correlation experiment has been proposed that yields the information of TRIPLE experiments.

Two-pulse ESEEM was re-examined on the basis of the new approach to non-ideal pulses of arbitrary strength and duration. It has been shown by both theory and experi-

ment that matching the mw field to the nuclear Zeeman field and prolonging the mw pulses (matched two-pulse ESEEM) provides sensitivity gains that can exceed one order of magnitude in favourable cases. Analysis of the coherence transfer pathways in two-pulse ESEEM has led to the nuclear-frequency enhanced and hyperfine-frequency enhanced matched ESEEM experiments that discriminate between the different peak types in two-pulse ESEEM spectra.

Hyperfine decoupling in ESEEM and ENDOR has been introduced as a new tool for spectrum simplification. Based on the theory of electron-nuclear spin systems with arbitrary S , the meaning of the term decoupling in $S > 1/2$ systems has been examined in some detail. The new DECENT sequence correlates decoupled ESEEM to three-pulse ESEEM. Application examples have been given for three different model systems. Two hyperfine-decoupled ENDOR sequences have been proposed and one of them has been applied to an $S > 1/2$ system.

The direct measurement of hyperfine couplings, termed hyperfine spectroscopy, has been investigated as a means for spectrum simplification and resolution enhancement. In the theoretical description particular consideration was given to second order effects. It has been shown in a simulation that it should be feasible to resolve nuclei of the same isotope in disordered systems *via* such second order effects. Pulse sequences for hyperfine spectroscopy have been developed that are based on ESEEM and chirp ENDOR methods. The easy to perform 2D HYEND experiment that correlates the hyperfine spectrum to the ENDOR spectrum has been introduced and a theoretical description has been given that considers anisotropic hyperfine couplings. The performance of all new hyperfine spectroscopy sequences has been demonstrated on both ordered and disordered systems.

As a means of resolution enhancement for disordered systems, zero-field ESEEM and ENDOR have been proposed. Peculiarities of half-integer electron spin (Kramers) systems at zero field have been discussed and the basics have been provided for the description of pulse ESR experiments at zero field on such systems. Conditions have been defined under which ESEEM effects at zero field and in very weak fields can be expected. Zero-field ESEEM and pulse ENDOR experiments have been applied for the first time to obtain structure information and methods for the assignment and analysis of

the resulting spectra have been described. The experimental results are in excellent agreement with theory.

Transient nutation spectroscopy has been discussed as a tool for disentangling ESR spectra. Care has been taken to identify the significant influences on the nutation frequencies and to define regimes in which good resolution in the nutation dimension is expected and where peak assignment is simple. The PEANUT sequence for the echo detection of the rotary echo has been introduced on the basis of the requirements in the measurement of nutation frequencies that follow from theory. First experimental tests of the sequence have been provided.

Finally, future trends in solid-state pulse ESR have been examined. An account of the opportunities and problems of high-field high-frequency ESR has been given and a case was made for designing high-frequency ESR spectrometers as two-frequency (ELDOR) spectrometers. Problems in the spectroscopy of quadrupole nuclei coupled to electron spins have been identified and possible approaches to their solution proposed. A simple but promising correlation experiment for disentangling ESR spectra in high-frequency ESR has been suggested. Technical problems have been pinpointed that limit the performance of a number of existing pulse ESR experiments and some of the new technical opportunities in pulse ESR have been mentioned.

Exact eigenvalues of the $S'=1/2$, $I=1/2$ spin Hamiltonian

The eigenvalues of the Hamiltonian

$$\mathcal{H}_{\text{ex}} = \Omega_S S_z + A' S_z I_z + B' S_z I_x + \omega_I' I_z + \omega_{Ix}' I_x + \omega_1' S_x \quad (\text{A.1})$$

during mw irradiation are given by

$$\varepsilon_1 = \frac{1}{4}(f_1 - f_3) , \quad (\text{A.2a})$$

$$\varepsilon_2 = -\frac{1}{4}(f_1 + f_3) , \quad (\text{A.2b})$$

$$\varepsilon_3 = \frac{1}{4}(f_2 - f_3) , \quad (\text{A.2c})$$

$$\varepsilon_4 = -\frac{1}{4}(f_2 + f_3) , \quad (\text{A.2d})$$

with

$$f_1 = \left[\frac{2}{3}c_1 - e_1 - \frac{8\Omega_S(A'\omega_I' + B'\omega_{Ix}')}{f_3} \right]^{1/2} , \quad (\text{A.3a})$$

$$f_2 = \left[\frac{2}{3}c_1 - e_1 + \frac{8\Omega_S(A'\omega_I' + B'\omega_{Ix}')}{f_3} \right]^{1/2} , \quad (\text{A.3b})$$

$$f_3 = \left(\frac{1}{3}c_1 + e_1 \right)^{1/2} , \quad (\text{A.3c})$$

$$e_1 = \frac{d_1}{24 \sqrt[3]{4} \sqrt[3]{d_2 + \sqrt{d_2^2 - 4d_1^3}}} + \frac{\sqrt[3]{d_2 + \sqrt{d_2^2 - 4d_1^3}}}{48 \sqrt[3]{2}} \quad (\text{A.4})$$

$$d_1 = 4^3(c_1^2 + 3c_2) , \quad (\text{A.5a})$$

$$d_2 = 4^5[c_1^3 + 3^2c_1c_2 + 12^3(A'\omega_I' + B'\omega_{Ix}')^2\omega_I'^2\Omega_S^2] , \quad (\text{A.5b})$$

$$c_1 = A'^2 + B'^2 + 4\omega_I'^2 + 4\omega_{Ix}'^2 + 4\Omega_S^2 + 4\omega_1'^2 , \quad (\text{A.6a})$$

$$c_2 = (A'^2 + B'^2 + 4\omega_I'^2 + 4\omega_{Ix}'^2 - 4\Omega_S^2 - 4\omega_1'^2)^2 + 16[A'^2(\omega_1'^2 - \omega_I'^2) + B'^2(\omega_1'^2 - \omega_{Ix}'^2) - 2A'B'\omega_I'\omega_{Ix}'] . \quad (\text{A.6b})$$

Instrumentation for chirped radio frequency pulses

The experiments with chirped rf pulses have been performed with a standard pulse ENDOR probehead [69,70]. The block diagram of the whole rf setup is displayed in Fig. B-1. The waveforms for the chirp pulses are calculated on the PC AT according to the formula

$$V_{\text{chirp}}(t) = E_{\text{pulse}}(t) \sin \left[2\pi \left(\nu_s t + \frac{\alpha_{\text{ch}}}{2} t^2 \right) + \phi_{\text{ch}} \right], \quad (\text{B.1a})$$

with the pulse envelope

$$E_{\text{pulse}}(t) = \begin{cases} \sin(2\pi t/t_p), & 0 \leq t \leq t_p/4 \\ 1, & t_p/4 < t \leq 3(t_p/4) \\ \sin[2\pi(t_p - t)/t_p], & 3t_p/4 < t \leq t_p \end{cases}, \quad (\text{B.1b})$$

where $\alpha_{\text{ch}} = (\nu_e - \nu_s)/t_p$ is the sweep rate, ν_s and ν_e are the start and end frequency of the chirp, respectively, t_p is the pulse length and ϕ_{ch} is the phase of the pulse. The pulse envelope can also be changed so as to provide a bandstop function in the region of the matrix line, this corresponds to two chirp pulses from ν_s to $\nu_m - \Delta_m/2$ and $\nu_m + \Delta_m/2$ to ν_e with zero output voltage for time $t_p \Delta_m / (\nu_e - \nu_s)$ between the two pulses. Both pulses are calculated by Eq. (B.1), Δ_m is the width of the band that is excluded from excitation. If no apodization is desired, one has $E_{\text{pulse}}(t) \equiv 1$. The waveforms are digitized according to the 8 bit vertical resolution of the arbitrary function generator (AFG) LeCroy 9100 and transferred via the IEEE-488 bus.

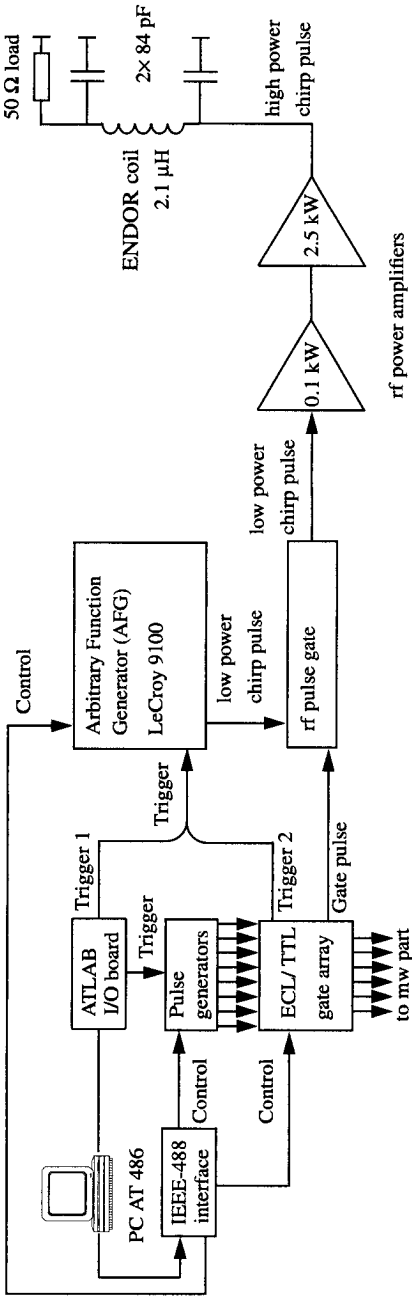


Fig. B-1 Block diagram of the radio frequency part of the spectrometer. Control lines are IEEE-488 bus lines driven by a Keithley Metrabyte KPC-488.2 AT interface. Trigger and gate lines use TTL levels except for the AFG trigger input (see text).

In the memory of the AFG, a sequence of chirp pulses is stored that corresponds to the required phase cycle, i.e., a sequence with $\phi_{\text{ch}}=0, 0, 0, \pi, \pi, 0, \pi, \pi$ for the phase cycle $[0,0]-[0,\pi]-[\pi,0]+[\pi,\pi]$ for chirp time-domain ENDOR. After that, an output amplitude of 1V (peak-to-peak) and a trigger level of 0.45 V are set on the AFG and the external single trigger mode is entered. The trigger level of 0.45 V has been found to provide stable operation though TTL levels are used on the trigger lines. The reason for this is the use of a 50 Ω , 6dB power divider/combiner (Huber&Suhner) instead of a TTL OR gate to combine the two trigger lines.

The experiment is started by a trigger output from the PC to the pulse generators which in turn provide the appropriately timed triggers to recall the two chirp waveforms. These trigger signals are combined in the ECL/TTL gate array and output to the AFG. The chirp pulses pass the rf pulse gate which is in its open state and are amplified by two power amplifiers (Amplifier Research, Model 100LMB, 1-200 MHz, 100W and Transworld Electronics, Model T1000, 2-30 MHz, pulse power 2.5 kW). The ENDOR coil ($L=2.5 \mu\text{H}$ if measured alone, $L=1.4 \mu\text{H}$ if built into the probehead) is roughly matched to the 50 Ω impedance of the amplifier by a π circuit (see Fig. B-2) [58,70].

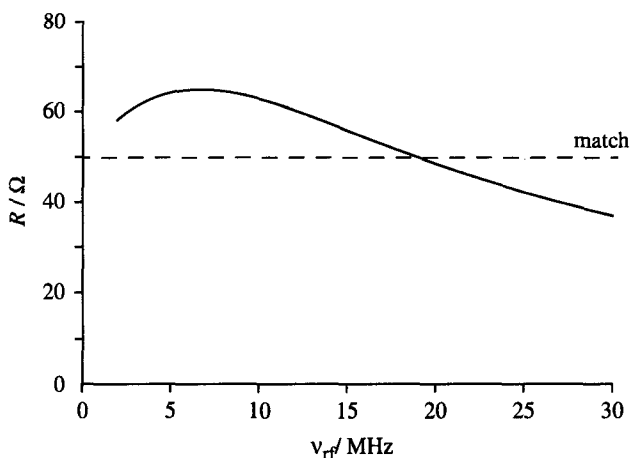


Fig. B-2 Impedance of a π circuit consisting of a $L=1.4 \mu\text{H}$ inductivity and two $C=125 \text{ pF}$ capacities as a function of the radio frequency. The curve has been calculated by applying Kirchoff's rules and C has been optimized. For the experimental setup, an optimum C of 84 pF has been found.

After each shot, six additional triggers are provided to the AFG via trigger line 1 to reset the sequence pointer in the AFG to the proper waveforms for the actual phase cycle step (see trigger scheme Fig. B-3). Switching to the next step of the phase cycle is performed by two additional triggers via line 1. This method ensures, that no time-consuming IEEE-488 messages need to be sent to the AFG during the acquisition of one data point. It is also the reason for the use of the rf pulse gate, which is closed during the unwanted chirp pulses to prevent them from being amplified and transmitted to the probehead. Between data points when overhead is large anyway because of programming other devices, the sequence pointer in the AFG is reset via an IEEE-488 command to limit the damage done by accidentally missed triggers. However, in practice it has not been found that triggers were missed.

For longer phase cycles it is wasteful in terms of AFG memory to store the whole sequence of chirp waveforms in the order in which they are needed. It is sufficient to have a string of waveforms that contains the needed sequences for all steps of the phase cycle as substrings, while the substrings may overlap. To see this, consider the complete sixteen-step phase cycle for the TRIPLE-type correlation experiment proposed in §4.4.3. ¹ It can be checked easily that the string $(0, \pi/2, 0, \pi/2, \pi, \pi/2, \pi, \pi/2, 0, 3\pi/2, 0, 3\pi/2, \pi, 3\pi/2, \pi, 3\pi/2, 0, 0, \pi, 0, \pi, \pi, \pi, 0, 0)$ contains any subsequence of three waveforms that is needed in the 16-step phase cycle. ² It is therefore sufficient to store 25 instead of 48 waveforms and use a table in the PC that says how many additional triggers have to be used to switch between steps of the phase cycle.

-
1. The subcycles for the three chirp pulses are $[0]-[\pi]$, $[0]+[\pi/2]+[\pi]+[3\pi/2]$, and $[0]-[\pi]$.
 2. Sequential triggering for the AFG is cyclic, so that the combination $0, 0, 0$ can also be recalled.

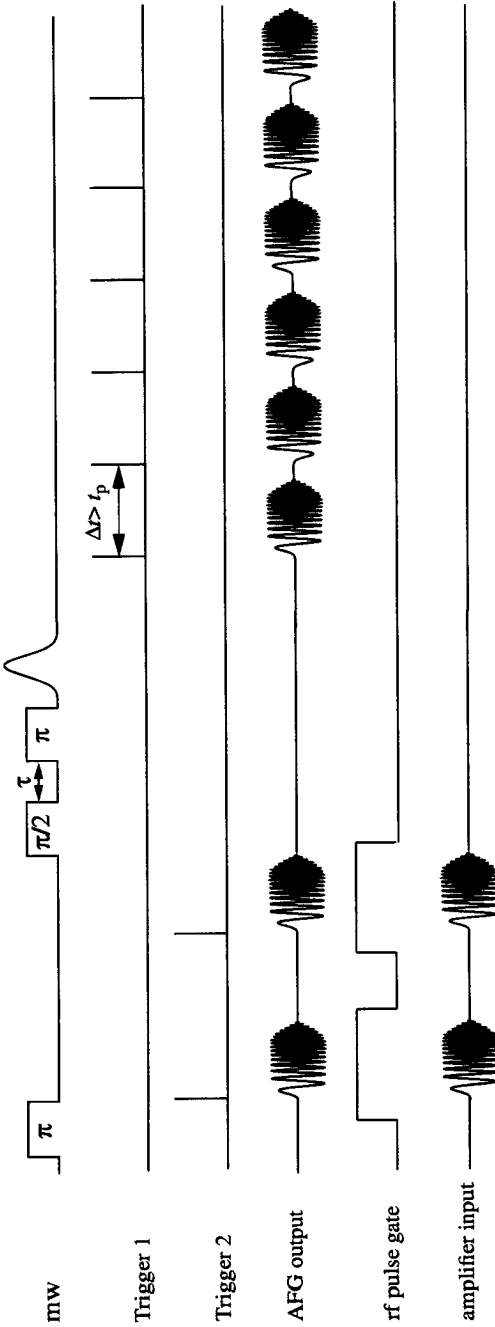


Fig. B-3 Trigger scheme for one shot in chirp time-domain ENDOR. The scheme corresponds to the first step in the phase cycle. Six additional triggers on trigger channel 1 are used to reset the sequence pointer in the AFG to the proper point in the waveform memory. To switch to the next step in the phase cycle, two additional triggers are sent via channel 1 (not shown).

Residual splittings and second order shift for $I > 1/2$ nuclei during decoupling

By treating a four-level subsystem as consisting of a fictitious electron spin 1/2 and a fictitious nuclear spin 1/2, we obtain the Hamiltonian during strong mw irradiation

$$\mathcal{H}_{\text{ff}} = \Omega_S S_z + \omega_1 S_x + A'' S_z I_z + B_x'' S_z I_x + B_y'' S_z I_y + \omega_I'' I_z + \omega_{I_x}'' I_x + \omega_{I_y}'' I_y . \quad (\text{C.1})$$

The matrix representation of this Hamiltonian can be diagonalized analytically. By expressing the eigenvalues in a Taylor series up to second order and identifying the nuclear frequencies, we find for the residual hyperfine splitting

$$A_{\text{res}}^{\text{ff}} = \frac{A'' \omega_I'' + B_x'' \omega_{I_x}'' + B_y'' \omega_{I_y}''}{\sqrt{\omega_I''^2 + \omega_{I_x}''^2 + \omega_{I_y}''^2}} \frac{\Omega_S}{\omega_1} , \quad (\text{C.2a})$$

and for the decoupled nuclear frequency

$$\begin{aligned} \omega_{\text{dec}}^{\text{ff}} = & \sqrt{\omega_I''^2 + \omega_{I_x}''^2 + \omega_{I_y}''^2} \\ & + [(A'' \omega_{I_x}'' - B_x'' \omega_I'')^2 + (A'' \omega_{I_y}'' - B_y'' \omega_I'')^2 + (B_x'' \omega_{I_y}'' - B_y'' \omega_{I_x}'')^2] \\ & \times \frac{(\omega_I''^2 + \omega_{I_x}''^2 + \omega_{I_y}''^2 - \Omega_S^2)}{8 \omega_1^2 (\omega_I''^2 + \omega_{I_x}''^2 + \omega_{I_y}''^2)^{3/2}} \end{aligned} \quad (\text{C.2b})$$

Spin Hamiltonian for $S'=1/2$, $I=1/2$ with orthorhombic hyperfine matrix

Consider an electron spin $S=1/2$ or a fictitious spin $S'=1/2$ coupled to a nuclear spin $I=1/2$ with the electron spin quantization axis being parallel to the external magnetic field axis. In general, the coupling can be described by an orthorhombic hyperfine interaction matrix \mathbf{A} with the principal values A_{11} , A_{22} , and A_{33} . The orientation of the external magnetic field with respect to the frame where \mathbf{A} is diagonal is characterized by the two polar angles θ and ϕ . For the hyperfine part of the spin Hamiltonian, we find

$$\mathcal{H}_{\text{HF}} = A S_z I_z + B S_z I_x, \quad (\text{D.1})$$

with

$$A = A_{33} \cos^2 \theta + \sin^2 \theta (A_{11} \cos^2 \phi + A_{22} \sin^2 \phi), \quad (\text{D.2a})$$

$$B = \left(B_x^2 + B_y^2 \right)^{1/2}, \quad (\text{D.2b})$$

$$B_x = \frac{1}{2} \sin \theta \cos \theta \left[(2A_{33} - A_{11} - A_{22}) + \cos(2\phi)(A_{22} - A_{11}) \right], \quad (\text{D.2c})$$

and

$$B_y = \frac{1}{2} \sin \theta \sin(2\phi)(A_{22} - A_{11}), \quad (\text{D.2d})$$

where terms containing S_x and S_y operators have been dropped, since they are non-secular as long as the high-field approximation is valid for the electron spin. With Eq.

(D.2c,d), one can check easily that the pseudo-secular part and hence the probability of forbidden transitions become zero if the static field is parallel to one of the principal axes.

If the quantization axis of the electron spin or fictitious spin is *not* parallel to the static magnetic field, one can no longer describe the hyperfine interaction by three principal values, since the HFI matrix then contains an antisymmetric part [187-189] which cannot be diagonalized. Note that such an antisymmetric part is present even in the case of a purely isotropic hyperfine interaction, it characterizes the transformation between the coordinate frames of the I spin and S spin rather than their interaction.¹ As a result, forbidden transitions $\Delta m_S=1, \Delta m_I=1$ can have finite probability even for isotropic hyperfine couplings much smaller than the *electron* Zeeman interaction, if either the g -anisotropy is large or the zero-field splitting is of a similar order of magnitude as the electron Zeeman interaction. Analogous effects occur for $I>1/2$ if the nuclear quadrupole interaction is of the same order of magnitude as the nuclear Zeeman interaction.

1. This explains why it is more precise to use the term interaction matrix instead of tensor (see §2.1).

References

- [1] E. Hoffmann and A. Schweiger, *Appl. Magn. Reson.* **9**, 1 (1995)
- [2] C. Bühlmann, A. Schweiger, and R.R. Ernst, *Chem. Phys. Lett.* **154**, 285 (1989)
- [3] P. Höfer, A. Grupp, H. Nebenführ, and M. Mehring, *Chem. Phys. Lett.* **132**, 279 (1986)
- [4] H.Y. Carr and E.M. Purcell, *Phys. Rev.* **94**, 630 (1954)
- [5] D. Gill and S. Meiboom, *Rev. Sci. Instrum.* **29**, 688 (1958)
- [6] A.V. Astashkin and A. Schweiger, *Chem. Phys. Lett.* **174**, 595 (1990)
- [7] M. Willer and A. Schweiger, *Chem. Phys. Lett.* **230**, 67 (1994)
- [8] A. Abragam, *Principles of Nuclear Magnetism* (Clarendon, Oxford, 1961)
- [9] R. R. Ernst, G. Bodenhausen, and A. Wokaun, *Principles of NMR in One and Two Dimensions* (Clarendon, Oxford, 1987).
- [10] C.P. Slichter, *Principles of Magnetic Resonance*, 3rd ed. (Springer, Berlin, 1990)
- [11] M. Goldman, *Quantum Description of High-Resolution NMR in Liquids* (Clarendon, Oxford, 1988)
- [12] S. R. Hartmann and E. L. Hahn, *Phys. Rev.* **128**, 2042 (1962)
- [13] C. Cohen-Tannoudji and S. Haroche, *Compt. Rend.* **262**, 37 (1966)
- [14] C. Cohen-Tannoudji, in *Cargise Lectures in Physics*, edited by M. Levy (Gordon and Breach, New York, 1968), Vol. 2, p. 347-393
- [15] J.R. Pilbrow, *Transition Ion Electron Paramagnetic Resonance* (Clarendon, Oxford, 1990)
- [16] A. Abragam and B. Bleaney, *Electron Paramagnetic Resonance of Transition Ions* (Clarendon, Oxford, 1970)

-
- [17] W. Gordy, *Theory and Applications of Electron Spin Resonance* (Wiley, New York, 1980)
- [18] J.S.M. Harvey and H. Kiefte, *J. Phys. B* **3**, 1326 (1970)
- [19] A. Abragam and M.H.L. Pryce, *Proc. R. Soc. A* **205**, 135 (1951)
- [20] J. Köhler, J.A.J.M. Disselhorst, M.C.J.M. Donckers, E.J.J. Groenen, J. Schmidt, and W.E. Moerner, *Nature (London)* **363**, 242 (1993)
- [21] J. Wrachtrup, C. von Borczykowski, J. Bernard, M. Orrit, and R. Brown, *Nature (London)* **363**, 244 (1993)
- [22] J. Wrachtrup, C. von Borczykowski, J. Bernard, R. Brown, and M. Orrit, *Chem. Phys. Lett.* **245**, 262 (1995)
- [23] M. H. Levitt, D. Suter, and R. R. Ernst, *J. Chem. Phys.* **84**, 4243 (1986)
- [24] O.W. Sørensen, G.W. Eich, M.H. Levitt, G. Bodenhausen, and R.R. Ernst, *Progress in NMR Spectroscopy* **16**, 163 (1983)
- [25] O.W. Sørensen, *Progress in NMR Spectroscopy* **21**, 503 (1989)
- [26] G.L. Bir, *Fiz. Tverd. Tela* **5**, 2236 (1963)
- [27] Ch.P. Poole Jr., and H.A. Farach, *Handbook of Electron Spin Resonance*, (AIP Press, New York, 1994)
- [28] W.B. Mims, *Phys. Rev.* **B5**, 2409 (1972)
- [29] A. Schweiger, in *Modern Pulsed and Continuous-Wave Electron Spin Resonance*, edited by L. Kevan, and M.K. Bowman (Wiley, New York, 1990), Chap. 2
- [30] A. Grupp, and M. Mehring, in *Modern Pulsed and Continuous-Wave Electron Spin Resonance*, edited by L. Kevan, and M. Bowman (Wiley, New York, 1990), Chap. 4
- [31] A. Schweiger, *Angew. Chem. Int. Ed. Engl.* **30**, 265 (1991)
- [32] C. Gemperle and A. Schweiger, *Chem. Rev.* **91**, 1481 (1991)
- [33] S.A. Dikanov and Yu. D. Tsvetkov, *Electron Spin Echo Envelope Modulation (ESEEM) Spectroscopy* (CRC Press, Boca Raton, 1992)
- [34] A. Schweiger, *Appl. Magn. Reson.* **5**, 229 (1993)
- [35] A. Ponti and A. Schweiger, *Appl. Magn. Reson.* **7**, 363 (1994)
- [36] A. Ponti and A. Schweiger, *J. Chem. Phys.* **102**, 5207 (1995)
- [37] M.K. Bowman and R.J. Massoth, in *Electronic Magnetic Resonance in the Solid State*, edited by J.A. Weil (Canadian Society of Chemistry, Ottawa, 1987)
- [38] G.M. Muha, *J. Magn. Reson.* **49**, 431 (1982)
- [39] G.M. Muha, *J. Magn. Reson.* **53**, 85 (1983)
- [40] E.C. Hoffmann, Ph. D. Thesis, ETH Zürich, (1996)
- [41] J.A. Weil, in *Electronic Magnetic Resonance in the Solid State*, edited by J.A. Weil (Canadian Society of Chemistry, Ottawa, 1987)

-
- [42] H. Cho, S. Pfenninger, J. Forrer, and A. Schweiger, *Chem. Phys. Lett.* **180**, 198 (1991)
- [43] C. Gemperle, G. Aebli, A. Schweiger, and R. R. Ernst, *J. Magn. Reson.* **88**, 241 (1990)
- [44] E.C. Hoffmann, G. Jeschke, and A. Schweiger, *Chem. Phys. Lett.* **248**, 393 (1996)
- [45] Th. Wacker, G.A. Sierra, and A. Schweiger, *Isr. J. Chem.* **32**, 305 (1992)
- [46] A. Lai, H. L. Flanagan, and D. J. Singel, *J. Chem. Phys.* **89**, 7161 (1988)
- [47] E.C. Hoffmann, M. Hubrich, and A. Schweiger, *J. Magn. Reson. A* **117**, 16 (1995)
- [48] M.K. Bowman, *Isr. J. Chem.* **32**, 330 (1992)
- [49] M.K. Bowman, R.J. Massoth, and Y.S. Yannoni, in: *Pulsed magnetic resonance: NMR, ESR and optics*, edited by D.M.S. Bagguley (Clarendon Press, Oxford, 1992), p.423
- [50] E. Hoffmann and A. Schweiger, *Chem. Phys. Lett.* **220**, 467 (1994)
- [51] E.L. Hahn, *J. Magn. Reson.* **116**, 230 (1995)
- [52] O. Burghaus and M. P. Klein, *Chem. Phys. Lett.* **243**, 480 (1995)
- [53] G. Jeschke and A. Schweiger, *Mol. Phys.* **88**, 355 (1996)
- [54] L. Müller and R. R. Ernst, *Mol. Phys.* **38**, 963 (1979)
- [55] G. Jeschke and A. Schweiger, *J. Chem. Phys.* **105**, 2199 (1996)
- [56] W. Magnus, *Commun. Pure Appl. Math.* **7**, 649 (1954)
- [57] F. Bloch and A. Siegert, *Phys. Rev.* **57** 522 (1940)
- [58] P. Höfer, Thesis Universität Stuttgart (1988)
- [59] D.H. Whiffen, *Mol. Phys.* **10**, 595 (1965)
- [60] S. Geschwind, in: *Hyperfine Interactions*, edited by A. J. Freeman and R. B. Franckel (New York, Academic, 1967) p. 225
- [61] A.L. Kwiram, *J. Chem. Phys.* **55**, 2484 (1971)
- [62] P. Höfer, A. Grupp, and M. Mehring, *Phys. Rev. A* **33**, 3519 (1986)
- [63] J. Delayre, Ph.D. Thesis, Université de Grenoble (1975)
- [64] A. G. Marshall and D.C. Roe, *J. Chem. Phys.* **73**, 1581 (1980)
- [65] J.-M. Böhlen, M. Rey, and G. Bodenhausen, *J. Magn. Reson.* **84**, 191 (1989)
- [66] J.A. Ferretti and R.R. Ernst, *J. Chem. Phys.* **65**, 4283 (1976)
- [67] G. Jeschke and A. Schweiger, *J. Chem. Phys.*, **103**, 8329 (1995)
- [68] Th. Wacker, Ph.D. Thesis, ETH Zürich, No. 9913, (1992)
- [69] J. Forrer, S. Pfenninger, J. Eisenegger, and A. Schweiger, *Rev. Sci. Instrum.* **61**, 3360 (1990)

- [70] J. Forrer, S. Pfenninger, G. Sierra, G. Jeschke, A. Schweiger, B. Wagner, and Th. Weiland, *Appl. Magn. Reson.* **10**, 263 (1996)
- [71] A. Schweiger, *J. Chem. Soc. Faraday Trans.* **91**, 177 (1995)
- [72] J. Sebbach, E. Hoffmann, and A. Schweiger, *J. Magn. Reson.* **A116**, 221 (1995)
- [73] H. Thomann, M. Bernardo, M. Baldwin, M. Lowery, and E.I. Solomon, *J. Am. Chem. Soc.* **113**, 5911 (1991)
- [74] E.J. Hustedt, A. Schweiger, and R.R. Ernst, *J. Chem. Phys.* **96**, 4954 (1992)
- [75] I.G. Rowan, E.L. Hahn, and W.B. Mims, *Phys. Rev.* **137A**, 61 (1965)
- [76] C. Gemperle, Ph.D. Thesis, ETH Zürich, No. 9192, (1990)
- [77] H. Cho, *J. Chem. Phys.* **94**, 2482 (1991)
- [78] W.B. Mims, *Proc. R. Soc. London*, **283**, 452 (1965)
- [79] E.R. Davies, *Phys. Lett.* **47A**, 1 (1974)
- [80] C. Gemperle, A. Schweiger, and R.R. Ernst, *Chem. Phys. Lett.* **145**, 1 (1988)
- [81] E.J. Hustedt, A. Schweiger, and R.R. Ernst, *J. Chem. Phys.* **96**, 4954 (1992)
- [82] A. Schenzle, N. C. Wong, and R. G. Brewer, *Phys. Rev.* **A21**, 887 (1980)
- [83] M. Kunimoto, T. Endo, S. Nakanishi, and T. Hashi, *Phys. Rev.* **A25**, 2235 (1982)
- [84] P. P. Borbat and A. M. Raitsimring, *J. Magn. Reson.* **A114**, 261 (1995)
- [85] P.F. Liao and S.R. Hartmann, *Phys. Rev.* **B8**, 69 (1973)
- [86] H. Cho, S. Pfenninger, C. Gemperle, A. Schweiger, and R.R. Ernst, *Chem. Phys. Lett.* **160**, 391 (1989)
- [87] P. Höfer, *J. Magn. Reson.* **A111**, 77 (1994)
- [88] O. Burghaus and M.P. Klein, *Chem. Phys. Lett.* **243**, 480 (1995)
- [89] S. A. Smith, T. O. Levante, B. H. Meier, and R. R. Ernst, *J. Magn. Reson.* **A106**, 75 (1994)
- [90] M. Hubrich, E.C. Hoffmann, and A. Schweiger, *J. Magn. Reson.* **A114**, 271 (1995)
- [91] M. Hubrich, G. Jeschke, and A. Schweiger, *J. Chem. Phys.* **104**, 2172 (1996)
- [92] A.M. Tyrishkin, S.A. Dikanov, and D. Goldfarb, *J. Magn. Reson.* **A105**, 271 (1993)
- [93] R. Song, Y. C. Zhong, C. J. Noble, J. R. Pilbrow, and D. R. Hutton, *Chem. Phys. Lett.* **237**, 86 (1995)
- [94] P. Höfer, A. Grupp, and M. Mehring, *Phys. Rev.* **A33**, 3519 (1986)
- [95] J.G. Powles and P. Mansfield, *Phys. Lett.* **2**, 58 (1962)
- [96] J.H. Davis, K.R. Jeffrey, M. Bloom, M.I. Valic, and T.P. Higgs, *Chem. Phys. Lett.* **42**, 390 (1976)
- [97] K.P. Dinse, R. Biehl, and K. Möbius, *J. Chem. Phys.* **61**, 4335 (1974)

-
- [98] M. Mehring, P. Höfer, and A. Grupp, *Ber. Bunsenges. Phys. Chem.* **91**, 1132 (1987)
- [99] P. Höfer, *private communication*
- [100] J.R. Niklas, R.U. Bauer, and J.M. Spaeth, *phys. stat. sol.* **B119**, 171 (1983)
- [101] A. Schweiger and Hs.H. Günthard, *Chem. Phys.* **32**, 35 (1978)
- [102] J.J. Shane, P. Höfer, E.J. Reijerse, and E. de Boer, *J. Magn. Reson.* **99**, 596 (1992)
- [103] V.J. DeRose and B.M. Hoffman, *Methods Enzymol.* **246**, 554 (1995)
- [104] L. Kevan, in *Time Domain Electron Spin Resonance*, edited by L. Kevan and R.N. Schwartz (Wiley-Interscience, New York, 1979), p. 279
- [105] L. Kevan, *Acc. Chem. Res.* **20**, 1 (1987)
- [106] Y.D. Tsvetkov and S.A. Dikanov, in *Metal Ions in Biological Systems*, edited by H. Sigel (Marcel Dekker, New York, 1987), vol. 22, p. 207
- [107] R.G. Larsen, G.J. Gerfen, and D.J. Singel, *Appl. Magn. Reson.* **3**, 369 (1992)
- [108] W.B. Mims and J. Peisach, *Biol. Magn. Reson.* **3**, 213 (1981)
- [109] M. Kunitomo, T. Endo, S. Nakanishi, and T. Hashi, *Phys. Rev.* **A25**, 2235 (1982)
- [110] A.L. Bloom, *Phys. Rev.* **98**, 1105 (1954)
- [111] G. Jeschke, *unpublished results*
- [112] A. Schweiger, M. Rudin, and Hs.H. Günthard, *Mol. Phys.* **41**, 63 (1980)
- [113] Y.C. Zhong and J.R. Pilbrow, *Chem. Phys. Lett.* **222** 592 (1994)
- [114] G. Jeschke and A. Schweiger, *Chem. Phys. Lett.* **231** 574 (1994)
- [115] M. Kashiwagi, *Bull. Chem. Soc. Japan* **39**, 2051 (1966)
- [116] W.B. Mims and J. Peisach, *J. Chem. Phys.* **69**, 4921 (1978)
- [117] J. McCracken, S. Pember, S.J. Benkovic, J.J. Villafranca, R.J. Miller, and J. Peisach, *J. Am. Chem. Soc.* **110**, 1069 (1988)
- [118] R. deBeer, H. Barkhuijsen, E.L. de Wild, and R.P.J. Merks, *Bull. Magn. Reson.* **2**, 420 (1981)
- [119] D. van Ormondt, R. De Beer, M. Brouha, and F. de Groot, *Z. Naturforsch.* **24a**, 1746 (1969)
- [120] A. Zalkin, J.D. Forrester, and D.T. Templeton, *J. Chem. Phys.* **39**, 2881 (1963)
- [121] X.Tan, R. Poyner, G.H. Reed, and Ch. P. Scholes, *Biochemistry*, **32**, 7799 (1993)
- [122] Th. Wacker and A. Schweiger, *Chem. Phys. Lett.* **191**, 136 (1992)
- [123] S. Dikanov and M.K. Bowman, *J. Magn. Reson. A* **116**, 125 (1995)
- [124] A. Pöpll and L. Kevan, *J. Phys. Chem.* **100**, 3387 (1996)
- [125] N.M. Atherton, *Principles of Electron Spin Resonance*, (Ellis Horwood, New York, 1993)

- [126] R. Song, Y.C. Zhong, C.J. Noble, J.R. Pilbrow, and D.R. Hutton, *Chem. Phys. Lett.* **237**, 86 (1995)
- [127] A. M. Tyryshkin, S. A. Dikanov, and D. Goldfarb, *J. Magn. Reson.* **A105**, 271 (1993)
- [128] G. Jeschke and A. Schweiger, *J. Magn. Reson.* **A119**, 45 (1996)
- [129] G.H. Rist and J.S. Hyde, *J. Chem. Phys.* **52**, 4633 (1970)
- [130] G. Jeschke and A. Schweiger, *Chem. Phys. Lett.* **246**, 431 (1995)
- [131] J. Stankowski, A. Wieckowski, and S. Hedewy, *J. Magn. Reson.* **15**, 498 (1974)
- [132] R. Böttcher, D. Heinhold, and W. Windsch, *Chem. Phys. Lett.* **49**, 148 (1977)
- [133] A. Schweiger and Hs. H. Günthard, *Chem. Phys.* **32**, 35 (1978)
- [134] A. Schweiger, *Struct. Bonding (Berlin)* **51**, 1 (1982)
- [135] A. Schweiger, R. Wolf, Hs.H. Günthard, J.H. Ammeter, and E. Deiss, *Chem. Phys. Lett.* **71**, 117 (1980)
- [136] R. Wolf, Ph.D. Thesis, ETH Zürich, No. 7165, (1982)
- [137] J. Krzystek, M. Notter, and A. L. Kwiram, *J. Phys. Chem.* **98**, 3559 (1994)
- [138] R. Tycko, *Adv. Magn. Reson.* **14**, 203 (1990)
- [139] R. Tycko, *J. Chem. Phys.* **92**, 5776 (1990)
- [140] R. Bramley and S. J. Strach, *Chem. Rev.* **83**, 49 (1983)
- [141] R. Bramley and S.J. Strach, *Chem. Phys. Lett.* **79**, 183 (1981)
- [142] R. Bramley and S. J. Strach, *J. Magn. Reson.* **61**, 245 (1985)
- [143] G.S. Bogle, H.F. Symmons, V.R. Burgess, and J.V. Sierins, *Proc. Phys. Soc. London* **77**, 561 (1961)
- [144] W. Urban, *Z. Angew. Phys.* **20**, 215 (1966)
- [145] L.E. Erickson, *Phys. Rev.* **143**, 295 (1966)
- [146] Alpha Industries Inc., *mikrowellen magazin*, **11**, 550 (1985)
- [147] I. Longo, *Meas. Sci. Technol.* **2**, 1169 (1991)
- [148] W.N. Hardy and L.A. Whitehead, *Rev. Sci. Instrum.* **52**, 213 (1980)
- [149] T. Christides, W. Froncisz, T. Oles, and J.S. Hyde, *Rev. Sci. Instrum.* **65**, 63 (1994)
- [150] G. Reed and D. Markham, in *Biological Magnetic Resonance*, ed. by L.J. Berliner and J. Reuben (Plenum, New York, 1984), vol. 6, p. 73
- [151] E. Münck, K. Surerus, and M.P. Hendrich, *Methods Enzymol., Part C* **227**, 463 (1993)
- [152] W.R. Hagen, in *Iron-Sulfur Proteins; Advances in Inorganic Chemistry* 38; ed. by R. Cammack (Academic Press, San Diego, 1992), p. 165

- [153] B.M. Hoffman, B.E. Sturgeon, P.E. Doan, V.J. DeRose, K.E. Liu, and S.J. Lippard, *J. Am. Chem. Soc.* **116**, 6023 (1994)
- [154] B.M. Hoffman, *J. Phys. Chem.* **98**, 11657 (1994)
- [155] S.M. Janes, H.C. Brenner, *Chem. Phys.* **91**, 449 (1984)
- [156] T. Kirski, B. Stein, F. Rothamel, and C. von Borczyskowski, *Appl. Magn. Reson.* **2**, 217 (1991)
- [157] M. Bloom, E.L. Hahn, and B. Herzog, *Phys. Rev.* **97**, 1699 (1955)
- [158] T.P. Das and A.K. Saha, *Phys. Rev.* **98**, 516 (1955)
- [159] V.B. Cheng, H.H. Suzukawa, and M. Wolfsberg, *J. Chem. Phys.* **59**, 3992 (1973)
- [160] A.L. Greenberg and G.H. Walden, *J. Chem. Phys.* **8**, 645 (1940)
- [161] T.J. Seed, *J. Chem. Phys.* **41**, 1486 (1964)
- [162] R. Bramley and S.J. Strach, *Chem. Phys. Lett.* **79**, 183 (1981)
- [163] S.S. Ishchenko, V.G. Grachev, S.M. Okulov, and A.A. Klimov, *Zh. Eksp. Teor. Fiz.* **93**, 2102 (1987); *Sov. Phys. JETP* **66**, 1200 (1987)
- [164] I. Chan, J. Schmidt, and J.H. van der Waals, *Chem. Phys. Lett.* **4**, 269 (1969)
- [165] Ch.B. Harris, D.S. Tinti, M.A. El-Sayed, and A.H. Maki, *Chem. Phys. Lett.* **4**, 409 (1969)
- [166] G. Sierra, Ph.D. Thesis, ETH Zurich, in preparation
- [167] G. Sierra and A. Schweiger, *Rev. Sci. Instrum.*, submitted for publication
- [168] H.C. Torrey, *Phys. Rev.* **76**, 1059 (1949)
- [169] St. Stoll, diploma thesis, TU Graz (1996)
- [170] M. Willer and A. Schweiger, Proceedings of the 38th Rocky Mountain Conference on Analytical Chemistry, Abstract No. 167 (1996)
- [171] I. Solomon, *Phys. Rev. Lett.* **2**, 301 (1959)
- [172] S.R. Hartmann and E.L. Hahn, *Phys. Rev.* **128**, 2042 (1962)
- [173] M. Kunitomo, T. Endo, S. Nakanishi, and T. Hashi, *Phys. Rev.* **A25**, 2235 (1982)
- [174] T.F. Prisner, *Pulsed High-field/ High-frequency EPR*, Habilitationsschrift, FU Berlin (1995)
- [175] Ya.S. Lebedev, *Appl. Magn. Reson.* **7**, 339 (1994)
- [176] R.T. Weber, J.A.J.M. Disselhorst, L.J. Prevo, J. Schmidt, and W.Th. Wenckebach, *J. Magn. Reson.* **81**, 129 (1989)
- [177] J.A.J.M. Disselhorst, H. van der Meer, O.G. Poluektov, and J. Schmidt, *J. Magn. Reson.* **A115**, 183 (1995)
- [178] T. F. Prisner, M. Rohrer, and K. Möbius, *Appl. Magn. Reson.* **7**, 167 (1994)
- [179] A. Yu. Bresgunov, A.A. Dubinskii, V.N. Krimov, Yu.G. Petrov, O.G. Poluektov, and Ya.S. Lebedev, *Appl. Magn. Reson.* **2**, 715 (1991)

-
- [180] T.F. Prisner, S. Un, and R.G. Griffin, *Isr. J. Chem.* **32**, 357 (1992)
- [181] C. Kutter, H.P. Moll, J. van Tol, H. Zuckermann, J.C. Maan, and P. Wyder, *Phys. Rev. Lett.* **74**, 2925 (1995)
- [182] L.R. Beccera, G.J. Gerfen, B.F. Bellew, J.A. Bryant, D.A. Hall, S.J. Inati, R.T. Weber, S. Un, T.F. Prisner, A.E. McDermott, K.W. Fishbein, K.E. Kreischer, R.J. Temkin, D.J. Singel, and R.G. Griffin, *J. Magn. Reson.* **A117**, 28 (1995)
- [183] P. Schosseler, Th. Wacker, and A. Schweiger, *Chem. Phys. Lett.* **224**, 319 (1994)
- [184] G.A. Rinard, R.W. Quine, and G.R. Eaton, Proceedings of the 38th Rocky Mountain Conference on Analytical Chemistry, Abstract No. 147 (1996)
- [185] S. Pfenninger, W. Froncisz, J. Forrer, J. Luglio, and J.S. Hyde, *Rev. Sci. Instrum.* **66**, 4857 (1995)
- [186] Bruker AG, *PatternJet E 585 nanosecond pulse programmer specification*
- [187] H.M. McConnell, *Proc. Natl. Acad. Sci USA*, **44**, 766 (1958)
- [188] F.K. Kneubühl, *Phys. Kondens. Mater* **1**, 410 (1963)
- [189] F.K. Kneubühl, *Phys. Kondens. Mater* **4**, 50 (1965)

Subject Index

- anisotropy 24, 193
anisotropy-resolved ESR 214
average Hamiltonian theory 80, 113
- blind spot 97, 124
 elimination 95, 98
 spin-locked ENDOR 153
- Bloch-Siegert shift 81, 91, 153
Boltzmann equilibrium 34, 47, 76
- chemical shift anisotropy 27
chirp pulse 83, 101, 233, 243
 as tool for refocusing 122
 coherence transfer echo detection
 with 185
 in hyperfine spectroscopy 174
 use in hyperfine spectroscopy 126
- coherence 32
 double-quantum 86
 multiple quantum 86
- coherence transfer 70, 76, 104, 116
coherence transfer echo 119, 132
coherent Raman beat 65, 66, 91, 110–
 113, 232, 234
 spin diffusion in 112
- combination peak 78, 206
continuous-wave methods 18, 213
correlation experiment 93, 124, 229
 at zero field 210
 ELDOR 230
 hyperfine spectroscopy 167
 HYSORE-type 128
 TRIPLE-type 129
 with hyperfine decoupling 145, 149,
 150
- CRB. *See* coherent Raman beat
- Cu(II)
 α -picolinate 181
 bis(glycinato) complex 179
 bis(glycinato) complex 126
 tetraimidazole complex 156
- Davies-ENDOR 101, 124, 128
 zero-field 208
- dead time 108, 109, 113, 131, 228, 233
- DECENT 150
 at zero field 211
 in strong mixing situations 167
 on disordered systems 156
 on $S > 1/2$ systems 160
 ordered system 156
- DEFENCE 119, 121
density operator 30
density operator formalism 197
deuterium modulation 139
 suppression 141
- dichloroacetamide
 γ -irradiated 154
- dipole-dipole coupling
 electron-nuclear 25, 165
 nuclear-nuclear 28

- disordered system 229
 - coherence refocusing 118
 - ESEEM on 131
 - ESR resolution 230
 - high resolution 193
 - hyperfine decoupling 156
 - hyperfine spectroscopy 169, 183, 186
 - HYSORE peak shape 187
 - nutaton frequency 216, 217
 - resolution 145
- dressed state 73, 153
- earth field 195
- edge echo 136
- effective spin 23
- ELDOR 19, 104, 228, 230, 232
- electric field gradient 27
- electron Zeeman interaction 24, 40, 193
- electron-Zeeman resolved ESR 214
- ENDOR
 - at high fields 227
 - continuous-wave 18, 19
 - hyperfine decoupled 146, 151
 - time-domain 126–130
 - zero-field 194
- EPR 23
- exact cancellation 63, 82, 158, 229
- excitation 56–91
 - bandwidth 40, 227, 228
 - non-selective 42, 58, 70
 - radio frequency 80
 - selective 60, 65
 - semi-selective 63, 68
- F-band 226
- Fermi contact interaction 26
- fictitious spin 40, 48, 148, 249
- fine structure 24
- forbidden transfer 74, 76, 124
- forbidden transition 33, 59, 63, 71, 76, 166, 252
- free radical 17
- g-matrix 24
- Hamiltonian
 - average 80, 113
 - in interaction representation 57
 - nuclear quadrupole part 55
 - nuclear spin 42, 205
 - partitioning 39
 - spin 23–28
 - time-reversal symmetry 31
- Hartmann-Hahn match 70, 73, 91, 191
- high-field approximation 20, 27, 226
- high-field high-frequency ESR 105, 225–228, 232
- high-temperature approximation 34, 226
- Hilbert space 30
 - dimension 39
- hole burning 62, 166, 232
- HYEND 175
 - on disordered systems 186, 192
 - probe-pulse detected 190
 - refocusing in 192
- hyperfine contrast selectivity 95
- hyperfine enhancement 81, 82
 - in $S > 1/2$ systems 163
- hyperfine interaction 25
 - anisotropy 145
 - anomaly 26
 - central atom 40, 231
 - decoupling 71, 145, 249
 - dipolar part 25
 - higher-order terms 26
 - in general symmetry 251
 - influence on nutation frequency 219
 - ligand 40
- hyperfine splitting 46
- HYSORE 119
 - analogous ENDOR experiment 128
 - as basis for hyperfine spectroscopy 171
 - at zero field 210
 - incrementation scheme 121
 - on $S > 1/2$ systems 159
 - peak shape 187
 - remote echo detection 110
 - six-pulse 171
- ideal pulse 20, 42
 - non-selective 58
 - selective 60
 - semi-selective 63
- isotope 26, 206
- Kramers system 195

- ligand interactions 41
- line broadening
 - homogeneous 61
 - inhomogeneous 61, 131
- Liouville space 31
- Liouville-von-Neumann equation 32

- Magnus expansion 80
- master equation
 - for populations 33
 - quantum-mechanical 31
- matched pulse 74, 109
 - optimum length 135
- microwave field 56
 - circularly polarized 57
 - linearly polarized 57, 198
- Mims-ENDOR 163
 - blind spots 100
 - two-dimensional 159
 - zero-field 208
- Mn(II)
 - diaquatetrachloro complex 202
 - hexaquo complex 159, 223
- modulation depth 79, 97
 - enhancement 103, 132
- multiplex advantage 18, 110, 113
- multiplicity 166

- NMR 18, 19, 41, 83, 123
 - pulse-ELDOR detected 232
- non-ideal pulse
 - non-selective 70
 - selective 65
 - semi-selective 68
- non-Kramers system 195
- notched echo 136
- NQR 197, 198
- nuclear quadrupole interaction 27, 55, 145, 229
 - influence on nutation frequency 219
 - refocusing 123, 192
 - refocusing, failure of 124
 - remote nitrogen 154
 - second order effect 119, 169
 - zero-field ESEEM 201
- nuclear Zeeman interaction 27, 40, 73, 145
 - anisotropy 27
 - apparent anisotropy 148
 - nuclear-Zeeman splitting 46
 - nutation frequency 58, 214
 - nuclear 82
 - radio frequency resonance 154
 - orientation selection 175, 217

- PEANUT 220
- PEANUT-ENDOR 153
- point-dipole approximation 26
- polarization 85, 86, 231
- poly(isobutene) 139
- poly(vinylidene)fluoride 183, 188
- polymer 139, 183
- population 32
- probe pulse 110, 190, 228, 232
- product operator formalism 33, 49, 85
 - expectation value in 37
- product rule 41

- Q-value 194, 228, 233, 234

- radio frequency field 80
- rare earth ion 23
- relaxation 19, 31, 33, 131
 - at high field 225, 232
 - measurement 37
 - nuclear spin 83, 103
 - superoperator 31
 - transverse 61
- relaxation time
 - longitudinal 33
 - rotating frame 135
 - transverse 28, 74
- remote echo detection 109
- resolution enhancement 93, 128, 145, 169, 193, 213, 225
- resonator 36, 194
 - bandwidth 228
 - bimodal 233
 - bridged loop-gap 194, 233
 - dielectric 194
 - field homogeneity 216
 - loop-gap 194
 - whispering gallery 194
- rotary echo 153, 220
- rotating frame 56, 80, 153, 197

- S-band 170, 194, 211, 233
SENSE subsequence 93
sensitivity enhancement 76, 103, 109,
132, 135, 225
shaped pulse 235
sign determination 122, 124, 226
single-spin spectroscopy 30
soft ESEEM 105, 228
solid echo 123
spectral hole burning *see* hole burning
spin diffusion 97, 103, 107, 112, 127
spin label 139, 183
 interaction with matrix 188
spin temperature 33
spin-locked ENDOR 151, 162
spin-locked ESEEM 148
spin-orbit coupling 23–25
stimulated echo 97
strain 195
strong mixing situation 145, 154, 162,
167
superhyperfine interaction 26
symmetry 24, 26
- TEMPOL 139
TEMPON 183, 188
tensor
 vs. interaction matrix 24, 252
three-pulse ESEEM 111, 131, 150, 154
 zero-field 200, 204
Torrey oscillation 214
transient nutation 213, 233
transition metal 40
 complex 26
 ion 23
transition metal ion 17
transition moment 40, 44, 46, 148, 216
transition probability 215
 see also transition moment
- TRIPLE 124, 129
 at zero field 210
two-pulse ESEEM 131, 142, 149
 zero-field 199, 204
- V(0)
 bis(η_6 -benzene) complex 183
VO(IV)
 pentaquo complex 142
- W-band 220, 225, 226, 227, 228
X-band 226, 227, 228, 230, 233
zero-field spectroscopy 193
zero-field splitting 24, 40, 194, 225, 232
 influence on nutation frequency 219

Acknowledgements

I wish to thank

-
- Prof. Dr. Arthur Schweiger who provided the ideal mixture of stimulation and scope to keep me spinning all the time.
 - Prof. Dr. Richard R. Ernst who teaches to think about things more thoroughly.
 - Dr. Rainer Bachmann who will find you any sign error,¹ any impurity, and any omitted thought.
 - Joe Eisenegger who builds any mechanical device you can imagine. And if you need a device that you cannot imagine, he can still build it.
 - Jörg Forrer who built the little electronic things that made the big machines work and fixed the big machines when they were broken.
 - Willy Groth who built what was needed for the ESP 380 installation.
 - Dr. Peter Höfer from Bruker who coached me on the ESP 380 and kept the advice coming whenever I called him up.
 - Dr. Eric C. Hoffmann who introduced me into the mysteries of Mathematica and into getting short results from extensive derivations.
 - Dr. Michael Hubrich who was the very demanding and very stimulating first author of a very long paper that I co-authored.

1. Unfortunately, Rainer has not yet read my whole thesis.

-
- Andreas Hunkeler who always found a way to satisfy my immense helium thirst.
 - Walter Lämmli who prepared all the samples used in this work and whom I admire for his lifestyle.
 - Erwin Pleisch who also knows about my helium thirst.
 - Dr. Alessandro Ponti who discussed a lot of things with me, first personally, than per e-mail.
 - Dr. Rafail Rakhmatoulline who knows about rare earth ions.
 - Axel Sammet who knows about good textbooks.
 - Paul Schosseler who makes few remarks. But these are remarkable.
 - Dr. Jochen Sebbach who told me in the beginning which articles to read and which programs to learn.
 - Dr. Johan Shane who will never be satisfied with any hardware you have. But he will know how to improve it.
 - Gustavo A. Sierra who has always a tip if you have a problem, be it about software or hardware.
 - Stefan Stoll who as a diploma student had always a question that kept me on my toes intellectually. And who filled our labs with his wonderful flute music.
 - Dr. Sabine van Doorslaer who knows about *real* samples. She also knows how to lead immense numbers of physicists and chemists into pubs and onto football fields.
 - Michael Willer who taught me two crash courses on measuring with the home-built machines. And I crashed neither of these machines (only parts, sometimes).
 - Verena Baumann, Konrad Boss, Karl Burkhalter, Walter Jäggi, Doris Kaufmann, Irene Müller, Marie-Therese Werder, and Heinrich Willi who were always there when I needed something, broke something, or did not know which form to fill in.
 - All the other people who contributed.
 - Stiftung Stipendienfonds of the Verband der Chemischen Industrie Germany for a Kekulé grant.

Curriculum vitae

Personal data

Name Gunnar Jeschke
Birthdate 19th May 1966
Birthplace Cottbus, German Democratic Republic
Citizenship German

Education

1972-1980 Primary and secondary school in Schwarzheide, GDR
1980-1984 High school in Lauchhammer, GDR

Studies

1988-1992 Studies of chemistry at the Technical University in Dresden, Germany
work in solid-state NMR on phosphorous compounds
1992 Diploma thesis "Errors in the Measurement and Evaluation of Solid-
State MAS NMR spectra. Causes and Elimination."
supervised by Prof. Grossmann, Lohmann medal of the TU Dresden
1992-1993 Research stay at the Institute of Physical and Chemical Research
(RIKEN) in Wako-shi, Japan, work in photochemistry
1993-1996 Postgraduate studies in the research groups of Prof. Dr. R. Ernst and
Prof. Dr. A. Schweiger in solid-state pulse ESR spectroscopy

